Separation of Muons and Pions in the Electronic Detector of OPERA

by Applying Classical Cuts

Diploma Thesis
Institut für Experimentalphysik
Universität Hamburg

– Corrected Version –

by
Annika Hollnagel
August 2010

Universität Hamburg

Separation of Muons and Pions in the Electronic Detector of OPERA

Abstract

Within the framework of this diploma thesis, new separation criteria for the identification of $\mu^{\pm}$ leptons and $\pi^{\pm}$ mesons – corresponding to the identification of ν_μ DIS CC and ν_μ DIS NC CNGS beam interactions – in the electronic detector of the OPERA experiment have been developed.

By taking into account several parameters related to the first reconstructed track of a detector event – namely the track length, the energy reconstructed inside the TT scintillators, the reconstructed momentum and its variance – the identification efficiencies and purities for both particle / interaction types could be significantly improved. This was shown by application of the respective cuts on MC-generated data.

Separation von Myonen und Pionen im Elektronischen Detektor von OPERA

Kurzfassung

Im Rahmen dieser Diplomarbeit wurden neue Separationskriterien zur Identifikation von $\mu^{\pm}$-Leptonen und $\pi^{\pm}$-Mesonen – entsprechend der Identifikation von ν_μ DIS CC und ν_μ DIS NC CNGS-Strahlwechselwirkungen – im elektronischen Detektor des OPERA-Experimentes entwickelt.

Durch Berücksichtigung verschiedener, auf die erste rekonstruierte Spur eines Detektorereignisses bezogener, Parameter – insbesondere der Spurlänge, der in den TT-Szintillatoren rekonstruierten Energie, des rekonstruierten Impulses und seiner Varianz – konnten die Identifikationseffizienzen und -reinheiten beider Teilchen- bzw. Wechselwirkungsarten signifikant verbessert werden. Dies wurde durch Anwendung der betreffenden Schnitte auf MC-generierte Daten demonstriert.

Contents

Chapter 1

Introduction

The OPERA[1] experiment is a neutrino oscillation experiment. Its detector is situated at the world's largest underground laboratory for particle physics LNGS[2] in Central Italy.

Studying the CNGS[3] ν_μ beam – created using the SPS[4] at CERN[5] – after a distance of 732 km from its source, the goal of OPERA is the first direct observation of $\nu_\mu \rightarrow \nu_\tau$ transitions by proving the appearance of ν_τ.

The detector itself has a hybrid structure: It consists of two Pb target units equipped with photo emulsions (totaling a target mass of about 1.25 kt), allowing the reconstruction of the $\sim$ 600 μm long tracks of τ^- leptons created in ν_τ CC[6] reactions within the Pb. Via an electronic detector and spectrometer, the charged τ^- lepton decay products, as well as μ^- or hadrons, created in ν_μ CC and NC[7] reactions, are identified, and their charge and momentum reconstructed.

As the hadrons created in ν_μ NC reactions and hadronic τ^- lepton decays are primarily $\pi^\pm$, which are of similar mass as the μ^- created in ν_μ CC reactions or from muonic τ^- decays, and therefore easily mistaken for each other, the separation of these particles is of fundamental importance for the OPERA experiment.

While the identification of particles within the photo emulsions has been detailed in other publications and notes (see e.g. [Roy05]), the focus of this diploma thesis lies on the separation of $\pi^\pm$ and $\mu^\pm$ inside the electronic detector of the OPERA experiment.

Chapter 2 will give a summary of neutrino physics, first describing the Standard Model of particle physics and the history of neutrino physics, before focusing on neutrino oscillations, being the main interest of the OPERA experiment. The open question of whether the neutrino is its own antiparticle is briefly discussed, and the chapter concludes with an overview of other neutrino experiments.

---

[1] OPERA: Oscillation Project with Emulsion tRacking Apparatus; Hybrid detector; LNGS, Gran Sasso, Italy; 2008−?.
[2] LNGS: Laboratori Nazionali del Gran Sasso; Gran Sasso, Italy.
[3] CNGS: CERN Neutrinos to Gran Sasso.
[4] SPS: Super Proton Synchrotron; CERN, Geneva, Switzerland; 1976−?.
[5] CERN: European Organization for Nuclear Research; Geneva, Switzerland.
[6] CC: Charged current.
[7] NC: Neutral current.

In Chapter 3, the energy loss and passage of particles through matter is described, explaining ionisation, multiple scattering, and the interactions of γ and $e^{\pm}$.

Chapter 4 details the OPERA experiment, starting with a description of the CNGS neutrino beam, before explaining the OPERA detector, the data analysis process, expected event topologies, and the sensitivity and physics reach of the experiment.

The OPERA software framework and data structure are explained in Chapter 5.

Chapter 6 forms the main part of this thesis, describing first the importance of $\pi^{\pm}$ / $\mu^{\pm}$ separation for the OPERA experiment and the corresponding difficulties, then the current implementation of $\mu^{\pm}$ identification for the electronic detector of OPERA. Subsequently, the Monte Carlo simulations used within the scope of this thesis are presented, followed by a detailed analysis of their properties, with the goal of finding suitable cut criteria for the separation of $\pi^{\pm}$ and $\mu^{\pm}$. Afterwards, the performance of the selected cuts on the simulated data is demonstrated, in comparison to the performance of the old cut criteria.

A summary of the analysis conducted within the framework of this diploma thesis is given in Chapter 7, along with an outlook on how the $\pi^{\pm}$ / $\mu^{\pm}$ separation might be further improved in the future.

In the following, the natural units of particle physics will be used, implying the reduced Planck constant $\hbar = 6.58211899 \cdot 10^{22}\,\mathrm{MeV\,s}$ and the speed of light in vacuum $c = 299{,}792{,}458\,\mathrm{m\,s^{-1}}$ to be set to $\hbar = c = 1$. Thus, the units of energies, momenta, and masses will all be eV, if not noted otherwise.

Chapter 2

Fundamentals of Neutrino Physics

To understand the process of neutrino oscillations, whose demonstration is the goal of the OPERA experiment, some essential understanding of the Standard Model of particle physics and beyond it is needed. This chapter will first give a short description of the Standard Model of particle physics and its interactions (Chapter 2.1), then provide an overview of the history of neutrino physics by presenting some important discoveries (Chapter 2.2), before explaining the theory and state of knowledge of neutrino oscillations (Chapter 2.3) and the open question whether the neutrino is its own antiparticle (Chapter 2.4), finally concluding with a summary of other experiments concerning neutrinos (Chapter 2.5).

2.1 The Standard Model of Particle Physics

The Standard Model (SM) of particle physics summarises the current state of knowledge concerning the elementary particles and their interactions. It is a gauge theory based on the mathematical framework of local $SU(3) \otimes SU(2) \otimes U(1)$ invariance with spontaneously broken symmetry. Three different types of fields, or particles, are described: The gauge fields, the fermion[1] mass fields, and the Higgs[2] field.

The twelve gauge fields account for the eight spin 1 bosons[3] mediating the strong interaction (the gluons g) and the four vector bosons[4] of the electroweak theory ($W^{\pm}$, Z^0, γ).

The fermion fields, describing quarks and leptons, are two-component spinor fields, arranged in three families, or generations, of identical structure. While the leptons only interact via the electromagnetic and weak interactions, the quarks are subject to all three interactions, including the strong interaction.

Lastly, the masses of the elementary particles are introduced via the Higgs field. Its gauge boson, the Higgs boson H, has not yet been observed, however new experiments at the LHC[5] at CERN might soon change this.

Table 2.1 shows the properties of the twelve elementary fermions: The three flavours of electrically charged leptons e (electron), μ (muon), τ (tauon), and their corresponding neutrinos

[1] Fermion: A particle of half-integer spin, subject to the Pauli exclusion principle.
[2] Higgs mechanism: Responsible for the elementary particle masses, named after physicist P. Higgs.
[3] Boson: A particle of integer spin, not subject to the Pauli exclusion principle.
[4] Vector boson: A boson of spin 1.
[5] LHC: Large Hadron Collider; CERN, Geneva, Switzerland; 2009−?.

ν_e (electron-neutrino), ν_μ (muon-neutrino), ν_τ (tau-neutrino), which do not carry electric charge, and the six quarks u (up), d (down), c (charm), s (strange), t (top), b (bottom), which are of fractional electric charge.

	I	II	III	Y	I	I_3	Q
Leptons	$\begin{pmatrix}\nu_e\\ e\end{pmatrix}_L$	$\begin{pmatrix}\nu_\mu\\ \mu\end{pmatrix}_L$	$\begin{pmatrix}\nu_\tau\\ \tau\end{pmatrix}_L$	-1	$+\frac{1}{2}$	$+\frac{1}{2}$ $-\frac{1}{2}$	0 -1
	e_R	μ_R	τ_R	-2	0	0	-1
Quarks	$\begin{pmatrix}u_i\\ d'_i\end{pmatrix}_L$	$\begin{pmatrix}c_i\\ s'_i\end{pmatrix}_L$	$\begin{pmatrix}t_i\\ b'_i\end{pmatrix}_L$	$+\frac{1}{3}$	$+\frac{1}{2}$	$+\frac{1}{2}$ $-\frac{1}{2}$	$+\frac{2}{3}$ $-\frac{1}{3}$
	$u_{i,R}$	$c_{i,R}$	$t_{i,R}$	$+\frac{4}{3}$	0	0	$+\frac{2}{3}$
	$d_{i,R}$	$s_{i,R}$	$b_{i,R}$	$-\frac{2}{3}$	0	0	$-\frac{1}{3}$

Table 2.1: Properties of quarks and leptons. Shown are the three generations of left- (L) and right-handed (R) elementary fermions and their quantum numbers of weak hypercharge Y, weak isospin I and I_3, and electric charge Q. Antiparticles have the same quantum numbers, but with reversed sign. $i = R, G, B$ denotes the three QCD colour states, and the primed states d', s', b' are mixed states in regard to the strong interaction eigenstates d, s, b.

For each of the quarks and leptons, there also exists an antiparticle that has the same characteristics (e.g. mass m) as its corresponding particle but opposite signs of additive quantum numbers, such as electric charge Q, colour charge, and lepton number L_α (with $\alpha = e, \mu, \tau$).

While the accuracy of the Standard Model has been tested and established by many experiments to a very high degree, in its simplest form, it treats neutrinos as massless particles[1] and thus has to be expanded to allow for neutrino masses and oscillations. Furthermore, massive neutrinos need not be of fixed helicity[2] ($H = -\frac{1}{2}$ for neutrinos and $H = \frac{1}{2}$ for antineutrinos, as supposed by the Standard Model), so, when going beyong the Standard Model and allowing for neutrino masses, it should also be possible to observe neutrinos of positive and antineutrinos of negative helicity.

With its different fields, the Standard Model describes three fundamental types of interactions of whose properties a short summary shall be given in the following: The electromagnetic interaction, the weak interaction (both summarised as the electroweak interaction, some aspect of whose theory shall be explained in more detail because of its importance to neutrino

[1] This, however, is not strictly required by gauge invariance, as it is for the photon and gluons.

[2] Helicity $H = \boldsymbol{s} \cdot \frac{\boldsymbol{p}}{|\boldsymbol{p}|}$: Projection of the spin $\boldsymbol{s}$ onto the direction of momentum $\boldsymbol{p}$. Massless particles moving at the speed of light c always have negative helicity $H = -|\boldsymbol{s}|$, while for all particles moving at less than c, there exist reference frames realising negative and positive helicity.

physics, see Chapter 2.1.3), and the strong interaction. Gravitation, the forth fundamental interaction, could not yet be included into the theoretical framework of the Standard Model, however – due to the small masses of the elementary particles – it is not relevant at the scales of particle physics, anyway.

All of these interactions are mediated by virtual gauge bosons.

2.1.1 The Electromagnetic Interaction (QED)

The intermediate gauge boson of the electromagnetic interaction, its theory being quantum electro dynamics (QED), is the massless photon γ, which couples to the electric charge. See Figure 2.1 for a typical Feynman graph[1] of electromagnetic interaction mediated by a photon.

With the photon itself being electrically neutral, there is no self-coupling. Due to the non-existent rest mass of the photon, its lifetime is unlimited, resulting in the infinite reach of the electromagnetic interaction.

All particles carrying electric charge are subject to the electromagnetic interaction: e^-, μ^-, τ^-, the quarks, and their respective antiparticles, as well as the $W^\pm$ bosons.

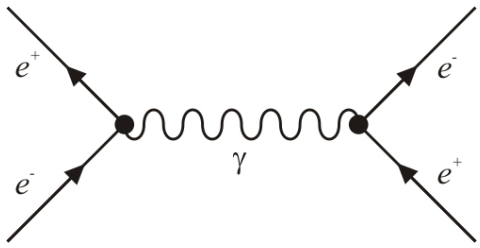

Figure 2.1: Feynman graph: $e^+ + e^- \to \gamma \to e^- + e^+$.

2.1.2 The Weak Interaction

The charge of the weak interaction is the weak charge, its gauge bosons are the electrically charged $W^\pm$ bosons, mediating the charged currents (CC), and the electrically neutral Z^0 boson, representing the neutral currents (NC). See Figures 2.2 and 2.3 for typical weak interaction processes by exchange of a Z^0 boson or W^- boson, respectively.

As the gauge bosons of the weak interaction are massive particles ($M_{W^\pm} = (80.398 \pm 0.025)\,\mathrm{GeV}$, $M_{Z^0} = (91.1876 \pm 0.0021)\,\mathrm{GeV}$ [PDG08]), their lifetime – and thus also the reach of the weak interaction – is limited:

$$R = \frac{\hbar}{mc}, \tag{2.1}$$

where R equals the reach of the interaction, $\hbar$ is the reduced Planck constant, m is the mass of the intermediate gauge boson, and c is the speed of light in vacuum.

[1] Feynman graph: A graphical depiction of scattering processes in particle physics, invented by R. Feynman.

The weak interaction operates on all fundamental fermions, however only left-handed particles and right-handed antiparticles are subject to it, implying a violation of parity[1] invariance. The coupling strength of the weak interaction to leptons of all generations is the same (Lepton Universality), and in all its processes, the lepton number L_α (with $\alpha = e, \mu, \tau$) has to be conserved.

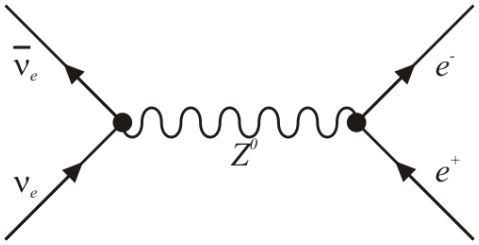

Figure 2.2: Feynman graph: $\overline{\nu}_e + \nu_e \rightarrow Z^0 \rightarrow e^- + e^+$ (NC).

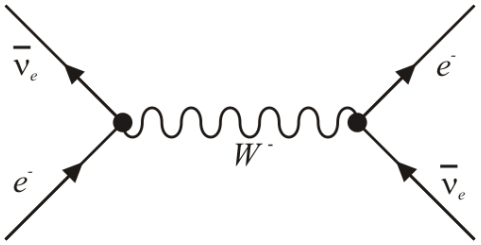

Figure 2.3: Feynman graph: $\overline{\nu}_e + e^- \rightarrow W^- \rightarrow e^- + \overline{\nu}_e$ (CC).

2.1.3 The Electroweak Unification (GSW Theory)

Based on the group $SU(2)_L \otimes U(1)_Y$, the electroweak unification (also called GSW theory[2]) presents a unified theory of electromagnetic and weak interaction that has later been extended also to the hadronic sector[3] and quark flavour mixing[4].

The gauge fields of $SU(2)_L$, corresponding to the weak isospin I, are the triplet W_1^μ, W_2^μ, W_3^μ that exclusively couple to fermions of left-handed chirality[5], or right-handed antifermions, and thus violate parity invariance. As this coupling is conducted via a common coupling constant g, its strength is the same for all particles being subject to the interaction – namely leptons of all flavours – resulting in the so-called 'Lepton Universality'.

The group $U(1)_Y$ associated to the weak hypercharge Y, on the other hand, is represented by the singlet B^μ with the coupling constant g', affecting both left- and right-handed fermions.

The fields of the physical gauge bosons $W^\pm$ are obtained via the transformations:

$$W^{(\pm)\mu} = \frac{1}{\sqrt{2}}(W_1^\mu \pm iW_2^\mu). \tag{2.2}$$

Thus resulting from a transformation of the gauge bosons W_1^μ , W_2^μ and only coupling to left-handed particles and right-handed antiparticles, the electrically charged $W^\pm$ bosons are the force carriers of the so-called charged weak currents CC with the coupling constant g_{CC}:

$$g_{CC} = \frac{g}{2\sqrt{2}}. \tag{2.3}$$

[1] Parity: Flip of one spatial coordinate.
[2] GSW theory: Named after physicists S. L. Glashow, A. Salam, and S. Weinberg.
[3] By physicists S. L. Glashow, J. Iliopoulos, L. Maiani.
[4] By physicists N. Cabibbo, M. Kobayashi, K. Maskawa.
[5] Chirality: Determined by the sign of a particle's helicity $H = s \cdot \frac{p}{|p|}$. If $H > 0$, the particle is called 'right-handed' (R), if $H < 0$, it is 'left-handed' (L). Thus, massless particles are always left-handed, while antiparticles are always right-handed.

Z^μ and A^μ – the fields of the physical gauge bosons Z^0 and γ – are acquired according to:

$$\begin{pmatrix} Z^\mu \\ A^\mu \end{pmatrix} = \begin{pmatrix} \cos\theta_W & -\sin\theta_W \\ \sin\theta_W & \cos\theta_W \end{pmatrix} \times \begin{pmatrix} W_3^\mu \\ B^\mu \end{pmatrix}, \tag{2.4}$$

with θ_W being the electroweak mixing angle:

$$\cos\theta_W = \frac{g}{\sqrt{g^2+g'^2}} \qquad \text{and} \qquad \sin\theta_W = \frac{g'}{\sqrt{g^2+g'^2}}. \tag{2.5}$$

A^μ can be identified with the massless photon γ, mediating the electromagnetic interaction and coupling to electric charge via its coupling constant e:

$$e = \frac{g \cdot g'}{\sqrt{g^2+g'^2}} = g \cdot \sin\theta_W = g' \cdot \cos\theta_W. \tag{2.6}$$

The electrically neutral Z^0 boson mediating the neutral weak currents NC, represents a mixed state of $W^\mu_{(3)}$ and B^μ, its coupling g_{NC} being:

$$g_{NC} = \frac{1}{2}\sqrt{g^2+g'^2} = \frac{e}{2\sin\theta_W\cos\theta_W}. \tag{2.7}$$

The masses of the massive gauge bosons $W^\pm$ and Z^0 are introduced via the scalar Higgs field:

$$\Phi = \frac{1}{\sqrt{2}}\begin{pmatrix} \Phi_1 + i\Phi_2 \\ \Phi_3 + i\Phi_4 \end{pmatrix} \qquad \text{and} \qquad \Phi_0 = \frac{1}{\sqrt{2}}\begin{pmatrix} 0 \\ v \end{pmatrix}, \tag{2.8}$$

with $v^2 > 0$, rendering the vacuum expectation value Φ_0 nonzero.

By coupling to the Higgs field, the isospin rotation symmetry of the massless gauge fields W_i^μ is spontaneously broken, leading to non-diagonal mass terms for the gauge fields in the Lagrangian energy density[1], thus effecting the above-mentioned transformations for the physical gauge fields, and resulting in the masses of the gauge bosons:

$$M_W = \frac{gv}{2} \tag{2.9}$$

$$M_Z = \frac{v}{2}\sqrt{g^2+g'^2} = \frac{M_W}{\cos\theta_W} \tag{2.10}$$

$$M_A = 0. \tag{2.11}$$

2.1.4 The Strong Interaction (QCD)

Quantum chromo dynamics (QCD), or the Yang-Mills[2] theory of strong interaction, is a non-abelian gauge theory[3] based on the local gauge group $SU(3)$. Its gauge bosons are the

[1] The Lagrangian of a system, named after J. L. Lagrange, summarises its dynamics. In field theory, the Lagrange function $L = T - V$ of classical dynamics converts into an integral over the Langrangian energy density.

[2] Yang-Mills theory: Named after physicists C. N. Yang and R. Mills.

[3] In contrast to QED, which is – due to its commutative symmetry group $U(1)$ – an abelian gauge theory. A characteristic of non-abelian gauge theories (with non-commutative symmetry groups) is their asymptotic freedom.

massless and electrically neutral gluons g that couple to colour, the charge of the strong interaction. See Figure 2.4 for a typical Feynman graph of strong interaction mediated by a gluon.

As the gluons themselves are carriers of colour charge (and, simultaneously, anti-colour charge), their self-coupling leads to an amplification of the interaction with growing distance, making the creation of quark-antiquark pairs energetically favourable to greater dislodgement of two individual quarks. This results in the the so-called quark confinement: The colour-charged quarks are being confined inside colour-neutral hadrons (mesons $q\overline{q}$ and baryons qqq) and may only be studied singly at very high energies (asymptotic freedom).

All quarks and gluons are subject to the strong interaction.

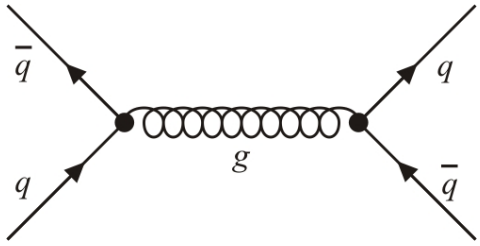

Figure 2.4: Feynman graph: $\overline{q} + q \rightarrow g \rightarrow q + \overline{q}$.

2.2 History of Neutrino Physics

2.2.1 'Invention' of the Neutrino (1930)

In 1930, the neutrino[1] was first postulated by W. Pauli as a hypothetical particle to ensure the conservation of energy during radioactive β decay [Pau30]:

$$n \rightarrow p^+ + e^- + \overline{\nu}_e, \tag{2.12}$$

where n and p^+ depict a neutron and proton, respectively, and $\overline{\nu}_e$ is the electron antineutrino.

The continuous spectrum $N(E)$ of the kinetic energy of the electron (see Figure 2.5) observed by L. Meitner and O. Hahn in 1911 could not be explained with a two-body decay: Without another yet undetected particle – the neutrino – carrying away some energy, the electron should always have the fixed kinetic energy E_{max}. Furthermore, this neutrino had to be of half-integer spin to preserve the angular momentum, as well as spin statistics.

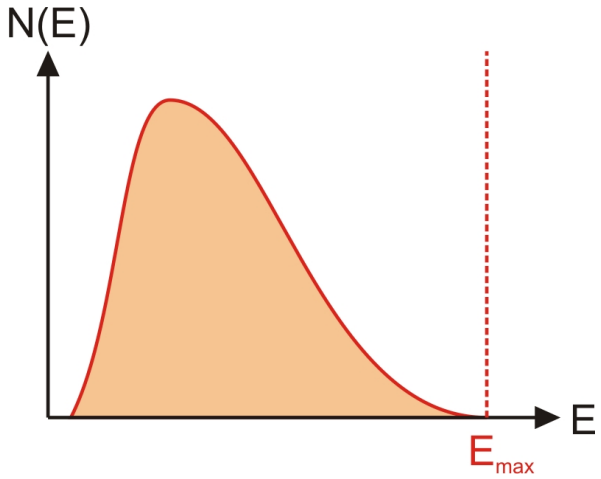

Figure 2.5: Schematic energy spectrum of the electron during radioactive β decay [Chr72]. In a two-body decay, the energy would be fixed at E_{max}, while in a three-body decay, it is continuous.

2.2.2 Discovery of the Neutrino (1956)

Due to the small cross section of the neutrino with matter ($\sigma = (1.1 \pm 0.3) \cdot 10^{-43}$ for Equation 2.13 [Rei59]), it took another 26 years until, in 1956, its existence could finally be proven by F. Reines and C. L. Cowan (Cowan-Reines Experiment[2]), using $\overline{\nu}_e$ with energies of some MeV from β decays (see Equation 2.12) at the Savannah River nuclear reactor[3] [Rei56][Rei59]. Their detector consisted of a tank filled with $CdCl_2$ dissolved in H_2O, encompassed by two

[1] At that time, this particle was still called 'neutron', being renamed to 'neutrino' by E. Fermi after the discovery of the neutron.
[2] Cowan-Reines Experiment: Liquid scintillator detector; First Hanford, Washington, then South Carolina; 1956.
[3] Savannah River nuclear reactor: South Carolina.

liquid scintillator detectors. The $\overline{\nu}_e$ reacts with a proton from the aqueous solution according to the so-called inverse β decay:

$$\overline{\nu}_e + p^+ \rightarrow e^+ + n, \tag{2.13}$$

which can be detected using the delayed coincidence technique: A first γ-pulse is created when the e^+ annihilates with an e^- from the surroundings, a second one – some μs later – by the capture of the n in Cd and the subsequent emission of a photon.

2.2.3 Observation of Two Different Kinds of Neutrinos (1962)

At the BNL[1], L. M. Lederman, M. Schwartz, J. Steinberger et al. were able to prove that two different kinds of neutrinos exist [Dan62]. By targeting a 7.5 cm thick Be block with the Brookhaven synchrotron 15 GeV p^+ beam, they created a ν_μ beam with energies of about 300 MeV − 800 MeV resulting from the in-flight decay of the produced $\pi^\pm$ (pi) mesons:

$$\pi^+ \rightarrow \mu^+ + \nu_\mu \qquad \text{or} \qquad \pi^- \rightarrow \mu^- + \overline{\nu}_\mu. \tag{2.14}$$

In a 10 t Al spark chamber detector situated behind a 13.5 m thick Fe absorber, 21 m downstream from the target, neutrino interactions could be observed by taking photos of the sparks created when an ionising particle crossed a spark chamber located between the Al plates. In 29 cases, the observed reaction corresponded to beam-induced reactions:

$$\nu_\mu + n \rightarrow \mu^- + p^+ \qquad \text{or} \qquad \overline{\nu}_\mu + p^+ \rightarrow \mu^+ + n, \tag{2.15}$$

while no similarly created $e^\pm$ could be found. Thus, the neutrinos produced according to Equation 2.14 had to be different from those resulting from radioactive β decay (see Equation 2.12):

$$\nu_\mu \neq \nu_e. \tag{2.16}$$

2.2.4 The Solar Neutrino Problem (1968)

Using the Homestake[2] detector, R. Davis and J. N. Bahcall observed in 1960 a deficit in the solar electron neutrino flux predicted by the Standard Solar Model (SSM) [Dav98].

Their detector was based on the inverse β decay reaction:

$$^{37}\mathrm{Cl} + \nu_e \rightarrow {}^{37}\mathrm{Ar} + e^-, \tag{2.17}$$

inside a tank filled with 615 t of C_2Cl_4, and the help of a low-background proportional counter.

As Davis and Bahcall measured only about 1/3 of the expected ν_e flux, this observation posed for many years a problem – hence called the 'solar neutrino problem' – to the understanding of neutrino production and propagation in the sun.

[1] BNL: Brookhaven National Laboratory; Upton, New York.
[2] Homestake: Radiochemical experiment; Homestake Gold Mine, South Dakota, USA; 1970 – 1994.

In 2001, SNO[1] confirmed this observation via the CC (see Chapter 2.1.3) reaction only possible for electron neutrinos:

$$\nu_e + d^+ \rightarrow e^- + 2p^+, \tag{2.18}$$

within their detector filled with 1000 t of ultra-heavy water (D_2O, or d), while at the same time the NC (see Chapter 2.1.3) reaction, which is open to neutrinos of all flavours:

$$\nu_\alpha + d^+ \rightarrow \nu_\alpha + p^+ + n \tag{2.19}$$

(with $\alpha = e, \mu, \tau$) produced a measured neutrino flux completely consistent with the SSM [SNO02].

These observations are best explained by the theory of neutrino oscillations proposed by B. Pontecorvo [Pon57][Pon69]: Lepton number-violating flavour conversion of neutrinos (see Chapter 2.3).

2.2.5 The Number of Light Neutrino Families (1989)

The number N_ν of light[2] neutrino families may be derived from the decay of Z^0 bosons created in e^+e^- collisions [LEP89]. By subtracting the measured visible partial widths from Z^0 decays into quarks or charged leptons – Γ_{had} and Γ_l, respectively[3] – from the total Z^0 width Γ_{tot}, the invisible partial width Γ_{inv}, which corresponds to decays into neutrinos, can be determined:

$$\Gamma_{inv} = \Gamma_{tot} - (3\Gamma_l + \Gamma_{had}). \tag{2.20}$$

According to the Lepton Universality (see Chapter 2.1.3), the contribution of each neutrino family to Γ_{tot} is expected to be the same as Γ_l. Thus results:

$$N_\nu = \frac{\Gamma_{inv}}{\Gamma_l} = 2.984 \pm 0.008, \tag{2.21}$$

with measurements from LEP[4] at CERN [PDG08].

Figure 2.6 compares the measured cross section of the reaction:

$$e^+ + e^- \rightarrow X, \tag{2.22}$$

where X denotes the hadronic final states, with the theoretical predictions for different numbers of neutrino families.

[1] SNO: Sudbury Neutrino Observatory; Deuterium Čerenkov detector; SNOLAB, Sudbury, Ontario, Kanada; 1999 – 2006

[2] Light neutrinos: Neutrinos with masses $M_\nu < {M_Z}^0/2$.

[3] $l = e, \mu, \tau$.

[4] LEP: Large Electron-Positron Collider; CERN, Geneva, Switzerland; 1989 – 2000.

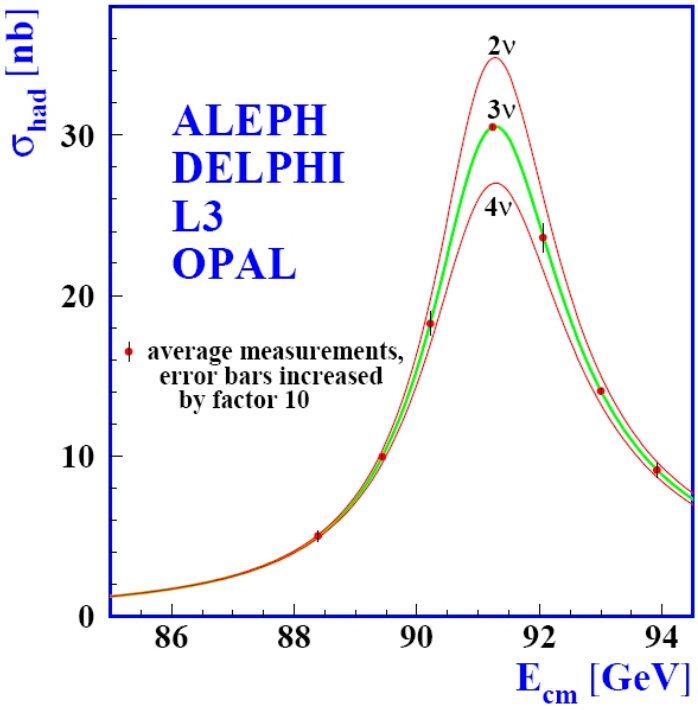

Figure 2.6: Cross section of the reaction $e^+e^- \to X$ vs. center-of-mass energy as well as the theoretical predictions for 2, 3, and 4 generations of light neutrinos [LEP06].

2.2.6 Direct Observation of the ν_τ (2000)

After, in 1975, the τ lepton had been discovered by M. L. Perl et al. with the LBL[1] magnetic detector at the SPEAR[2] e^+e^- collider at SLAC[3] [Per75], and from Z^0 decays at LEP a third generation of neutrinos had been predicted in 1989 (see Chapter 2.2.5), the τ neutrino could finally be observed in 2000 by the DONuT[4] detector [DON00]. Situated at Fermilab[5], the experiment used the 800 GeV p^+ beam provided by the TeVatron[6], directing it at a tungsten alloy target and so creating prompt[7] ν_τ, e.g. via the decay of D_s mesons [DON07]:

$$D_s^+ \to \nu_\tau \tau^+ \qquad \text{or} \qquad D_s^- \to \overline{\nu}_\tau \tau^-. \tag{2.23}$$

The detector itself consisted of a hybrid structure of 250 kg ECC[8] nuclear emulsion targets, SFT[9] for real-time tracking, and a spectrometer (made from a dipole magnet, six drift chambers, an electromagnetic calorimeter, and a muon ID-system) for particle identification and energy measurement.

Via the study of ν_τ CC reactions with the nucleons N in the ECC target (X depicting the

[1]LBL: Lawrence Berkeley Laboratory, Berkeley, California.
[2]SPEAR: Stanford Positron Electron Asymmetric Ring; SLAC, Stanford, California; 1972−?.
[3]SLAC: Stanford Linear Accelerator Center, Stanford, California.
[4]DONuT: Direct Observation of Nu Tau; Hybrid detector; Fermilab, Batavia, Illinois; 1997.
[5]Fermilab: Fermi National Accelerator Laboratory, Batavia, Illinois.
[6]TeVatron: p^+p^- synchrotron with $E_p \leq 1$ TeV; Fermilab, Batavia, Illinois; 1983−?.
[7]Prompt ν_τ: Originating from the decay of charmed particles.
[8]ECC: Emulsion Cloud Chamber.
[9]SFT: Scintillating Fibre Tracker.

respective hadronic or leptonic products):

$$\nu_\tau + N \to \tau^- + X \qquad \text{or} \qquad \overline{\nu}_\tau + N \to \tau^+ + X, \tag{2.24}$$

the DONuT experiment was able to prove the existence of the ν_τ.

2.3 Neutrino Oscillations

In 1957, even prior to the 'solar neutrino problem' (see Chapter 2.2.4), B. Pontecorvo had proposed neutrino oscillations as an analogy to the oscillations of K^0 mesons, implying that the neutrino, too, is a superposition of other particles [Pon57]. These flavour-changing oscillations describe the periodic transition of a neutrino of generation L_α into another neutrino of generation L_β, thus violating lepton number conservation:

$$\nu_\alpha \rightarrow \nu_\beta, \tag{2.25}$$

with $\alpha \neq \beta$.

Neutrinos participating in weak interaction processes are orthonormal eigenstates $|\nu_\alpha\rangle$ of the lepton number operator L_α:

$$L_\alpha|\nu_\beta\rangle = \delta_{\alpha\beta}|\nu_\beta\rangle, \tag{2.26}$$

with $\alpha, \beta = e, \mu, \tau$, assuming three generations of neutrinos. However, these flavour eigenstates differ from the orthonormal mass eigenstates $|\nu_i\rangle$ of the mass operator M:

$$M|\nu_i\rangle = m_i\delta_{ij}|\nu_i\rangle, \tag{2.27}$$

where $i, j = 1, 2, 3$.

With the help of the unitary PMNS[1] mixing matrix U, which is an $n \times n$ matrix with $n^2 - n = n(n-1)$ physically significant free parameters, usually chosen as $\frac{1}{2}(n-1)$ mixing angles and $\frac{1}{2}(n-1)$ complex phases, that satisfies the following equations:

$$U^\dagger U = 1 \tag{2.28}$$

$$\sum_i U_{\alpha i}U^*_{\beta i} = \delta_{\alpha\beta} \tag{2.29}$$

$$\sum_\alpha U_{\alpha i}U^*_{\alpha j} = \delta_{ij}, \tag{2.30}$$

the flavour eigenstates may be expressed as a linear combination of the mass eigenstates:

$$|\nu_\alpha\rangle = \sum_i U^*_{\alpha i}|\nu_i\rangle \qquad \text{and} \qquad |\overline{\nu}_\alpha\rangle = \sum_i U_{\alpha i}|\overline{\nu}_i\rangle, \tag{2.31}$$

and v.v., the mass eigenstates result to:

$$|\nu_i\rangle = \sum_\alpha U_{\alpha i}|\nu_\alpha\rangle \qquad \text{and} \qquad |\overline{\nu}_i\rangle = \sum_\alpha U^*_{\alpha i}|\overline{\nu}_\alpha\rangle. \tag{2.32}$$

As the mass eigenstates are solutions to Schrödinger's Equation – in contrast to the flavour eigenstates which are not – in the laboratory system, their time and space propagation can be described by plane waves:

$$|\nu_i(t,x)\rangle = e^{-i(E_it - p_ix)}|\nu_i\rangle, \tag{2.33}$$

[1]PMNS matrix: Named after physicists B. Pontecorvo, Z. Maki, M. Nakagawa, S. Sakata.

with E_i and p_i being the energy and impulse of the respective mass eigenstate ν_i.

Consequently, neutrinos produced as a certain flavour $|\nu_\alpha\rangle = |\nu_{initial}\rangle$ in weak interaction processes may later – after time and space propagation according to their mass eigenstates took place – be observed to be of a different flavour $|\nu_{final}\rangle$.

$$|\nu_{final}(T,L)\rangle = \sum_i U^*_{\alpha i} e^{-iE_iT} |\nu_i\rangle \tag{2.34}$$

$$= \sum_\beta \sum_i U^*_{\alpha i} U_{\beta i} e^{-i(E_iT - p_iL)} |\nu_\beta\rangle, \tag{2.35}$$

where T is the time that has passed and L the distance travelled with respect to the laboratory system. The probability amplitude for this transition is:

$$\langle \nu_{final}(T,L)|\nu_{initial}\rangle = \langle \nu_\beta| \sum_\beta \sum_i U^*_{\alpha i} U_{\beta i} e^{-i(E_iT - p_iL)} |\nu_\alpha\rangle, \tag{2.36}$$

which results to:

$$\langle \nu_{final}(T,L)|\nu_{initial}\rangle = \sum_i U^*_{\alpha i} U_{\beta i} e^{-i(E_iT - p_iL)}, \tag{2.37}$$

by employing the orthonormality condition $\langle \nu_\beta|\nu_\alpha\rangle = \delta_{\alpha\beta}$.

Thus, the transition probability $P(\nu_\alpha \to \nu_\beta) = P_{\nu_\alpha\nu_\beta}(t,x)$ – being the square of the absolute value of the amplitude – for observing a neutrino created as $|\nu_\alpha\rangle$ in a weak interaction process to be later observed as $|\nu_\beta\rangle$ is:

$$P_{\nu_\alpha\nu_\beta}(T,L) = \left| \sum_i U^*_{\alpha i} U_{\beta i} e^{-i(E_iT - p_iL)} \right|^2, \tag{2.38}$$

with L being the distance between neutrino source and detector, and T the corresponding time of flight.

For neutrinos with rest masses of no more than some eV and energies in the GeV range – as it is the case for the OPERA experiment (see Chapter 4) – being highly relativistic particles with $p \gg m_i$ – it may be presumed that $E \approx p$, resulting in the relativistic approximation:

$$E_i = \sqrt{m_i^2 + p_i^2} \tag{2.39}$$

$$\simeq p_i + \frac{m_i^2}{2p_i} \tag{2.40}$$

$$\simeq E + \frac{m_i^2}{2E}, \tag{2.41}$$

where E denotes the energy of the neutrino.

Further assuming that $L \approx cT$, Equation 2.38 gives:

$$P_{\nu_\alpha\nu_\beta}(L) = \left|\sum_i U^*_{\alpha i} U_{\beta i} e^{-i\frac{m_i^2}{2E}L}\right|^2 \tag{2.42}$$

$$= \sum_{i,j} U^*_{\alpha i} U_{\alpha j} U_{\beta i} U^*_{\beta j} e^{-i\frac{\Delta m^2_{ij}}{2E}L} \tag{2.43}$$

$$= \sum_i |U^*_{\alpha i} U_{\beta i}|^2 + 2Re\sum_{i>j} U^*_{\alpha i} U_{\alpha j} U_{\beta i} U^*_{\beta j} e^{-i\frac{\Delta m^2_{ij}}{2E}L} \tag{2.44}$$

$$= \delta_{\alpha\beta} - 2Re\sum_{i>j} U^*_{\alpha i} U_{\alpha j} U_{\beta i} U^*_{\beta j}\left(1 - e^{-i\frac{\Delta m^2_{ij}}{2}\frac{L}{E}}\right), \tag{2.45}$$

by using Equation 2.29.

It is now obvious that such neutrino oscillations are only possible if $\Delta m^2_{ij} = m^2_i - m^2_j = 0$ does not hold for all Δm^2_{ij}, i.e. not all mass eigenstates $|\nu_i\rangle$ are of the same value. This contradicts the erstwhile assumption of all neutrinos being massless particles, thus requiring an expansion of the Standard Model of particle physics.

2.3.1 3-Flavour Oscillation Formalism

In the case of $n = 3$ orthonormal eigenstates $|\nu_i\rangle$ with $i = 1, 2, 3$ and $|\nu_\alpha\rangle$ with $\alpha = e, \mu, \tau$ – corresponding to three generations of neutrinos – the unitary PMNS mixing matrix U (see Chapter 2.3) features three mixing angles θ_{ij} and three complex phases δ, ϵ_1, and ϵ_2:

$$U = \begin{pmatrix} 1 & 0 & 0 \\ 0 & c_{23} & s_{23} \\ 0 & -s_{23} & c_{23} \end{pmatrix} \times \begin{pmatrix} c_{13} & 0 & s_{13}e^{-i\delta} \\ 0 & 1 & 0 \\ -s_{13}e^{i\delta} & 0 & c_{13} \end{pmatrix} \times \begin{pmatrix} c_{12} & s_{12} & 0 \\ -s_{12} & c_{12} & 0 \\ 0 & 0 & 1 \end{pmatrix} \times \begin{pmatrix} e^{i\epsilon_1/2} & 0 & 0 \\ 0 & e^{i\epsilon_2/2} & 0 \\ 0 & 0 & 1 \end{pmatrix}, \tag{2.46}$$

with the abbreviations $s_{ij} = \sin\theta_{ij}$ and $c_{ij} = \cos\theta_{ij}$.

ϵ_1 and ϵ_2 are the so-called Majorana[1] phases which are irrelevant to neutrino oscillations (but important to e.g. neutrinoless double-β decay, see Chapter 2.4), and δ is the CP-violating[2] Dirac[3] phase, that – if nonzero – would imply different treatment of ν and $\overline{\nu}$. If neutrinos are Dirac particles, $\epsilon_1 = \epsilon_2 = 0$, and the mixing matrix U results to:

$$U = \begin{pmatrix} 1 & 0 & 0 \\ 0 & c_{23} & s_{23} \\ 0 & -s_{23} & c_{23} \end{pmatrix} \times \begin{pmatrix} c_{13} & 0 & s_{13}e^{-i\delta} \\ 0 & 1 & 0 \\ -s_{13}e^{i\delta} & 0 & c_{13} \end{pmatrix} \times \begin{pmatrix} c_{12} & s_{12} & 0 \\ -s_{12} & c_{12} & 0 \\ 0 & 0 & 1 \end{pmatrix} \tag{2.47}$$

$$= \begin{pmatrix} c_{12}c_{13} & s_{12}c_{13} & s_{13}e^{-i\delta} \\ -s_{12}c_{23} - c_{12}s_{23}s_{13}e^{i\delta} & c_{12}c_{23} - s_{12}s_{23}s_{13}e^{i\delta} & s_{23}c_{13} \\ s_{12}s_{23} - c_{12}s_{23}s_{13}e^{i\delta} & -c_{12}s_{23} - s_{12}c_{23}s_{13}e^{i\delta} & c_{23}c_{13} \end{pmatrix}. \tag{2.48}$$

[1] Majorana particle: A fermion that is identical with its antiparticle, $\nu \equiv \overline{\nu}$.
[2] CP violation: Violation of charge-parity invariance, with CP transformation implying the simultaneous flip of a spatial coordinate and the exchange of a particle for an antiparticle.
[3] Dirac particle: A fermion that is not identical with its antiparticle, $\nu \neq \overline{\nu}$.

Usually, the mixing angles are represented by the Euler angles θ_{12}, θ_{23}, and θ_{13} with $0 \leq \theta_{ij} \leq \frac{\pi}{2}$. The complex phase δ, with $-\pi \leq \delta \leq \pi$, is only nonzero if neutrino oscillations violate CP invariance.

In this 3-flavour neutrino oscillation formalism, there are three mass square differences, Δm^2_{21}, Δm^2_{32}, and Δm^2_{31}, with only two of them being linearly independent, due to:

$$\Delta m^2_{31} = \Delta m^2_{32} + \Delta m^2_{21}. \tag{2.49}$$

2.3.2 2-Flavour Oscillation Formalism

By assuming that the mass square differences Δm^2_{21} and $\Delta m^2_{31} \approx \Delta m^2_{32}$ are set apart from each other by at least two orders of magnitude – implying that two generations of neutrinos are of similar mass while the third one is much heavier or lighter – the mixing matrix U may be simplified to a 2×2 rotation matrix with only one rotation angle θ_{ij} and no CP-violating phase, and Equation 2.46 transforms into:

$$\begin{pmatrix} \nu_\alpha \\ \nu_\beta \end{pmatrix} = \begin{pmatrix} \cos\theta_{ij} & \sin\theta_{ij} \\ -\sin\theta_{ij} & \cos\theta_{ij} \end{pmatrix} \times \begin{pmatrix} \nu_i \\ \nu_j \end{pmatrix}, \tag{2.50}$$

with only two flavour eigenstates, $|\nu_\alpha\rangle$ and $|\nu_\beta\rangle$, and two mass eigenstates, $|\nu_i\rangle$ and $|\nu_j\rangle$.

The oscillation probability $P_{\nu_\alpha\nu_\beta}(L)$ (see Equation 2.45) now results to:

$$P_{\nu_\alpha\nu_\beta}(L,E) = \sin^2 2\theta_{ij} \cdot \sin^2\left(\frac{\Delta m^2_{ij}}{4}\frac{L}{E}\right) \tag{2.51}$$

$$= \sin^2 2\theta_{ij} \cdot \sin^2\left(1.27\Delta m^2_{ij}[\mathrm{eV}^2] \cdot \frac{L[\mathrm{km}]}{E[\mathrm{GeV}]}\right), \tag{2.52}$$

where in the last step $\hbar c = 197\,\mathrm{MeV\,fm}$ has been re-converted to SI units. As can be seen, the frequency of these oscillations depends on the mass difference Δm_{ij} of the respective mass eigenstates, while the amplitude is determined by the mixing angle θ_{ij}.

2.3.3 Neutrino Oscillations in Matter

The phenomenological formalism described above applies for neutrino oscillations taking place in vacuum. In the case of neutrinos crossing matter, their interaction via processes of weak interaction has to be taken into account. Named after physicists S. Mikheyev, A. Smirnov, L. Wolfenstein, this is called the MSW effect [Wol78].

On the one hand, coherent forward scattering of neutrinos in matter occurs via the neutral current (NC) reactions by exchange of a Z^0 boson (see Chapter 2.1.3):

$$\nu_\alpha + e^- \rightarrow \nu_\alpha + e^- \tag{2.53}$$

$$\nu_\alpha + p^+ \rightarrow \nu_\alpha + p^+ \tag{2.54}$$

$$\nu_\alpha + n \rightarrow \nu_\alpha + n, \tag{2.55}$$

where $\alpha = e, \mu, \tau$. This introduces effective neutrino masses and phases by shifting the respective eigenvalues of all neutrinos, due to Lepton Universality (see Chapter 2.1.3), by a common amount. As neutrino oscillations are sensisitive to the mass square difference $\Delta^2 m_{ij}$ – which thus remains unchanged – no significant perturbation should be expected from this source.

However, there is also the charged current (CC) process mediated by W^- bosons (see Chapter 2.1.3):

$$\nu_e + e^- \rightarrow e^- + \nu_e, \tag{2.56}$$

which is open exclusively to electron neutrinos, effecting additional shifts for them that have to be taken into account when dealing with $\nu_e \leftrightarrow \nu_\mu$ or $\nu_e \leftrightarrow \nu_\tau$ oscillations (as is the case e.g. for solar neutrino experiments). Depending on deviations of the electron density in the respective matter crossed, there may arise resonances substantially boosting the oscillation probabilities.

Matter effects are negligible for $\nu_\mu \rightarrow \nu_\tau$ oscillations investigated by the OPERA experiment [Fer10b].

2.3.4 State of Knowledge

Table 2.2 lists the state of knowledge 2010 concerning neutrino oscillation parameters, with:

$$\Delta m^2_{21} = m^2_2 - m^2_1 \quad (2.57)$$
$$\Delta m^2_{31} = m^2_3 - m^2_1 \quad (2.58)$$
$$\Delta m^2_{32} = m^2_3 - m^2_2, \quad (2.59)$$

and furthermore:

$$\Delta m^2_{sol} = \Delta m^2_{21} \quad (2.60)$$
$$\Delta m^2_{atm} \approx \Delta m^2_{31} \approx \Delta m^2_{32}. \quad (2.61)$$

Parameter		Best Global Fit	2σ	3σ
Δm^2_{21}	$[10^{-5}\,\mathrm{eV}^2]$	$7.59^{+0.23}_{-0.18}$	$7.22 - 8.03$	$7.03 - 8.27$
$\lvert\Delta m^2_{31}\rvert$	$[10^{-3}\,\mathrm{eV}^2]$	$2.40^{+0.12}_{-0.11}$	$2.18 - 2.64$	$2.07 - 2.75$
$\sin^2\theta_{12}$		$0.318^{+0.019}_{-0.016}$	$0.29 - 0.36$	$0.27 - 0.38$
$\sin^2\theta_{23}$		$0.50^{+0.07}_{-0.06}$	$0.39 - 0.63$	$0.36 - 0.67$
$\sin^2\theta_{13}$		$0.013^{+0.013}_{-0.009}$	≤ 0.039	≤ 0.053

Table 2.2: Neutrino oscillation parameters, state of knowledge 2010 (best global fit) [Sch08][Sch10].

As can be seen, the measured values of Δm^2_{21} and $\Delta m^2_{32} \approx \Delta m^2_{31}$ differ by approximately two orders of magnitude, enabling many experiments studying neutrino oscillations to use the 2-flavour formalism (see Chapter 2.3.2) to conduct their calculations.

The sign of $\Delta m^2_{32} \approx \Delta m^2_{31}$ is still unknown, so there remain two possible hierarchies of neutrino masses (see Figure 2.7).

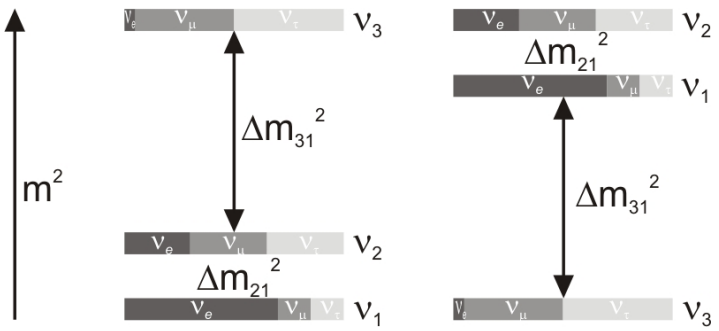

Figure 2.7: 'Normal' (**left**) and 'inverted' hierarchy (**right**) of neutrino masses, depending on the sign of Δm^2_{31}.

2.3.5 Oscillations of Solar Neutrinos: θ_{12} and Δm^2_{21}

Via solar neutrino oscillation studies (ν_e, see Chapter 2.5.2), the parameters θ_{12} and Δm^2_{21} may be investigated.

The values displayed in Table 2.2 represent a global fit of the data provided by the SNO, BOREXINO[1], GALLEX[2], and GNO[3] solar neutrino experiments, as well as the KamLAND[4] ($L = 180\,\text{km}$) reactor neutrino results ($\overline{\nu}_e$, see Chapter 2.5.7) from up to 2010, while Figure 2.8 shows the 2008 allowed regions for the parameters $\sin^2\theta_{12}$ and Δm^2_{21}.

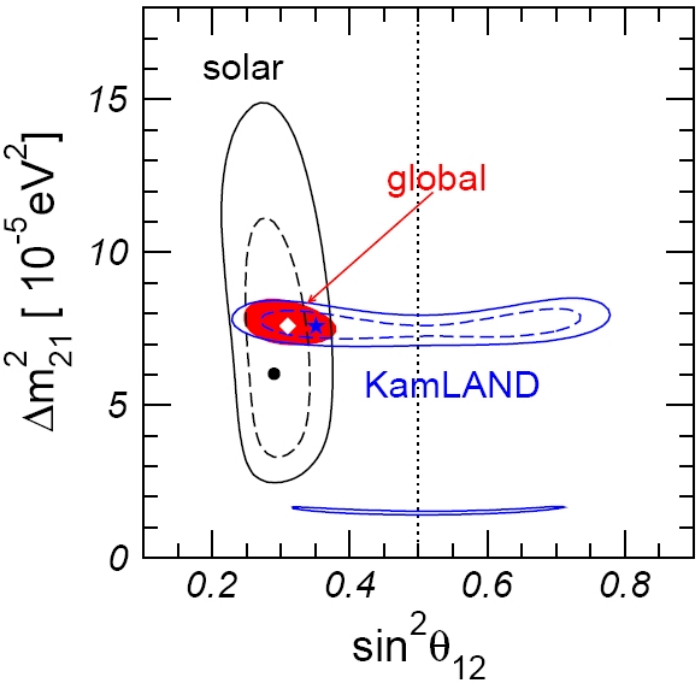

Figure 2.8: Solar neutrino oscillation parameters, state of knowledge 2008 [Sch08]. Shown are the 90% (dashed) and 99.73% (solid) CL allowed regions for $\sin^2\theta_{12}$ and Δm^2_{21}.

[2]GALLEX: Gallium Experiment; Radiochemical experiment; LNGS, Gran Sasso, Italy; 1991 – 1997.
[3]GNO: Gallium Neutrino Observatory; Radiochemical experiment; LNGS, Gran Sasso, Italy; 1998 – 2002.
[4]KamLAND: Kamioka Liquid Scintillator Antineutrino Detector; Liquid scintillator detector; Kamioka Observatory, below Mt. Kamiokakō, Gifu, Japan; 2002–?.

2.3.6 Oscillations of Atmospheric Neutrinos: θ_{23}, Δm^2_{31}, and Δm^2_{32}

By using either atmospheric (ν_e, $\overline{\nu}_e$, ν_μ, $\overline{\nu}_\mu$, see Chapter 2.5.1) or long-baseline ($L \sim 1000\,\mathrm{km}$) accelerator neutrinos (ν_μ, $\overline{\nu}_\mu$, see Chapter 2.5.8), the oscillation parameters θ_{23}, Δm^2_{31}, and Δm^2_{32} can be studied.

Table 2.2 shows a global fit including the results for solar neutrinos from SuperKamiokande[1], as well as the accelerator neutrino measurements conducted by MINOS[2] and K2K[3] from up to 2010. In Figure 2.9, the 2008 allowed regions for θ_{23} and Δm^2_{31} are depicted.

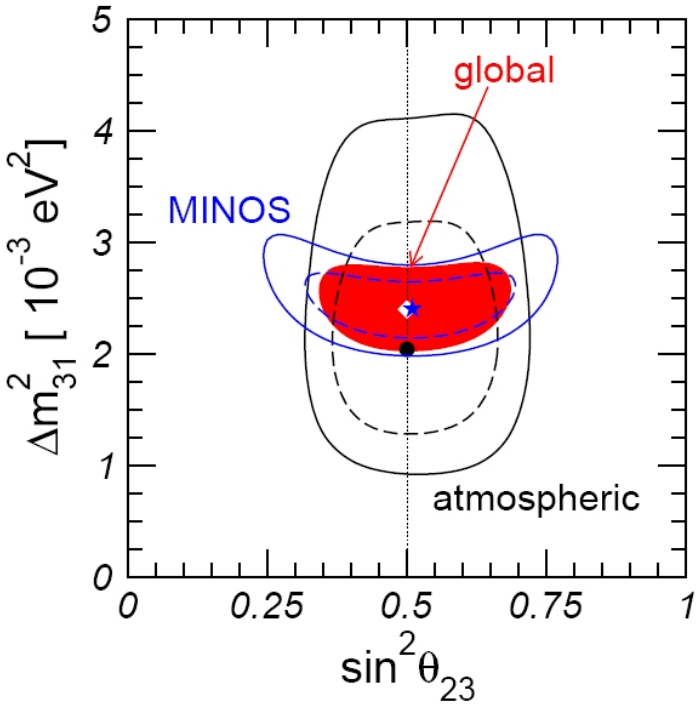

Figure 2.9: Atmospheric neutrino oscillation parameters, state of knowledge 2008 [Sch08]. Shown are the 90% (dashed) and 99.73% (solid) CL allowed regions for $\sin^2\theta_{23}$ and Δm^2_{31}.

[1]SuperKamiokande: Successor experiment to Kamiokande; Water Čerenkov detector; Kamioka Observatory, below Mt. Kamiokakō, Gifu, Japan; 1996−?.
[2]MINOS: Main Injector Neutrino Oscillation Search; Hybrid detector; Fermilab, Batavia, Illinois; 2005−?.
[3]K2K: KEK to Kamioka; Water Čerenkov detector; Kamioka Observatory, below Mt. Kamiokakō, Gifu, Japan; 1999 − 2004.

2.3.7 The Mixing Angle θ_{13}

Via a combination of the results from experiments studying solar or atmospheric, nuclear reactor or accelerator neutrinos (see Chapter 2.5), bounds for the parameter θ_{13}, which characterises the magnitude of CP violation in neutrino oscillations, may be derived.

The results from CHOOZ[1], KamLAND, MINOS, and SNO are included in the global best fit of Table 2.2 (state of knowledge 2010), while Figure 2.10 shows the 2008 90% CL allowed regions for $\sin^2\theta_{13}$ and Δm^2_{31}.

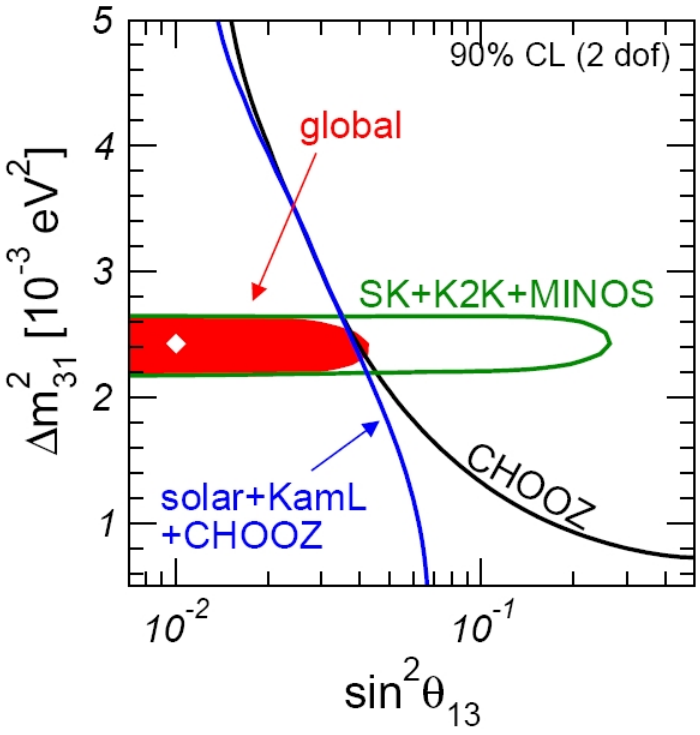

Figure 2.10: θ_{13}, state of knowledge 2008 [Sch08]. Shown are the 90% CL allowed regions for $\sin^2\theta_{13}$ and Δm^2_{31}.

[1]CHOOZ: Chooz Reactor Neutrino Experiment; Liquid scintillator detector; Chooz, France; 1997 – 1998.

2.4 Neutrinos and Antineutrinos

One of the questions still remaining open in neutrino physics is whether the neutrino – apparently carrying neither electric charge nor electric or magnetic momentum – is its own antiparticle, making it a Dirac particle if $\nu \neq \overline{\nu}$, or a Majorana particle in the case that $\nu \equiv \overline{\nu}$. Solely the conservation of lepton number L_α observed in weak interaction seems to require ν and $\overline{\nu}$ to be distinguishable.

Already many experiments have tried to answer this question, either by investigating reactions of inverse β decay (see Equation 2.13) induced by antineutrinos from nuclear reactors:

$$\overline{\nu}_e + n \rightarrow e^- + p^+ \qquad [L_e = -1 + 0 \rightarrow L_e = 1 + 0], \tag{2.62}$$

as was conducted by R. Davis et.al. at the Savannah River reactor (see Chapter 2.2.2), or via the so-called neutrinoless double-β decay ($0\nu\beta\beta$, see also Figure 2.11) of suitable isotopes:

$$n \rightarrow p^+ + e^- + \overline{\nu}_e \qquad \text{and} \qquad n + \nu_e \rightarrow p^+ + e^-, \tag{2.63}$$

whilst

$$\overline{\nu}_e \rightarrow \nu_e, \tag{2.64}$$

thus netting:

$$2n \rightarrow 2p^+ + 2e^- \qquad [L_e = 0 \rightarrow L_e = 0 + 2], \tag{2.65}$$

that e.g. the GERDA[1] experiment will be searching for.

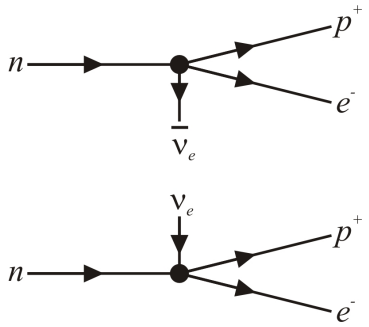

Figure 2.11: Feynman graph: $0\nu\beta\beta$.

Apart from the controversially discussed Heidelberg-Moscow[2] experiment [Kla04], no experiment of this kind – being further complicated by helicity[3] – was yet able to find evidence for the identity of neutrinos and antineutrinos.

[1] GERDA: GERmanium Detector Array; ^{76}Ge semiconductor detector; LNGS, Gran Sasso, Italy; ?.
[2] Heidelberg-Moscow: ^{76}Ge semiconductor detector; LNGS, Gran Sasso, Italy; 1995 – 2003.
[3] So far, only neutrinos with $H < 0$ and antineutrinos with $H > 0$ have been observed.

2.5 Other Neutrino Experiments

There are multiple experiments studying the properties of neutrinos, both from natural and artifical sources (see Figure 2.12 for their fluxes). However, due to the small cross sections of neutrino interactions with matter (see Figure 2.13) they all have some things in common: The need for large target masses and detectors as well as very effective means of background reduction.

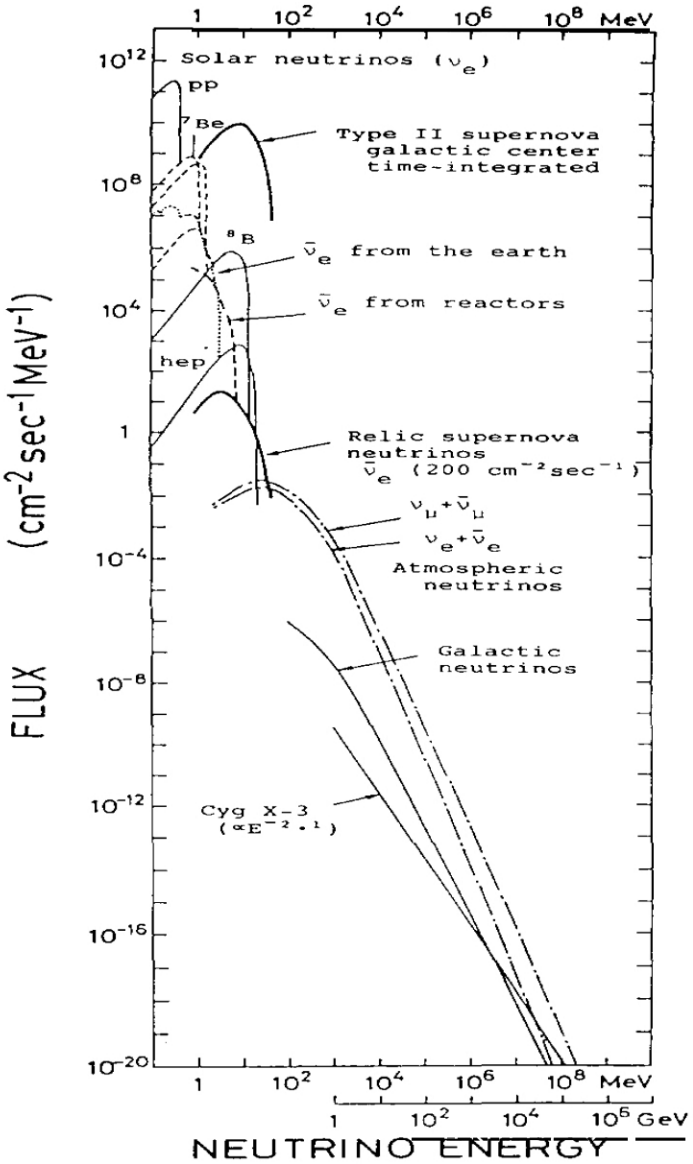

Figure 2.12: Flux spectra of neutrinos from different sources [Kos92].

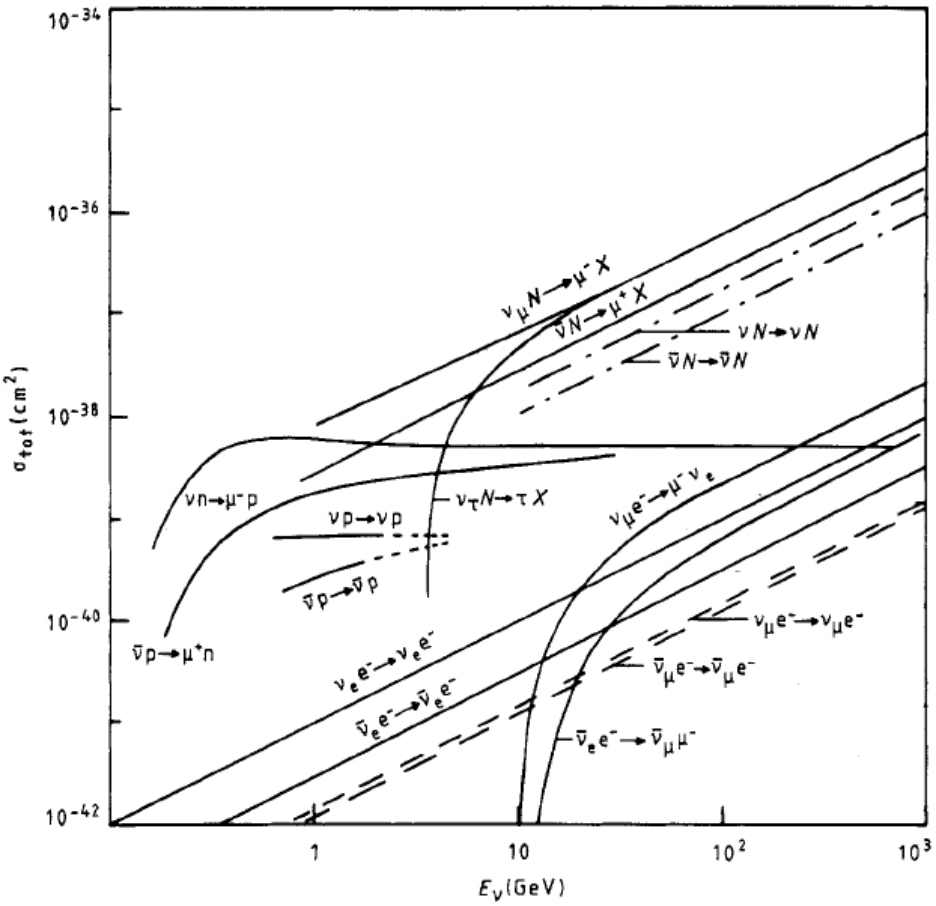

Figure 2.13: Energy dependence of various neutrino interaction cross sections [Eis86].

2.5.1 Atmospheric Neutrinos: ν_e, $\overline{\nu}_e$, ν_μ, $\overline{\nu}_\mu$

Mainly from the scattering of p^+ with atomic nuclei of the atmosphere originate energetic showers containing, among others, $\pi^\pm$ and $K^\pm$ which decay into μ and ν:

$$\pi^+ \to \mu^+ + \nu_\mu \qquad \text{or} \qquad \pi^- \to \mu^- + \overline{\nu}_\mu, \tag{2.66}$$

$$K^+ \to \mu^+ + \nu_\mu \qquad \text{or} \qquad K^- \to \mu^- + \overline{\nu}_\mu \tag{2.67}$$

and

$$\mu^+ \to e^+ + \nu_e + \overline{\nu}_\mu \qquad \text{or} \qquad \mu^- \to e^- + \overline{\nu}_e + \nu_\mu. \tag{2.68}$$

The respective energies are about $1 - 10^4$ GeV for ν_μ or $\overline{\nu}_\mu$ and $10^{-1} - 10^3$ GeV for ν_e or $\overline{\nu}_e$ [Sch97].

Notable experiments include Frejus[1], ICARUS[2], IMB[3], Kamiokande[4], MACRO[5], NUSEX[6],

[1]Frejus: Hybrid detector; Frejus tunnel, France; 1984 – 1988.
[2]ICARUS: Imaging Cosmic And Rare Underground Signal; Liquid Ar detector; LNGS, Gran Sasso, Italy; 2010−?.
[3]IMB: Irvine Michigan Brookhaven; Water Čerenkov detector; Below Lake Erie, Irvine, USA; 1982 – 1991.
[4]Kamiokande: Kamioka Nucleon Decay Experiment; Water Čerenkov detector; Kamioka Observatory, below Mt. Kamiokakō, Gifu, Japan; 1983 – 1995.
[5]MACRO: Monopole Astrophysics and Cosmic Ray Observatory; Liquid scintillator detector; LNGS, Gran Sasso, Italy; 1989 – 2000.
[6]NUSEX: Nuclear Stability Experiment; Hybrid detector; Mont Blanc tunnel, France; 1982 – 1988.

SNO, SuperKamiokande, and Soudan2[1], many of which studying neutrino oscillations (see Chapter 2.3) via the $\nu_\mu \to \nu_\tau$ disappearance channel.

2.5.2 Solar Neutrinos: ν_e

In the thermonuclear fusion, neutrinos are mainlycreated according to:

$$4p^+ \to {}^4\mathrm{He} + 2e^+ + 2\nu_e, \tag{2.69}$$

with average energies of 0.6 MeV [PDG08].

BOREXINO, GALLEX, GNO, ICARUS, Kamiokande, SAGE[2], and SuperKamiokande are some of the experiments analysing the properties of solar neutrinos from reaction 2.69 and other subsequent fusion reactions, as well as the Standard Solar Model (SSM) and its corresponding reactions inside the sun.

A deficit of the expected ν_e and $\overline{\nu}_e$ flux has first been observed by the Homestake experiment in 1968 – giving rise to the 'solar neutrino problem' (see Chapter 2.2.4) – while the total number of neutrinos stays the same, as proven by SNO and KamLAND in 2002, encouraging the theory of neutrino oscillations (see Chapter 2.3).

2.5.3 Supernova Neutrinos: ν_e, $\overline{\nu}_e$, ν_μ, $\overline{\nu}_\mu$, ν_τ, $\overline{\nu}_\tau$

In a supernova type II, the inner core of a massive star collapses via the decay of p^+ to n:

$$p^+ + e^- \to n + \nu_e, \tag{2.70}$$

thus creating a neutron star, with the huge amount of released energy being carried away by the neutrinos. However, still more neutrinos (about 90%) originate from the cooling of the core by thermic ν pair production:

$$e^- + e^+ \to \nu_\alpha + \overline{\nu}_\alpha, \tag{2.71}$$

where $\alpha = e, \mu, \tau$.

In both cases, the neutrino energies are averaging some 10 MeV [Sch97].

Experiments studying these supernova neutrinos are, for example, ICARUS, IMB, Kamiokande, LVD[3], MACRO, NUSEX, SNO, and SuperKamiokande, not only analysing the supernovae themselves but also setting constraints on neutrino properties such as mass, lifetime, and number of families.

[1] Soudan2: Hybrid detector; Soudan Mine, Northern Minnesota, USA; 1989 – 2001.
[2] SAGE: Soviet American Gallium Experiment; Radiochemical experiment; Baksan Neutrino Observatory, below Mt. Andyrchi, Russia; 1989−?.
[3] LVD: Large Volume Detector; Liquid scintillator detector; LNGS, Gran Sasso, Italy; 1992−?.

2.5.4 Cosmological Neutrinos: ν_e, $\overline{\nu}_e$, ν_μ, $\overline{\nu}_\mu$, ν_τ, $\overline{\nu}_\tau$

There are two kinds of cosmological neutrinos: Those remaining from the thermodynamic equilibrium right after the big bang:

$$\nu_\alpha + \overline{\nu}_\alpha \quad \leftrightarrow \quad \nu_\beta + \overline{\nu}_\beta, \tag{2.72}$$

$$e^+ + e^- \quad \leftrightarrow \quad \nu_\alpha + \overline{\nu}_\alpha, \tag{2.73}$$

where $\alpha, \beta = e, \mu, \tau$, and those created during early nucleosynthesis of the light elements (D, ^{3}He, ^{4}He, ^{7}Li):

$$p^+ + \overline{\nu}_e \quad \leftrightarrow \quad n + e^+, \tag{2.74}$$

$$n + \nu_e \quad \leftrightarrow \quad p^+ + e^-, \tag{2.75}$$

$$n \quad \leftrightarrow \quad p^+ + e^- + \overline{\nu}_e. \tag{2.76}$$

With energies of $5 \cdot 10^{-4}$ eV and 0.72 MeV [Sch97], respectively, and the resulting diminutive cross sections, there are not yet experiments able to directly investigate these neutrinos which are handled as candidates for at least some part of the non-baryonic hot dark matter suspected to be in the universe.

2.5.5 High-Energy Cosmic Neutrinos: ν_e, $\overline{\nu}_e$, ν_μ, $\overline{\nu}_\mu$

Cosmic neutrinos of high energies – classified as VHE[1] ($E_\nu \geq 50$ GeV) and UHE[2] ($E_\nu \geq 10^5$ GeV) [Sch97] – are created in decays of $\pi^\pm$ or $K^\pm$ (see Equations 2.66, 2.67, 2.68) produced by the scattering of cosmic rays[3] with target nuclei or γ in cosmos:

$$p^+ + p^+ \rightarrow \pi^0 + \pi^\pm + K^\pm + X. \tag{2.77}$$

Another possible source is the hypothetical decay of super-massive particles (e.g. neutralinos) which are candidates for non-baryonic cold dark matter.

AMANDA[4], ANITA[5], ANTARES[6], and IceCube[7] are just some of the experiments investigating these high-energy cosmic neutrinos.

2.5.6 Low-Energy Neutrinos from β Decays: $\overline{\nu}_e$

The natural radioactive β decay of instable nucleons (see Equation 2.12), during which neutrinos with energies no larger than some 10 keV are emitted, may be used to investigate neutrino mass, as will be attempted by KATRIN[8].

[1] VHE: Very high energy.
[2] UHE: Ultra high energy.
[3] From cosmic accelerators: Remnants of young supernovae, binary systems, active galactic nuclei etc.
[4] AMANDA: Antarctic Muon And Neutrino Detector Array; Ice Čerenkov detector; Amundsen-Scott South Pole Station, Antarctica; 1996 – 2005.
[5] ANITA: Antarctic Impulse Transient Antenna; Radio pulse detector; 35,000 m above Antarctica; 2006.
[6] ANTARES: Astronomy with a Neutrino Telescope and Abyss Environmental RESearch; Water Čerenkov detector; Mediterranean Sea, France; 2006−?.
[7] IceCube: IceCube Neutrino Observatory; Water Čerenkov detector; Amundsen-Scott South Pole Station, Antarctica; 2007−?.
[8] KATRIN: Karlsruhe Tritium Neutrino Experiment; MAC-E filter spectrometer; Karlsruhe, Germany; ?.

Another class of experiments searches for neutrinoless double-β decay ($0\nu\beta\beta$) of certain isotopes whose observation would imply that the neutrino is a Majorana particle (see Chapter 2.4). GERDA and COBRA[1], for example, are going to conduct such measurements whereas the debatable Heidelberg-Moscow experiment already claims to have seen this kind of reaction.

2.5.7 Nuclear Reactor Neutrinos: $\overline{\nu}_e$

Like their counterparts from natural radioactivity, the neutrinos created by β decays (see Equation 2.12) at nuclear reactors have the same low energies of up to 10 MeV [Sch97]. Thus, oscillation experiments using these nuclear reactor neutrinos – such as CHOOZ and KamLAND – are sensitive to relatively small mass differences δm^2 (see Chapter 2.3), whereas the famous Cowan-Reines Experiment (see Chapter 2.2.2) used the Savannah River nuclear reactor to discover the neutrino.

2.5.8 Accelerator Neutrinos: ν_μ, $\overline{\nu}_\mu$

By using the proton beams of particle accelerators and guiding them on suitable targets (e.g. C) creating $\pi^\pm$ and $K^\pm$ decaying according to Equations 2.66 – 2.68, intensive high-energy ν_μ and $\overline{\nu}_\mu$ beams can be produced. By focusing or defocusing the charged $K^\pm$ and $\pi^\pm$ mesons with magnetic horns, it may be discriminated between neutrinos and antineutrinos, and the shape of the resulting beam controlled. See Chapter 4 for a detailed description of the OPERA detector and the CNGS neutrino beam.

Accelerator-based experiments are categorised according to the distance L between neutrino source and detector as short-baseline ($L \sim 1\,\text{km}$), medium-baseline ($L \sim 10\,\text{km}$), or long-baseline ($L \sim 1000\,\text{km}$) experiments.
There are – and have been – many experiments studying neutrinos produced at accelerators, e.g. CHORUS[2], DONuT, MINERνA[3], MINOS, NOMAD[4], OPERA, and T2K[5].

[2]CHORUS: CERN Hybrid Oscillation Research apparatUS; Hybrid detector; CERN, Geneva, Switzerland; 1994 – 1997.
[3]MINERνA: Main Injector Experiment for ν-A; Hybrid detector; Fermilab, Batavia, Illinois; 2009−?.
[4]NOMAD: Neutrino Oscillation MAgnetic Detector; Hybrid detector; CERN, Geneva, Switzerland; 1995 – 1999.
[5]T2K: Tokai to Kamioka; Water Čerenkov detector; Kamioka Observatory, below Mt. Kamiokakō, Gifu, Japan; 2010−?.

Chapter 3

Energy Loss of Particles in Matter

There are many different ways the energy loss of particles when passing through matter – and thus also their detection and identification – can take place.

In the following, the energy loss via ionisation and excitation (Chapter 3.1), multiple scattering (Chapter 3.2), and the interactions of γ and $e^{\pm}$ with matter (Chapter 3.3) shall be explained in detail, as these mechanisms are the most important for the OPERA experiment.

3.1 Ionisation and Excitation

When passing through matter, the energy loss of moderately relativistic heavy charged particles (other than electrons) occurs primarily through ionisation and excitation of atoms and molecules.

3.1.1 Mean Energy Loss (Bethe-Bloch Equation)

The mean rate of energy loss (also called stopping power) of charged particles via ionisation is described by the Bethe-Bloch equation [PDG08]:

$$-\frac{dE}{dx} = 4\pi N_A r_e^2 m_e c^2 z^2 \frac{Z}{A}\frac{1}{\beta^2}\left(\frac{1}{2}\ln\frac{2m_e c^2\beta^2\gamma^2 T_{max}}{I^2} - \beta^2 - \frac{\delta(\beta\gamma)}{2}\right), \tag{3.1}$$

with

M	Incident particle mass
E	Incident particle energy (γMc^2)
$m_e c^2$	Electron mass $\times c^2$ ($0.510998918(44)\,\mathrm{MeV}$)
r_e	Classical electron radius ($e^2/4\pi\epsilon_0 m_e c^2 = 2.817940325(28)\,\mathrm{fm}$)
N_A	Avogadro's number ($(6.0221415(10)\cdot 10^{23}\,\mathrm{mol}^{-1}$)
ze	Charge of incident particle
Z	Atomic number of absorber
A	Atomic mass of absorber
I	Mean excitation energy
$\delta(\beta\gamma)$	Density effect correction to ionisation energy loss
T_{max}	Maximum kinetic energy transferred to a free electron in a single collision

In the above-mentioned form, the Bethe-Bloch equation describes the energy loss of, e.g., $\pi^{\pm}$ with energies between 6 MeV and 6 GeV in Cu with an accuracy of 1%. However, at lower energies various corrections must be applied, and at higher energies radiative effects considered – their exact domains depending on both the effective atomic number of the absorber and the mass of the slowing particle.

Figure 3.1 depicts the stopping power for μ^+ in Cu, showing the approximations assumed for the respective ranges of energy.

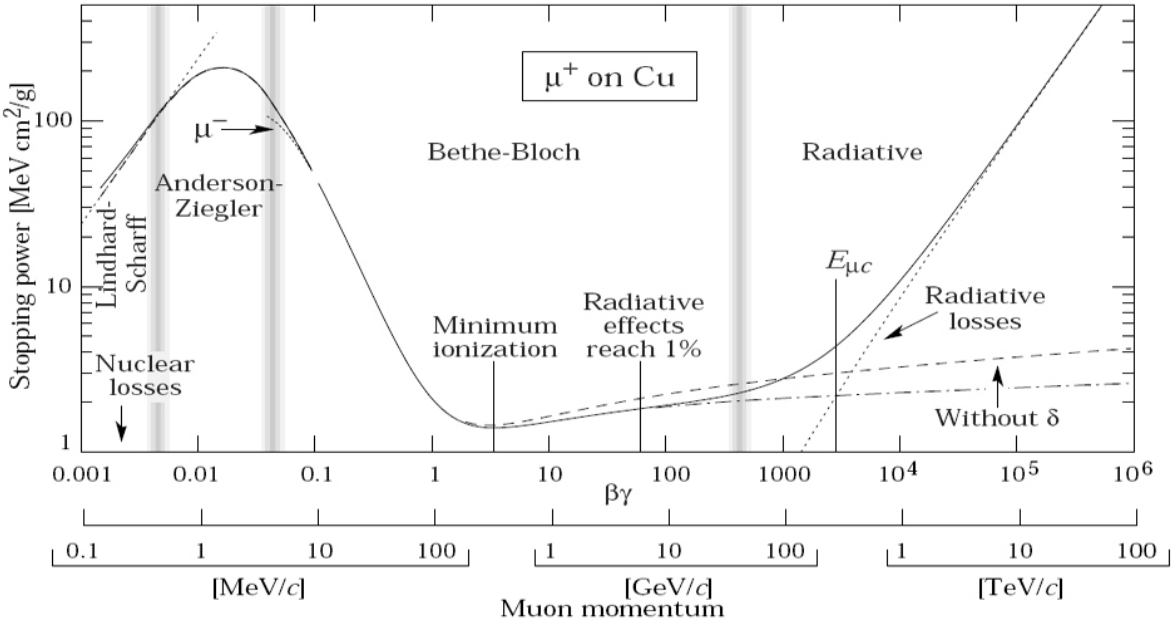

Figure 3.1: Stopping power $-dE/dx$ for μ^+ in Cu as a function of $\beta\gamma = p/Mc$ [PDG08].

In Figure 3.2, the mean energy loss rate for $\mu^{\pm}$, $\pi^{\pm}$, and p^+ in various materials, according to the Bethe-Bloch equation, is shown, while Figure 3.3 depicts the corresponding continuous slowing down approximation (CSDA) range R, obtained via integration of the reciprocal of Equation 3.1 with respect to the energy.

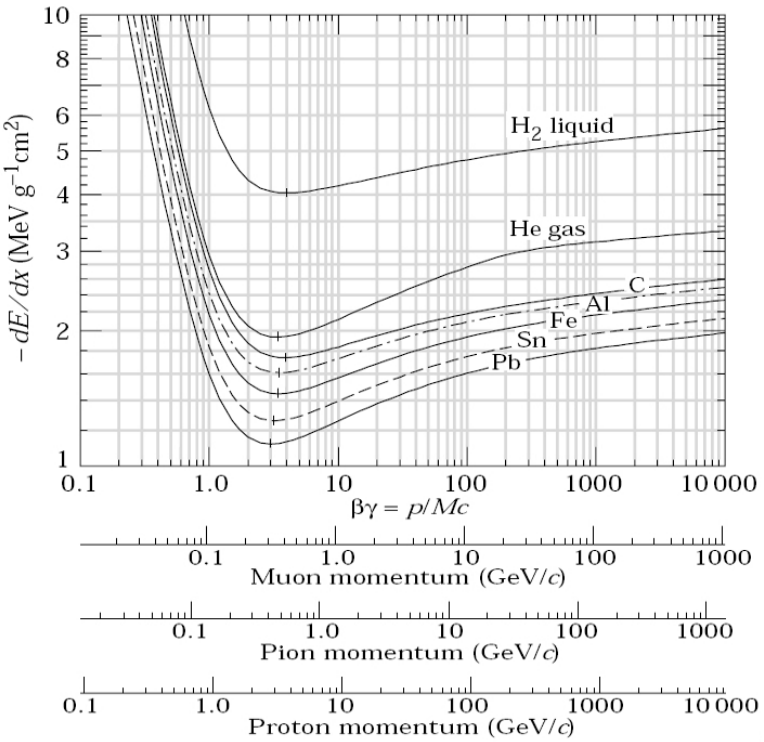

Figure 3.2: Mean energy loss rate for $\mu^{\pm}$, $\pi^{\pm}$, and p^{+} in various materials [PDG08].

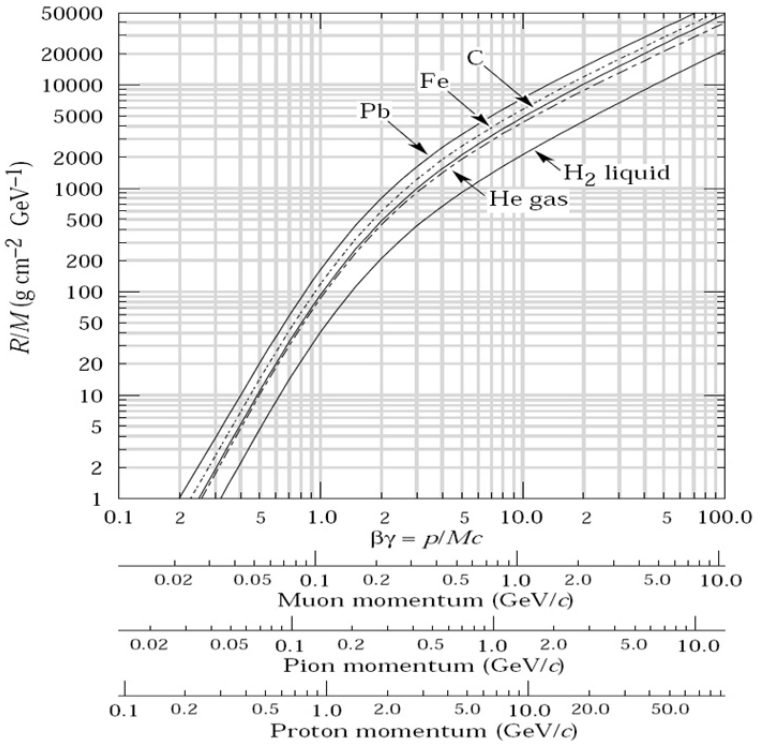

Figure 3.3: Range of heavy charged particles in various materials [PDG08].

In high energy physics, the mean energy loss in a given material solely depends on β, with T_{max} constituting only a minor dependence on M at the highest energies. The stopping power for particles of like energies is similar, and slowly decreases with increasing Z. $-dE/dx$ has a broad minimum around $\beta\gamma = 3.5$ for $Z = 7$ to $\beta\gamma = 3.0$ for $Z = 100$ (see Figure 3.2), corresponding to minimum ionisation and characterising minimum ionising particles (m.i.p.) – as are most relativistic particles.

3.1.2 Most Probable Energy Loss (Landau-Vavilov Distribution)

The mean energy loss given by the Bethe-Bloch equation is considerably higher than the most probable energy loss, and thus a poor means to describe individual particles.

The Landau-Vavilov distribution – suitable for detectors of moderate thickness x, such as scintillators – on the other hand, describes the most probable energy loss [PDG08]:

$$\Delta_p = \xi \left(\ln \frac{2mc^2\beta^2\gamma^2}{I} + \ln \frac{\xi}{I} + j - \beta - \delta(\beta\gamma) \right), \tag{3.2}$$

with $\xi = (4\pi N_A r_e^2 m_e c^2/2)\langle Z/A\rangle(x/\beta)$ and $j = 0.200$.

Figure 3.4 shows the Bethe-Bloch equation (mean energy loss) in comparison with the Landau-Vavilov distribution (most probable energy loss) for $\mu^{\pm}$ in Si. For high energies, the Landau-Vavilov distribution reaches a so-called Fermi plateau.

In Figure 3.5 the Landau-Vavilov distribution for m.i.p. in Si of various thickness is depicted, along with the mean energy loss rate predicted by the Bethe-Bloch equation. With increasing absorber thickness, the Landau-Vavilov distribution becomes less skewed, however, it never approaches a Gaussian.

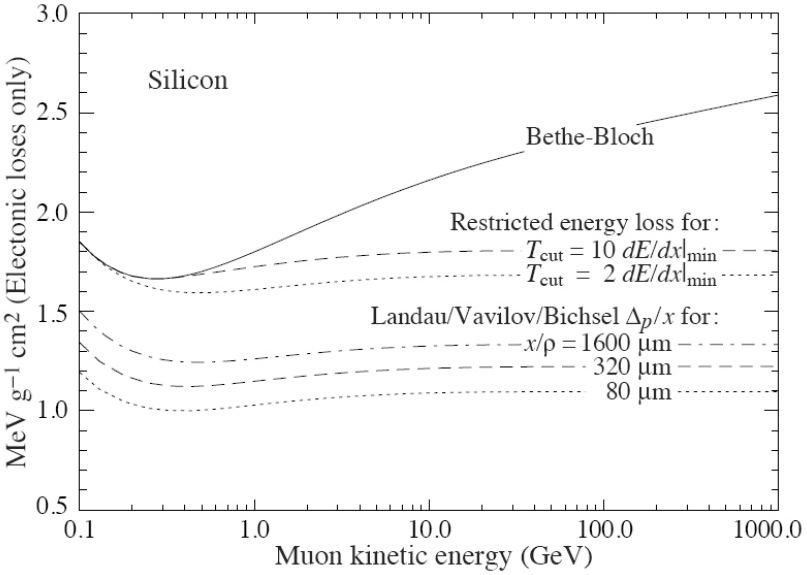

Figure 3.4: Mean energy loss (Bethe-Bloch equation) and most probable energy loss (Landau-Vavilov distribution) for $\mu^{\pm}$ in Si [PDG08].

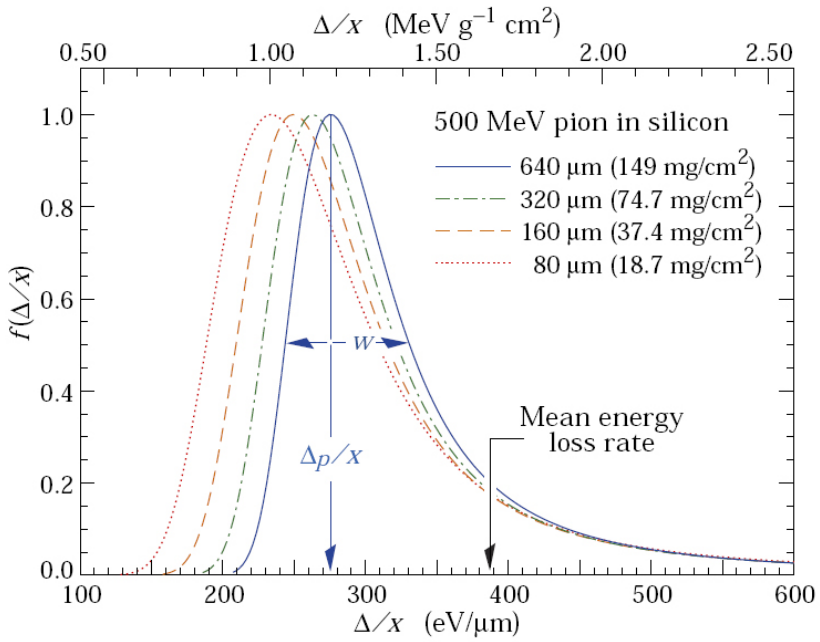

Figure 3.5: Mean energy loss and most probable energy loss (Landau-Vavilov distribution) in comparison (m.i.p. in Si) [PDG08].

3.2 Multiple Scattering

Due to Coulomb scattering with nuclei (hence called multiple Coulomb scattering) – and, in the case of hadrons, also the strong interaction – charged particles passing through matter are deflected by many small-angle scatters.

While at deflection angles greater than some θ_0 (see Equation 3.3), Rutherford scattering is better suited to describe the Coulomb scattering distribution, at small angles, a Gaussian approach may be used, its RMS[1] given by [PDG08]:

$$\theta_0 = \frac{13.6\,\text{MeV}}{\beta cp} z\sqrt{x/X_0}[1 + 0.038\ln(x/X_0)], \tag{3.3}$$

with x/X_0 being the thickness of the scattering medium in radiation lengths X_0 (see Chapter 3.3.1).

This value of θ_0 results from a fit to a Molière distribution for particles with $z = 1$ and $\beta = 1$ (being accurate to $< 11\%$ for $10^{-3} < x/X_0 < 100$), and describes the scattering inside a single type of material. For different layers or mixtures of scattering materials, a combined x/X_0 has to be inserted.

[1] RMS: Root mean square.

3.3 γ and $e^{\pm}$ Interactions

While high-energy photons lose energy through e^+e^- pair production (see Figure 3.6), high-energy electrons in matter lose their energy primarily via bremsstrahlung (see Figure 3.7). Both processes are characterised by the radiation length X_0.

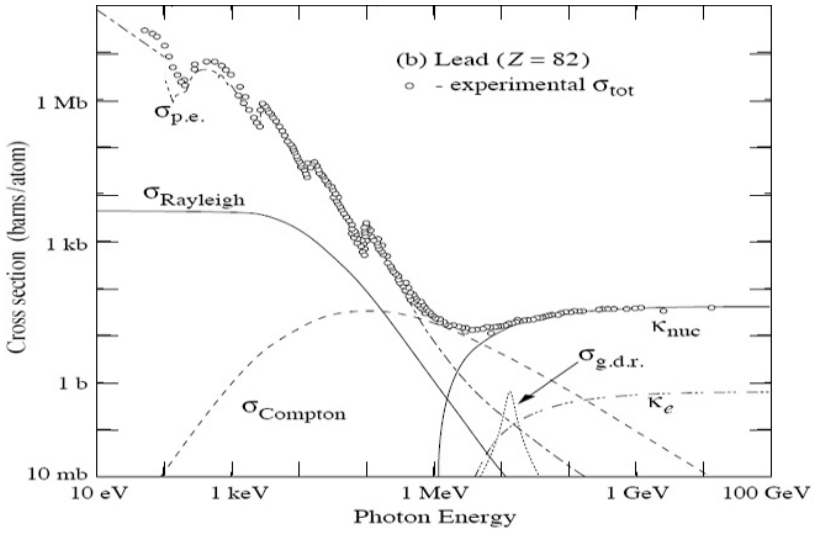

Figure 3.6: γ cross sections of different processes in Pb [PDG08]. κ_{nuc} and κ_e indicate pair production inside nuclear and electron fields, respectively. At low energies, the photoelectric effect $\sigma_{p.e.}$ dominates.

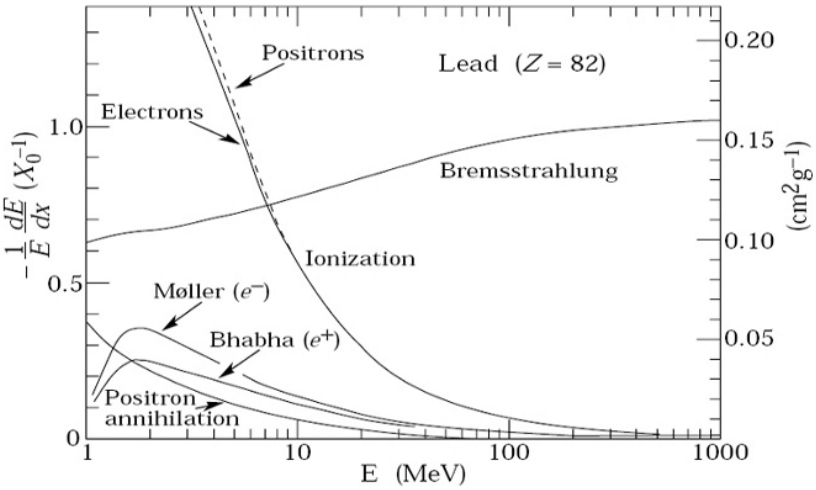

Figure 3.7: Fractional Energy loss of $e^{\pm}$ per X_0 in Pb as a function of particle energy [PDG08].

For energies of $E_\gamma \lesssim 1\,\text{MeV}$, the energy loss of photons due to the photoelectric effect, Rayleigh scattering, and Compton scattering has to be taken into account. For $e^{\pm}$ of $E_e \lesssim 10\,\text{MeV}$, the contributions by ionisation, Møller scattering, and Bhabha scattering need to be considered. Due to the respective low energies, however, these processes are not important for the OPERA experiment.

3.3.1 Radiation Length

The radiation length X_0 sets the scale for high-energy electromagnetic cascades (see Chapter 3.3.2): On the one hand, it describes the mean distance after which high-energy $e^{\pm}$ have lost all but a fraction $1/e$ of their energy, on the other hand, it indicates 7/9 of the mean free path of a high-energy photon before producing an e^+e^- pair.

X_0 is usually measured in $\mathrm{g\,cm^{-2}}$ and can be estimated by [PDG08]:

$$X_0 = \frac{7.164\,\mathrm{g\,cm^{-2}} A}{Z(Z+1)\ln(287/\sqrt{Z})}. \tag{3.4}$$

For a mixture or compound of different materials, the radiation length may be approximated as [PDG08]:

$$\frac{1}{X_0} = \sum_j \frac{w_j}{X_j}, \tag{3.5}$$

with X_j being the radiation length (weighted by w_j) for the jth element.

3.3.2 Electromagnetic Cascades

Via bremsstrahlung and pair production, high-energy $e^{\pm}$ and γ inside thick absorbers create cascades of other $e^{\pm}$ and γ at lower energies. After falling below the critical energy[1] E_c, however, the $e^{\pm}$ are more likely to lose their energy via ionisation and excitation.

The longitudinal development of these showers depends on the energy E_0 of the initiating particle and its radiation length X_0 inside the absorber. A gamma distribution may be used to describe the mean longitudinal profile of the energy deposition after the first two radiation lengths [PDG08]:

$$\frac{dE}{dt} = E_0 b \frac{(bt)^{a-1} e^{-bt}}{\Gamma(a)}, \tag{3.6}$$

with the scale variable $t = x/X_0$, a maximum at $t_{max} = (a-1)/b$, and a shower length of $X_s = X_0/b$ (a and b depending on both Z and E_0, with b often chosen as ~ 0.5).

The transverse development of electromagnetic cascades can be described by the Molière radius R_M [PDG08]:

$$R_M = X_0 \frac{E_s}{E_c}, \tag{3.7}$$

where $E_s = 21\,\mathrm{MeV}$. For material compounds, it may be calculated as:

$$\frac{1}{R_M} = \frac{1}{E_s} \sum \frac{w_j E_{cj}}{X_j}. \tag{3.8}$$

A cylinder of radius R_M contains about 90% of the energy deposited.

[1] The energy at which the ionisation loss per X_0 and the energy loss via bremsstrahlung are equal to the electron energy: $E_e \approx E/X_0 \approx |dE/dx|_{brems}$.

Chapter 4

The OPERA Experiment

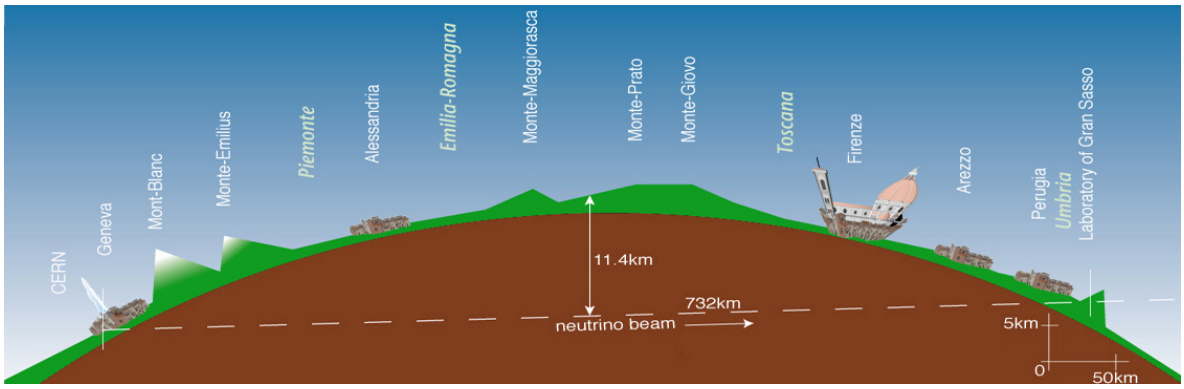

Figure 4.1: Schematic overview of the OPERA experiment [CER10].

The OPERA experiment at LNGS is a neutrino oscillation (see Chapter 2.3) experiment, studying the CERN neutrinos to Gran Sasso (CNGS) long-baseline ν_μ beam for $\nu_\mu \rightarrow \nu_\tau$ transitions (see Figure 4.1).

While many oscillation experiments – such as K2K, MACRO, MINOS, Soudan2, SuperKamiokande – have already shown the disappearance of atmospheric or accelerator ν_μ, OPERA strives to make the first observation of ν_τ appearance. However, the OPERA detector is also able to observe ν_μ – theoretically enabling it to conduct another disappearance measurement – and prompt e^- from ν_e CC interactions (see Chapter 2.1.3), so the sub-leading oscillation channel $\nu_\mu \rightarrow \nu_e$ may be studied as well.

Similar to the CHORUS experiment, that had been unsuccessfully searching for ν_τ appearance in short-baseline (600 m) $\nu_\mu \rightarrow \nu_\tau$ oscillations [CHO96], though now at a much larger scale, the OPERA detector employs the ECC technique used for DONuT (see Chapter 2.2.6) for sub-micrometric resolution of ionising particle tracks, combined with a real-time electronic detector.

This chapter will give an overview of the OPERA experiment, first detailing the CNGS neutrino beam (Chapter 4.1), then the OPERA detector, consisting of veto (Chapter 4.2.1), spectrometer (Chapter 4.2.2), and target area (Chapter 4.2.3), and concluding with a brief

summary of the data analysis and event topologies (Chapter 4.3), and the sensitivity of the experiment (Chapter 4.4).

4.1 CERN Neutrinos to Gran Sasso (CNGS)

4.1.1 The CNGS Beam Facility

Located at CERN, the CNGS beam facility uses the 400 GeV p^+ beam from the SPS synchrotron to create the almost pure ν_μ beam studied by the OPERA experiment. See Figure 4.2 for a schematic overview.

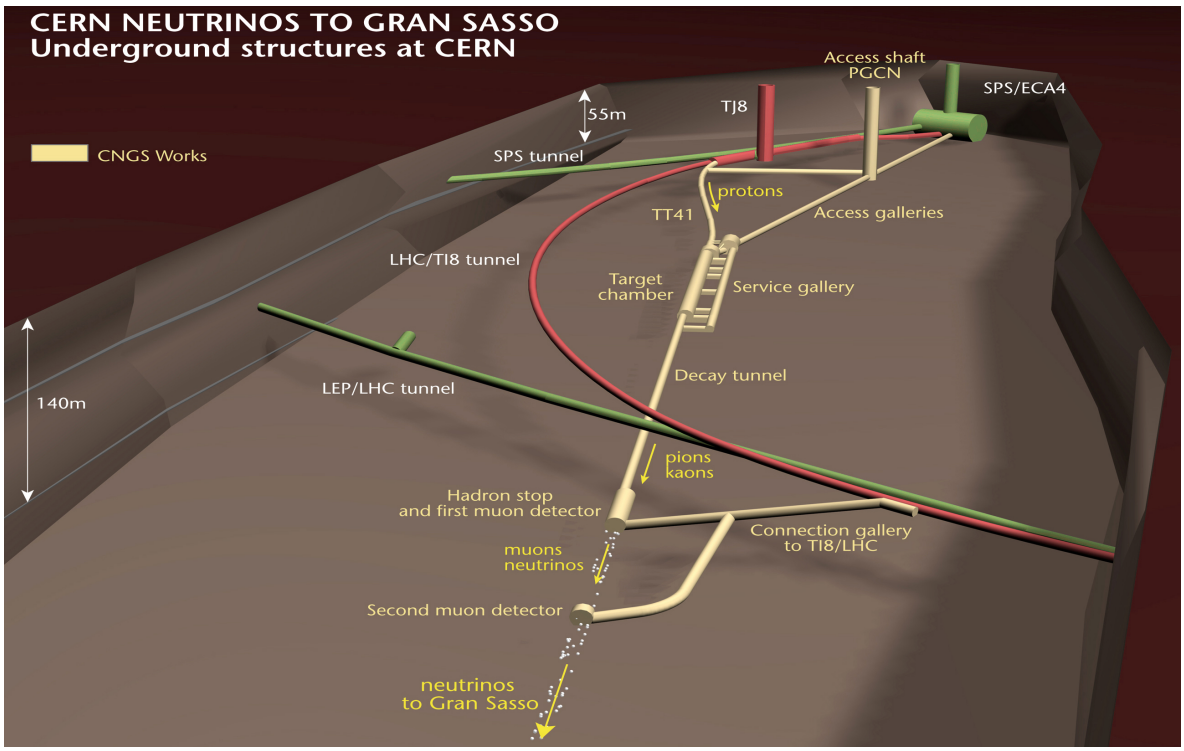

Figure 4.2: Schematic view of the CNGS beam facility at CERN [CER10].

For proton extraction, the same extraction channel as for the LHC p^+ beam is used [God00], with one CNGS cycle[1] taking 6 s. Assuming a run time of 200 days/year, a maximum intensity[2] of $4.5 \cdot 10^{19}$ p.o.t./year is realised.

The CNGS beam line allows for proton energies between 350 GeV and 450 GeV (the maximum SPS energy), and is equipped with multiple beam monitors to ensure its stability.

[1] CNGS cycle: Consisting of two 10.5 μs SPS extractions, separated by 50 ms.
[2] Measured in p.o.t.: Protons on target.

The nominal beam parameters are listed in Table 4.1.

Parameter		Nominal Value
# extractions / cycle		2
Extraction spacing	[ms]	50
Extraction batch length	[μs]	10.5
Intensity / extraction	[p.o.t.]	$2.4 \cdot 10^{13}$
# p^+ bunches / extraction		2100
Bunch spacing	[ns]	5
Bunch length (4σ)	[ns]	2
Beam diameter (400 GeV) (σ)	[mm]	0.5

Table 4.1: CNGS p^+ beam parameters [OPE09a].

In Figure 4.3, the CNGS secondary beamline is schematically depicted.

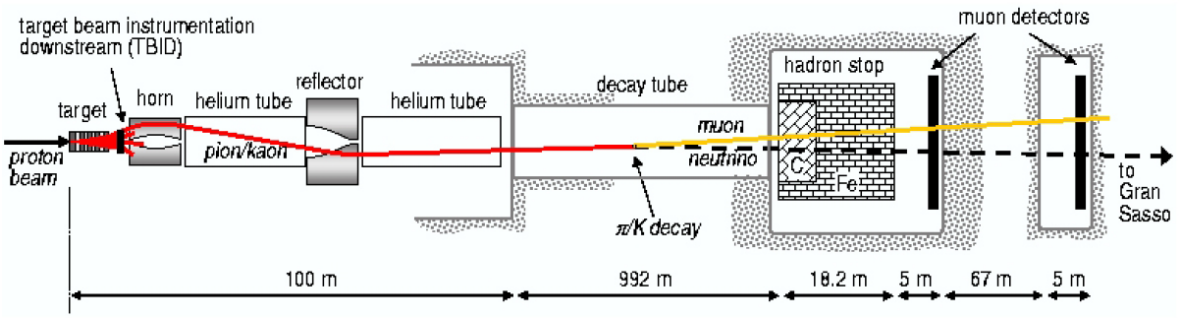

Figure 4.3: Schematic view of the CNGS secondary beamline [OPE09a].

840 m after being extracted from the SPS accelerator and already bent towards the LNGS underground laboratory by a system of 73 dipole magnets, the proton beam is sent onto an air-cooled and iron-shielded carbon target[1], thus creating $\pi^\pm$ and $K^\pm$ mesons through nuclear interactions with the C atoms.

Via two toroidal magnetic focusing lenses[2] – called horn and reflector, respectively – interspaced with and followed by tubes[3] filled with He at 20 mbar, the negatively charged π^- and K^- are defocused, while the positive mesons are focused and directed towards the OPERA detector, with a resulting incline of 3.3°, with respect to the horizontal.

Thereafter, the decay of π^+ and K^+ – primarily to ν_μ and μ^+, according to Table 4.2 – takes place inside a decay tube[4] at vacuum of less than 1 mbar, to minimise the loss of secondary particles via interactions with air molecules.

[1]One out of five identical units (the other four being in-situ spares) consisting of an Al cylinder with Be

Decay Mode	Branching Ratio [%]
$\pi^+ \to \mu^+ + \nu_\mu$	99.98770 ± 0.00004
$K^+ \to \mu^+ + \nu_\mu$	63.54 ± 0.14
$K^+ \to \pi^+ + \pi^0$	20.68 ± 0.13
$K^+ \to 2\pi^+ + \pi^-$	5.59 ± 0.04
$K^+ \to \pi^0 + e^+ + \nu_e$	5.08 ± 0.05
$K^+ \to \pi^0 + \mu^+ + \nu_\mu$	3.35 ± 0.04
$K^+ \to \pi^+ + 2\pi^0$	1.761 ± 0.022

Table 4.2: CNGS beam π^+ and K^+ most important decay modes [PDG08].

A water-cooled 2 kt hadron absorber[1] at the end of the decay tube absorbs up to 100 kW of hadrons and protons that did not interact with the target, followed by two downstream muon detectors[2]. At these muon detector stations, the intensity, direction, and profile of the μ^+, created in association with the ν_μ during π^+ and K^+ decays, is measured, thus allowing for inferences on the ν_μ beam properties.

While the neutrinos nearly unimpededly travel all the 732 km to the OPERA detector within about 2.44 ms, the muons, which also pass the hadron absorber, are stopped after about 500 m of rock – nowhere near reaching the LNGS laboratory.

4.1.2 The CNGS Neutrino Beam

The OPERA experiment does not include a near detector for measuring the original neutrino flux and energy spectra at CERN. Therefore, comprehensive Monte Carlo studies are crucial for understanding the original CNGS neutrino beam, its propagation to LNGS, and its interaction with the OPERA detector.
The simulation of the CNGS neutrino beam is conducted using the FLUKA[3] code [Frr06].

Starting with the 400 GeV SPS p^+ beam hitting the center of the CNGS graphite target rod at $4.5 \cdot 10^{19}$ p.o.t./year with Gaussian spatial and angular distributions of $\sigma_X = \sigma_Y = 0.53$ mm and $\sigma_\theta = 0.053$ mrad, respectively, the production of $\pi^\pm$ and $K^\pm$ is simulated. These particles – as well as their decay products (see Table 4.2) – are propagated through the various elements of the CNGS secondary beamline instrumentation, hadron absorber and rock[4]. With the

windows, and containing 13 graphite rods.
[2]Each one 7 m long.
[3]31 m and 41 m long, respectively.
[4]994 m long, 2.45 m in diameter, with a 3 mm Ti entrance window, a water-cooled 50 mm carbon steel window, and shielded by 50 cm of concrete.
[1]Made of 3 m graphite and 15 m Fe.
[2]Separated from each other by 67 m of rock.
[3]FLUKA: Fluktuierende Kaskade; Fully integrated Monte Carlo simulation package for the interaction and transport of particles and nuclei in matter [FLU10].
[4]Rock composition: Simulated as 29.4% Si, 54.0% O, 12.2% Ca, 0.7% H, 3.7% C, with a density of 2.4 g/cm^3.

two muon detector stations being the main monitors for CNGS neutrino beam quality and position, special care is taken in the evaluation of the $\mu^{\pm}$ distribution measured therein.

The composition of the resulting neutrino beam is listed in Table 4.3. Shown are the contributions from the different neutrino flavours in comparison to those from ν_μ, as well as their average energies and expected CC event rates on isoscalar[1] targets.

ν_α	$\Phi\nu_\alpha/\Phi\nu_\mu$ [%]	$\langle E_\nu \rangle$ [GeV]	CC event rates ν_α/ν_μ [%]
ν_μ	–	17.9	–
ν_e	0.65	24.5	0.89
$\overline{\nu}_\mu$	3.9	21.8	2.4
$\overline{\nu}_e$	0.08	24.4	0.06
ν_τ	$< 10^{-4}$	–	$< 10^{-4}$

Table 4.3: CNGS ν_μ beam contamination, average energies, and CC event rates on isoscalar targets for $E_\nu < 100\,\text{GeV}$ [Frr06].

Thus, the CNGS neutrino beam mainly consists of ν_μ with average energies of $E_\nu = 17.9\,\text{GeV}$, and small contaminations of $\overline{\nu}_\mu$ (3.9%), ν_e (0.65%), and $\overline{\nu}_e$ (0.08%). The fraction of prompt ν_τ is completely negligible ($< 10^{-6}$ for all energies) and will be omitted in the following simulation steps.

After propagation for 732 km to the LNGS underground laboratory site, the neutrino flux spectra depicted in Figure 4.4 are obtained. At LNGS, the beam is less intensive, but also much wider (it has been simulated for a radius of 400 m), covering the whole underground laboratory and enabling many experiments to study its properties. The multiplication of the neutrino spectra with their respective cross sections leads to the CC event rates given in Table 4.3, resulting in about 2,800 CC neutrino interactions per kt of isoscalar target material and year.

[1] Isoscalar Atom: Containing the same numbers of protons p and neutrons n. For non-isoscalar target material – such as the OPERA detector, consisting mainly of Pb ($\#p = 82$, $\#n = 125.2$) and Fe ($\#p = 26$, $\#n = 29.845$) – corrections have to be applied, due to the CC DIS coupling of ν to d quarks and $\overline{\nu}$ to u quarks (in the quark parton model, p consists of duu and n of ddu).

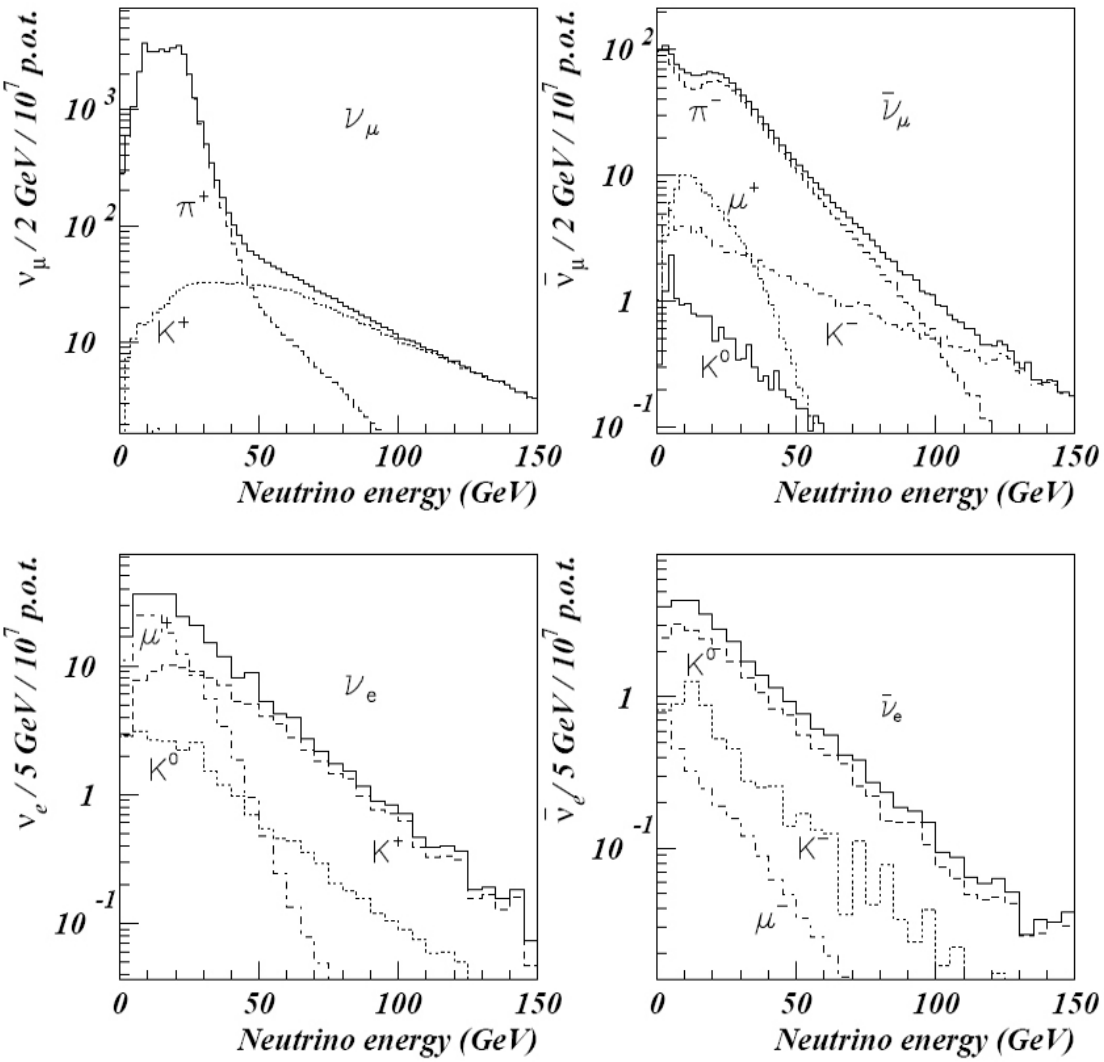

Figure 4.4: CNGS ν_μ (**top left**), $\overline{\nu}_\mu$ (**top right**), ν_e (**bottom left**), $\overline{\nu}_e$ (**bottom right**) flux at LNGS, as well as the corresponding parent particles [Frr06].

With large statistics of 10^7 p.o.t. events, the statistical uncertainty of the FLUKA simulation is $< 1\%$ for ν_μ and $\sim 5\%$ for the other flavours in the energy region of interest (i.e. for $E_\nu < 40\,\mathrm{GeV}$). Systematic errors amount to $\sim 5\%$ on the neutrino flux, as well as $\sim 3.1\%$ (normalisation) and $3-4\%$ (energy-dependent) on the ratio ν_e/ν_μ.

Finally, the neutrino oscillations – mainly the 'atmospheric' $\nu_\mu \to \nu_\tau$ channel, as the $\nu_\mu \to \nu_e$ channel is strongly suppressed [CHO99] – which are to be studied by the OPERA experiment, have to be taken into account (see Chapter 2.3):

$$P_{\nu_\mu\nu_\tau}(L, E_\nu) = \sin^2 2\theta_{23} \cdot \sin^2\left(1.27\Delta m^2_{32}\ [\mathrm{eV}^2] \cdot \frac{L\ [\mathrm{km}]}{E_\nu\ [\mathrm{GeV}]}\right). \tag{4.1}$$

The resulting theoretical ν_τ flux spectrum may be obtained by multiplying the ν_μ spectrum with the oscillation probability given in Equation 4.1, while the ν_μ flux spectrum has to be reduced by a corresponding amount.

With average energies of $E_\nu = 17.9\,\text{GeV}$ and $L = 732\,\text{km}$, the OPERA experiment is clearly off-peak[1] and far away from the first maximum of the oscillations, as can be seen in Figure 4.5, where the $\nu_\mu \to \nu_\tau$ oscillation probability $P_{\nu_\mu\nu_\tau}(L)$ has been plotted for maximal mixing ($\sin^2 2\theta_{23} = 1$) and different values of Δm^2_{32}. The increase in ν_τ flux gained by an even longer baseline, however, would be more than canceled by the resulting greater divergence of the neutrino beam.

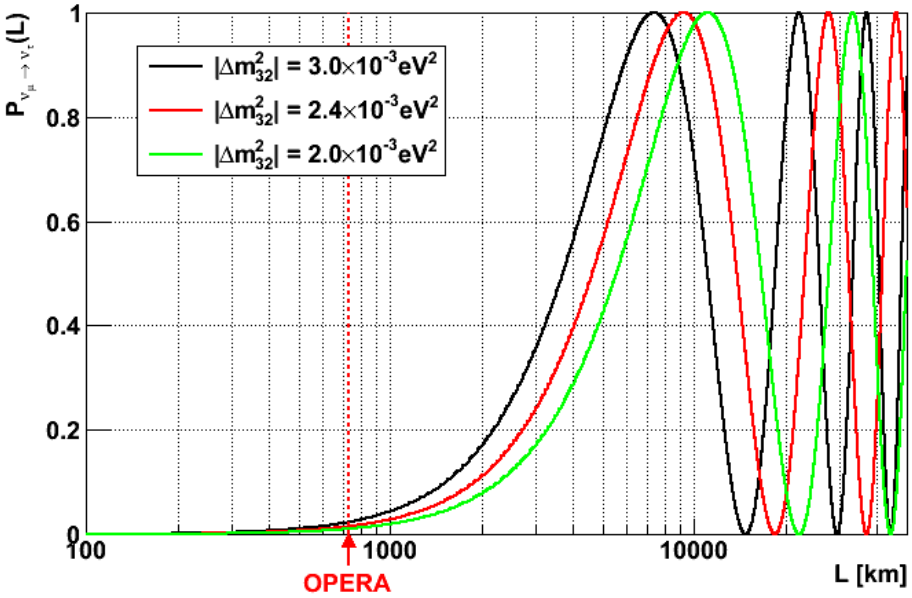

Figure 4.5: $\nu_\mu \to \nu_\tau$ oscillation probability for maximal mixing ($\sin^2 2\theta_{23} = 1$) and $E_\nu = 17.9\,\text{GeV}$.

Figure 4.6 shows the total CC cross section for ν_τ on an isoscalar target.

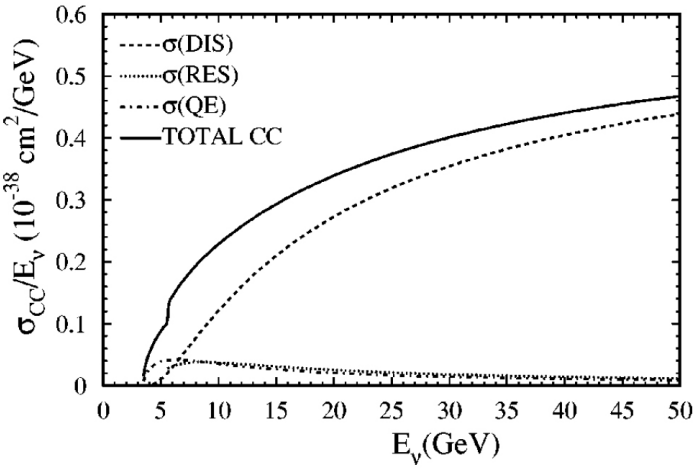

Figure 4.6: ν_τ CC cross sections on isoscalar targets, depending on the neutrino energy E_ν [Pas02].

As the LNGS underground laboratory is in an on-axis position, at the center of the widened beam, the broadly distributed average neutrino energy $E_\nu = 17.9\,\text{GeV}$ is maximal and therefore well above the required threshold of $E_\nu > 3.4\,\text{GeV}$ for τ lepton production (see Figure

[1] In contrast to on-peak experiments at or near the maximum oscillation probability.

4.6). In off-axis experiments, E_ν may be more distinctly selected, as the energy of neutrinos produced in $\pi^\pm$ decays kinematically depends on the angle of their emission. However, the average energy would also be lower, resulting in diminished cross sections.

The chosen ratio of $\frac{L}{E} \approx 41\,\mathrm{km\,GeV^{-1}}$ thus represents an optimisation for a maximum number of ν_τ CC interactions inside the OPERA detector.

4.2 The OPERA Detector

Specifically designed for proving ν_τ appearance, the OPERA detector is located in Hall C of the LNGS underground laboratory below Mt. Corno Grande of Gran Sasso. With a maximum vertical coverage of 1,400 m of rock – corresponding to 3,800 m water equivalent – an excellent shielding against cosmic particles and natural radioactivity is provided[1] [INF10].

The OPERA detector consists of a hybrid structure of about 150,000 brick units[2] (bricks) made from nuclear emulsion films interleaved with lead plates – amounting to an average target mass of 1.25 kt – complemented with scintillator strips, resistive plate chambers, and drift tubes constituting an electronic detector allowing for real-time detection of ionising particles. By observing the tracks of τ leptons (mainly created in ν_τ interactions with Pb) and their decay products in the emulsion films (see Chapter 4.3), the ν_τ can be identified.

Figure 4.7 provides a labeled wide-angle photo of the OPERA detector, showing its different components.

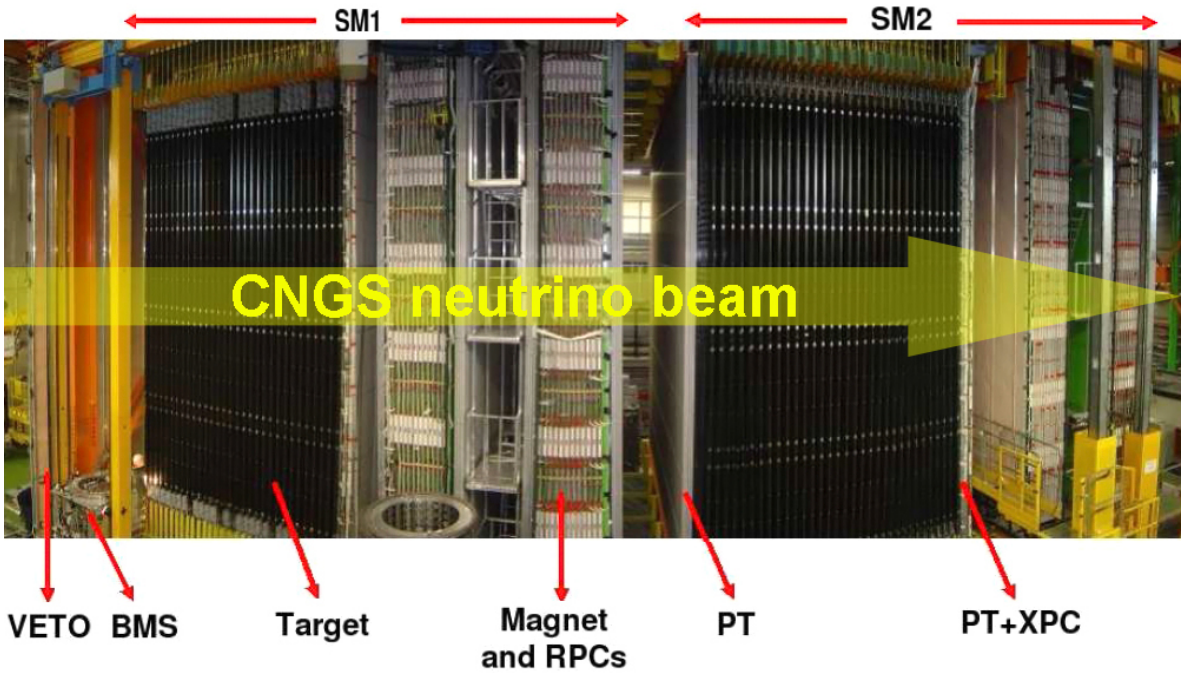

Figure 4.7: Wide-angle photo of the OPERA detector [OPE09a]. Shown are both super modules (SM) consisting of the target (bricks and target tracker plastic scintillators (TT)) and spectrometer (magnets, resistive plate chambers (RPC), crossed resistive plate chambers (XPC), and precision trackers (PT)) as well as the veto (VETO) and the brick manipulator system (BMS). The CNGS neutrino beam enters the detector from the left.

The detector is split up into two identical units, called super modules (SM1, SM2). Each consists of emulsion / lead bricks arranged in 31 vertical walls of 64 horizontal rows, alternating with layers of horizontally and vertically aligned target tracker (TT) scintillator strips – both composing the target (see Chapter 4.2.3) – followed by a spectrometer (see Chapter 4.2.2)

[1] The number of cosmic rays is diminished by a factor of 10^6, the neutron flux by a factor of 10^3.
[2] In the proposal, a design with more than 200,000 bricks was presented.

made of a precision tracker (PT) of high-precision drift tubes and resistive plate chamber detectors (RPC). The RPC are situated inside a nearly uniform magnetic field of 1.53 T provided by a large magnet. Other resistive plate chamber detectors (XPC[1]), oriented at an angle of $\pm 42.6°$ with respect to the horizontal, eliminate ambiguities in case of multiple tracks. Two additional perpendicular glass RPC planes in front of the first super module allow to reject charged particles entering the detector from the outside (VETO) (see Chapter 4.2.1).

Via a GPS[2]-locked, bidirectional clock distribution system, all the readout channels of the electronic detector parts are synchronised, with an accuracy of $\sim$ 20 ns. Furthermore, a synchronisation with the CNGS beam takes place, enabling the preselection of beam-induced 'on-time' events [Mar09], while background events occurring in-between SPS extractions[3] are rejected.

4.2.1 The OPERA Veto System

To exclude secondary particles from CNGS beam neutrino interactions occurring upstream[4] of the OPERA target volume from the analysis, a veto system of two glass resistive plate chamber (GRPC) planes has been installed upstream of the first super module.

The two layers – each consisting of eight rows of four units (three of them measuring $2.60 \times 1.14\,\mathrm{m}^2$, the forth unit $2.20 \times 1.14\,\mathrm{m}^2$) and equipped with 384 horizontal and 416 vertical copper strips – are totaling a sensitive area of $200\,\mathrm{m}^2$ with 1,600 electronic channels. They cover the whole detector XY-plane[5], detecting charged particles passing them.

4.2.2 The OPERA Spectrometer

The OPERA spectrometer is consisting of two identical structures (schematically depicted in Figure 4.8) located downstream of the first and second target, respectively (see Figure 4.7). It has been designed to precisely measure the electric charge and momentum of charged particles – primarily $\mu^{\pm}$ – crossing it.

[1] XPC: Crossed RPC.
[2] GPS: Global Positioning System.
[3] Extraction spacing: 50 ms, batch length: 10.5 μs, see Chapter 4.1.1, Table 4.1.
[4] E.g. in the rock and concrete surrounding the LNGS underground laboratory, or the BOREXINO experiment, lying upstream from OPERA also in HALL C.
[5] Z being the direction of the CNGS neutrino beam.

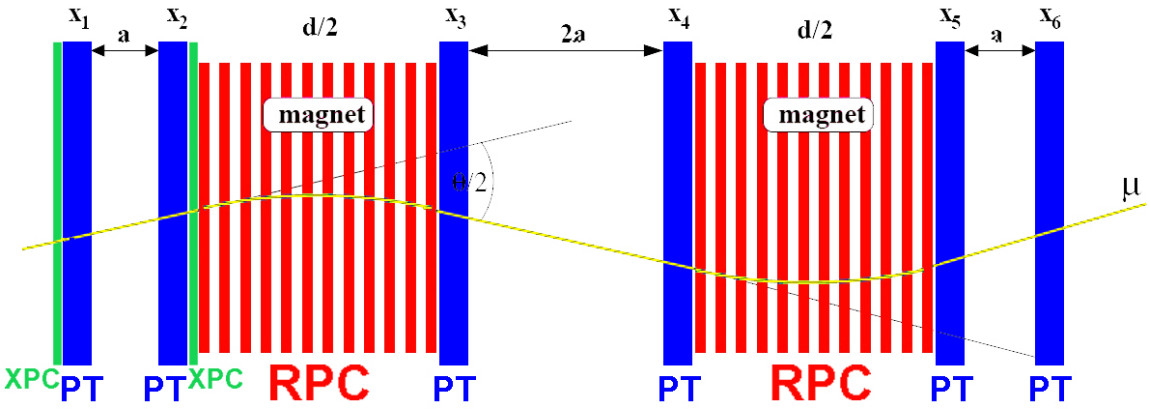

Figure 4.8: Schematic structure of a spectrometer, showing the magnets with resistive plate chambers (RPC), crossed resistive plate chambers (XPC), and precision trackers (PT), as well as the bent path of a μ [Zim05].

The magnet horizontally deflects charged particles from their original tracks, resulting in a curvature that may be measured by the 22 RPC inner tracker planes, placed inside the 2 cm gaps between the iron slabs of the magnet (see Figure 4.10). The deflection angle $\theta/2$ and horizontal shift are registered by the six walls of PT drift tubes located up- and downstream of, and in-between the magnetised iron (see Figure 4.9), thus allowing to infer the particle's momentum and charge [Zim07].

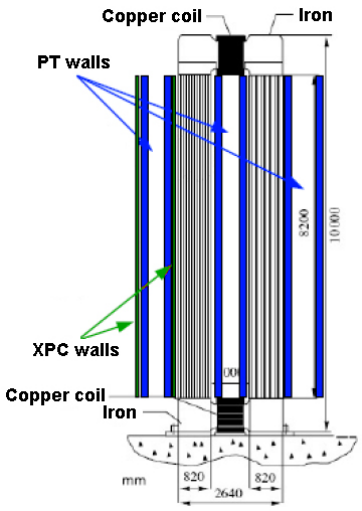

Figure 4.9: Side view of a spectrometer super module (SM), showing the magnet with resistive plate chambers (RPC), crossed resistive plate chambers (XPC), and precision trackers (PT) [Won07].

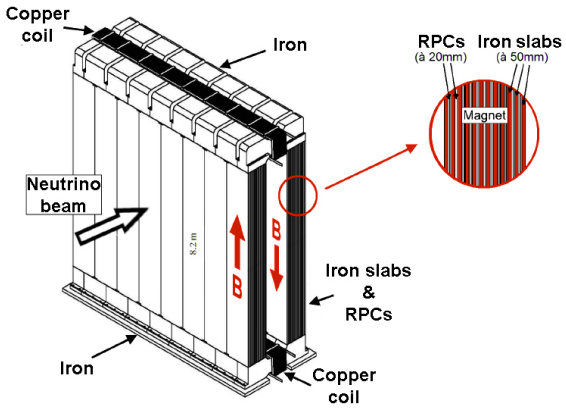

Figure 4.10: Isometric view of an OPERA magnet and resistive plate chambers (RPC) [OPE00].

The XPC, located upstream of the first and downstream of the second drift tube wall of each super module (see Figures 4.8, 4.9), provide additonal track position information, thus increasing vertical track resolution and removing multiple track ambiguities. Together with the RPC, they also act as a trigger for the precision tracker.

The Magnets

Each of the two identical OPERA magnets consists of two vertical walls (arms) – comprising twelve 5 cm thick iron layers[1], interspaced with 2 cm gaps providing room for the RPC planes – and a top and bottom yoke[2] (see Figures 4.9, 4.10).

Two copper coils[3] – of 20 turns each and wound around the upper and lower yoke, respectively – are connected in series and carrying currents of ±1,600 A DC, resulting in an average vertical magnetic field of 1.53 T. By reversing the direction of the electrical current, the polarity of the magnetic field may be changed with no loss of detector performance [Fer10].

Together, both magnets weigh a total of 990 t.

The Resistive Plate Chambers (RPC & XPC)

Located inside the gaps between the iron slabs of the magnets are the inner tracker RPC planes (11 per magnet arm, 22 per super module, 44 in total), each covering 70 m^2 for a total area of 3080 m^2. Their task is the reconstruction of tracks inside the magnet (particularly those of stopping $\mu^{\pm}$, whose momentum may be derived from their range), measurement of the energy of hadronic showers, and giving trigger signals to the PT TDC[4] readout electronics.

The resistive plate chambers use a similar technology to the one developed for BaBar[5], Argo[6], and LHC experiments. Figure 4.11 shows a schematic cross section of an OPERA RPC: Two 2 mm electrodes consisting of bakelite with lineseed oil ($\rho > 5 \cdot 10^{11}\,\Omega\,\mathrm{cm}$), their external surfaces coated with graphite and 190 μm PET[7] insulator, are separated by a lattice of 2 mm PVC [8] spacers ($\rho > 10^{13}\,\Omega\,\mathrm{cm}$) [OPE09a]. The so-formed cavity between the electrodes, to which a HV[9] of 5.7 kV is applied, is flushed with a gas mixture of $Ar : C_2H_2F_4 : iC_4H_{10} : SF_6$ (75.4 : 20.0 : 4.0 : 0.6) at 1 atm [Pao10].

[1] Consisting of seven $50 \times 1250 \times 8200\,\mathrm{mm}^3$ Fe slabs.
[2] Made of six steel basements of 1250 mm width and two 625 mm half-basements.
[3] Built from $100 \times 20\,\mathrm{mm}^2$ Cu bars.
[4] TDC: Time-to-Digital Converter.
[5] BaBar: B and B-bar; High-energy B physics experiment; SLAC, Stanford, California; 1999 – 2008.
[6] Argo: Observation system for the Earth's oceans; International collaboration; 2000−?.
[7] PET: Polyethylene terephtalate.
[8] PVC: Polyvinyl chloride.
[9] HV: High voltage.

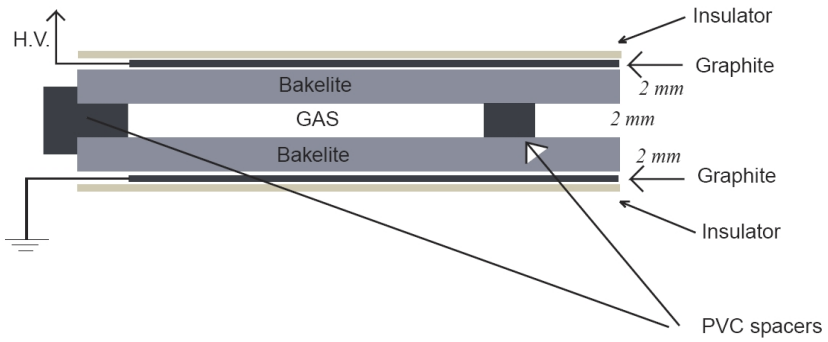

Figure 4.11: Schematic cross section of a resistive plate chamber [OPE00].

Similar to the principle of drift tubes (see next section), the molecules and atoms of the gas inside the RPC are ionised by charged particles crossing them, creating a pulse that is intensified to $\sim 100\,\mathrm{mV}$ by gas amplification between the two electrodes. No further amplification is needed to register these pulses. However – due to the high resistivity of the bakelite electrodes – the deposited charge only slowly dissipates (taking about 150 ms), thus reducing the local electric field and rendering the respective spot of the RPC momentarily blind to other passing particles. The rest of the detector is not subject to this effect and still sensitive.

One RPC plane consists of 21 $2.91 \times 1.134\,\mathrm{m}^2$ RPC arranged in seven rows and three columns (totaling a number of 21 RPC per plane, 462 per magnet, 924 for the whole detector). It is read-out by 8 m long orthogonal Cu strip panels horizontally or vertically aligned at 3.5 cm or 2.6 cm intervals, respectively, and providing an acceptance of 97%.

The XPC readout strips are placed under a relative angle of 42.6° with respect to those of the inner tracker RPC, outside the magnetic field 1 cm in front of the first (covering an area of $7.5 \times 8\,\mathrm{m}^2$) and after the second PT wall (measuring $8.7 \times 8\,\mathrm{m}^2$) of each super module. They are composed of seven rows of three RPC (thus totaling 21 RPC per plane, 42 per SM, and 84 for the whole detector), equipped with Cu strips 2.6 cm apart.

As some of them are instrumented with timing boards[1] (TB), both RPC and XPC are used to trigger the precision trackers with rates of up to 10 Hz per SM [OPE09a].

The Precision Trackers (PT)

The task of the precision tracker is the precise measurement of the horizontal track coordinates of ionising particles both before and after they are deflected by the OPERA magnets. It consists of twelve walls of vertically oriented drift tubes, six per SM: two upstream of the magnet, two between its arms, and two downstream (see Figures 4.8, 4.9).

The PT planes are built from modules of 50 cm wide segments, consisting of four adjacent layers of twelve nearly 8 m long drift tubes. The relative position of the drift tube layers has been optimised via Monte Carlo simulations, requiring at least three drift tubes per module to be hit by muons of different incident angles. The resulting structure of two pairs of layers arranged in hexagonal close packing, with a relative shift of 11 mm, is depicted in Figure 4.12.

[1] High-impedance discriminators operating at low threshold.

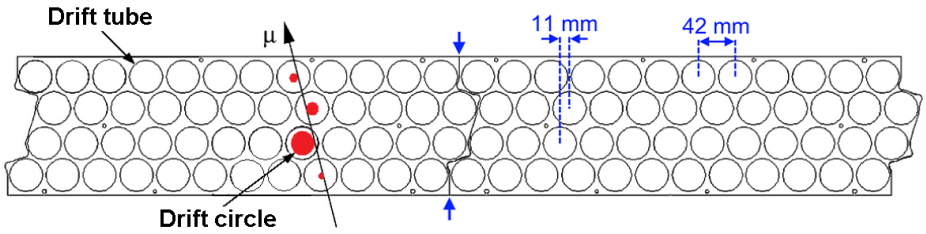

Figure 4.12: Top view of drift tube arrangement [Kro10]. Two module end plates are shown.

To allow for BMS[1] movement and brick access, the three drift tube planes directly adjacent to the target only consist of 15 modules (thus comprising 720 drift tubes and covering an area of 60 m^2), while the other nine are composed of 17 modules (corresponding to 816 drift tubes and 64 m^2), totaling a number of 9,504 drift tubes for the whole detector [Fer06].

The outer diameter of a drift tube is 38 mm, with an Al wall thickness of 0.85 mm. The gold-plated tungsten sense wire has a diameter of 45 μm and is held at both ends of a drift tube, without any further support. Its position accuracy is better than 150 μm. The drift tubes are filled with a gas mixture of $Ar : CO_2$ (80 : 20) at 1005 ± 5 mbar.

Whenever an ionising particle – such as a muon – passes a drift tube, it creates clusters of ionised gas molecules and free electrons along its path. With a HV of 2.45 kV between wire and tube, the electrons are accelerated towards the wire, thereby gaining enough kinetic energy to ionise even more gas molecules (gas amplification). Via such avalanches, measurable pulses are created. By measuring the drift time the electrons need to reach the wire, the distance of the ionising particle that created the pulse from the wire (drift circle radius) may be calculated. The particle's track is then given by the tangent to the resulting drift circles in different drift tubes (see Figure 4.12).

Charged particles passing the OPERA magnets are affected by the Lorentz force, resulting in a deflection angle $\theta/2$:

$$\frac{\theta}{2} = \frac{qBd}{p}, \tag{4.2}$$

with B being the magnetic field, d the distance traveled, q the particle's charge, and p its momentum. In this example, the energy loss of particles in matter and the resulting reduction in momentum has not been taken into account.

Thus deflected by $\pm\theta/2$ inside each of the two magnet arms, the particles' tracks become S-shaped, and their momenta may be derived from the resulting horizontal shift, whose sign indicates the sign of the particle's charge (see Figure 4.8).

The momentum resolution is given by [Zim05]:

$$\frac{\Delta p}{p} \approx \frac{\Delta\theta}{\theta} = \frac{1}{qBd}\sqrt{6\left(\frac{\epsilon p}{a}\right)^2 + \frac{d}{X_0}\left(\frac{14\,\mathrm{MeV}}{c}\right)^2}, \tag{4.3}$$

with a being the distance between the two first and the two last PT planes, $X_0 = 0.0176$ m the radiation length of $\mu^{\pm}$ in iron, $d = 1.2$ m the width of the iron, and ϵ the total spatial resolution.

[1] BMS: Brick manipulator system.

Triggered by the RPC and XPC timing boards, the single-tube hit efficiency of the precision tracker amounts to $> 98\%$, with a a momentum resolution of $\frac{\Delta p}{p} \leq 0.25$ for $\mu^{\pm}$ energies of $E_{\mu} > 25\,\mathrm{GeV}$. The total spatial resolution is better than $636\,\mu\mathrm{m}$ [Zim05].

4.2.3 The OPERA Target

The instrumented target of the OPERA detector consists of 62 walls (31 per super module, of which 29 are filled with bricks), each of them covering an area of $6.7 \times 6.7\,\mathrm{m}^2$, holding the ECC bricks, and followed by a plane of target tracker (TT) scintillator strips (see Figure 4.13). The walls are subdivided into two identical semi walls (SW), composed of 27 lightweight stainless steel ribbons suspended by springs, allowing the two automated BMS on the sides of the detector ('rock side' and 'corridor side', respectively) to access one half of the bricks each.

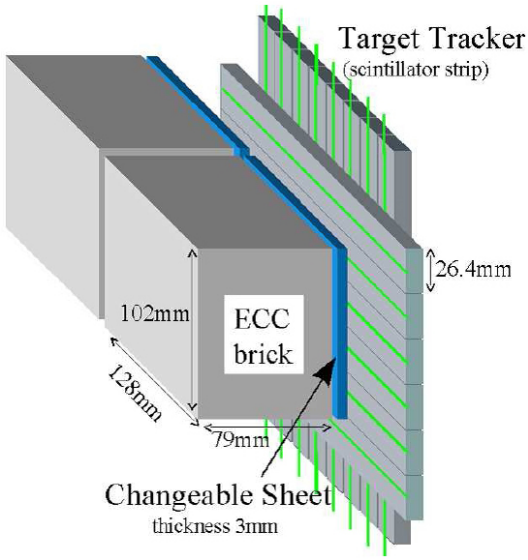

Figure 4.13: Schematic view of the OPERA target structure: An ECC brick with attached changeable sheet, followed by two perpendicular target tracker scintillator strips [OPE08].

Whenever a neutrino interaction has been identified by the electronic detector parts (the RPC, XPC, PT of the spectrometer, and the TT of the target) the respective brick where it took place is tracked down and scheduled to be investigated. Then, the BMS moves to its respective SW and row, extracting any other bricks lying in-between, storing them inside a drum, and reinserting them after the brick in question has been removed. Thus, an analysis of these emulsions may take place, while the rest of the detector stays intact and sensitive.

If the changeable sheets (CS) attached to the brick suspected to contain a neutrino interaction prove positive (see below), the brick will be disassembled and analysed. Otherwise, it is reinserted, while adjacent bricks are being studied. As there are no replacements for bricks ultimately removed from the detector[1], the target volume and mass will decrease with time: The maximum number of about 149,000 bricks (1.28 kt) is expected to have declined by about 12,000 bricks ($\sim 100\,\mathrm{t}$) at the end of the 5-year data taking phase.

[1]Other bricks from periphery of the walls will be relocated to keep the target compact.

The Target Trackers (TT)

The OPERA target trackers are planes of scintillator strip detectors located behind each wall of bricks (see Figure 4.13). Their main task is the real-time location of ECC bricks containing neutrino interactions, and the provision of calorimetric information.

A plane is composed of four horizontal and four vertical modules, each consisting of 64 scintillator strips measuring 6.86 m × 10.6 mm × 26.3 mm, together covering the whole target area. Figure 4.14 provides a schematic cross section of a scintillator strip, showing its wavelength shifting (WLS) fiber which is read out at both ends by multi-anode photomultipliers (PMT).

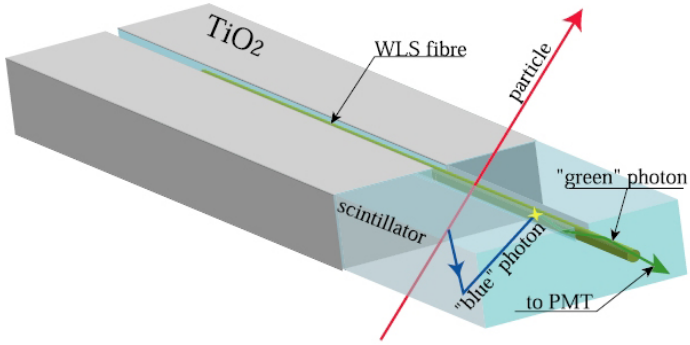

Figure 4.14: Schematic view of a target tracker scintillator strip with wavelength shifting fibre (WLS) [Ada07].

The calorimetric calibration of the TT was conducted using a radioactive ^{90}Sr source emitting e^- of about 1.8 MeV. At nine points, uniformly distributed along the length of each scintillator strip, the measured number of photo electrons (p.e.) is extrapolated to an energy of 2.15 MeV – the mean energy released by a minimum ionising particle (see Chapter 3.1).

With a trigger efficiency of 99% and a spatial resolution of 1.5 cm for CC events, the brick finding efficiency[1] of the target trackers amounts to 80%, thus requiring a second check that is realised by the changeable sheets attached to the ECC bricks (see next section).

Lead / ECC Bricks

The OPERA emulsion cloud chamber (ECC) bricks consist of alternating layers of 56 lead plates of 1 mm thickness and 57 AgBr photo emulsion[2] layers of about 293 μm thickness[3] (altogether corresponding to $\sim$ 10 radiation lengths X_0, see Chapter 3.3.1), oriented perpendicular to the CNGS beam [OPE09a]. With each of the 149,000 ECC bricks measuring $10.2 \times 12.7 \times 7.5\,\text{cm}^3$ and weighing about 8.3 kg, the total target mass amounts to 1.28 kt. They are arranged in 58 walls (29 per SM), each holding about 51 rows of 52 bricks[4].

[1] The probability for selecting the right brick, containing the respective neutrino interaction.
[2] AgBr crystals of 0.2 μm diameter scattered in gelatine binder.
[3] Two emulsion layers of 44 μm, on both sides of a transparent 205 μm thick triacetylcellulose base.
[4] Due to the reduction of the total number of bricks with respect to the proposal, not all of the 62 walls and 64 rows are filled.

Wrapped inside 0.13 mm thick Al foil to ensure light tightness, each brick is equipped with two extra double layers of emulsion – the changeable sheets – on its downstream side (see Figure 4.15). Whenever the electronic detector components indicate a brick to contain a neutrino interaction, it is extracted by the BMS, its CS removed and developed, allowing a swift check for secondary particles. If the CS prove positive, the brick is disassembled, its emulsion layers developed and scanned. If they show no particle tracks, however, the brick is furnished with new CS and reinserted into the detector.

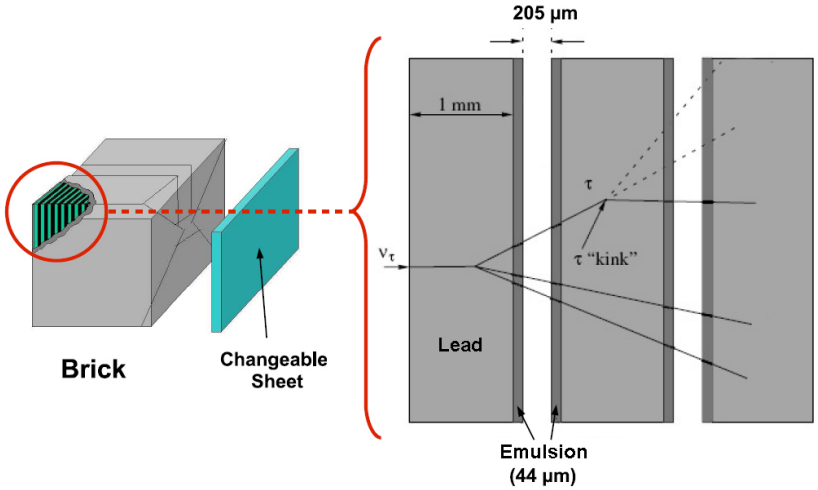

Figure 4.15: Schematic view of an OPERA brick, consisting of alternating layers of lead and emulsions, as well as the changeable sheet [Ste08].

The ECC technique is now applied at a very large scale: The total emulsion area of the OPERA experiment amounts to $> 100{,}000\,\mathrm{m}^2$, requiring industrial production of the emulsion films[1]. The automated brick assembly was conducted by a dedicated brick assembly machine (BAM), and advanced emulsion scanning methods are realised by fully automated CCD microscopes.

Neutrinos interacting in the lead plates via CC interactions (see Chapter 2.1.3) create electrically charged leptons of corresponding flavour, that – when passing the emulsion sheets – create electron-hole pairs in the AgBr[2] crystals. With the e^- trapped in lattice defects of the crystal surface, Ag atoms are created, acting as latent image centers. During development, the number of Ag atoms is multiplied by several orders of magnitude[3], resulting in $0.6\,\mu$m grains of silver atoms that are visible under optical microscopes. The sensitivity of the emulsion films is high enough to detect minimum ionising particles (m.i.p., see Chapter 3.1.1), which leave about 36 grains/$100\,\mu$m.

[1] Carried out in collaboration with Fuji Film.
[2] AgBr is a semiconductor with a band gap of 2.6 eV.
[3] Through the latent image center, the reducer is able to give e^- to the crystal.

4.3 Data Analysis & Event Topologies

4.3.1 Data Analysis

Figure 4.16 shows both projections of a charged current ν_μ interaction, as it is seen by the electronic detector of OPERA. The momentum and charge of the secondary particle can be inferred from its deflection inside the OPERA magnets (see Chapter 4.2.2), measured by the PT, while the task of the TT is to identify the brick in which the interaction took place (see Chapter 4.2.3).

A reconstruction of the same event inside an OPERA ECC brick is depicted in Figure 4.17.

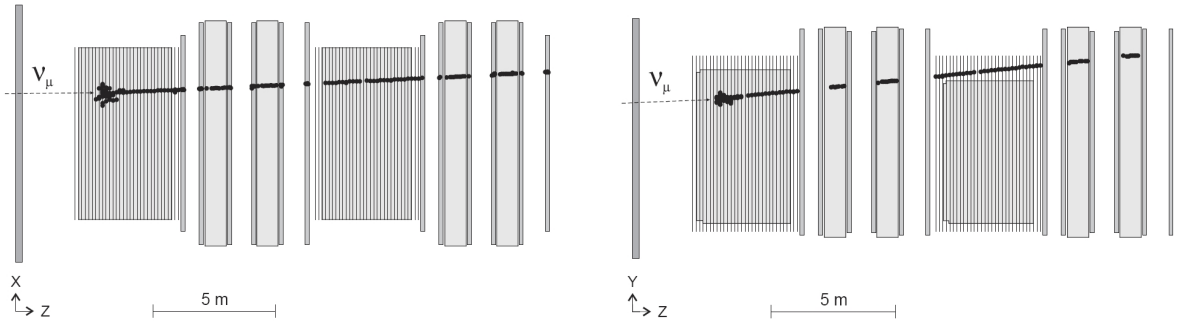

Figure 4.16: Electronic detector reconstruction of a CC event (same as in Figure 4.17) [OPE09b]. **Left:** XZ-view. **Right:** YZ-view.

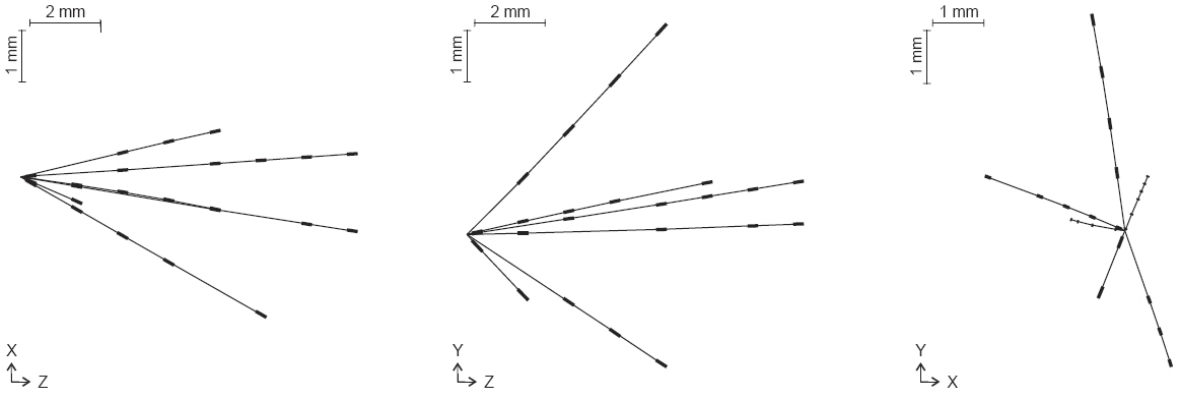

Figure 4.17: Emulsion reconstruction of a CC event (same as in Figure 4.16) [OPE09b]. **Left:** XZ-view. **Middle:** YZ-view. **Right:** YX-view.

When a track corresponding to an interaction observed in the electronic detector has been found in the scanning of the CS, the most downstream emulsion sheets of the respective brick are searched for the same track, inside a small volume of $1\,\mathrm{cm}^3$, predicted by the preceding analysis (point scan[1] or general scan[2]). Once the track has been detected, a scan-back of the upstream emulsions of the brick is performed, following the base track and any others

[1]Point scan: The position and angle of the searched-for base track (i.e. the track segment found inside an emulsion double layer) are known to some degree, allowing a precise search.
[2]General scan: All base tracks inside the selected volume are read out.

connected to it. Furthermore, a net scan[1] of the other emulsion sheets is conducted. When the neutrino interaction vertex has been found, the search for a τ lepton decay signature (see Chapter 4.3.2) is carried out.

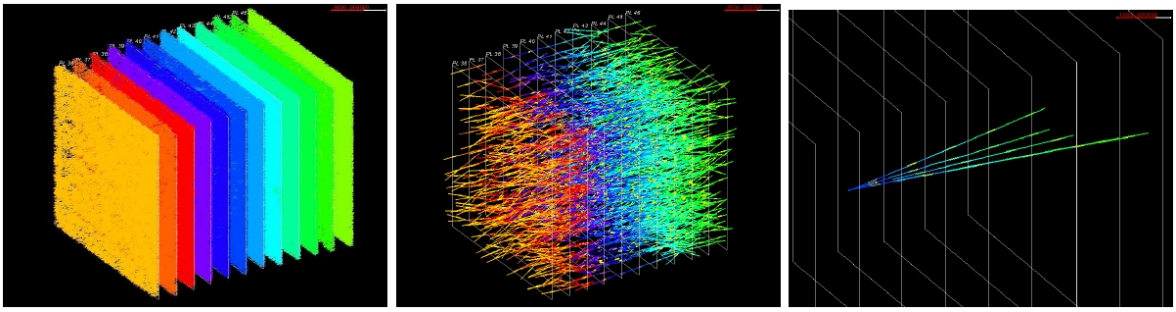

Figure 4.18: Different steps of the emulsion data processing [OPE09a]. **Left:** All base tracks found within $1\,\mathrm{cm}^3$ of emulsion. **Middle:** Reconstructed tracks participating in the alignment procedure. **Right:** Passing-through tracks have been discarded and the vertex reconstructed.

Figure 4.18 shows some steps of the emulsion data processing. Prior to the disassembly of the brick, it has been exposed to cosmic rays, to provide straight tracks to be used during the alignment procedure of the emulsion sheets.

Momentum reconstruction in the bricks is conducted via the measurement of multiple Coulomb scattering in the lead plates (applicable in the case of charged hadrons and muons), or by measuring the density of track segments in electromagnetic showers (for electrons) (see Chapter 4.3.3).

4.3.2 τ Lepton Decay Topologies

The goal of the OPERA experiment is the detection of $\nu_\mu \rightarrow \nu_\tau$ oscillations in the nearly pure ν_μ CNGS beam (see Chapter 4.1) via the appearance of τ neutrinos. In CC interactions (see Chapter 2.1.2) with nucleons N of the ECC target, the ν_τ produce τ leptons (as well as other hadronic or leptonic products X), according to:

$$\nu_\tau + N \rightarrow \tau^- + X. \tag{4.4}$$

With a mean lifetime $\tau = (290.6 \pm 1.0) \cdot 10^{-15}\,\mathrm{s}$ [PDG08], a τ lepton at OPERA decays after a distance of some $100\,\mu\mathrm{m}$ ($c \cdot \tau = 87.11\,\mu\mathrm{m}$). Table 4.4 shows the most important 1-prong[2] decay modes, classified as 'muonic', 'electronic', and 'hadronic', respectively, depending on the decay daughters.

[1] Net scan: A general scan on different emulsions, alignment of their relative positions and connection of base tracks.

[2] 1-prong decay: The final state features 1 charged particle.

Decay Mode		Branching Ratio [%]
$\tau^- \to \mu^- + \nu_\tau + \overline{\nu}_\mu$	(muonic)	17.36 ± 0.05
$\tau^- \to e^- + \nu_\tau + \overline{\nu}_e$	(electronic)	17.85 ± 0.05
$\tau^- \to h^- + \nu_\tau + X^0$	(hadronic)	49.21 ± 0.42
$\pi^- + \nu_\tau$		10.91 ± 0.07
$\pi^- + \nu_\tau + \pi^0$		25.52 ± 0.10
$\pi^- + \nu_\tau + 2\pi^0$		9.27 ± 0.12

Table 4.4: Most important 1-prong τ decay modes [PDG08]. h^- denotes a negatively charged hadron (in 84% of cases being π^-), X^0 are other neutral particles, in 70.70% of the hadronic decays being π^0, while the decay solely to $h^- + \nu_\tau$ makes up 23.57%.

Due to heavy backgrounds, multi-prong decay modes are more complicated to identify. They amount to about 14.64% of the τ decays.

Figure 4.19 depicts the two topologies searched for at OPERA, classified as 'long' and 'short' decays, respectively.

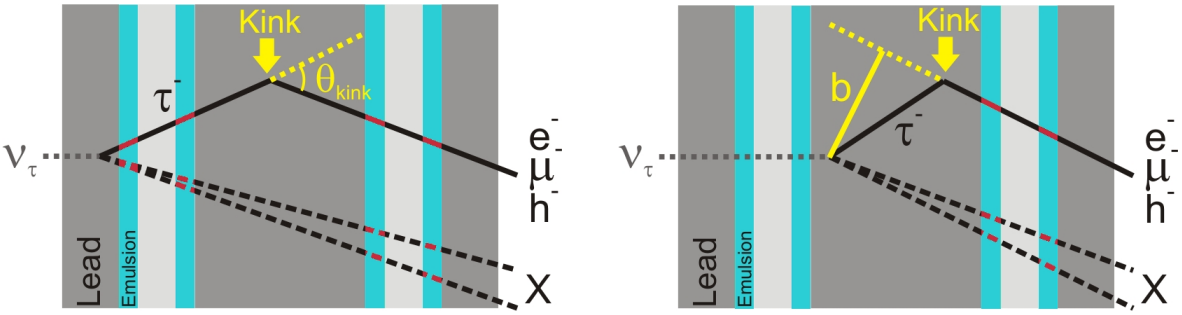

Figure 4.19: Characteristic τ decay topologies in OPERA bricks with ν_τ interactions in lead. **Left:** 'Long' decay with kink angle θ_{kink}. **Right:** 'Short' decay with impact parameter b. The ν_τ and $\overline{\nu}_e$ or $\overline{\nu}_\mu$ created in τ^- lepton decays have been omitted in the depiction.

In long decays, the τ lepton is produced in a lead plate of an OPERA brick, passes an emulsion sheet, and subsequently decays (via the muonic, electronic, or hadronic channel) inside the next downstream lead plate. The reconstruction of the track in the emulsions will exhibit a visible 'kink' with a kink angle θ_{kink} of about 100 mrad, indicating the secondary τ decay vertex.

Short decays describe those 60% of cases where the τ lepton production and decay take place inside the same lead plate. No kink will be visible in the track reconstruction, but an impact parameter $b > 5 - 20\,\mu$m can be measured, as the charged particle from the τ lepton decay does not originate from the same vertex as the others.

4.3.3 Momentum Reconstruction

The reconstruction of particle momenta is necessary for their identification, and to apply kinematical cuts for the reduction of background events.

In the following, two methods for momentum reconstruction (called 'angular method' and 'coordinate method', respectively) shall be described in more detail. Both are relying on the multiple Coulomb scattering of charged particles (see Chapter 3.2) inside the OPERA bricks. Afterwards, a short discussion of momentum reconstruction for the different τ decay modes is given.

The RMS of the approximately Gaussian distribution of the angle under which a particle of momentum p and velocity βc is scattered, is given by [OPE00]:

$$\theta_0 = \frac{13.6\,\mathrm{MeV}}{\beta c p}\sqrt{X}, \tag{4.5}$$

when passing a 1 mm OPERA lead plate with $X = x/X_0 = 1/5.6$.

Angular Method

θ_0 can be measured simply by taking the difference of angles θ_i, θ_j (obtained by connecting two track segments on both surfaces of the film) in two consecutive emulsion films:

$$\theta_M = \theta_j - \theta_i, \tag{4.6}$$

with the RMS of the measured scattering angle θ_M being the quadratic sum of θ_0 and the measurement error $\delta\theta$ [OPE00]:

$$\theta_M^2 = \theta_0^2 + \delta\theta^2. \tag{4.7}$$

With a typical resolution of $\delta\theta = 2.1$ mrad and the requirement that $\theta_0 \geq 2\delta\theta$, the maximum detectable momentum for a single film results to 1.4 GeV. With about 50 emulsion films, an accuracy of $\delta p/p \sim 10\%$ – corresponding to a maximum measurable momentum of 7.1 GeV – may be obtained [OPE00].

This method has the advantage, that – as long as the surfaces of the individual films are parallel to each other with an accuracy of 1 mrad – its error solely depends on the accuracy of the measurement, and not the alignment of different films to each other.

Coordinate Method

For the coordinate method to be applied, at least three emulsion films, precisely aligned to each other, must be available. Then, the scattering angle θ_M in one film may be obtained by measuring the displacement Δx (between the real position of the track and the one interpolated from the track positions in the other films) over the cell length L (the distance between the films):

$$\theta_M = \frac{\Delta x}{L}, \tag{4.8}$$

with the relation of the measured scattering angle θ_M and θ_0 being:

$$\theta_M^2 = \frac{2}{3}\theta_0^2 + \delta\theta^2. \tag{4.9}$$

As this method measures the particle track angles over greater distances, it is more sensitive to higher momenta (up to $\sim 5.9\,\text{GeV}$ for three emulsion films) than the angular method. Due to the fact that at least three emulsion films are needed for an independent measurement, however, the momentum resolution $\delta p/p = 14\%$ gained by following a track for an entire brick is slightly worse than for the angular method.

Electronic τ Decays

The energy loss of e^- produced in the decays of τ^- leptons (see Table 4.4) takes place primarily through bremsstrahlung (see Chapter 3.3) [OPE00]:

$$E_e(x) = E_0 e^{-x/X_0}, \tag{4.10}$$

thus creating electromagnetic cascades (E_e being the electron energy after a distance x).

By evaluating the number of tracks – corresponding to the energy deposited – within a specific solid angle area, the momentum and energy of the primary particle causing the cascade may be inferred (see Chapter 3.3.2).
Alternately, a multiple scattering analysis is conducted (see Equation 4.5) .

Hadronic τ Decays

Like the e^- of electronic τ^- decays, hadrons originating from the hadronic decay of τ leptons (see Table 4.4) also create showers inside the bricks. Their energy loss occurs mainly via ionisation of the matter passed (see Chapter 3.1) [OPE00]:

$$E_h(x) = E_0 \left(1 - \frac{dE}{dx}x\right), \tag{4.11}$$

with E_h being the hadron energy after a distance x.

The process of energy reconstruction is similar to the multiple scattering analysis and evaluation of the electromagnetic cascades in electronic τ decays, while the differences in their specific energy loss are used to distinguish between these particles.

Muonic τ Decays

In contrast to the particles produced in other τ lepton decay modes, most μ^- created in muonic τ^- decays (see Table 4.4) nearly unimpededly cross the whole target region, as they do not create electromagnetic cascades.

While the momentum of low-energetic μ^- may also be measured with the OPERA TT scintillators or emulsion films using multiple scattering, this is not possible for $\mu^\pm$ of high energy. The reconstruction of high-energy $\mu^\pm$ momenta and charge thus is the task of the spectrometer PT (see Chapter 4.2.2).

4.3.4 Background Events

Depending on the respective τ decay modes (see Table 4.4), different sources of background mimicking the expected topologies (see Chapter 4.3.2) have to be taken into account.

Prompt ν_τ Background

Originating from the decay of τ leptons created in the decay of D_S mesons in the CNGS target, the rate of prompt ν_τ CC interactions (see Chapter 2.1.2) in the OPERA detector target region is expected to be less than a fraction 10^{-6} of the ν_μ CC interaction rate (see Table 4.3) – several orders of magnitude below the expected oscillation signal. Furthermore taking into account the detection efficiency, its contribution is completely negligible [OPE00].

1-Prong Decay of Charmed Particles

In ν_μ CC and NC interactions with nucleons N of the OPERA target, charmed particles are created according to:

$$\nu_\mu + N \rightarrow c + \mu^- + X \qquad \text{(CC : Single charm production)} \tag{4.12}$$

$$\nu_\mu + N \rightarrow c + \overline{c} + \mu^- + X \qquad \text{(CC: Associated charm production)} \tag{4.13}$$

$$\nu_\mu + N \rightarrow c + \overline{c} + \nu_\mu + X \qquad \text{(NC : Associated charm production)} \tag{4.14}$$

As they have lifetimes and masses similar to those of a τ lepton, the 1-prong decay of these charmed hadrons may constitute a background, if the primary μ^- remains undetected (single charm production, CC associated charm production), or if one or both of the charmed hadrons are not observed (CC and NC associated charm production).

The most relevant source of background is constituted by the single charm production ($N_c/N_{CC} = (3.3 \pm 0.5)\%$, with N_{CC} and N_c depicting the number of CC and charm events, respectively), the cross section for NC associated charm production being smaller by an order of magnitude. Altogether, a number of about $16.5 \cdot 10^{-6} \times N_{CC}$ background events from the decay of charmed particles is expected [OPE00].

Background from π^0 and Prompt e^-

The electronic τ lepton decay channel (see Table 4.4) may be mimicked by primary e^- produced in ν_e CC interactions and scattering in lead, as well as by the electronic decay of π^0 created via pion charge exchange processes ($\pi^- + p^+ \rightarrow \pi^0 + n$) in ν_μ NC reactions.

While the background from promt e^- to τ lepton long decays ($< 10^{-6} \times N_{CC}$) can be eliminated by applying kinematical cuts, as has been shown via Monte Carlo studies [OPE00], the contribution from electrons produced in pion charge exchanges constitutes a background of about $0.2 \cdot 10^{-6} \times N_{CC}$.
Furthermore, short decays may be faked by prompt e^- and γ-conversions inside the lead plate containing the vertex, together resulting in a background of $\sim 0.1 \cdot 10^{-6} \times N_{CC}$.

Large-Angle μ^- Scattering

Another source of background arises from μ^- produced in ν_μ CC events, scattering in the lead plate downstream from the one containing the vertex, and featuring topologies similar to those of long muonic τ lepton decays (see Table 4.4).

While many of these events may be discarded with a cut on the muon transverse momentum p_t, a background of $\sim 5 \cdot 10^{-5} \times N_{CC}$ remains, however with a large error of about 50%, due to uncertainties of the Monte Carlo simulations [OPE00].

Hadronic Reinteractions

Hadronic reinteractions – hadrons that are produced in ν_μ NC reactions (or ν_μ CC reactions where the primary muon is not detected), undergoing a second interaction in the vertex lead plate or the next downstream one – constitute a background of $\sim 5 \cdot 10^{-6} \times N_{CC}$ (with an error of $\sim 50\%$) to the hadronic τ decay channel (see Table 4.4) [OPE00].

Additionally, these reinteractions may mimic the muonic τ decays (see Table 4.4), if the primary muon of a ν_μ NC or ν_μ CC reaction is not identified, and the hadron is misidentified as a muon.

4.4 Sensitivity of the OPERA Experiment

With up to 149,000 bricks, a maximum target mass of 1.28 kt, and 5 years of data taking at a beam intensity of $4.5 \cdot 10^{19}$ p.o.t., a total number of about 26,000 CC and NC events are expected inside the OPERA detector[1].

Table 4.5 lists the predicted numbers of events for the different neutrino flavours contained in the CNGS beam (see Chapter 4.1.2, Table 4.3) and respective interaction types (CC or NC, respectively). As already discussed, the contamination with prompt ν_τ is negligible.

Interaction Type	# Events
ν_μ CC	19,572
ν_μ NC	5,880
$\overline{\nu}_\mu$ CC	411
ν_e CC	156
$\overline{\nu}_e$ CC	13
Total	26,032

Table 4.5: Expected number of CNGS beam-induced ν interactions observed in the OPERA detector for 5 years of data taking and $4.5{\cdot}10^{19}$ p.o.t./year [OPw10]. The 25% target mass reduction with respect to the proposal has been taken into account.

The number of expected ν_τ interactions, resulting from τ neutrinos created in $\nu_\mu \rightarrow \nu_\tau$ oscillations (see Chapter 2.3), depends – apart from the neutrino energy E_ν and the baseline L of the experiment – on the exact values of the mixing angle $\sin^2 2\theta_{23}$ and the mass difference Δm^2_{32} (see Chapter 4.1.2, Equation 4.1 and Figure 4.5).
For maximal mixing ($\sin^2 2\theta_{23} = 1$) and three different values of Δm^2_{32}, the predicted numbers of CNGS-beam induced ν_τ interactions inside the OPERA detector are given in Table 4.6.

Δm^2_{32}	# Events
$1.0 \cdot 10^{-3}\,\mathrm{eV}^2$	20
$2.0 \cdot 10^{-3}\,\mathrm{eV}^2$	80
$3.0 \cdot 10^{-3}\,\mathrm{eV}^2$	180

Table 4.6: Expected number of CNGS beam-induced ν_τ interactions observed in the OPERA detector for 5 years of data taking, $4.5 \cdot 10^{19}$ p.o.t./year, maximal mixing ($\sin^2 2\theta_{23} = 1$), and various mass differences Δm^2_{32} [OPw10]. The 25% target mass reduction with respect to the proposal has been taken into account.

The numbers listed in Table 4.6, however, do not yet take into account the detection efficiencies

[1] In the proposal, a maximum target mass of ~ 1.7 kt (206,336 bricks) was presumed, but most numbers given in this chapter are referring to the actual maximum target mass of ~ 1.28 kt, corresponding to a reduction of about 25%.

of the different decay modes and interaction types of the OPERA experiment, given in Table 4.7 for an average target mass of 1.6 kt. The total detection efficiency thus results to about 9.1% [Zim06].

Decay Mode	QES Long [%]	DIS Long [%]	DIS Short [%]	Weighted Total [%]
$\tau^- \to \mu^-$	2.5	2.4	0.7	2.8
$\tau^- \to e^-$	2.3	2.7	1.3	3.4
$\tau^- \to h^-$	3.5	2.8	–	2.9
Weighted Total [%]	8.3	8.0	1.3	9.1

Table 4.7: Expected ν_τ detection efficiencies for the OPERA detector [Zim06]. QES: Quasi-elastic scattering, DIS: Deep inelastic scattering. An average target mass of 1.6 kt is presumed, and the weighted total incorporates branching ratios and efficiencies.

For a reduced target mass of about 1.28 kt and maximal mixing ($\sin^2 2\theta_{23} = 1$), the expected number of ν_τ events observed in the OPERA detector in 5 years of data taking at $4.5 \cdot 10^{19}$ p.o.t./year is given in Table 4.8 for the values $\Delta m^2_{32} = 2.5 \cdot 10^{-3}\,\mathrm{eV}^2$ and $\Delta m^2_{32} = 3.0 \cdot 10^{-3}\,\mathrm{eV}^2$, along with the predicted number of background events. For $\sin^2 2\theta_{23} = 1$ and $\Delta m^2_{32} = 2.5 \cdot 10^{-3}\,\mathrm{eV}^2$, about 10 τ leptons are predicted to be observed[1], while the number of expected background events is smaller than 1.

Decay Mode	# Events		# Background Events
	$\Delta m^2_{32} = 2.5 \cdot 10^{-3}\,\mathrm{eV}^2$	$\Delta m^2_{32} = 3.0 \cdot 10^{-3}\,\mathrm{eV}^2$	
$\tau^- \to \mu^-$	2.9	4.2	0.17
$\tau^- \to e^-$	3.5	5.0	0.17
$\tau^- \to h^-$	3.1	4.4	0.24
$\tau^- \to 3h$	0.9	1.3	0.17
Total	10.4	15.0	0.76

Table 4.8: Expected number of different CNGS beam-induced ν_τ decays and background events observed in the OPERA detector for 5 years of data taking at $4.5 \cdot 10^{19}$ p.o.t./year, maximal mixing ($\sin^2 2\theta_{23} = 1$), and mass differences $\Delta m^2_{32} = 2.5 \cdot 10^{-3}\,\mathrm{eV}^2$ and $\Delta m^2_{32} = 3.0 \cdot 10^{-3}\,\mathrm{eV}^2$ [OPw10]. The 25% target mass reduction with respect to the proposal has been taken into account.

When the significance of the ν_τ signal observed with the OPERA experiment reaches, e.g., 4σ – corresponding to a probability of 1/16,000 that the observed number of events is produced by background – the $\nu_\mu \to \nu_\tau$ oscillations will be firmly established.

The one τ candidate event already detected in the $2008 - 2009$ data sample analysed so far corresponds to a significance of 2.01σ [OPE10].

Figure 4.20 shows the discovery probability of OPERA for $\nu_\mu \to \nu_\tau$ oscillations, depending

[1] Current measurements at MINOS give $\Delta m^2_{32} = 2.35^{+0.11}_{-0.08} \cdot 10^{-3}\,\mathrm{eV}^2$ [MIN10].

on Δm^2_{32}, and reaching 90% (4σ significance) and 97.5% (3σ significance) at the value of $\Delta m^2_{32} = 2.35 \cdot 10^{-3}\,\mathrm{eV}^2$, measured by MINOS [MIN10].

In case that the $\nu_\mu \rightarrow \nu_\tau$ oscillation search with OPERA should prove to be unsuccessful, Figure 4.21 provides an exclusion plot for parameters Δm^2_{32} and $\sin^2 2\theta_{23}$ at 90% CL.

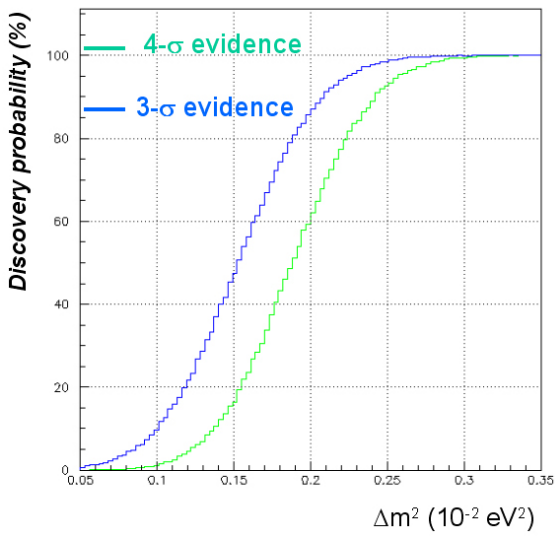

Figure 4.20: Probability for the discovery of $\nu_\mu \rightarrow \nu_\tau$ oscillations with the OPERA experiment for 5 years of data taking at $4.5 \cdot 10^{19}$ p.o.t./year [OPw10]. The 25% target mass reduction with respect to the proposal has been taken into account.

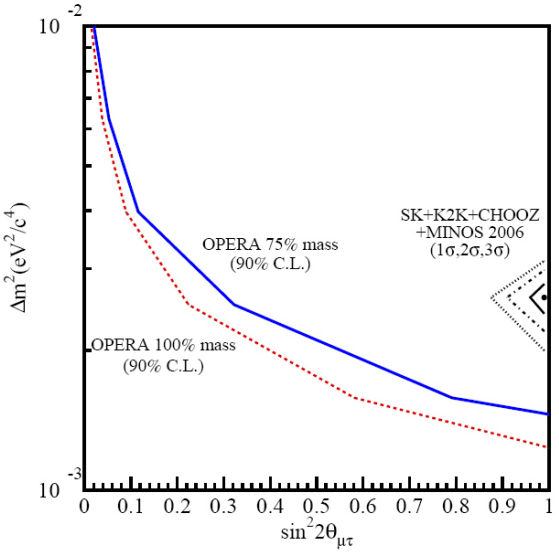

Figure 4.21: Exclusion plot for parameters Δm^2_{32} and $\sin^2 2\theta_{23}$ for 5 years of data taking with the OPERA detector at $4.5 \cdot 10^{19}$ p.o.t./year [OPw10].

Chapter 5

The OPERA Software Framework OpRelease

Continuously under development, the OPERA software framework *OpRelease* is based on ROOT[1] and managed by CMT[2] for setting environment variables and creating the make-files for compilation. An official CVS[3] software revision control system (and its successor SVN[4], used inside the Hamburg PT group) allows keeping track of changes to *OpRelease* and downloading the latest versions from a central repository.

OpRelease includes sub-packages for Monte Carlo (MC) event generation and detector simulation, as well as various programs used in the event reconstruction process for both simulated and real data, some of which shall be discussed in detail in the following.

5.1 OpGeom

With the sub-package *OpGeom* (based on the ROOT geometry class *TGeoManager*) of *OpRelease*, the full geometry of all detector parts is implemented, as well as the major environs of the detector, such as the BOREXINO experiment and the surrounding rock.

Via a modular structure, an idealised detector geometry is realised: Detector components – e.g. PT drift tubes (see Chapter 4.2.2) or TT scintillators (see Chapter 4.2.3) – whose dimensions and material parameters are given inside the sub-package *OpDim*, are summarised to modules, their positions saved in *OpGeom*. Furthermore, a map of the magnetic field is provided. As alignment corrections are not accounted for, they have to be applied during event reconstruction.

The whole OPERA detector – including all passive parts – is contained and simulated inside a box-shaped volume (OPDY), while the surrounding rock is simulated as a large tube, 400 m long and 200 m in diameter. The WRLD volume encompasses both.

[1] ROOT: An Object-Oriented Data Analysis Framework; written in C++ [ROO10].
[2] CMT: Configuration Management Tool [CMT10].
[3] CVS: Concurrent Versioning System.
[4] SVN: Subversion.

All this data may be accessed from other OPERA programs, with the exact operation of *OpRelease* depending on the volume chosen: The FULL mode considers the WRLD volume, while the OPERA mode takes into account only the OPDY volume. With *OpDisplay*, a full 3D detector visualisation inside the ROOT framework is available.

Lengths in *OpRelease* are measured in cm. Also, the default coordinate system is defined, with Z describing the direction of the CNGS neutrino beam, oriented perpendicular to X and Y, implying the horizontal and vertical direction, respectively.

5.2 OpData and OpRData

The OPERA file format is identical for both simulated and real data. Thus, the same analysis and reconstruction programs may be applied.

The data itself is divided into two classes: Data (*OpData*) and resistant data (*OpRData*) – both of similar structure, but with slight differences in object and function names. While *OpRData* is the class as which the data is saved by ROOT programs, it is converted into *OpData* to be processed by analysis algorithms, e.g. for track and momentum reconstruction. Afterwards, the temporary *OpData* objects have to be reconverted into *OpRData* for saving.

The data structure is managed by the *TreeManager*, defined in the sub-package *OpRData* of *OpRelease*. The *TreeManager* is able to create and read ROOT files of the OPERA format. Some important *OpRData* objects comprised by it are:

RRunHeader:
Containing information concerning the run, usually applying to all events (e.g. the run number (*RunNumber*), number of events (*NumberOfEvents*), number of p.o.t. (*NumberOfPot*), run start and stop time (*TimeStart, TimeStop*), type of the run, i.e. REAL or MC (*RunType*)).

REvtHeader:
Containing general information for each event (e.g. the date and time of the event (*Date, Time*), event number (*DayEvNumber*), event type as given by *OpCarac* (*EventType*), interaction type, i.e. CC or NC (*InteractionType*), synchronisation with the CNGS beam (*OnTimeWithCNGS*)).

RParticle:
Containing MC particle information for simulated data (e.g. the energy (*Energy*), pdg code (*pdgCode*), momentum (*Px, Py, Pz*)).

RVertex:
Containing MC vertex information for simulated data (e.g. the pdg codes of incoming and outgoing particles (*IncomingPart, OutgoingPart*), time of the event (*Time*), location of the vertex (*X, Y, Z*)).

RTrackKinematics:
Containing reconstructed kinematical information for each track (e.g. information of

whether the particle is a $\mu^{\pm}$ or not (*MuonID*), reconstructed energy, charge, vertex coordinates and slopes (*Parameter*), variances of the reconstruction (*Variance*)).

RSDTHit, RSRPCHit, RTSCINHit, RVETOHit, RXPCHit:
Hit lists, corresponding to particle interactions with the respective sub-detector (only available for simulated data).

RSDTDigit, RSRPCDigit, RTSCINDigit, RVETODigit, RXPCDigit:
Digit lists, corresponding to signals measured inside the respective sub-detector (available for both simulated and real data).

Data already used for the analysis is stored inside 'used lists' (existing only for *RData*), whose name is an extended version of the respective original data list (e.g. *RSDTDigitUsedList*). For MC-created data, more lists exist than for real data, providing additional information on the simulation.

5.3 OpRealIO

Real data taken by the detector is first saved in the ASCII format. Via the package *OpRealIO*[1], it is converted to OPERA *Digits*. Magnetic field polarity, alignment corrections, and signal transit times are taken into account.

5.4 Monte Carlo Event Simulation

The energy spectrum of incoming CNGS neutrinos is simulated using the FLUKA framework, taking into account their production at CNGS (see Chapter 4.1.2).

The OPERA software chain for simulated data is then started by the event generator *NEGN*[2] (or, in some cases, *GENIE*[3]), calculating for CC and NC the deep inelastic (DIS[4]), elastic or quasi-elastic (QE[5]), or resonant (RES[6]) neutrino interactions inside the OPERA detector for CNGS beam neutrinos. Via *OpConverter*, the beam files created by *NEGN* are converted to the OPERA ROOT format. Furthermore, cosmic muons and showers may be generated (using the package *OpCosmic*), and a particle gun is provided. Particle identification takes place using the pdg codes defined by [PDG08].

Subsequently, the package *OpSim* (based on Geant3) simulates the *Hits* these particles create when entering active detector volumina, taking into account the geometry defined in *OpGeom*. *OpDigit* then translates this information into *Digits*, considering detector effects (such as efficiency, dead time, space and time resolution).

[1] IO: Input/Output.
[2] NEGN: NOMAD Event Generator.
[3] GENIE: Generates Events for Neutrino Interaction Experiments.
[4] DIS: Deep inelastic scattering; Scattering of leptons with quarks.
[5] QE: Quasi-elastic scattering; Scattering with momentum and charge transfer, the particles stay mainly intact.
[6] RES: Resonant scattering; Scattering via creation of short-lived particles.

At this point, the MC-simulated data includes (in addition to MC-specific facts) all the information that would be available for real data taken by the detector. It may thus be analysed using the same reconstruction algorithms, allowing for direct comparison.

5.5 OpAlgo

The *OpAlgo* tool provides a structure and basic methods for data (i.e. *OpData*) processing inside the *OpRelease* framework. While data access is managed by a *RunManager*, the *OpAlgoManager* is responsible for the algorithms and software packages.

Each software package making use of *OpAlgo* includes a main program file **ana.cpp*, calling the method *algoFactory*, which contains a list of all the algorithms required.

Every program based upon *OpAlgo* – as well as the **ana.cpp* file – comprises three basic methods: *init*, *execute*, and *finalize*. When the respective program is activated, the required algorithms are initialised as part of the *init* method. Next, the *execute* method will be carried out for each event contained in the respective input file – thus constituting the main part of the algorithm. Eventually, the *finalize* method concludes the process, saving possibly created data.

5.6 OpRec

The identification and kinematical reconstruction of particle tracks (both for real and simulated data) is conducted using the package *OpRec*.

Via *RecoLoader*, the data is loaded, afterwards *RecoAna.cpp* calls more sub-packages:

Alignment adjusts the data, previously based on the ideal geometry assumed by *OpGeom*, to the real circumstances. Individual *Digits* are then comprised to *PatHits* by *Pattern*, combined to *PatCells* via *PatCellBuilder*, finally giving $2D$ (XZ or YZ projection) χ^2-optimised *PatSegments*, created by *PatSegmentBuilder*, for the respective sub-detector. These $2D$ *PatSegments* are then connected via *PatSegmentConnector* and saved as *TrackElements* by *TrackElementBuilder*. Eventually, the sub-package *Merging3D* tries to match *TrackElements* of XZ projection and YZ projection, resulting in *TrackKinematics* objects. Afterwards, *DTubeReco* attaches track and momentum information of reconstructed tracks inside the PT as *DTubeInfo* to the respective *TrackKinematics*.

With the *Tracking* sub-package, a kinematical fit – using an iterative Kalman filter[1] – is conducted for each *TrackKinematics* object, reconstructing the particle charge and momentum, its coordinates (X, Y, Z), as well as the corresponding errors. For the vertex, this information is stored as *Parameter* (status vector) and *Variance* (covariance matrix) inside *TrackKinematics*.

Then, the *MuonID* package (see Chapter 6.3) applies its criteria on the fit result, providing a value for the member *muonId* of *TrackKinematics*.

[1]Kalman filter: Named after physicist R. E. Kálmán; Mathematical method allowing for inferences on a true system's state to be made, based on observations weighted by their accuracy.

Finally, all the created data is saved to a new ROOT file by *RecoSaver*.

5.7 OpCarac

The sub-package *OpCarac* characterises events detected by the OPERA detector and reconstructed by *OpRec*, depending on the location of the interaction. Each event is assigned to one of the following classes:

CONTAINED:
The vertex of the interaction lies inside the OPERA target region.

SPECTRO:
The interaction took place inside the spectrometer.

SIDEMUON:
Detector events caused by muons (and other particles) entering the detector from the sides, e.g. from cosmic showers or CNGS neutrino interactions with the surrounding rock.

FRONTMUON:
Similar to SIDEMUON, but the particles are entering the detector from the front – mainly caused by CNGS neutrino interactions inside the upstream rock or BOREXINO experiment.

UNKNOWNTYPE:
All other events that cannot be classified (e.g. due to insufficient track reconstruction) as one of the above-mentioned.

As *EventType*, this information is stored inside the *REvtHeader*.

5.8 OpBrickFinder

After the event reconstruction – including pattern recognition and $\mu^{\pm}$ identification – has been conducted by *OpRec*, the sub-package *OpBrickFinder* tries to track down the brick where the respective neutrino interaction (flagged as CONTAINED by *OpCarac*) occurred.

Different algorithms are used, depending on the interaction type: If a $\mu^{\pm}$ has been identified (as is most often the case in ν_{μ} CC QES reactions), the vertex position of its track indicates the brick in question. If, on the other hand, a hadronic shower is detected and reconstructed, its point of origin will denote the brick to be extracted and analysed.

Chapter 6

Separation of $\pi^{\pm}$ and $\mu^{\pm}$ inside the Electronic Detector of OPERA

6.1 Motivation and Importance for the OPERA Experiment

The identification of high-energy $\mu^{\pm}$ and the reconstruction of their momenta and charge is the fundamental task of the OPERA spectrometer.

For the oscillation signal detection efficiency of the τ^- lepton muonic decay mode ($\tau^- \rightarrow \mu^- + \nu_\tau + \overline{\nu}_\mu$, see Table 4.4) created in ν_τ CC reactions, it is crucial to identify the outgoing μ^-. By requiring the reconstructed charge of the particle to be negative, the respective background – i.e. from $\mu^{\pm}$ rescattering in ν_μ CC reactions, $\pi^{\pm}$ created in hadronic reinteractions in NC and CC events and misidentified as $\mu^{\pm}$, or charm di-muonic events with wrong matching between electronic detector tracks and brick emulsions – may be significantly reduced, and the signal-to-noise ratio improved.

Unidentified μ^- from ν_μ CC reactions may pose a background to the hadronic τ^- decay modes ($\tau^- \rightarrow h^- + \nu_\tau + X^0$, see Table 4.4). In contrast, hadrons created in hadronic τ^- lepton decays wrongly identified as $\mu^{\pm}$ and connected to the primary vertex in the emulsion scans will lead to a classification of the respective event as ν_μ CC and its consequent rejection from the analysis, implying an immediate loss of signal.

Also, the background arising from the 1-prong decay of charmed particles (see Chapter 4.3.4) to all τ^- decay modes strongly depends on the identification of the produced $\mu^{\pm}$: If the primary μ^- created in ν_μ CC processes according to Equations 4.12 (single charm production) or 4.13 (CC associated charm production) is not identified, a topology similar to that of a τ^- lepton decay is observed.

Furthermore, the brick finding efficiency of CC reactions relies on the reconstructed tracks of $\mu^{\pm}$, while for events classified as NC, other algorithms will be applied.

As the hadrons created in the hadronic τ^- lepton decay modes are primarily π^- (see Table 4.4), which are of similar mass as μ^- and therefore difficult to distinguish from, special care has to be taken in the separation of $\pi^{\pm}$ mesons and $\mu^{\pm}$ leptons.

6.2 General Preface on the Separation of $\pi^{\pm}$ and $\mu^{\pm}$

The properties of $\mu^{\pm}$ and $\pi^{\pm}$, as well as their most important decay modes are shown in Table 6.1.

	$\mu^{\pm}$ Lepton Properties	$\pi^{\pm}$ Meson Properties
Mass m [MeV]	105.658367 ± 0.000004	139.57018 ± 0.00035
Mean life τ [s]	$(2.197019 \pm 0.000021) \cdot 10^{-6}$	$(2.6033 \pm 0.0005) \cdot 10^{-8}$
$c\tau$ [m]	658.650	7.8045
Decay modes	$\mu^- \rightarrow e^- + \overline{\nu}_e + \nu_\mu$ ($\sim 100\%$)	$\pi^+ \rightarrow \mu^+ + \nu_\mu$ ($(99.98770 \pm 0.00004)\%$)

Table 6.1: $\mu^{\pm}$ and $\pi^{\pm}$ properties and decay modes [PDG08].

As the masses of these particles are similar, so is their mean energy loss via ionisation and resulting range in absorbers (see Chapter 3.1, Figures 3.2 and 3.3). Due to their larger mass, however, the energy loss $-dE/dx$ of $\pi^{\pm}$ will by slightly greater than that of $\mu^{\pm}$, a criterion that can be used to distinguish between them.

Also, $\pi^{\pm}$ of similar momenta as $\mu^{\pm}$ will be of lower velocities, enabling high-precision time-of-flight (TOF) measurements for a given distance to separate these particles from each other. E.g., for known momenta of $65 - 160\,\text{MeV}$ and a distance of 1.5 m, the TOF difference results to $1 - 3\,\text{ns}$ [Fra00].

While, on the one hand, the range of particles depends on their energy loss in absorbers, it is also determined by their mean lifetime τ, after which their decay into other particles takes place. For $\pi^{\pm}$, τ is much smaller than for $\mu^{\pm}$, resulting in shorter ranges $c\tau$ (see Table 6.1).

As $\pi^{\pm}$ are hadrons, their multiple scattering (see Chapter 3.2) inside matter occurs not only via Coulomb scattering, but also as a result of strong interaction processes. Furthermore, the mean deflection angle θ_0 of multiple Coulomb scattering will be larger for $\pi^{\pm}$ than for $\mu^{\pm}$ of the same energies, due to their mass. Hence, a multiple scattering analysis may be used for the separation of $\pi^{\pm}$ / $\mu^{\pm}$ of known energies [Dak74]. Accordingly, a particle has to be correctly identified for multiple scattering analyses to be successful in the reconstruction of its momentum.

6.3 Current Implementation of $\mu^{\pm}$ Identification

The current implementation of $\mu^{\pm}$ identification inside the electronic detector parts of OPERA strongly relies on the track length of the reconstructed particle track.

If, for the first 3D track – i.e. the longest track reconstructed in both XZ and YZ detector planes – of an event that is flagged as 'on time' with the CNGS ν_μ beam, the track is found

to be exiting the detector at its back, or the track length is measured to be larger than $660\,\mathrm{g/cm^2}$, the respective particle is identified as a muon. For reconstructed tracks stopping inside the detector with track lengths smaller than $660\,\mathrm{g/cm^2}$, the particle is supposed not to have been a muon [Jol09].

Correspondingly, if an electronic detector event cannot be matched to emulsion tracks, the event is denoted as ν_μ CC and rejected from the τ search procedure, if the first track exits the detector at its back or has a track length of at least $660\,\mathrm{g/cm^2}$ [Jol09]. Otherwise, it is treated as a NC event, for which another brick finding algorithm will be applied.

Table 6.2 lists the $\mu^{\pm}$ CSDA ranges (see Chapter 3.1.1) for different momenta in Pb and Fe, the main constituents of the OPERA detector. The corresponding $\pi^{\pm}$ collision lengths for these materials are shown in Table 6.3. The numbers of interaction lengths are similar for an OPERA target wall (0.33λ) and a 5 cm spectrometer iron slab (0.3λ), as is the energy loss of minimum ionising $\mu^{\pm}$ with 71.4 MeV for a target wall and 57.1 MeV for an iron slab [Her04].

$\mu^{\pm}$ Momentum [GeV]	CSDA Range in Pb [g/cm^2]	CSDA Range in Fe [g/cm^2]
1.101	816.5	640.2
10.11	6691	5532
100.1	$4500 \cdot 10$	$4314 \cdot 10$

Table 6.2: $\mu^{\pm}$ CSDA range in Pb and Fe [PDG08].

$\pi^{\pm}$ Collision Length in Pb [g/cm^2]	$\pi^{\pm}$ Collision Length in Fe [g/cm^2]
137.3	107.0

Table 6.3: $\pi^{\pm}$ collision length in Pb and Fe [PDG08].

At first glance, the currently applied cut seems to be a good idea, and for $\mu^{\pm}$ of momenta $> 3\,\mathrm{GeV}$ that are able to cross the entire detector, a purity of nearly 100% is attained [Her04]. However, $\mu^{\pm}$ of low momenta will be misidentified by this cut.

If the charge of the respective particle has been reconstructed inside the spectrometer, the background from $\pi^{\pm}$, created at equal rates in NC reactions and misidentified as μ^- from muonic τ^- decays, can be reduced by about 50% by further requiring the particle to be of negative charge [Ter03].

Inside the ECC bricks, low-energy $\mu^{\pm}$ and $\pi^{\pm}$ are identified mainly via their specific energy loss $-dE/dx$ through ionisation (see Chapter 3.1) [Roy05].

6.4 Monte Carlo Simulation

For the following analysis, different Monte Carlo simulations have been conducted, enabling the study of particle interactions within the OPERA detector, as well as the resulting event topologies inside the electronic detector parts and the impact of cuts on particle identification efficiencies.

6.4.1 Simulation of Single π^+ and μ^- (Particle Gun)

To gain a first understanding of the interactions of $\mu^{\pm}$ and $\pi^{\pm}$ within the OPERA detector, beams of single μ^- and π^+ of various momenta p_Z between 0.25 GeV and 20 GeV have been simulated at 2,000 events each, using the tool *OpConverter* as a particle gun.

See Figure 6.1 for the total numbers of simulated μ^- and π^+, resulting when requiring the events to be tagged as CONTAINED or SPECTRO by the OPERA reconstruction algorithms (indicating a first interaction inside the OPERA target or spectrometer region, respectively), and to contain a reconstructed 3D track[1]. Figure 6.2 shows the corresponding momentum distribution of the particles fulfilling these conditions.

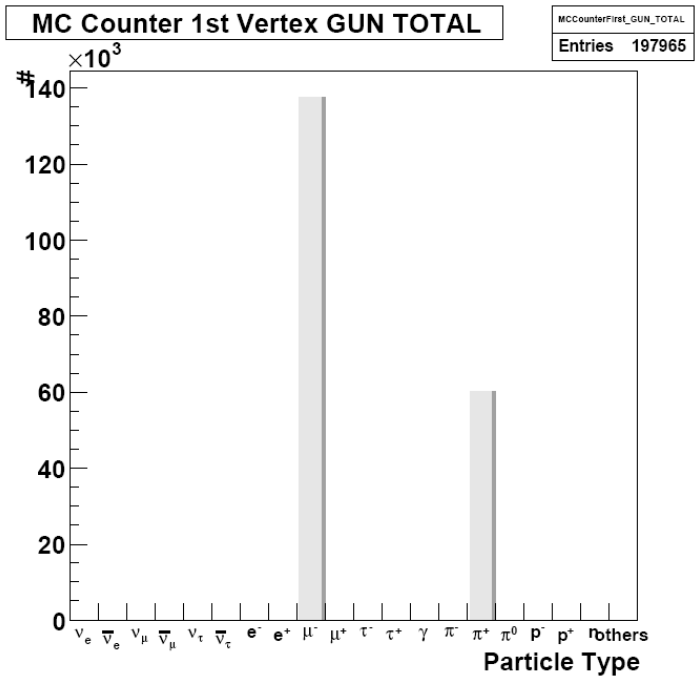

Figure 6.1: Particle gun MC primary particles counter.

[1]These conditions will also be applied to all other events and plots in this chapter.

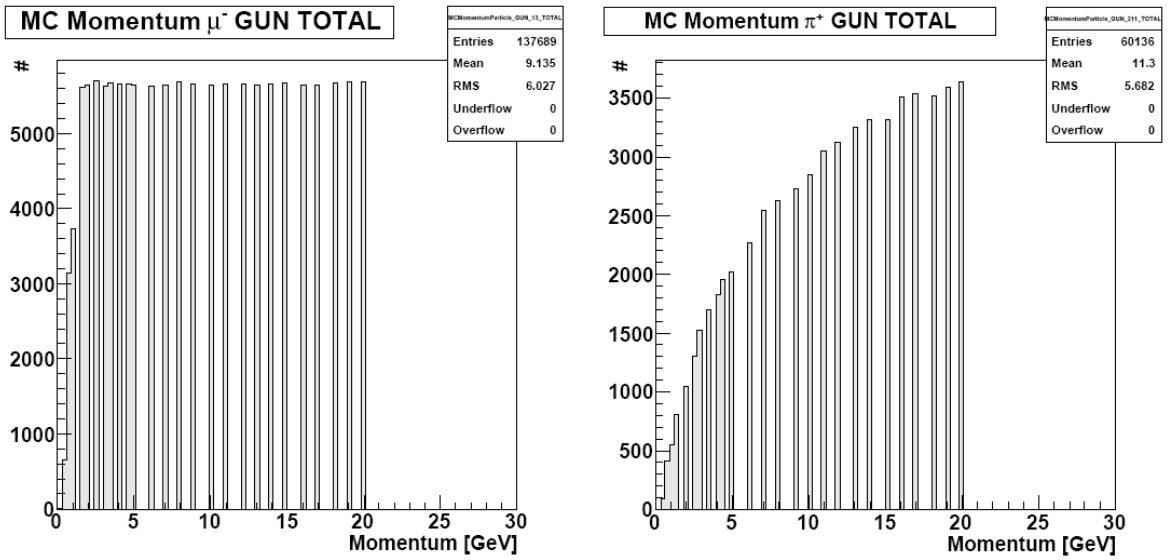

Figure 6.2: Particle gun MC momentum distribution. **Left:** μ^-, **right:** π^+.

Via *OpSim*, the μ^- and π^+ interactions inside the OPERA detector have been simulated for starting vertices TARGET (front center of the first target), SPECTRO (front of the first and second spectrometers), and CENTER (center of the first target). Figure 6.3 shows the total primary vertex distribution of the μ^- and π^+, as well as the secondary vertices of their decay or interactions with the detector. The direction of flight has been chosen to be parallel to the detector Z axis, similar to the CNGS beam.

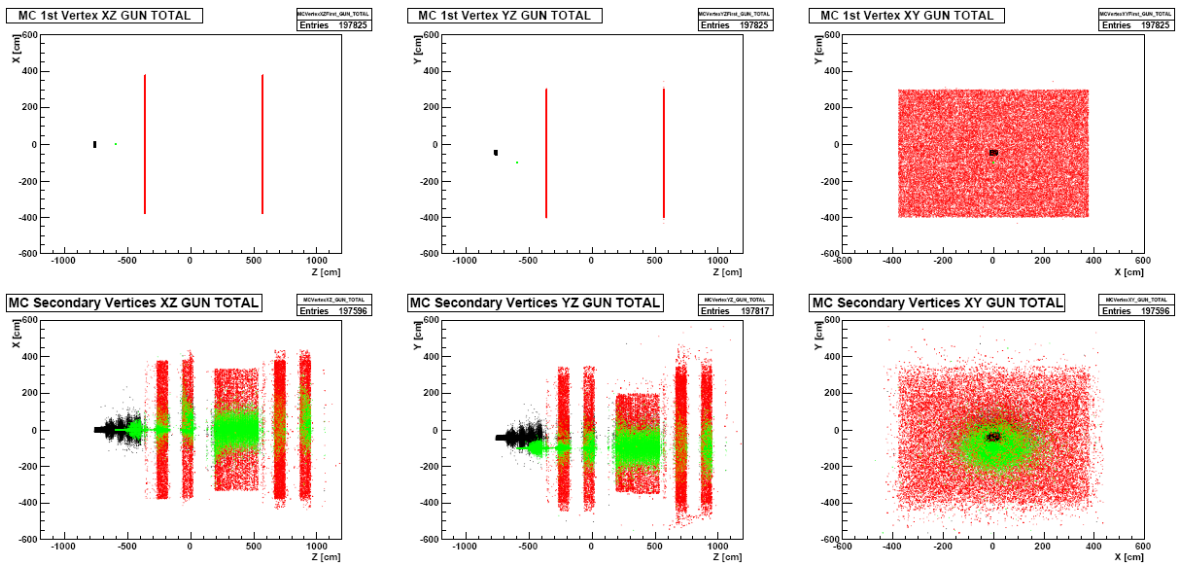

Figure 6.3: Particle gun μ^- and π^+ (TOTAL). **Top:** MC vertex distribution, XZ view, YZ view, XY view. **Bottom:** MC decay vertex distribution XZ view, YZ view, XY view. **Black:** TARGET events, **red:** SPECTRO events, **green:** CENTER events. See Appendix A.1.1 for separate plots.

A first topological difference of μ^- and π^+ interactions becomes immediately obvious when looking at the separate plots for the μ^- and π^+ secondary vertices (see Appendix A.1.1): While for μ^- events, the secondary vertices are broadly distributed within the detector, the

decay or interaction of π^+ takes place much closer to the primary vertex of the particle's production. Apparently, a cut on the reconstructed track length – i.e. the range of the particles – will indeed be a good cut criterion for $\mu^{\pm}$ / $\pi^{\pm}$ separation.

The particles created at the secondary vertices of μ^- and π^+ are shown in Figure 6.4. While the particles created in μ^- interactions and decays are mainly $e^{\pm}$ and γ, the particles prevailing in π^+ interactions and decays are n, p^+, $\pi^{\pm}$, and π^0.

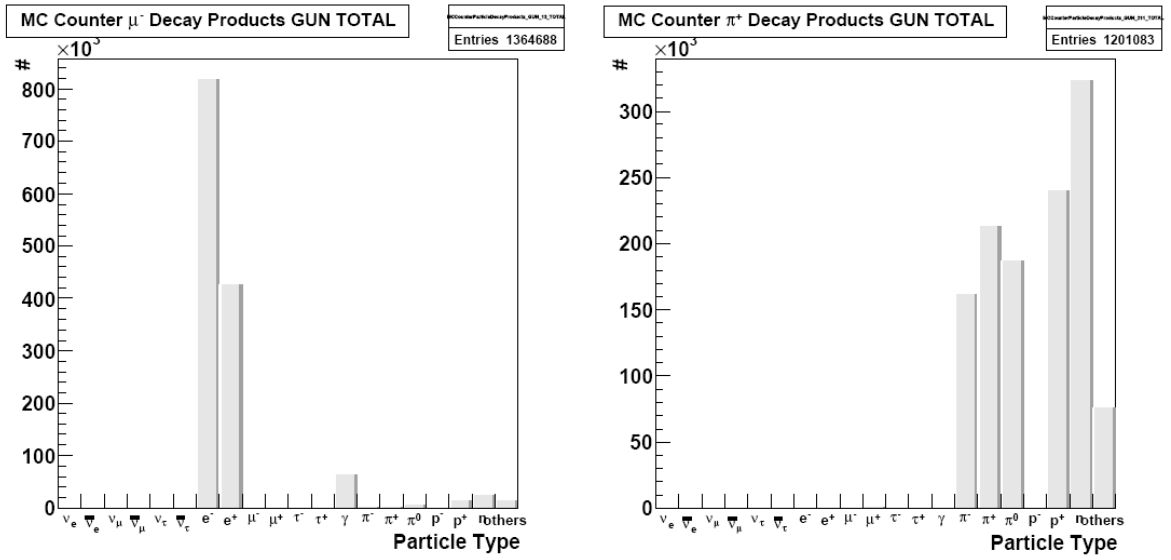

Figure 6.4: Particle gun MC secondary particles. **Left:** μ^-, **right:** π^+.

The slopes dX/dZ and dY/dZ, under which these secondary particles are exiting the interaction vertices, might also be a possible separation cut criterion, as can be seen in Figure 6.5: The MC slope distribution is much broader for π^+ secondary particles ($RMS_X = 0.0110$, $RMS_Y = 0.0112$) than for those of μ^- ($RMS_X = 0.0066$, $RMS_Y = 0.0063$).

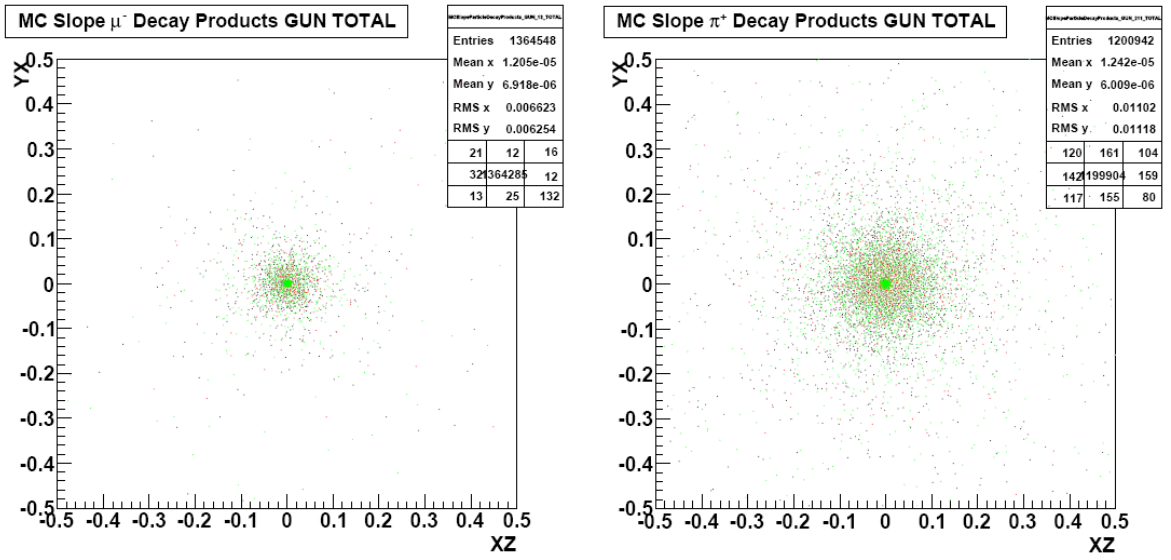

Figure 6.5: Particle gun secondary particles MC slope. **Left:** μ^-, **right:** π^+.

6.4.2 Simulation of the CNGS Neutrino Beam

In the simulation of the CNGS ν_μ beam, the contaminations from $\overline{\nu}_\mu$, ν_e, and $\overline{\nu}_e$ (see Chapter 4.1.2, Table 4.3 for their relative fluxes and CC event rates) have been omitted for this analysis, to concentrate on the predominant ν_μ reactions.

Using the FLUKA MC-simulated ν_μ energy spectrum (shown in Chapter 4.1.2, Figure 4.4), the deep inelastic (DIS), resonant (RES), and quasi-elastic (QEL) ν_μ scattering processes with Pb atoms have been simulated with *NEGN*. The resulting data was then processed by the OPERA software chain for detector simulation (*OpSim*, *OpDigit*), and event reconstruction (*OpRec*).

From the CNGS ν_μ beam spectrum and the respective interaction cross sections, the relative rates shown in Table 6.4 have been computed for the different CC scattering processes inside the OPERA detector.

ν_μ Interaction Type	Ratio [%]
ν_μ DIS CC	71.2
ν_μ RES CC	3.2
ν_μ QEL CC	3.3

Table 6.4: CNGS ν_μ beam relative CC interaction rates [Cor10].

With a ratio of:

$$\frac{NC}{CC} = 0.3, \tag{6.1}$$

the interactions have been weighted according to Table 6.5, to adequately reproduce the real CNGS beam ν_μ component.

ν_μ Interaction Type	Weight [%]
ν_μ DIS CC	71.2
ν_μ DIS NC	21.3
ν_μ RES CC	3.2
ν_μ RES NC	1.0
ν_μ QEL	3.3

Table 6.5: CNGS ν_μ beam interaction weights used within the scope of this analysis.

Figure 6.6 shows the resulting total numbers of particles created at the first ν_μ interaction vertex, again requiring the event to be tagged as 'on time' and CONTAINED or SPECTRO, as well as asking for a reconstructed 3D track[1].

[1]These conditions will also be applied to all other events and plots in this chapter.

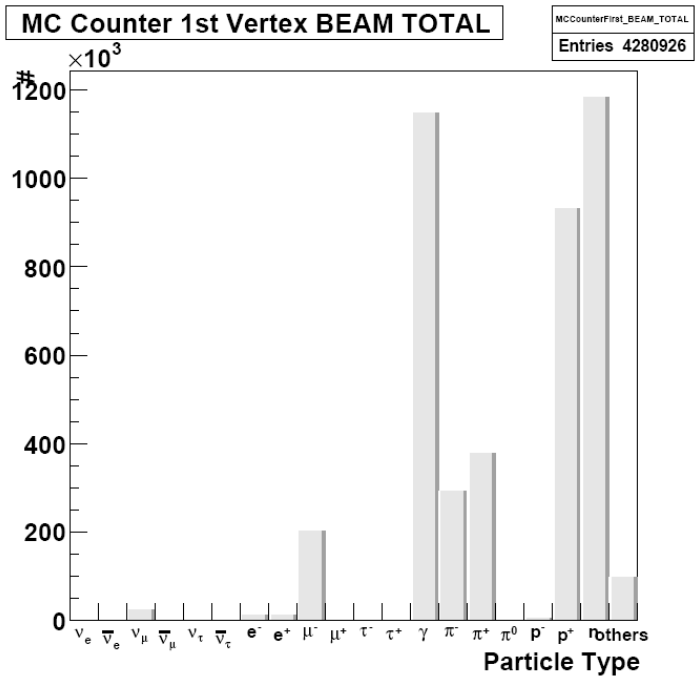

Figure 6.6: CNGS ν_μ beam MC primary particles (TOTAL). See Figure 6.7 and Appendix A.2.1 for separate plots.

Figure 6.7 and Appendix A.2.1 provide separate plots for the different interaction types. In ν_μ DIS CC, ν_μ RES CC, and ν_μ QEL CC interactions, the reconstructed first track will usually be associated with a μ^-, rather than with a $\pi^{\pm}$, if both particles are present. In ν_μ DIS NC and ν_μ RES NC events, no μ^- are created, and the first track has a high probability of belonging to the track left by a $\pi^{\pm}$.

As most reconstructed values relevant for this analysis (e.g. track length, momentum) are relying on the first reconstructed track of an event, the $\pi^{\pm}$ / $\mu^{\pm}$ separation for CNGS beam events has to be interpreted rather as a separation of ν_μ CC and ν_μ NC events. In the following, the focus will be on ν_μ DIS CC and ν_μ DIS NC reactions, as they represent the largest part of the CNGS beam. However, most MC and reconstructed properties of ν_μ RES CC, ν_μ RES NC, and ν_μ QEL CC interactions feature similar characteristics, as will be shown by their corresponding plots provided in the appendix.

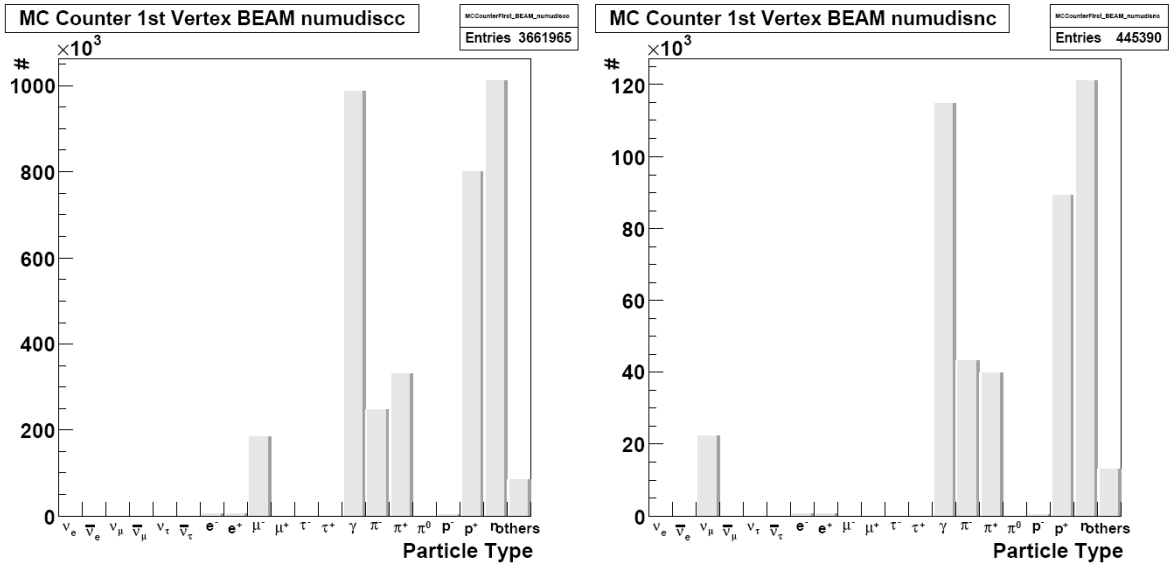

Figure 6.7: MC beam ν_μ reactions primary particles counter. **Left:** DIS CC reactions. **Right:** DIS NC reactions.

The MC momentum distribution for all CNGS ν_μ beam events ('on time', with a reconstructed 3D track, and characterised as CONTAINED or SPECTRO) is shown in Figure 6.8 individually for particles $\mu^\pm$ and $\pi^\pm$. In Appendix A.2.2 the corresponding MC momentum distributions are given separately for the different interaction types. While the MC momentum distribution for μ^- exhibits a broad maximum between about $2-15\,\mathrm{GeV}$, the distribution for $\pi^\pm$ is much narrower, with a maximum at momenta of $< 1\,\mathrm{GeV}$.

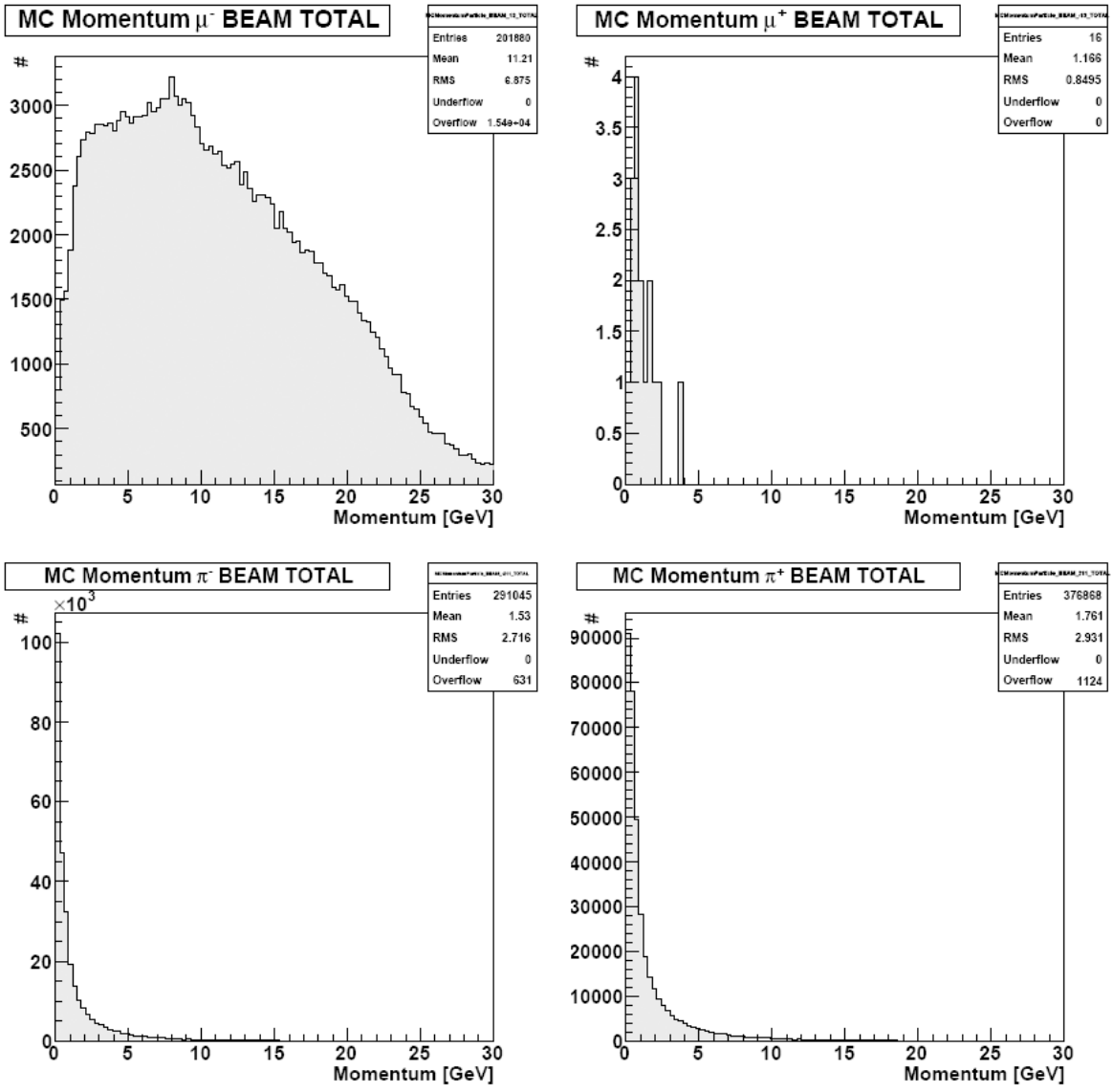

Figure 6.8: CNGS ν_μ beam MC momentum distribution (TOTAL). **Top left:** μ^-, **top right:** μ^+, **bottom left:** π^-, **bottom right:** π^+.

Figure 6.9 shows the simulated primary vertices in the OPERA Pb target for all CNGS ν_μ beam interactions, as well as the secondary vertices of decaying or interacting particles, also outlining the OPERA Fe spectrometer.

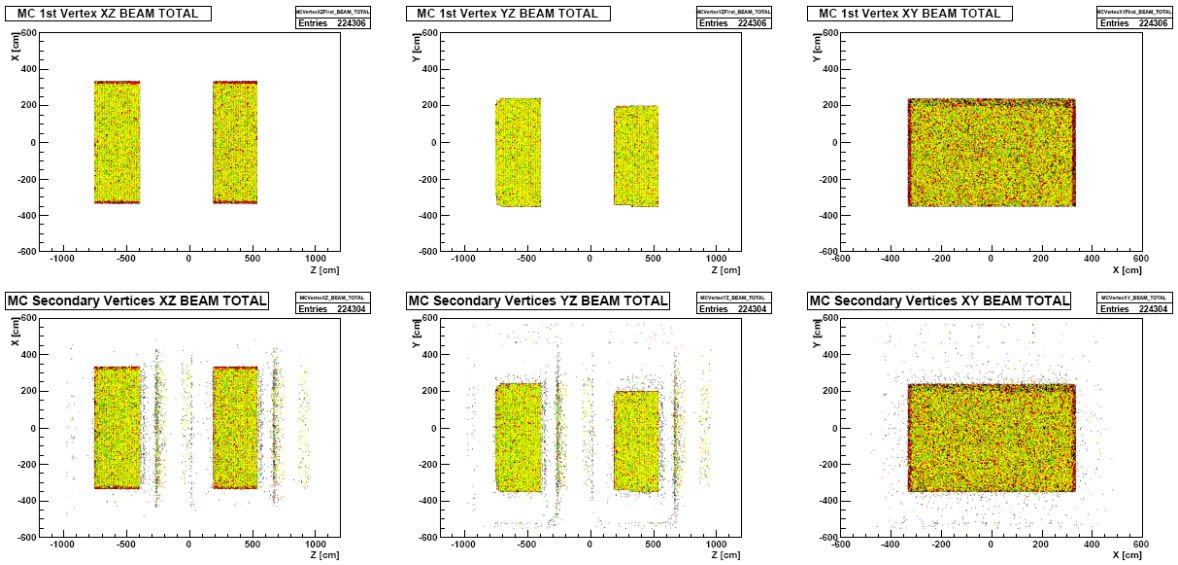

Figure 6.9: CNGS ν_μ beam (TOTAL), **top:** MC vertex distribution, XZ view, YZ view, XY view. **Bottom:** MC decay vertex distribution XZ view, YZ view, XY view. **Black:** ν_μ DIS CC interactions, **red:** ν_μ DIS NC interactions, **green:** ν_μ RES CC interactions, **blue:** ν_μ RES NC interactions, **yellow:** ν_μ QEL CC interactions.

The MC slopes (dX/dZ and dY/dZ) for all CNGS ν_μ beam reactions are depicted in Figure 6.10. For $\pi^\pm$, the distribution is much broader ($RMS_X = 0.009808$, $RMS_Y = 0.009921$ for π^- and $RMS_X = 0.009358$, $RMS_Y = 0.009555$ for π^+) than for μ^- ($RMS_X = 0.001582$, $RMS_Y = 0.001758$), indicating a possible $\pi\pm$ / $\mu^\pm$ separation cut criterion.

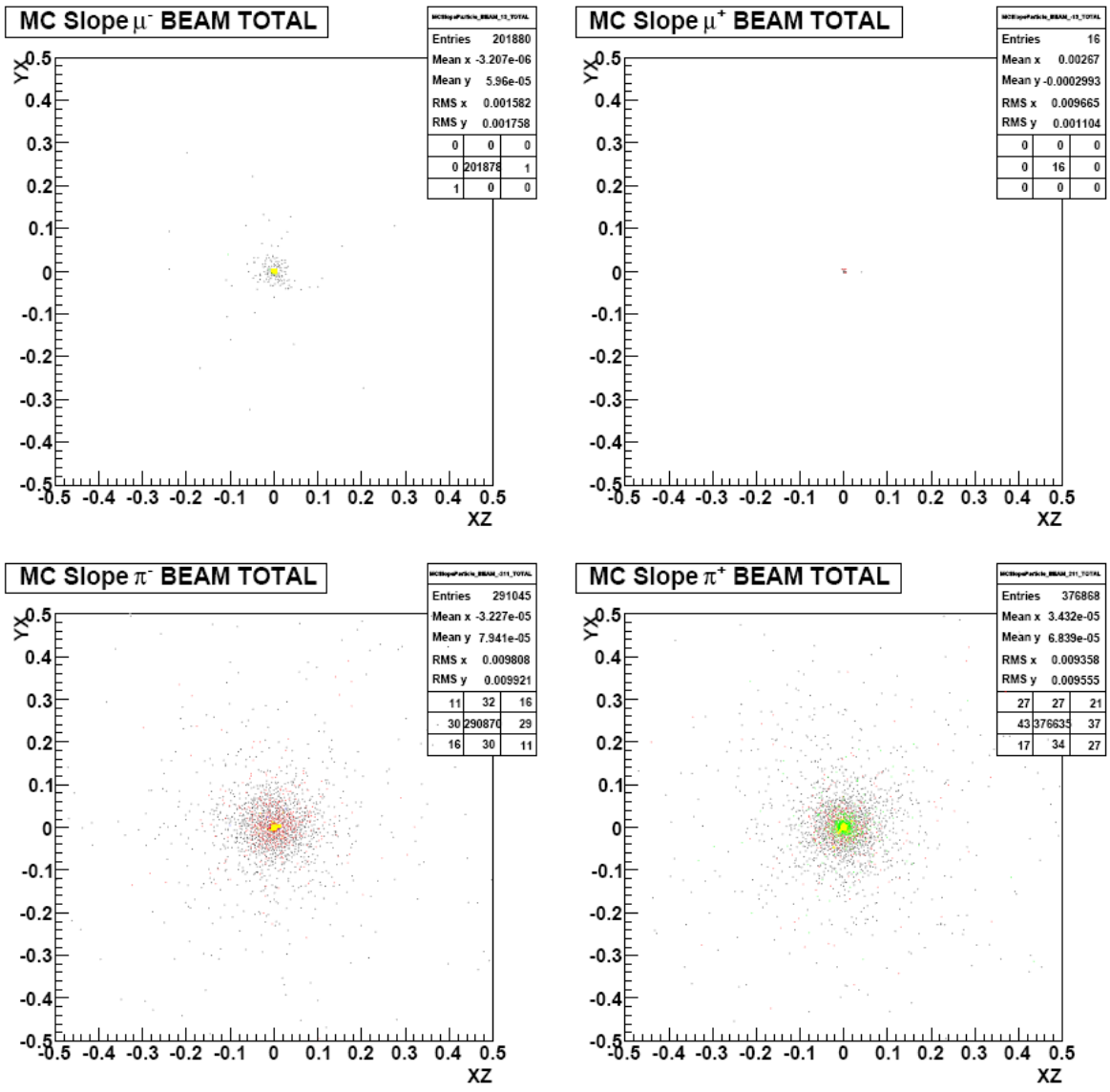

Figure 6.10: CNGS ν_μ beam MC slope distribution (TOTAL). **Top left:** μ^-, **top right:** μ^+, **bottom left:** π^-, **bottom right:** π^+. **Black:** ν_μ DIS CC interactions, **red:** ν_μ DIS NC interactions, **green:** ν_μ RES CC interactions, **blue:** ν_μ RES NC interactions, **yellow:** ν_μ QEL CC interactions.

In Figure 6.11 the numbers of particles created at the secondary vertices of $\mu^{\pm}$ and $\pi^{\pm}$ are shown for all CNGS ν_μ beam interactions. Again, the particles created in μ^- interactions are mainly $e^{\pm}$ and γ, while the $\pi^{\pm}$ primarily decay into other hadrons and γ.

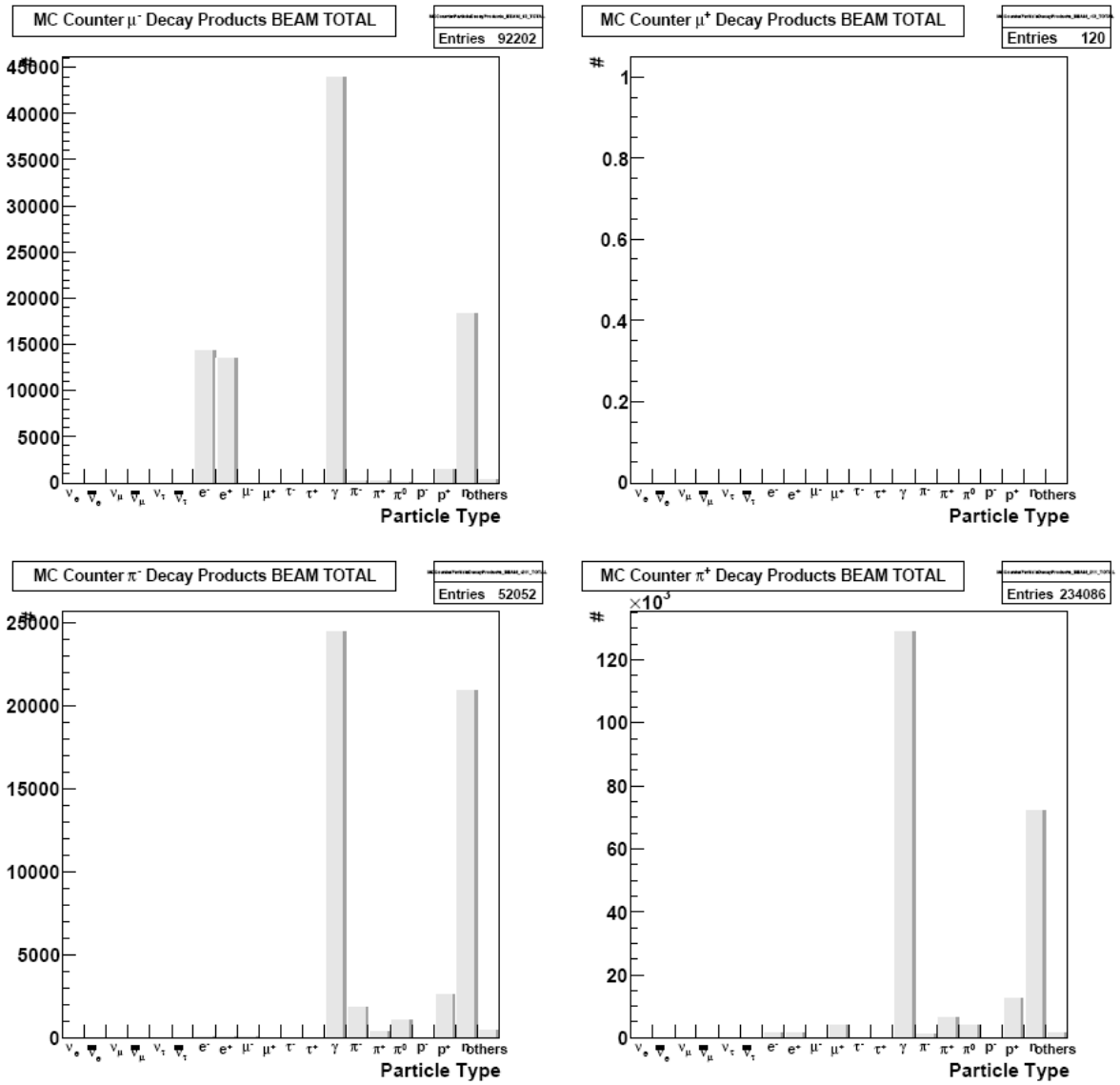

Figure 6.11: CNGS ν_μ beam MC secondary particles. **Top left:** μ^-, **top right:** μ^+, **bottom left:** π^-, **bottom right:** π^+. **Black:** ν_μ DIS CC interactions, **red:** ν_μ DIS NC interactions, **green:** ν_μ RES CC interactions, **blue:** ν_μ RES NC interactions, **yellow:** ν_μ QEL CC interactions.

The slopes (dX/dZ and dY/dZ) under which the secondary particles are leaving the interaction vertices are shown in Figure 6.12. In contrast to the differences found for the MC slopes of μ^- and π^+ secondary particles in particle gun events, the distributions for μ^- ($RMS_X = 0.01507$, $RMS_Y = 0.01561$) and $\pi^{\pm}$ ($RMS_X = 0.01661$, $RMS_Y = 0.01658$ for π^- and $RMS_X = 0.01617$, $RMS_Y = 0.01585$ for π^+) are very similar. No separation will be possible based on this criterion.

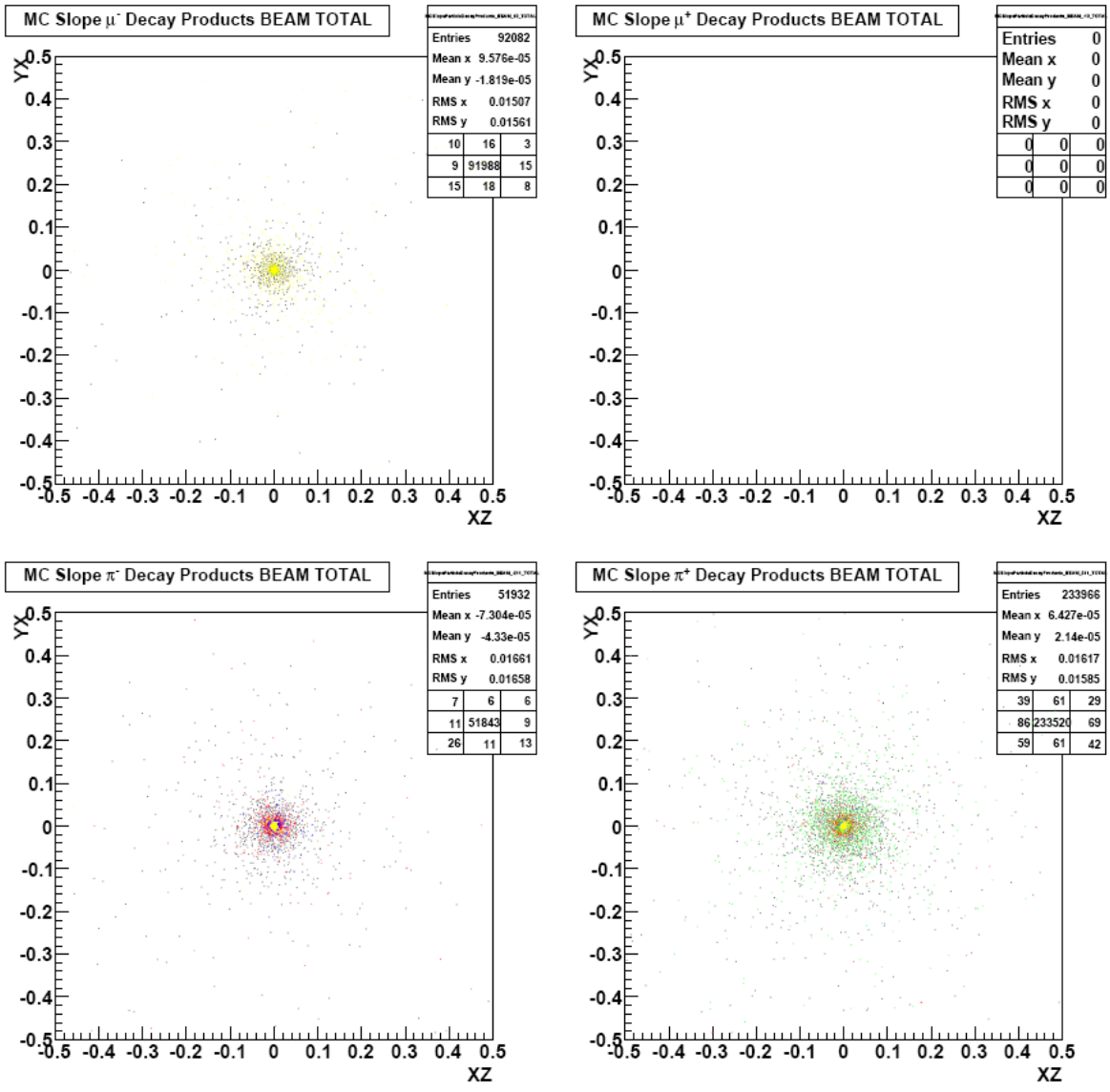

Figure 6.12: CNGS ν_μ beam secondary particles MC slope. **Top left:** μ^-, **top right:** μ^+, **bottom left:** π^-, **bottom right:** π^+. **Black:** ν_μ DIS CC interactions, **red:** ν_μ DIS NC interactions, **green:** ν_μ RES CC interactions, **blue:** ν_μ RES NC interactions, **yellow:** ν_μ QEL CC interactions.

6.5 Selection of Cut Parameters

6.5.1 Accessible Parameters with the Electronic Detector of OPERA

In contrast to the OPERA photo emulsions, no precise $-dE/dx$ measurements are possible for the separation of $\pi^{\pm}$ and $\mu^{\pm}$ by using the electronic detector. As neither the incoming particles' momenta are known to an adequately high degree, nor the time resolution of OPERA is within the ns range, TOF measurements will also not be able to distinguish between these particles.

Thus, apart from the reconstructed track length, other parameters have to be investigated. In the framework of this thesis, these are: The reconstructed momentum and its uncertainty (momentum variance), the slope of the reconstructed track, the branching of the track, the energy deposited in the TT scintillators associated with the track (TSCIN energy) – as well as possible correlations of these variables.

6.5.2 Selection of Cut Parameters for Single π^+ and μ^-

For a first study of individual particles, rather than complete CNGS beam ν_μ interactions, the sample of simulated π^+ and μ^- particle gun events is investigated in regard to potential cut criteria for the separation of π^+ and μ^-.

The first and obvious parameter is the track length (measured in $\mathrm{g\,cm^{-2}}$, as the product of range [cm] and density [$\mathrm{g\,cm^{-3}}$]), on which the current $MuonID$ cut is based.

Figure 6.13 shows the reconstructed track length for μ^- and π^+ particle gun events. While the track length for μ^- is broadly distributed from $0\,\mathrm{g\,cm^{-2}}$ to about $5{,}500\,\mathrm{g\,cm^{-2}}$, with some peaks caused by the detector structure[1], the π^+ track length distribution features a narrow peak at $\sim 500\,\mathrm{g\,cm^{-2}}$, rapidly decreasing afterwards.

The chosen boundary of $660\,\mathrm{g\,cm^{-2}}$ ($\mu^{\pm}$: track length $> 660\,\mathrm{g\,cm^{-2}}$, no $\mu^{\pm}$: track length $< 660\,\mathrm{g\,cm^{-2}}$) of the current $MuonID$ cut correctly identifies many μ^-, yet a large portion of π^+ will be misidentified as μ^-. By selecting a safe cut of $> 2{,}000\,\mathrm{g\,cm^{-2}}$ for identification as a $\mu^{\pm}$, the purity is greatly improved. However, more cuts on other variables will be necessary to obtain a comparable efficiency.

[1] I.e. tracks reconstructed as crossing one or both targets, with or without hitting the spectrometer.

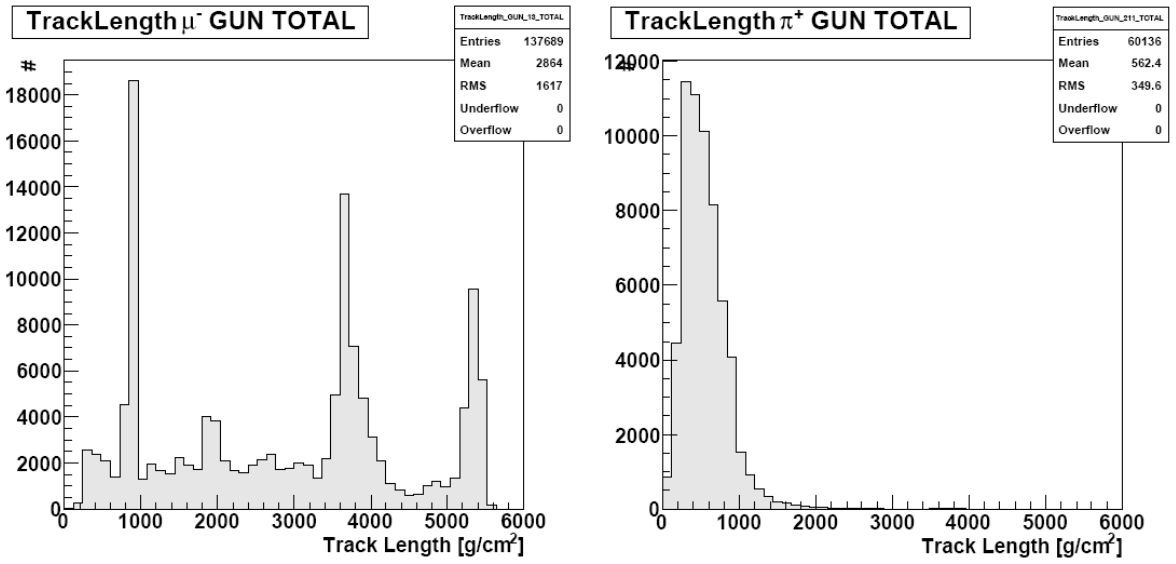

Figure 6.13: Particle gun reconstructed track length. **Left:** μ^-, **right:** π^+.

The reconstructed momentum for μ^- and π^+ particle gun events is shown in Figure 6.14. For μ^-, the distribution is broad, with a maximum between about 1 GeV and 5 GeV, and another significant number of events up to $\sim$ 20 GeV. The reconstructed momentum distribution for π^+, again is very narrow, with its maximum at $\sim$ 1 GeV. A relatively safe cut for $\mu^{\pm}$ identification can be realised by requiring the reconstructed momentum to be larger than 3.0 GeV.

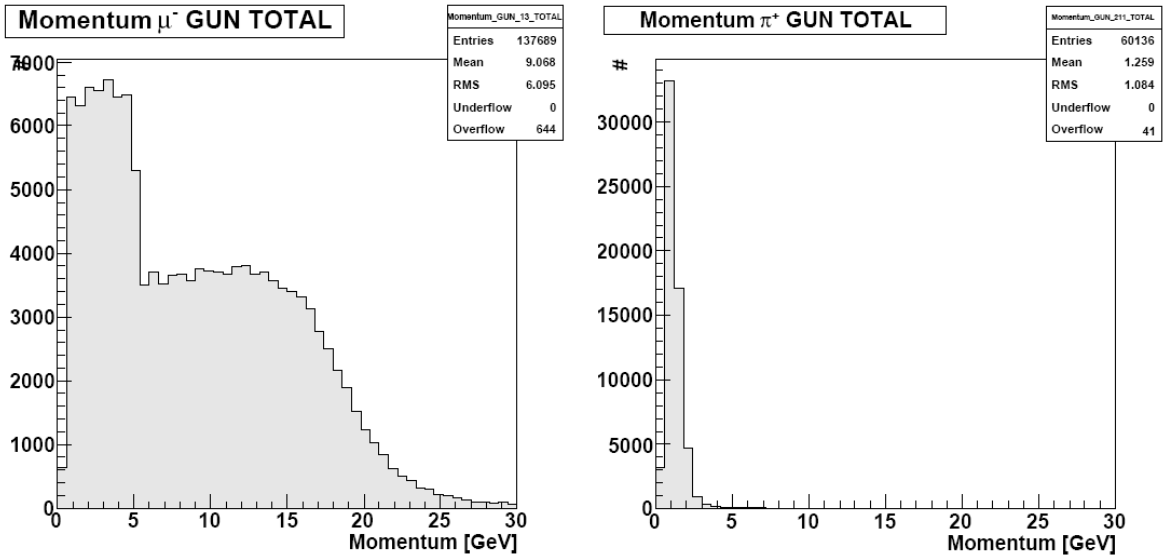

Figure 6.14: Particle gun reconstructed momentum. **Left:** μ^-, **right:** π^+.

Figure 6.15 shows the reconstructed momentum for particle gun μ^- and π^+ vs the MC momentum. While for μ^-, the reconstructed values are in good agreement with the simulated ones, π^+ momenta are seldomly reconstructed above $\sim$ 3.0 GeV.

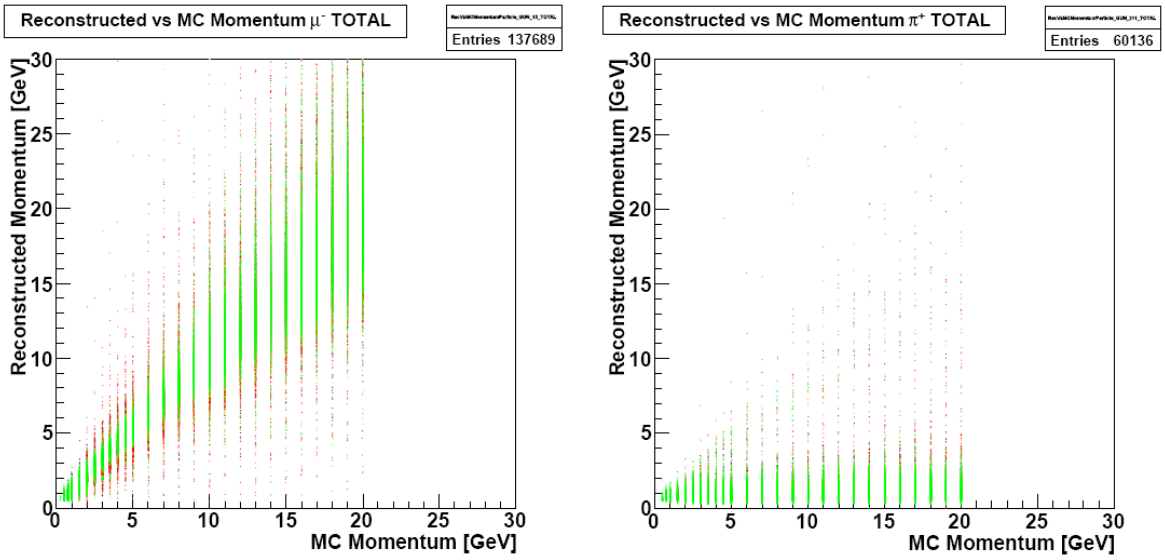

Figure 6.15: Particle gun reconstructed vs MC momentum. **Left:** μ^-, **right:** π^+. **Black:** TARGET events, **red:** SPECTRO events, **green:** CENTER events

The large uncertainty on momentum reconstruction for π^+ visible in Figure 6.15 also has an effect on the momentum variance: The uncertainty of the reconstructed momentum, computed by the reconstruction algorithms. In Figure 6.16, the momentum variance is shown for particle gun μ^- and π^+ events. For μ^-, the variance is very close to 0, while for π^+, it is more broadly distributed. Thus, a relatively safe cut can be defined, identifying events with a momentum variance of > 0.0025 as $\pi^\pm$.

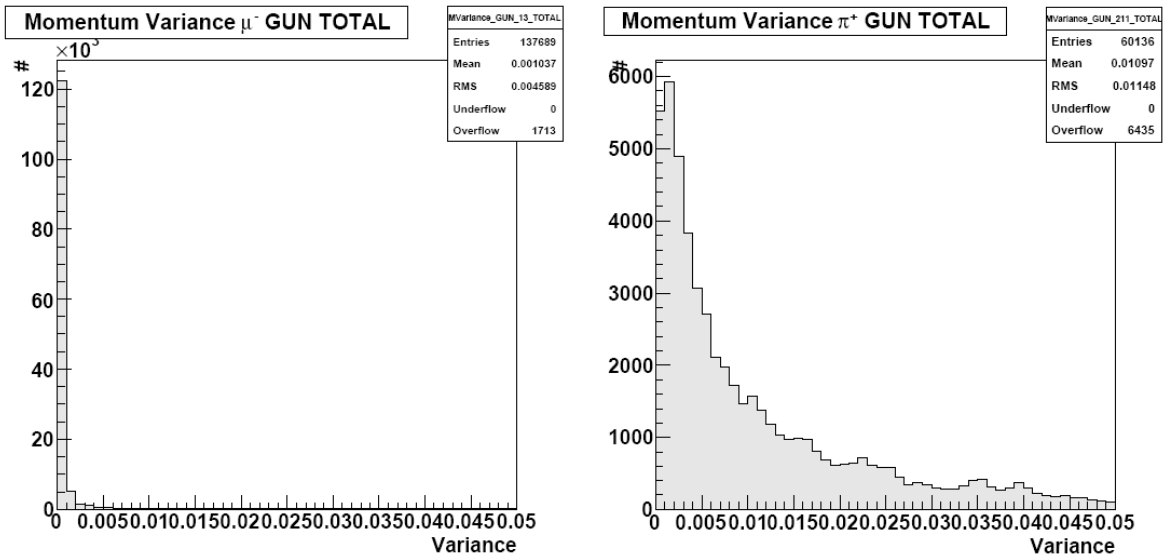

Figure 6.16: Particle gun momentum variance. **Left:** μ^-, **right:** π^+.

Figure 6.17 shows the energy reconstructed inside the TT scintillators for the first track of particle gun μ^- and π^+ events. While for μ^-, the distribution is broad, for π^+ it is narrower, with a maximum at low energies of $< 0.025\,\text{MeV}$, allowing a safe cut of $> 0.065\,\text{MeV}$ for $\mu^\pm$ identification.

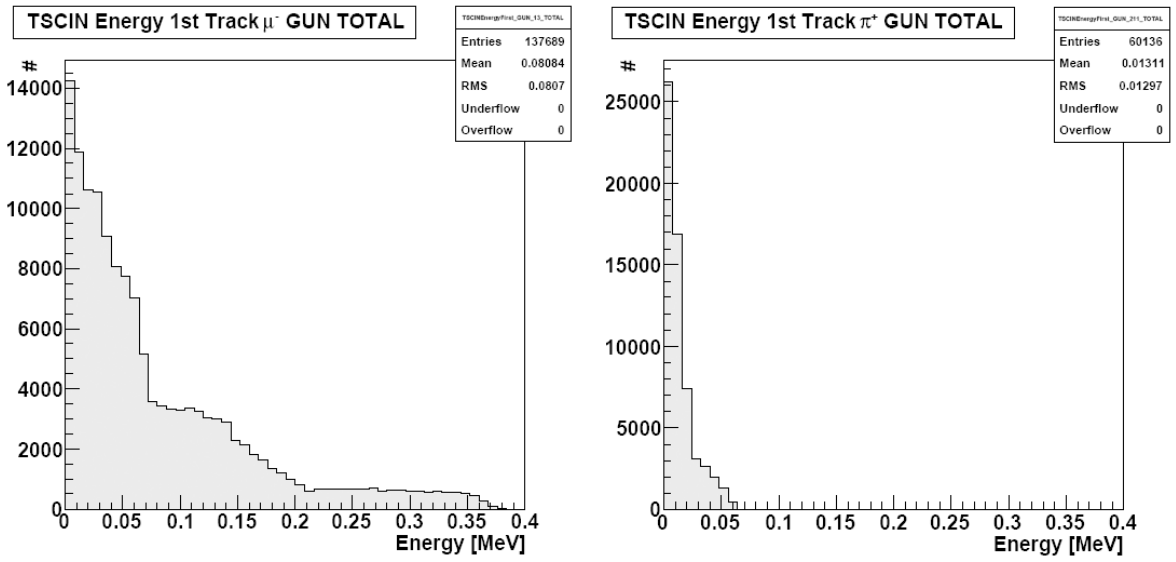

Figure 6.17: Particle gun reconstructed TSCIN energy. **Left:** μ^-, **right:** π^+.

In Figure 6.18, the energy reconstructed inside the TT scintillators for the first track vs the track length of particle gun μ^- and π^+ events is shown. By simultaneously requiring the energy to be $< 0.05\,\text{MeV}$ and the track length $< 800\,\text{g}\,\text{cm}^{-2}$ many $\pi^{\pm}$ can be identified.

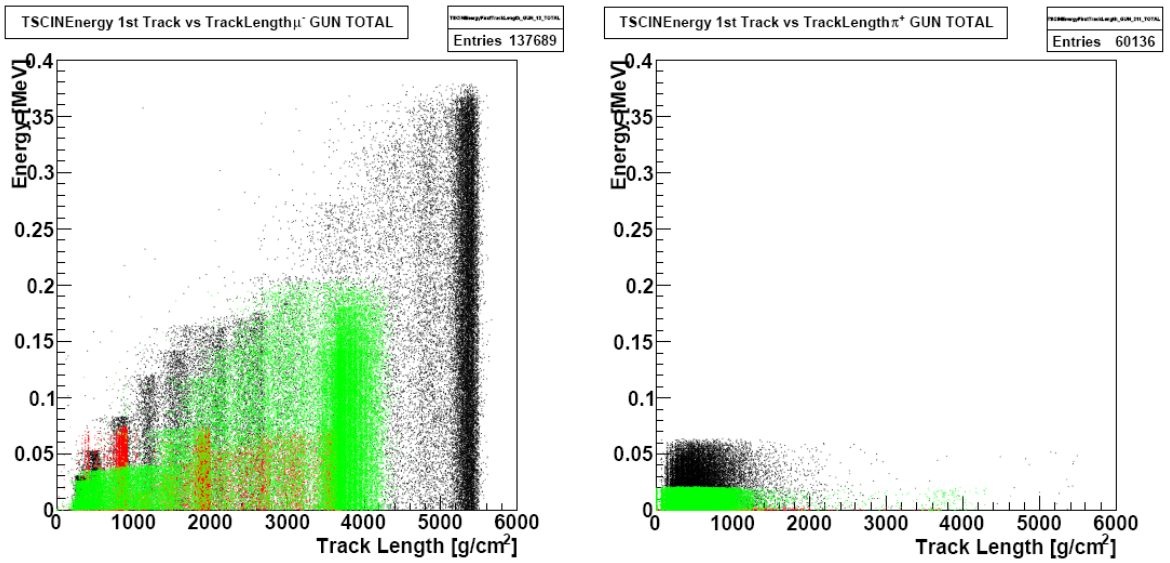

Figure 6.18: Particle gun reconstructed TSCIN energy vs track length. **Left:** μ^-, **right:** π^+. **Black:** TARGET events, **red:** SPECTRO events, **green:** CENTER events

The energy reconstructed inside the TT scintillators for the first track vs the reconstructed momentum is shown in Figure 6.19 for particle gun μ^- and π^+ events. By simultaneously requiring the energy to be $< 0.05\,\text{MeV}$ and the momentum $< 1.5\,\text{GeV}$ many $\pi^{\pm}$ can be identified.

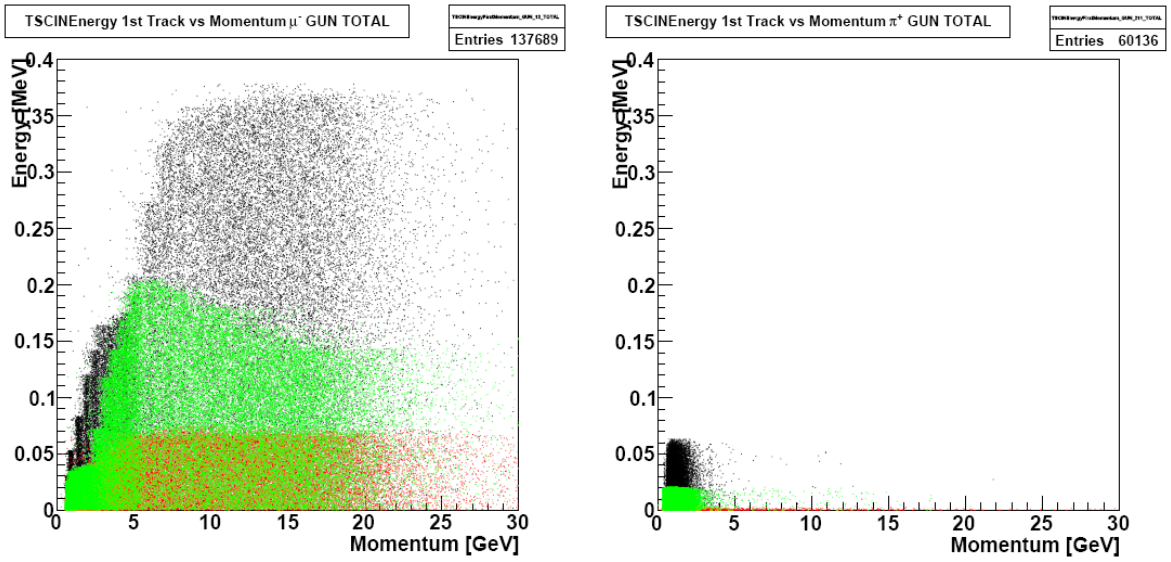

Figure 6.19: Particle gun reconstructed TSCIN energy vs momentum. **Left:** μ^-, **right:** π^+. **Black:** TARGET events, **red:** SPECTRO events, **green:** CENTER events

By requiring the slope of the first reconstructed track of particle gun μ^- and π^+ events – shown in Figure 6.20 – to be greater than 0.2 for either dX/dZ or dY/dZ a relatively safe cut for $\pi^\pm$ identification can be defined.

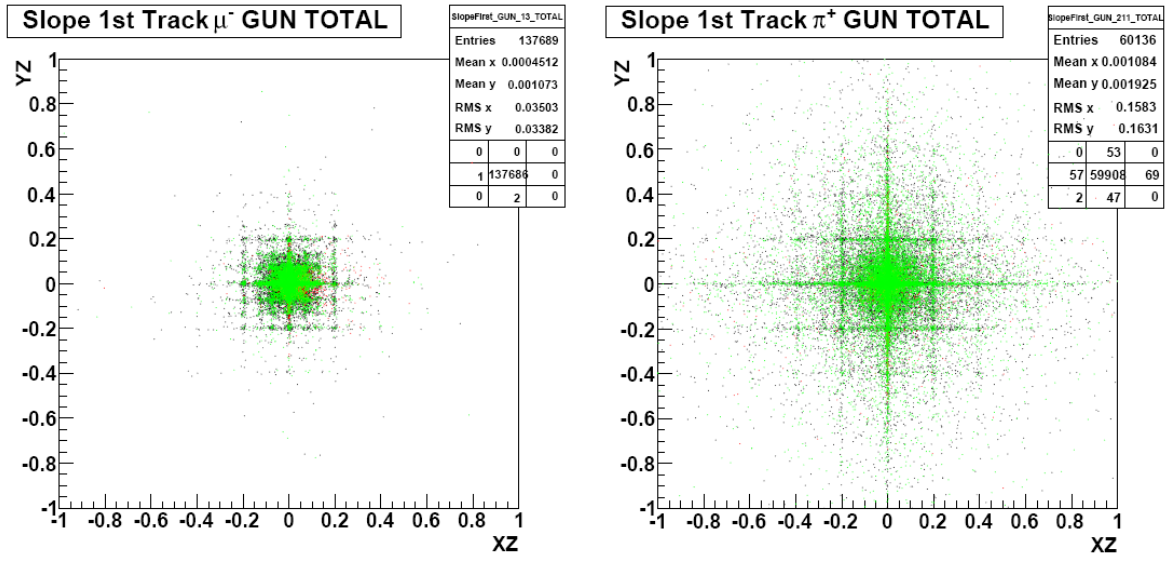

Figure 6.20: Particle gun reconstructed slope of first track. **Left:** μ^-, **right:** π^+. **Black:** TARGET events, **red:** SPECTRO events, **green:** CENTER events

The greater branching of $\pi^\pm$ tracks when compared to those of $\mu^\pm$, visible in Figure 6.21 for particle gun μ^- and π^+, also provides a separation cut criterion: By requiring the vertex distance in Z-axis direction to be greater than 50 cm (to exclude tracks originating from a primary vertex from this analysis), at the same time asking for a 3D distance of < 25 cm between the second track vertex and the first track, and requiring the difference in dY/dZ slopes to be > 0.2 (to exclude tracks reconstructed from the same particle track), a safe

identification criterion for $\pi^{\pm}$ is found.

Figures 6.22 and 6.23 show the corresponding reconstructed 3D distance between tracks and their slope difference.

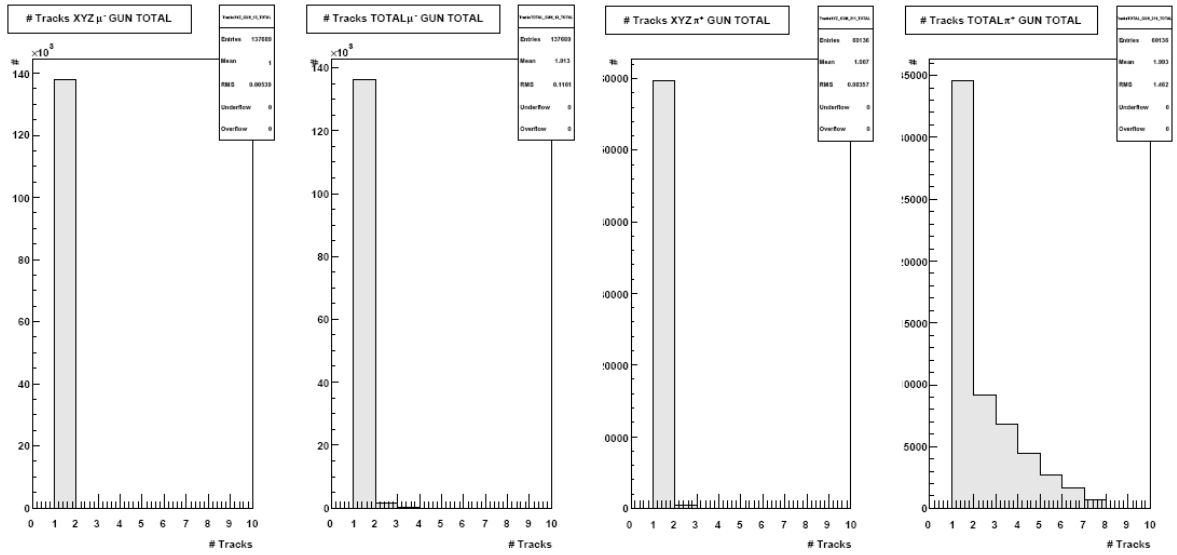

Figure 6.21: Particle gun number of reconstructed tracks. **Left:** μ^{-}, all tracks and 3D tracks, **right:** π^{+} all tracks and 3D tracks.

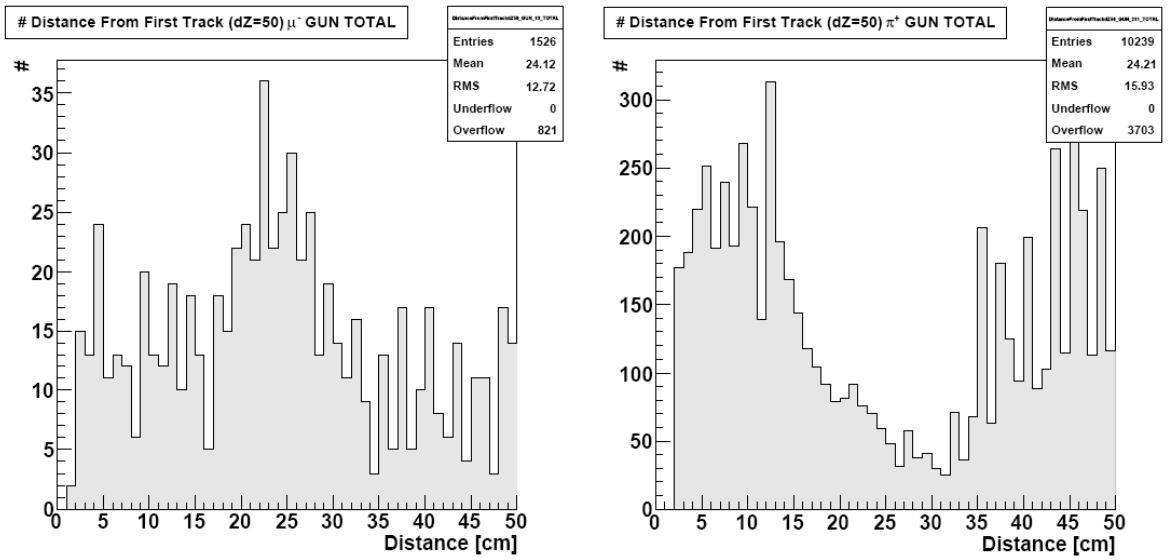

Figure 6.22: Particle gun reconstructed 3D distance between tracks ($dZ > 50\,\mathrm{cm}$). **Left:** μ^{-}, **right:** π^{+}.

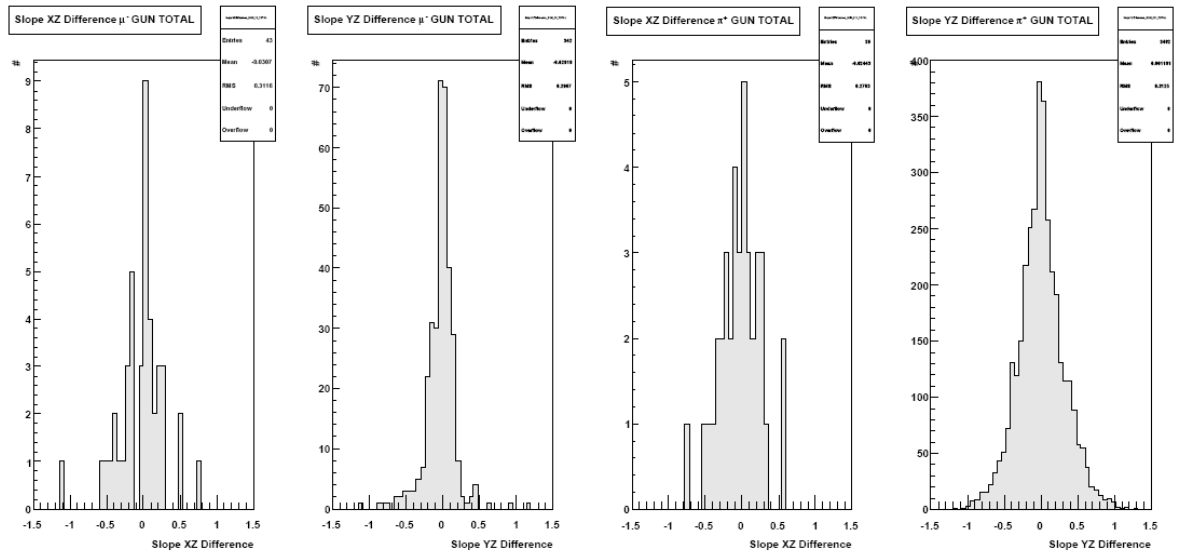

Figure 6.23: Particle gun reconstructed slope difference between tracks. **Left:** μ^-, dX/dZ and dY/dZ , **right:** π^+ dX/dZ and dY/dZ.

6.5.3 Selection of Cut Parameters for the Simulated CNGS ν_μ Beam

After the cut parameters for individual $\pi^{\pm}$ and $\mu^{\pm}$ have been defined in the preceding chapter, the same properties will now be investigated in regard to the simulated CNGS ν_μ beam.

As, for the CNGS beam, the separation of $\pi^{\pm}$ and $\mu^{\pm}$ can most efficiently be conducted by comparing CC and NC events, only ν_μ DIS CC and ν_μ DIS NC interactions will be examined in the following analysis, while the corresponding plots for the other event classes are provided in the appendix.

The plots presented are showing ν_μ DIS CC events with at least one μ^-, and ν_μ DIS NC interaction where at least one π^+ has been confirmed by the MC data. While μ^+ cannot be found in the CNGS ν_μ beam at a significantly large number, equal amounts of π^- as of π^+ are available and exhibiting similar properties (see Appendix A.2).

Figure 6.24 shows the reconstructed track length for CNGS beam ν_μ DIS CC and ν_μ DIS NC interactions. Again, the track length is broadly distributed for ν_μ DIS CC μ^- events, exhibiting two peaks induced by the detector structure. The ν_μ DIS NC π^+ track length distribution features a narrower peak at $500 - 1{,}000\,\mathrm{g\,cm^{-2}}$, rapidly decreasing afterwards. Thus, a safe $\mu^{\pm}$- identifying cut can be defined by requiring the track length to be larger than $2{,}000\,\mathrm{g\,cm^{-2}}$.

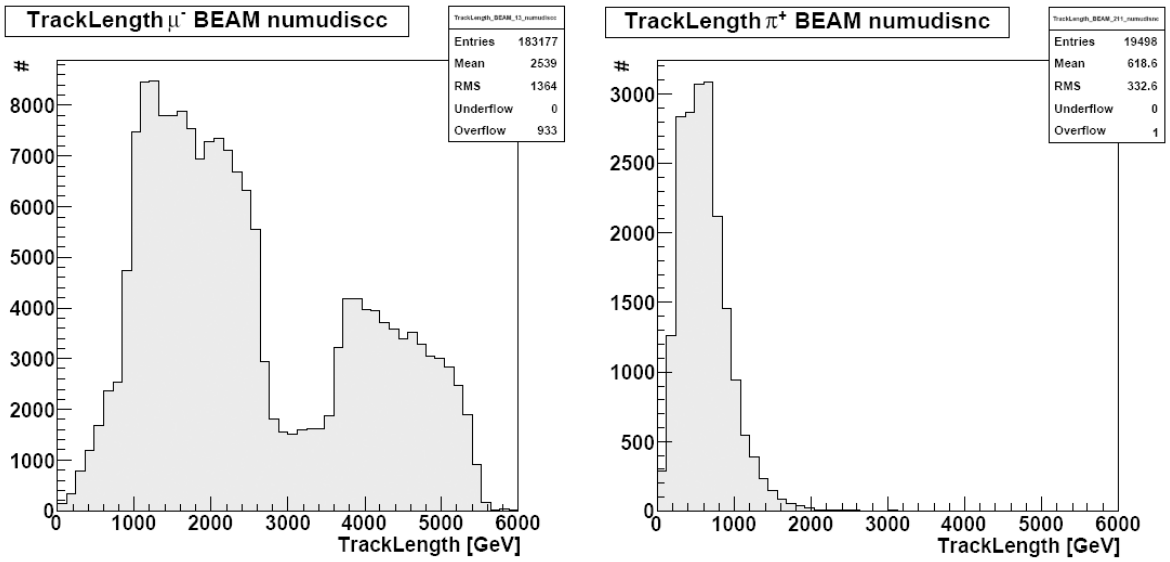

Figure 6.24: CNGS ν_μ beam reconstructed track length. **Left:** ν_μ DIS CC μ^-, **right:** ν_μ DIS NC π^+. See Appendix A.2.3 for plots of other ν_μ reactions and particles.

The reconstructed momentum for CNGS beam ν_μ DIS CC and ν_μ DIS NC events is shown in Figure 6.25. The distributions are similar to those found in μ^- and π^+ particle gun events, and again a safe cut for $\mu^{\pm}$ identification is given by requiring the reconstructed momentum to be larger than 3.0 GeV.

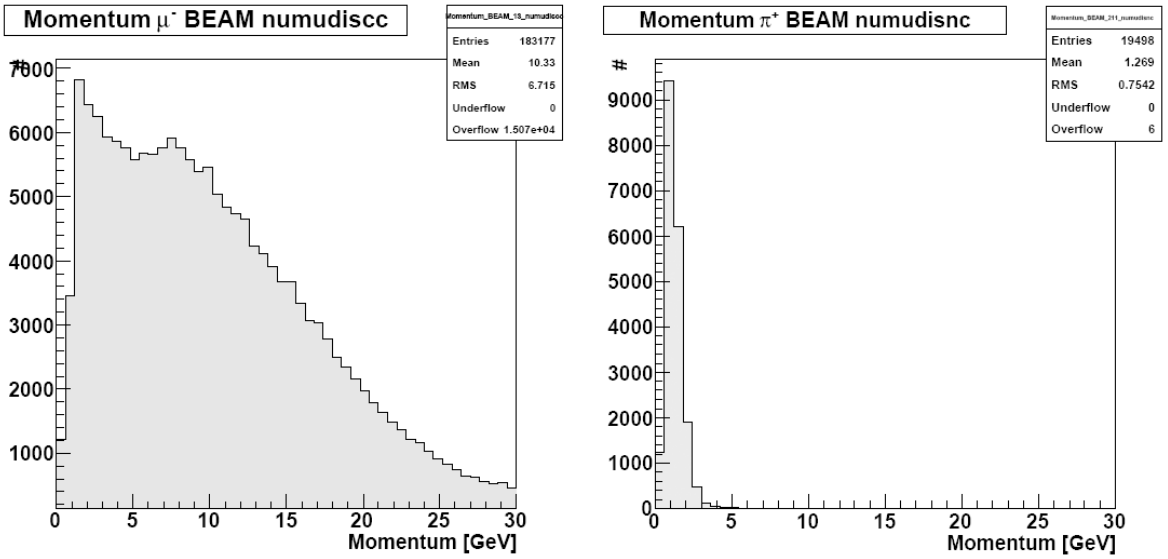

Figure 6.25: CNGS ν_μ beam reconstructed momentum. **Left:** ν_μ DIS CC μ^-, **right:** ν_μ DIS NC π^+. See Appendix A.2.4 for plots of other ν_μ reactions and particles.

Figure 6.26 shows the reconstructed momentum vs the MC momentum for CNGS beam ν_μ DIS CC and ν_μ DIS NC events. Again, the reconstructed values for ν_μ DIS CC μ^- are in good agreement with the simulated ones, while ν_μ DIS NC π^+ momenta are seldomly reconstructed above $\sim 3.0\,\text{GeV}$.

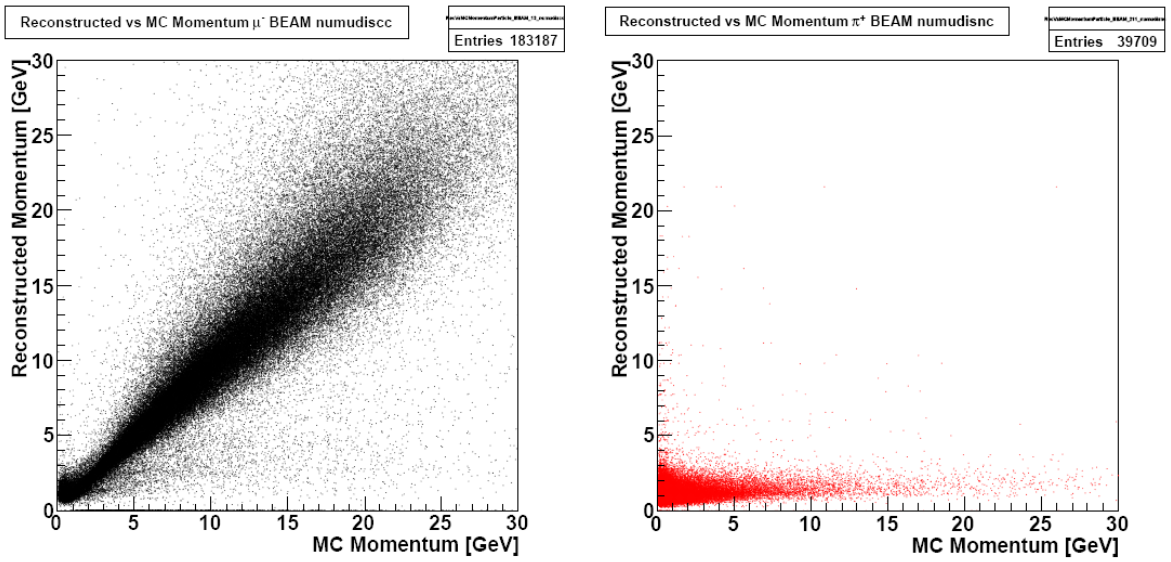

Figure 6.26: CNGS ν_μ beam reconstructed vs MC momentum. **Left:** ν_μ DIS CC μ^-, **right:** ν_μ DIS NC π^+. **Black:** ν_μ DIS CC interactions, **red:** ν_μ DIS NC interactions. See Appendix A.2.5 for plots of other ν_μ reactions and particles.

In Figure 6.27, the momentum variance for CNGS beam ν_μ DIS CC and ν_μ DIS NC interactions is shown. As in particle gun μ^- and π^+ events, a relatively safe cut can be defined for $\pi^{\pm}$ with a momentum variance of > 0.0025.

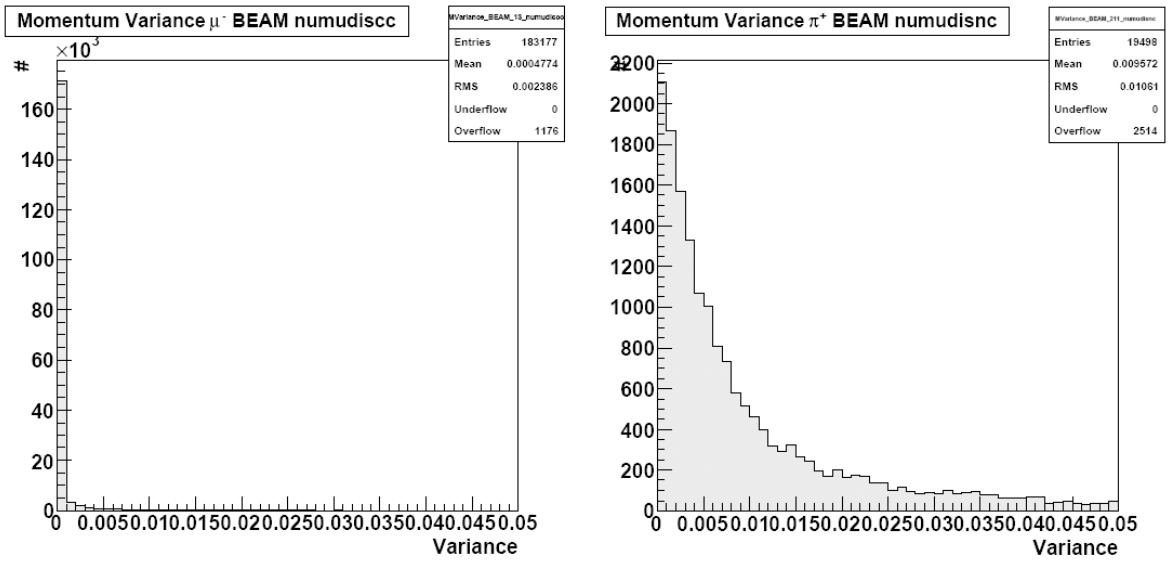

Figure 6.27: CNGS ν_μ beam momentum variance. **Left:** ν_μ DIS CC μ^-, **right:** ν_μ DIS NC π^+. See Appendix A.2.6 for plots of other ν_μ reactions and particles.

Figure 6.28 shows the energy reconstructed inside the TT scintillators for the first track of CNGS beam ν_μ DIS CC and ν_μ DIS NC events. While for ν_μ DIS CC μ^-, the reconstructed TSCIN energy reaches $> 0.2\,\text{MeV}$, for ν_μ DIS NC π^-, it is seldomly greater than $\sim 0.05\,\text{MeV}$. Thus, a relatively safe cut for $\mu^\pm$ identification can be defined by requiring $> 0.05\,\text{MeV}$.

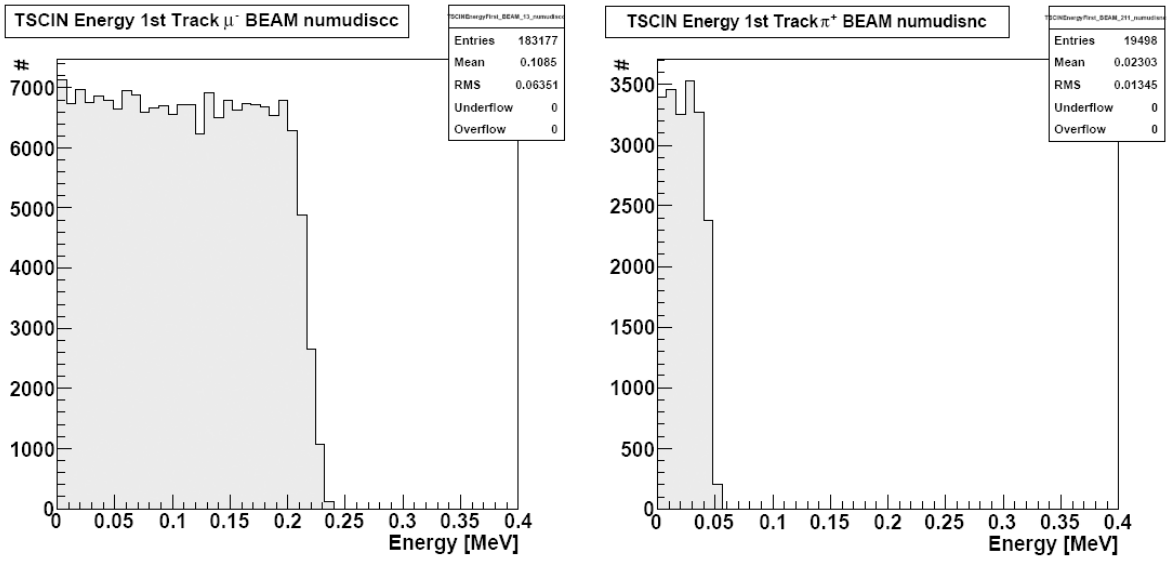

Figure 6.28: CNGS ν_μ beam reconstructed TSCIN energy. **Left:** ν_μ DIS CC μ^-, **right:** ν_μ DIS NC π^+. See Appendix A.2.7 for plots of other ν_μ reactions and particles.

In Figure 6.29, the energy reconstructed inside the TT scintillators for the first track vs the track length of CNGS beam ν_μ DIS CC and ν_μ DIS NC interactions is shown. By simultaneously requiring the energy to be $< 0.05\,\text{MeV}$ and the track length $< 800\,\text{g}\,\text{cm}^{-2}$ many $\pi^\pm$ can be identified, as was also the case for μ^- and π^+ particle gun MC.

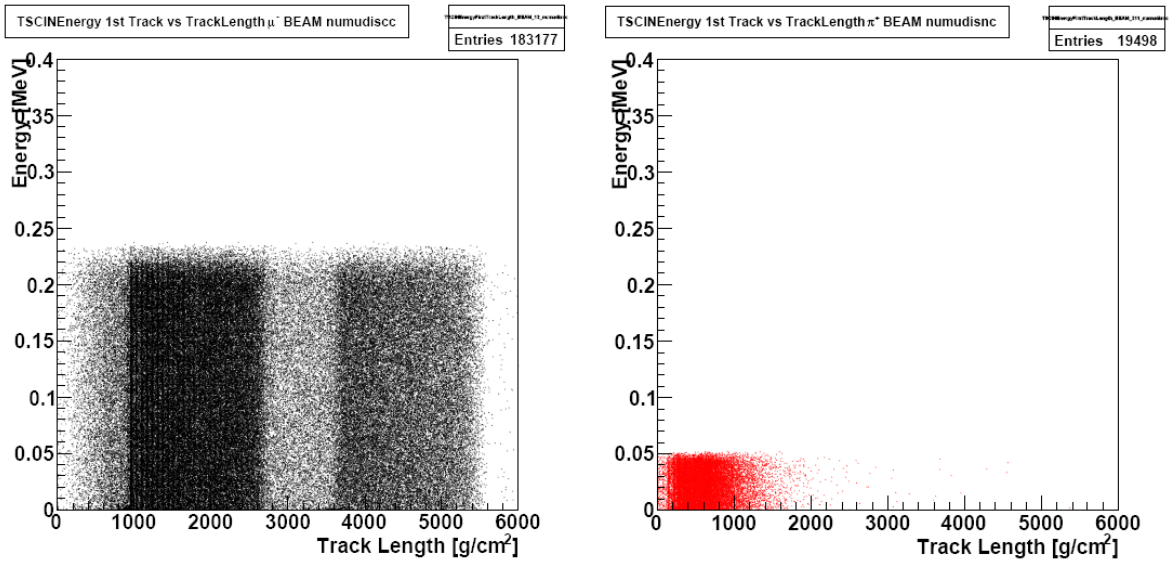

Figure 6.29: CNGS ν_μ beam reconstructed TSCIN energy vs track length.. **Left:** ν_μ DIS CC μ^-, **right:** ν_μ DIS NC π^+. **Black:** ν_μ DIS CC interactions, **red:** ν_μ DIS NC interactions. See Appendix A.2.8 for plots of other ν_μ reactions and particles.

The energy reconstructed inside the TT scintillators for the first track vs the reconstructed momentum is shown in Figure 6.30 for CNGS beam ν_μ DIS CC and ν_μ DIS NC events. Similar to the μ^- and π^+ particle gun MC, many $\pi^{\pm}$ can be identified by simultaneously requiring the energy to be $< 0.05\,\text{MeV}$ and the momentum $< 1.5\,\text{GeV}$.

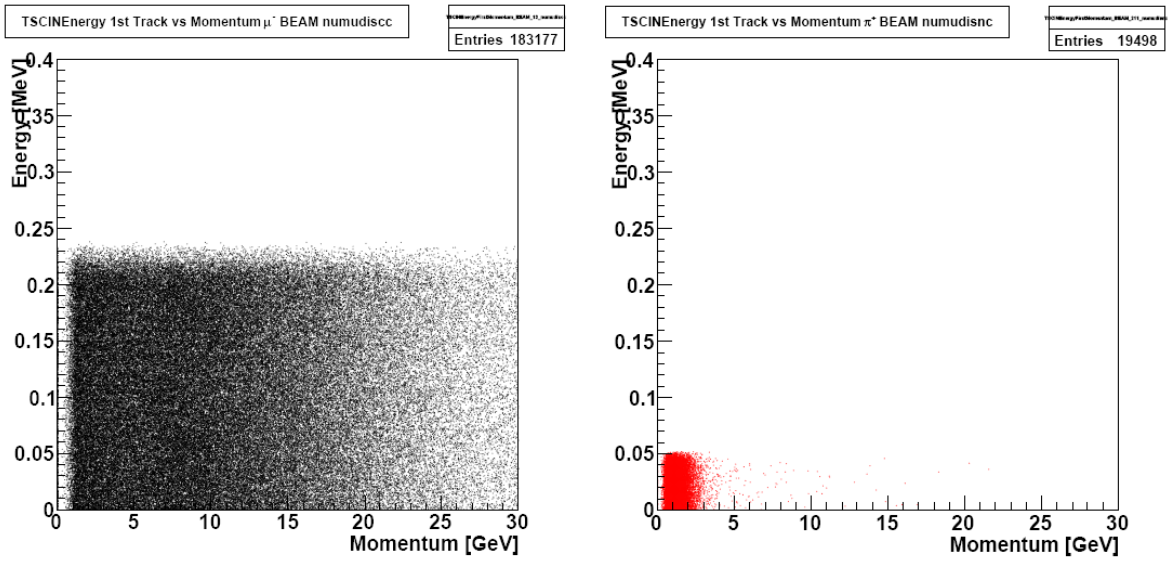

Figure 6.30: CNGS ν_μ beam reconstructed TSCIN energy vs momentum. **Left:** ν_μ DIS CC μ^-, **right:** ν_μ DIS NC π^+. **Black:** ν_μ DIS CC interactions, **red:** ν_μ DIS NC interactions. See Appendix A.2.9 for plots of other ν_μ reactions and particles.

Figure 6.31 shows the slope of the first reconstructed track of CNGS beam ν_μ DIS CC and ν_μ DIS NC interactions. Contrary to the μ^- and π^+ particle gun MC, no significant difference between the two distributions can be found.

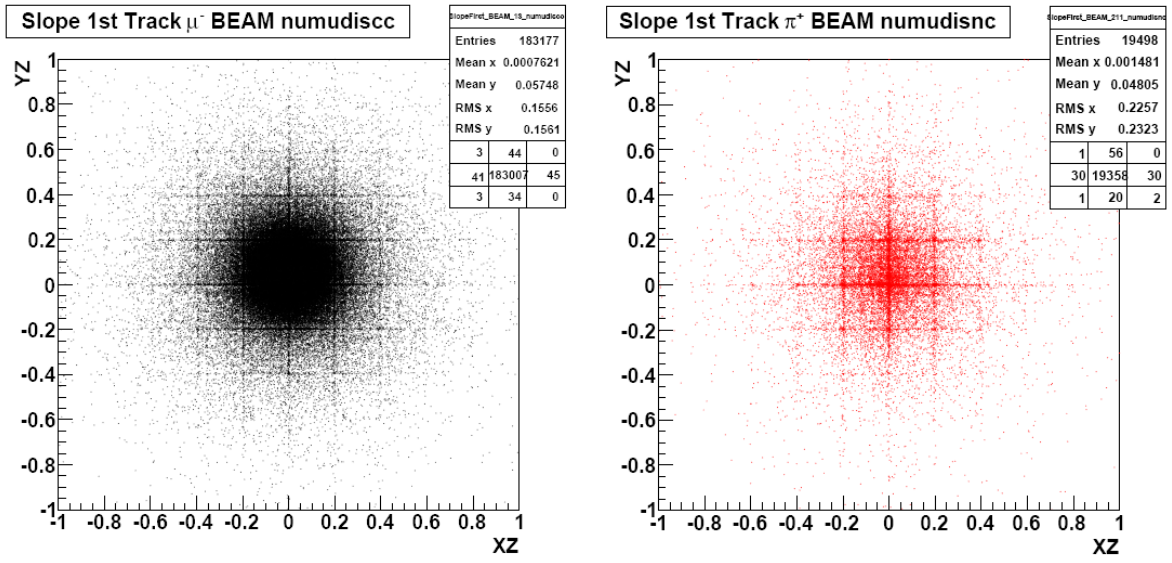

Figure 6.31: CNGS ν_μ beam reconstructed 1st track slope. **Left:** ν_μ DIS CC μ^-, **right:** ν_μ DIS NC π^+. See Appendix A.2.10 for plots of other ν_μ reactions and particles.

No further cuts could be defined based on the track branching of CNGS beam ν_μ DIS CC and ν_μ DIS NC events. The numbers of reconstructed tracks, their distributions of 3D distance and slope differences are shown in Figures 6.32, 6.33, and 6.34, but no identifying criteria for μ^- or π^+ could be found.

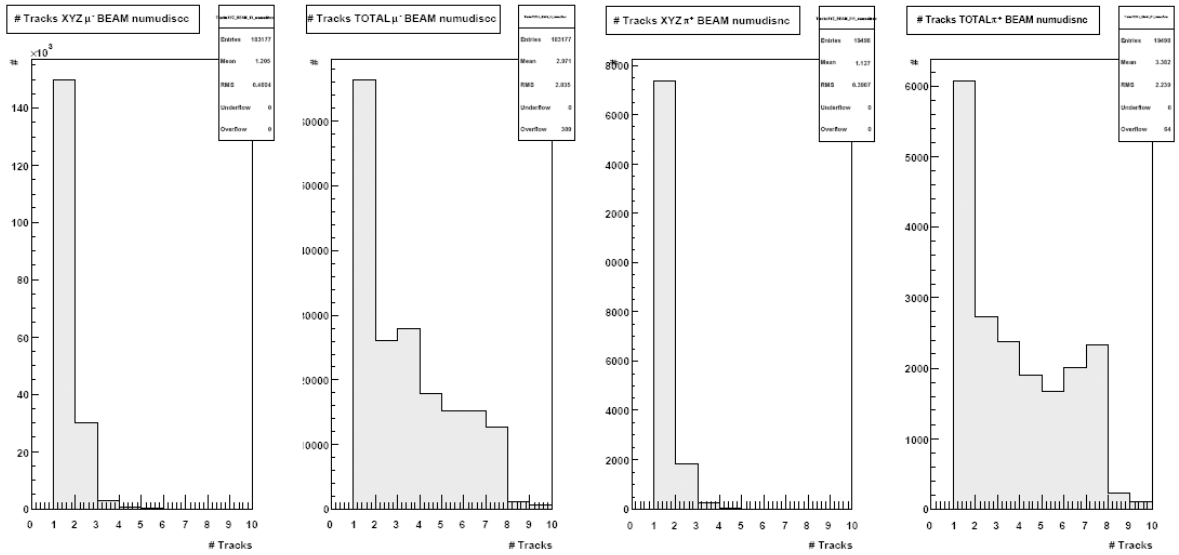

Figure 6.32: CNGS ν_μ beam number of reconstructed tracks. **Left:** ν_μ DIS CC μ^- all tracks and 3D tracks, **right:** ν_μ DIS NC π^+ all tracks and 3D tracks.

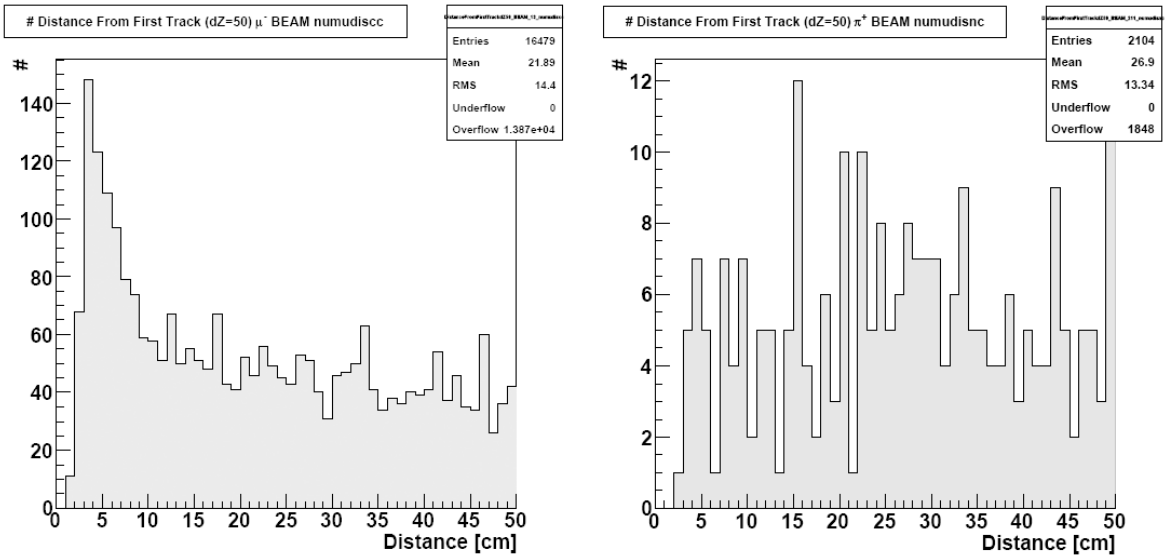

Figure 6.33: CNGS ν_μ beam reconstructed distance from 1st track. **Left:** ν_μ DIS CC μ^-, **right:** ν_μ DIS NC π^+. See Appendix A.2.11 for plots of other ν_μ reactions and particles.

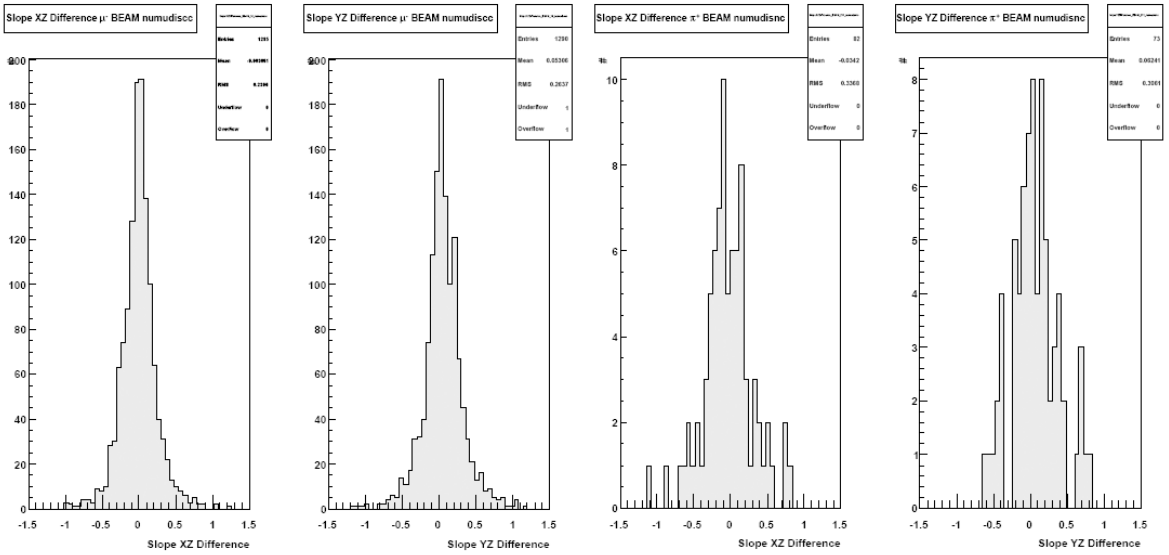

Figure 6.34: CNGS ν_μ beam reconstructed track length. **Left:** ν_μ DIS CC μ^-, **right:** ν_μ DIS NC π^+. See Appendix A.2.3 for plots of other ν_μ reactions and particles.

6.6 Final Cut Parameters

Several tests have been conducted for both the μ^- and π^+ particle gun MC sample and the simulated CNGS ν_μ DIS CC and DIS NC beam events, varying the exact values of the cut parameters, as well as their order.

The final cut parameters will be presented in the following.

6.6.1 μ^- and π^+ Particle Gun MC (*GUN Cut*)

The final cut parameters for MC particle gun μ^- and π^+ events are given in Table 6.6, as well as the order by which they are applied.

1	$\mu^{\pm}$:	Reconstructed track length	$>$	2,000	$\mathrm{g\,cm^{-2}}$
2	$\mu^{\pm}$:	Reconstructed TSCIN energy	$>$	0.065	MeV
3	$\pi^{\pm}$:	Track vertex distance	$>$	50	cm
		Track 3D distance	$<$	25	cm
		Track slope difference	$>$	0.2	
4	$\pi^{\pm}$:	Momentum variance	$>$	0.0025	
5	$\mu^{\pm}$:	Reconstructed Momentum	$>$	3.0	GeV
6	$\pi^{\pm}$:	Reconstructed Slope	$>$	0.2	
7	$\pi^{\pm}$:	Reconstructed TSCIN energy	$<$	0.05	MeV
		Reconstructed track length	$<$	800	$\mathrm{g\,cm^{-2}}$
8	$\pi^{\pm}$:	Reconstructed TSCIN energy	$<$	0.05	MeV
		Reconstructed Momentum	$<$	1.5	GeV
9	$\mu^{\pm}$:	Reconstructed track length	$>$	660	$\mathrm{g\,cm^{-2}}$

Table 6.6: *GUN Cut* parameters and their order.

The last cut step represents the current *MuonID* cut (*OLD Cut*).

6.6.2 CNGS ν_μ Beam MC (*BEAM Cut*)

The final cut parameters for MC CNGS ν_μ beam events are given in Table 6.7, as well as the order by which they are applied.

1	$\mu^{\pm}$:	Reconstructed track length	$>$	2,000	$\mathrm{g\,cm^{-2}}$
2	$\mu^{\pm}$:	Reconstructed TSCIN energy	$>$	0.05	MeV
3	$\pi^{\pm}$:	Momentum variance	$>$	0.0025	
4	$\mu^{\pm}$:	Reconstructed Momentum	$>$	3.0	GeV
5	$\pi^{\pm}$:	Reconstructed TSCIN energy	$<$	0.05	MeV
		Reconstructed track length	$<$	800	$\mathrm{g\,cm^{-2}}$
6	$\pi^{\pm}$:	Reconstructed TSCIN energy	$<$	0.05	MeV
		Reconstructed Momentum	$<$	1.5	GeV
7	$\mu^{\pm}$:	Reconstructed track length	$>$	660	$\mathrm{g\,cm^{-2}}$

Table 6.7: *BEAM Cut* parameters and their order.

The last cut step represents the current *MuonID* cut (*OLD Cut*).

6.7 Cut Performance

For cut performance evaluation, the identification efficiency has been defined for $\mu^{\pm}$ and $\pi^{\pm}$ as:

$$E_{\mu} = \frac{N_{\mu Correct}}{N_{\mu TOTAL}}, \tag{6.2}$$

$$E_{\pi} = \frac{N_{\pi Correct}}{N_{\pi TOTAL}}, \tag{6.3}$$

and the identification purity for $\mu^{\pm}$ and $\pi^{\pm}$ is given by:

$$P_{\mu} = \frac{N_{\mu Correct}}{N_{\mu Correct} + N_{\pi Wrong}}, \tag{6.4}$$

$$P_{\pi} = \frac{N_{\pi Correct}}{N_{\mu Correct} + N_{\pi Wrong}}, \tag{6.5}$$

with $N_{\mu Correct}$ and $N_{\pi Correct}$ being the numbers of correctly identified particles, $N_{\mu Wrong}$ and $N_{\pi Wrong}$ the numbers of wrongly identified particles, $N_{\mu TOTAL}$ and $N_{\pi TOTAL}$ the total numbers of particles.

6.7.1 Cut Performance on the Simulated Particle Gun π and μ Sample

Figure 6.35 shows efficiency and purity for particle gun μ^- and π^+ identification, using the final cut parameters defined in Chapter 6.6 (*GUN Cut*).

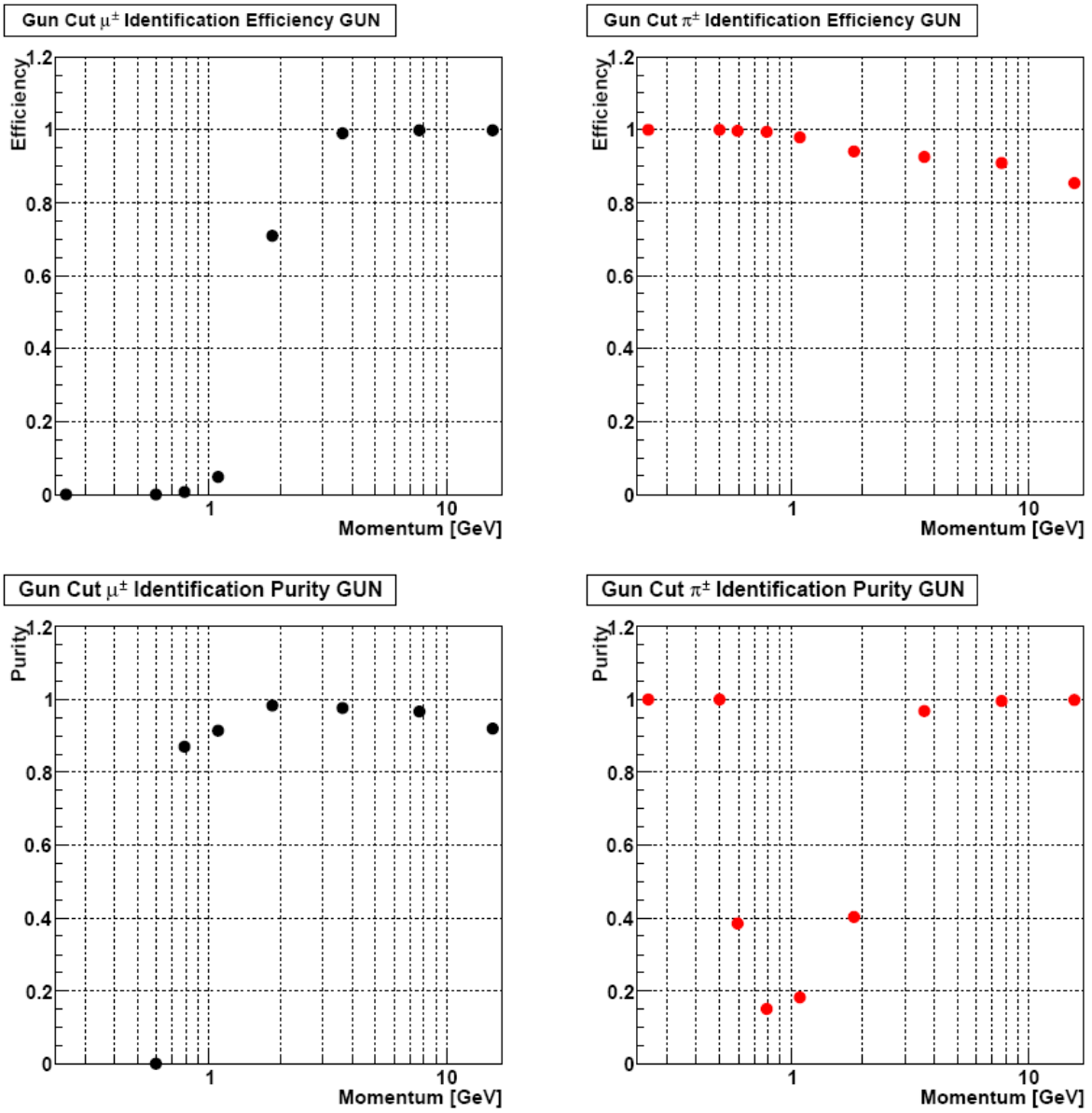

Figure 6.35: Final cut efficiciency and purity for particle gun μ^- and π^+, using the final cut parameters defined in Chapter 6.6 (*GUN Cut*). **Top left:** μ^- identification efficiency, **top right:** π^+ identification efficiency, **bottom left:** μ^- identification purity, **bottom right:** π^+ identification purity.

For different momenta p, the performances of *OLD Cut*, *GUN Cut*, and *BEAM Cut* for particle gun μ^- and π^+ are given in Tables 6.8 and 6.9, respectively.

p Bin [GeV]	$< p >$ [GeV]	# Events	Cut E_μ			Cut P_μ		
			OLD	GUN	BEAM	OLD	GUN	BEAM
$0.000 - 0.250$	–	–	–	–	–	–	–	–
$0.250 - 0.375$	0.250	9	0.000	0.000	0.000	0.000	0.000	0.000
$0.375 - 0.500$	–	–	–	–	–	–	–	–
$0.500 - 0.750$	0.597	656	0.023	0.000	0.000	0.652	0.000	0.000
$0.750 - 1.000$	0.788	3150	0.051	0.006	0.006	0.847	0.870	0.870
$1.000 - 1.500$	1.089	3743	0.162	0.048	0.071	0.868	0.914	0.936
$1.500 - 2.500$	1.842	11262	0.954	0.710	0.733	0.970	0.983	0.983
$2.500 - 5.000$	3.637	28318	0.991	0.990	0.991	0.944	0.977	0.975
$5.000 - 10.00$	7.668	33904	0.995	0.998	0.999	0.912	0.966	0.960
$10.00 - 100.0$	15.563	56647	0.996	0.999	0.999	0.819	0.920	0.885
Total	–	137689	0.942	0.920	0.923	0.879	0.948	0.929

Table 6.8: Particle gun μ^- identification efficiencies and purities for different momenta p, using the final cut parameters defined in Chapter 6.6.

p Bin [GeV]	$< p >$ [GeV]	# Events	Cut E_π			Cut P_π		
			OLD	GUN	BEAM	OLD	GUN	BEAM
$0.000 - 0.250$	0.250	1	1.000	1.000	1.000	1.000	1.000	1.000
$0.250 - 0.375$	–	0	–	–	–	–	–	–
$0.375 - 0.500$	0.500	95	1.000	1.000	1.000	1.000	1.000	1.000
$0.500 - 0.750$	0.597	413	0.981	0.998	0.998	0.387	0.386	0.386
$0.750 - 1.000$	0.788	557	0.948	0.995	0.995	0.150	0.150	0.150
$1.000 - 1.500$	1.089	810	0.886	0.979	0.978	0.186	0.182	0.185
$1.500 - 2.500$	1.842	2353	0.858	0.941	0.939	0.796	0.404	0.424
$2.500 - 5.000$	3.637	9048	0.815	0.926	0.921	0.968	0.968	0.971
$5.000 - 10.00$	7.668	13014	0.750	0.909	0.891	0.982	0.995	0.996
$10.00 - 100.0$	15.563	33845	0.631	0.854	0.783	0.990	0.998	0.998
Total	–	60136	0.703	0.884	0.839	0.842	0.828	0.826

Table 6.9: Particle gun π^+ identification efficiencies and purities for different momenta p, using the final cut parameters defined in Chapter 6.6.

The total particle gun μ^- and π^+ identification efficiencies for the *GUN Cut* result to:

$$E_{\mu GUN} = 0.920, \tag{6.6}$$
$$E_{\pi GUN} = 0.884, \tag{6.7}$$

and the total μ^- and π^+ identification purities are given by:

$$P_{\mu GUN} = 0.948, \tag{6.8}$$
$$P_{\pi GUN} = 0.828. \tag{6.9}$$

6.7.2 Cut Performance on the Simulated CNGS ν_μ Beam Sample

Figure 6.36 shows identification efficiency and purity for the simulated CNGS beam ν_μ DIS CC μ^- and ν_μ DIS NC π^+, using the final cut parameters defined in Chapter 6.6 (*BEAM Cut*), as well as the *MuonID* cut currently used by the OPERA reconstruction software (*OLD Cut*).

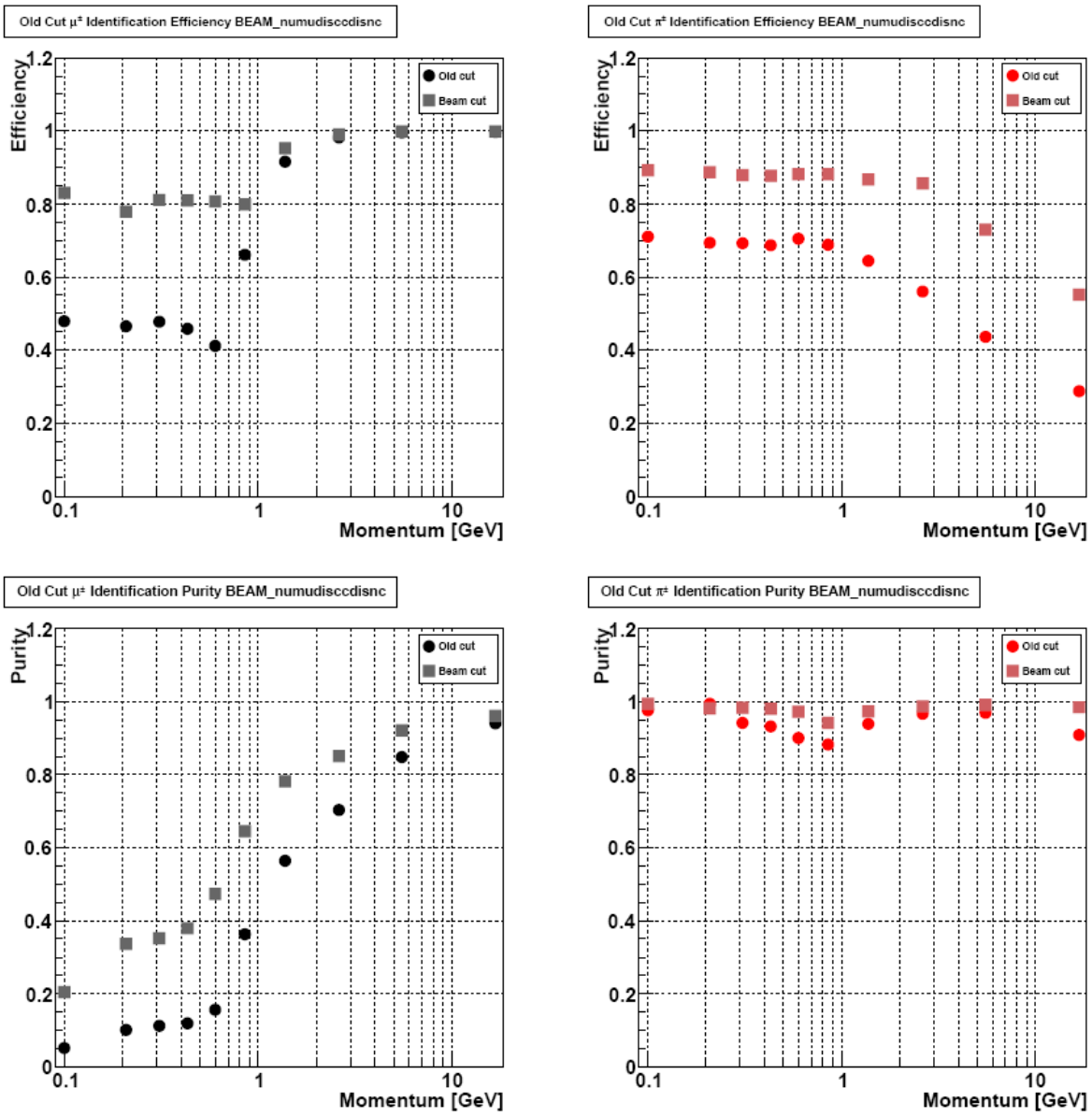

Figure 6.36: Final cut efficiciency and purity for CNGS beam ν_μ DIS CC μ^- and ν_μ DIS NC π^+ identification (*BEAM Cut* and *OLD Cut*). **Top left:** μ^- identification efficiency **top right:** π^+ identification efficiency, **bottom left:** μ^- identification purity, **bottom right:** π^+ identification purity.

For different momenta p, the performances of *OLD Cut*, *GUN Cut*, and *BEAM Cut* for the simulated CNGS beam μ^- and π^+ are given in Tables 6.10 and 6.11, respectively.

p Bin [GeV]	$< p >$ [GeV]	# Events	Cut E_μ			Cut P_μ		
			OLD	GUN	BEAM	OLD	GUN	BEAM
$0.000 - 0.250$	0.159	589	0.479	0.750	0.830	0.052	0.230	0.204
$0.250 - 0.375$	0.308	565	0.465	0.719	0.779	0.101	0.377	0.337
$0.375 - 0.500$	0.438	608	0.477	0.734	0.811	0.112	0.395	0.353
$0.500 - 0.750$	0.617	1310	0.459	0.752	0.809	0.120	0.422	0.379
$0.750 - 1.000$	0.868	1336	0.412	0.754	0.807	0.156	0.512	0.474
$1.000 - 1.500$	1.235	3623	0.661	0.736	0.799	0.363	0.678	0.645
$1.500 - 2.500$	1.964	8902	0.916	0.820	0.952	0.564	0.798	0.782
$2.500 - 5.000$	3.617	23299	0.982	0.956	0.991	0.703	0.872	0.851
$5.000 - 10.00$	7.285	46239	0.996	0.996	0.998	0.849	0.934	0.921
$10.00 - 100.0$	22.616	96716	0.997	0.999	0.999	0.940	0.968	0.962
Total	–	183187	0.971	0.973	0.987	0.775	0.908	0.890

Table 6.10: Simulated CNGS beam ν_μ DIS CC μ^- identification efficiencies and purities for different momenta p, using the final cut parameters defined in Chapter 6.6.

p Bin [GeV]	$< p >$ [GeV]	# Events	Cut E_π			Cut P_π		
			OLD	GUN	BEAM	OLD	GUN	BEAM
$0.000 - 0.250$	0.161	17776	0.711	0.917	0.893	0.976	0.991	0.994
$0.250 - 0.375$	0.309	7638	0.695	0.912	0.886	0.946	0.978	0.982
$0.375 - 0.500$	0.438	7472	0.692	0.909	0.879	0.942	0.977	0.982
$0.500 - 0.750$	0.619	14125	0.687	0.904	0.877	0.932	0.975	0.980
$0.750 - 1.000$	0.867	10114	0.706	0.905	0.882	0.901	0.965	0.972
$1.000 - 1.500$	1.235	13457	0.688	0.906	0.882	0.883	0.927	0.942
$1.500 - 2.500$	1.958	17725	0.644	0.896	0.867	0.939	0.908	0.973
$2.500 - 5.000$	3.565	21970	0.561	0.852	0.817	0.967	0.948	0.988
$5.000 - 10.00$	6.968	14538	0.436	0.776	0.730	0.969	0.984	0.992
$10.00 - 100.0$	18.057	8579	0.287	0.623	0.552	0.909	0.975	0.984
Total	–	133394	0.613	0.865	0.832	0.940	0.958	0.979

Table 6.11: Particle gun π^+ identification efficiencies and purities for different momenta p, using the final cut parameters defined in Chapter 6.6.

For the final cut, the total μ^- and π^+ identification efficiencies for momenta between 0 GeV and 100 GeV result to:

$$E_{\mu BEAM} = 0.987, \tag{6.10}$$
$$E_{\pi BEAM} = 0.832, \tag{6.11}$$

and the total μ^- and π^+ identification purities are given by:

$$P_{\mu BEAM} = 0.890, \tag{6.12}$$
$$P_{\pi BEAM} = 0.979, \tag{6.13}$$

while the currently used cut total μ^- and π^+ identification efficiencies result to:

$$E_{\mu OLD} = 0.971, \tag{6.14}$$
$$E_{\pi OLD} = 0.613, \tag{6.15}$$

and the total μ^- and π^+ identification purities are given by:

$$P_{\mu OLD} = 0.775, \tag{6.16}$$
$$P_{\pi OLD} = 0.940. \tag{6.17}$$

Thus, the identification efficiencies and purities for both μ^- and π^+ – corresponding to ν_μ DIS CC and ν_μ DIS NC events – could be significantly improved in the momentum range of $0 - 100$ GeV.

Chapter 7

Conclusion and Outlook

Within the framework of this diploma thesis, the separation of $\mu^{\pm}$ leptons and $\pi^{\pm}$ mesons – corresponding to a separation of CNGS beam ν_μ DIS CC and ν_μ DIS NC events – inside the electronic detector of the OPERA experiment has been investigated.

For both particle / interaction types, the identification efficiencies and purities for momenta between 0 GeV and 100 GeV could be significantly improved by employing a more complex series of cuts than before:

* The total $\mu^{\pm}$ / ν_μ DIS CC identification efficiency has been improved by 1.6%. (From 97.1% to 98.7%.)
* The total $\mu^{\pm}$ / ν_μ DIS CC identification purity has been improved by 11.5%. (From 77.5% to 89.0%.)
* The total $\pi^{\pm}$ / ν_μ DIS NC identification efficiency has been improved by 22.0%. (From 61.3% to 83.2%.)
* The total $\pi^{\pm}$ / ν_μ DIS NC identification purity has been improved by 3.9%. (From 94.0% to 97.9%.)

The new cut parameters include the reconstructed track length, the energy reconstructed in the TT scintillators, and the reconstructed momentum as well as its uncertainty.

The above-mentioned numbers do not yet discriminate between particles stopping inside the detector and those that exit at the back, another criterion which is examined in the actual reconstruction software for $\mu^{\pm}$ identification. However, both cuts are expected to be about equally improved regarding the $\mu^{\pm}$ identification efficiencies and purities.

Afterwards, the next step should be a test of the cuts on real data.

In the future, the presented cuts might still be improved by looking at the total event topology or secondary tracks (in this analysis, only parameters referring to the reconstructed first track have been used), or by changes to the momentum reconstruction algorithm.

The training of a neural network or a more sophisticated likelihood analysis could also further improve the performance.

Appendix A

Appendix

A.1 μ^- / π^+ Particle Gun MC

A.1.1 Vertices

TARGET

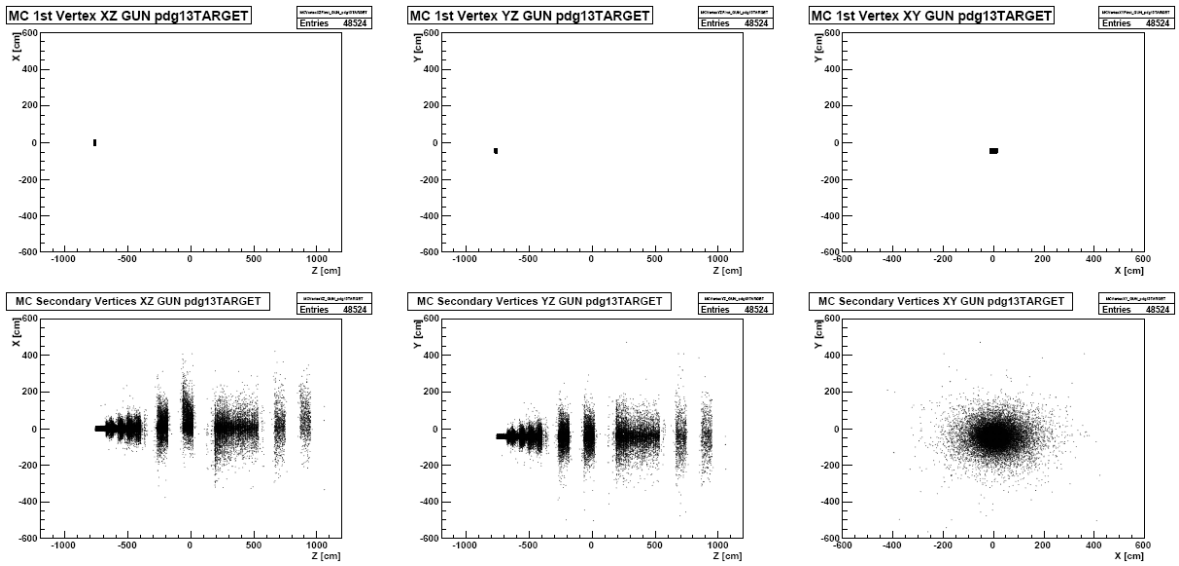

Figure A.1: Particle gun μ^- (TARGET). **Top:** MC vertex distribution XZ view, YZ view, XY view, **bottom:** MC decay vertex distribution XZ view, YZ view, XY view.

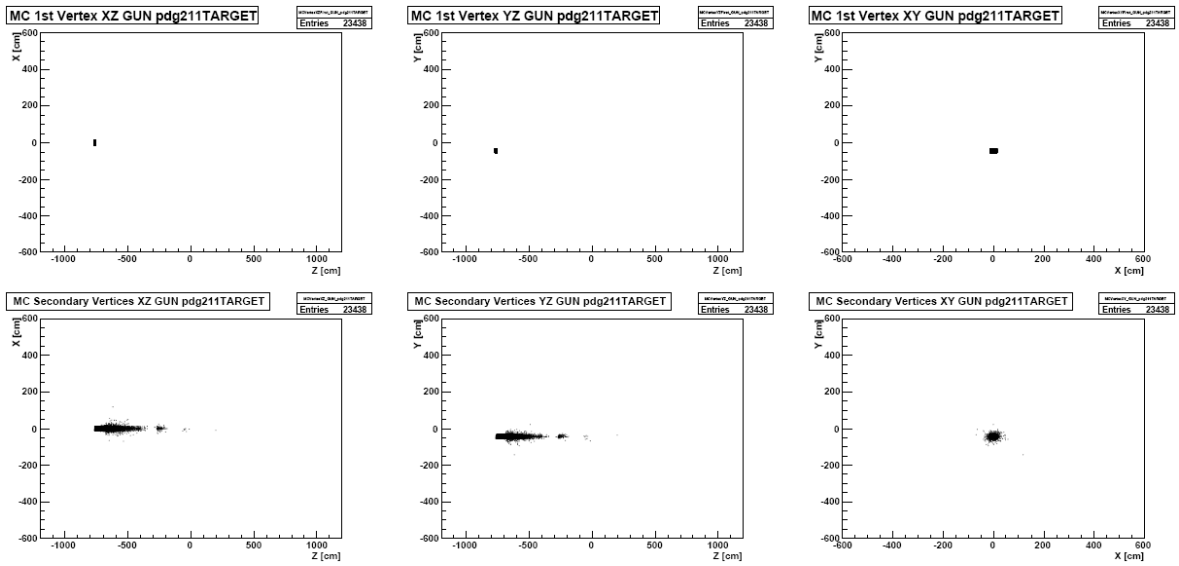

Figure A.2: Particle gun π^+ (TARGET). **Top:** MC vertex distribution XZ view, YZ view, XY view, **bottom:** MC decay vertex distribution XZ view, YZ view, XY view.

SPECTRO

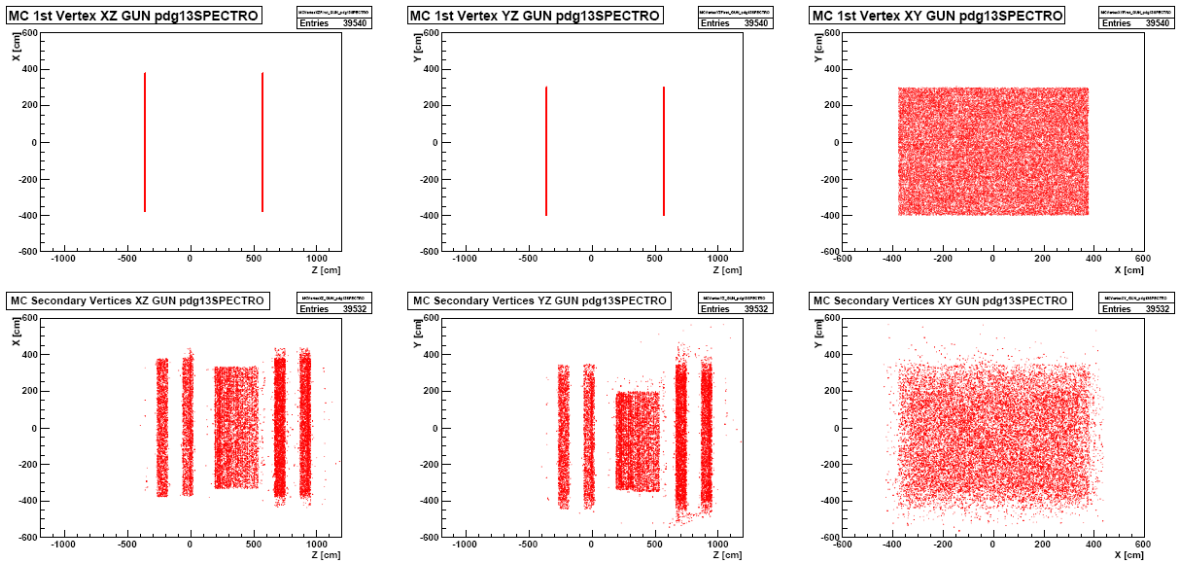

Figure A.3: Particle gun μ^- (SPECTRO). **Top:** MC vertex distribution XZ view, YZ view, XY view, **bottom:** MC decay vertex distribution XZ view, YZ view, XY view.

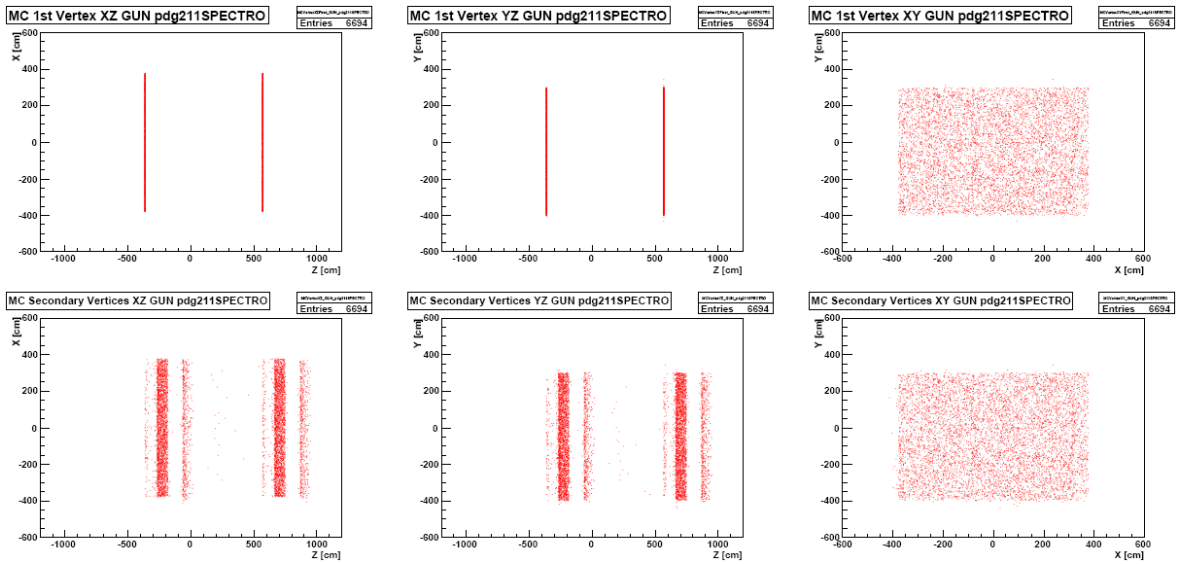

Figure A.4: Particle gun π^+ (SPECTRO). **Top:** MC vertex distribution XZ view, YZ view, XY view, **bottom:** MC decay vertex distribution XZ view, YZ view, XY view.

CENTER

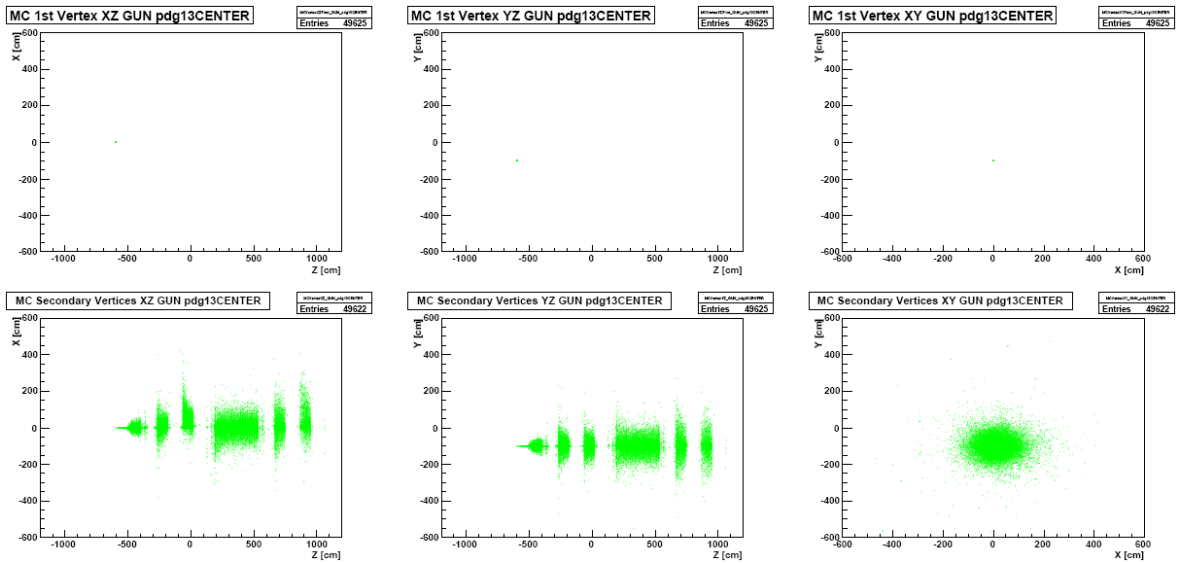

Figure A.5: Particle gun μ^- (CENTER). **Top:** MC vertex distribution XZ view, YZ view, XY view, **bottom:** MC decay vertex distribution XZ view, YZ view, XY view.

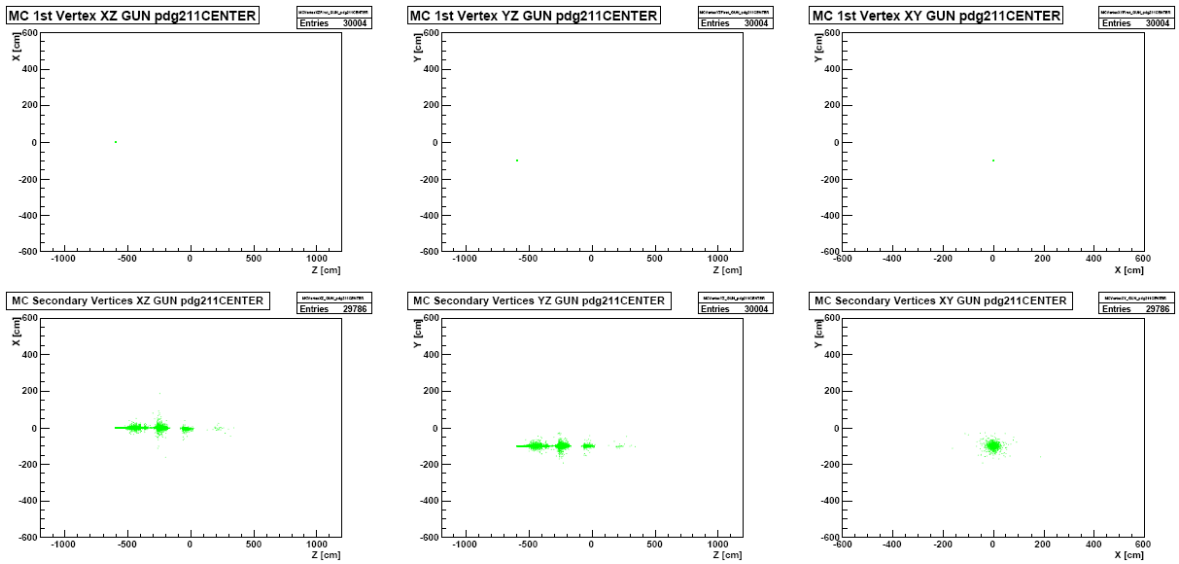

Figure A.6: Particle gun π^+ (CENTER). **Top:** MC vertex distribution XZ view, YZ view, XY view, **bottom:** MC decay vertex distribution XZ view, YZ view, XY view.

A.2 CNGS ν_μ Beam MC

A.2.1 MC Particle Counter

ν_μ RES CC Reactions

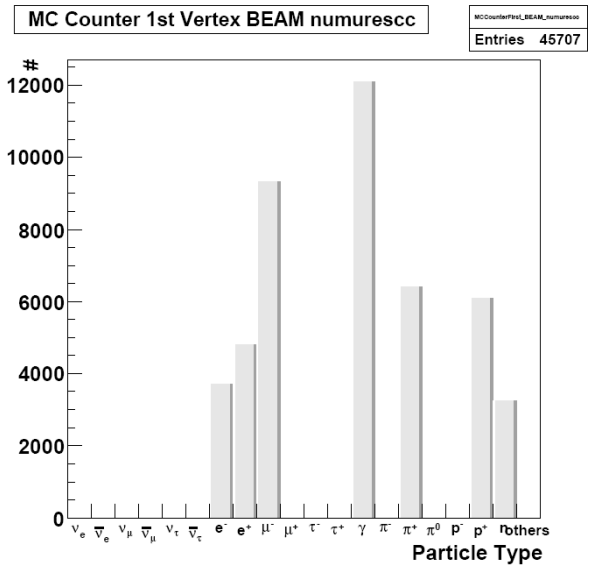

Figure A.7: Beam ν_μ RES CC reactions MC primary particles counter.

ν_μ RES NC Reactions

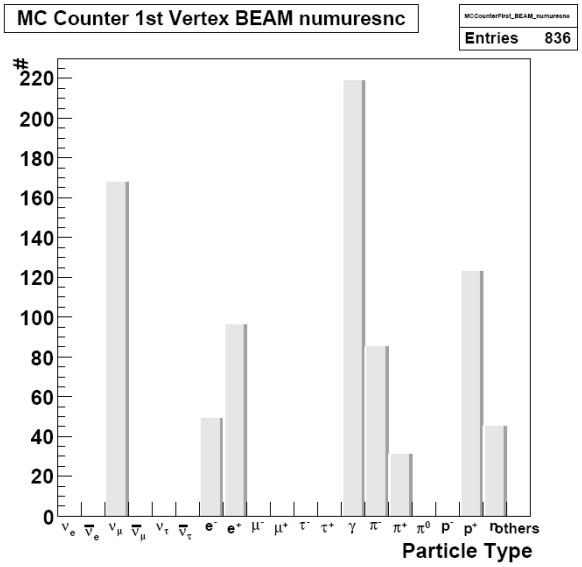

Figure A.8: Beam ν_μ RES NC reactions MC primary particles counter.

ν_μ QEL CC Reactions

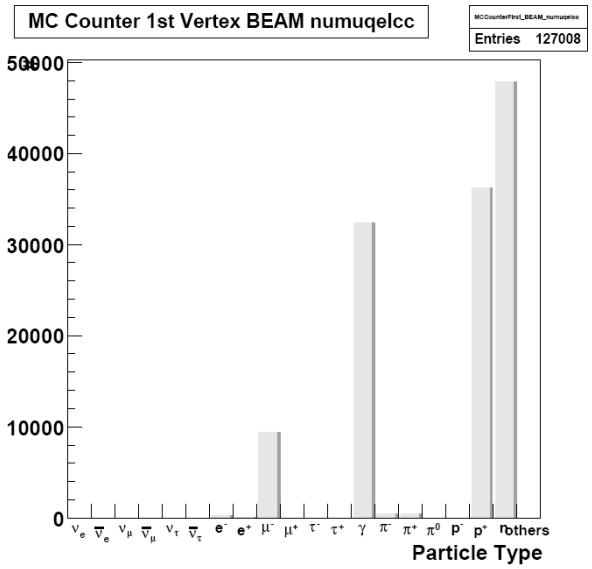

Figure A.9: Beam ν_μ QEL CC reactions MC primary particles counter.

A.2.2 MC Momentum

ν_μ DIS CC Reactions

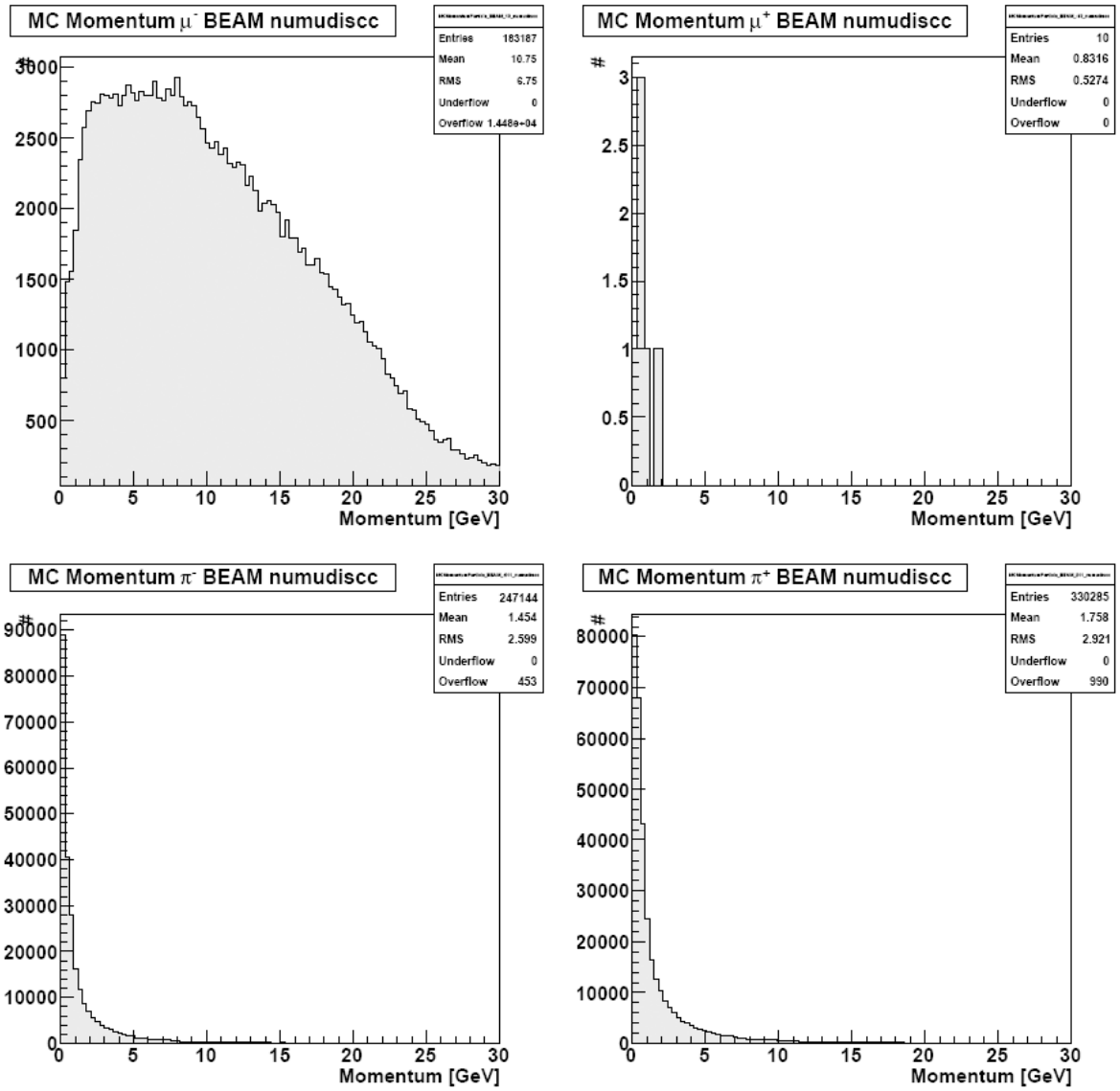

Figure A.10: Beam ν_μ DIS CC reactions MC momentum. **Top left:** μ^-, **top right:** μ^+, **bottom left:** π^-, **bottom right:** π^+.

ν_μ DIS NC Reactions

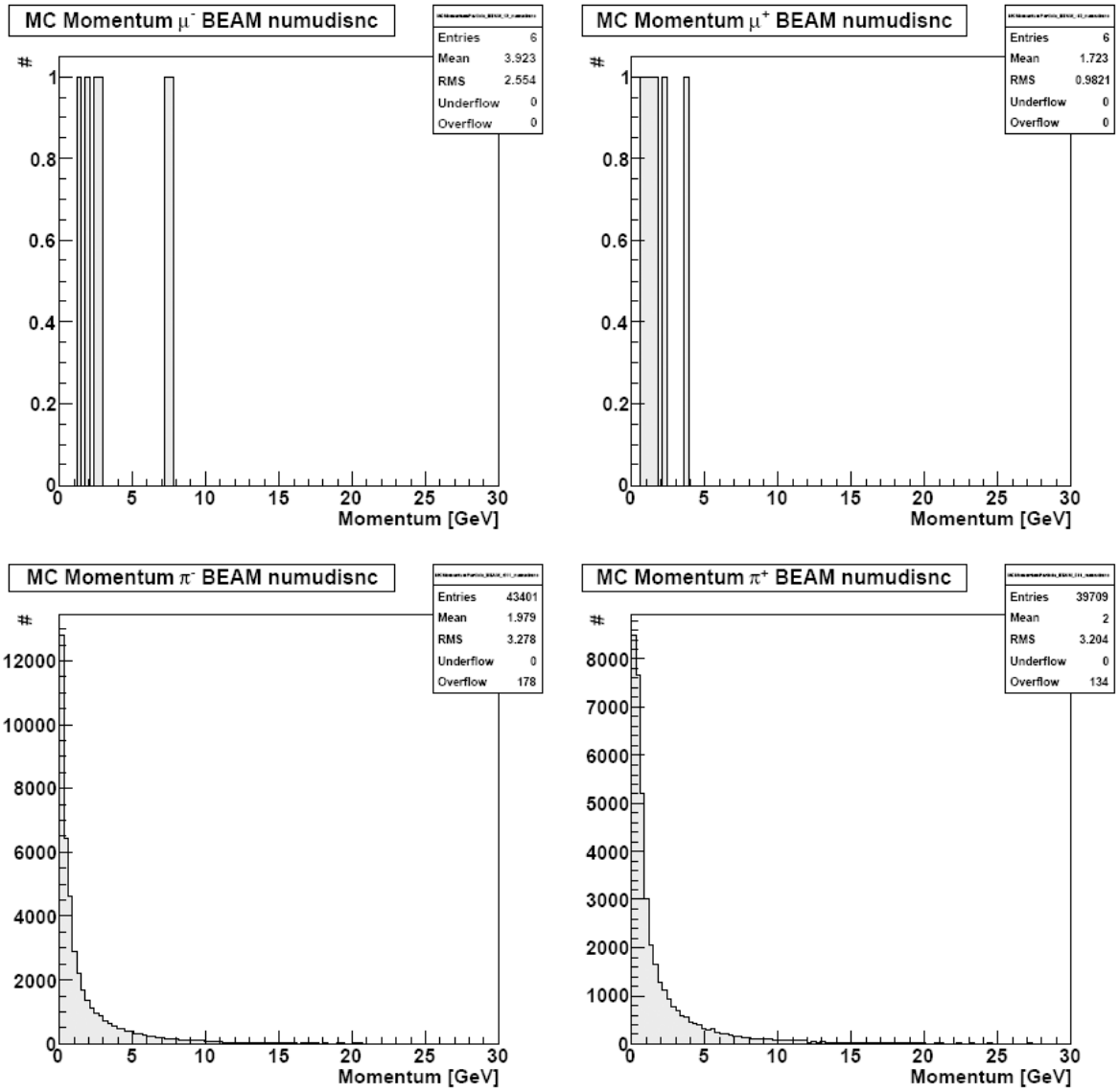

Figure A.11: Beam ν_μ DIS NC reactions MC momentum. **Top left:** μ^-, **top right:** μ^+, **bottom left:** π^-, **bottom right:** π^+.

ν_μ RES CC Reactions

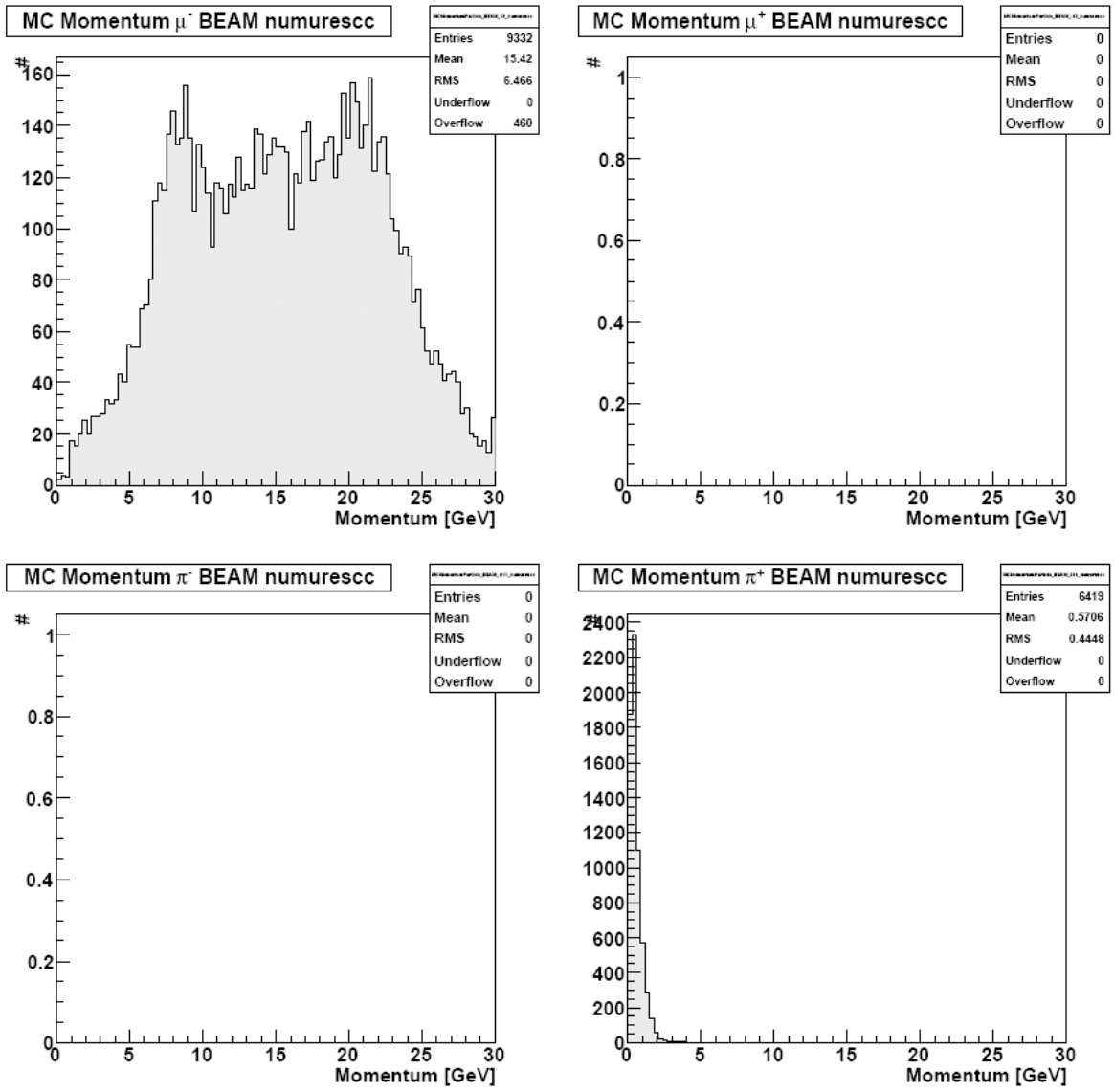

Figure A.12: Beam ν_μ RES CC reactions MC momentum. **Top left:** μ^-, **top right:** μ^+, **bottom left:** π^-, **bottom right:** π^+.

ν_μ RES NC Reactions

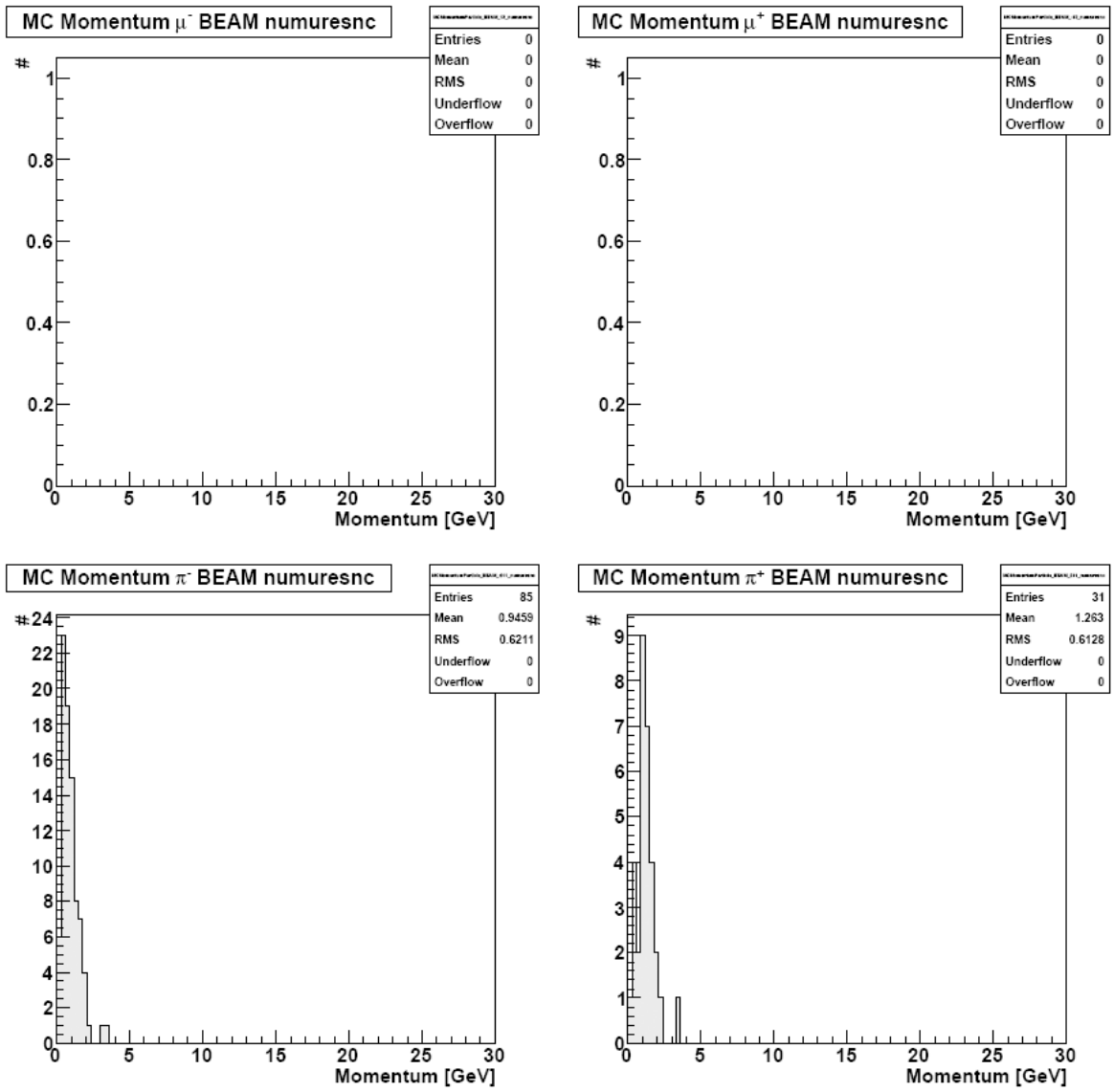

Figure A.13: Beam ν_μ RES NC reactions MC momentum. **Top left:** μ^-, **top right:** μ^+, **bottom left:** π^-, **bottom right:** π^+.

ν_μ QEL CC Reactions

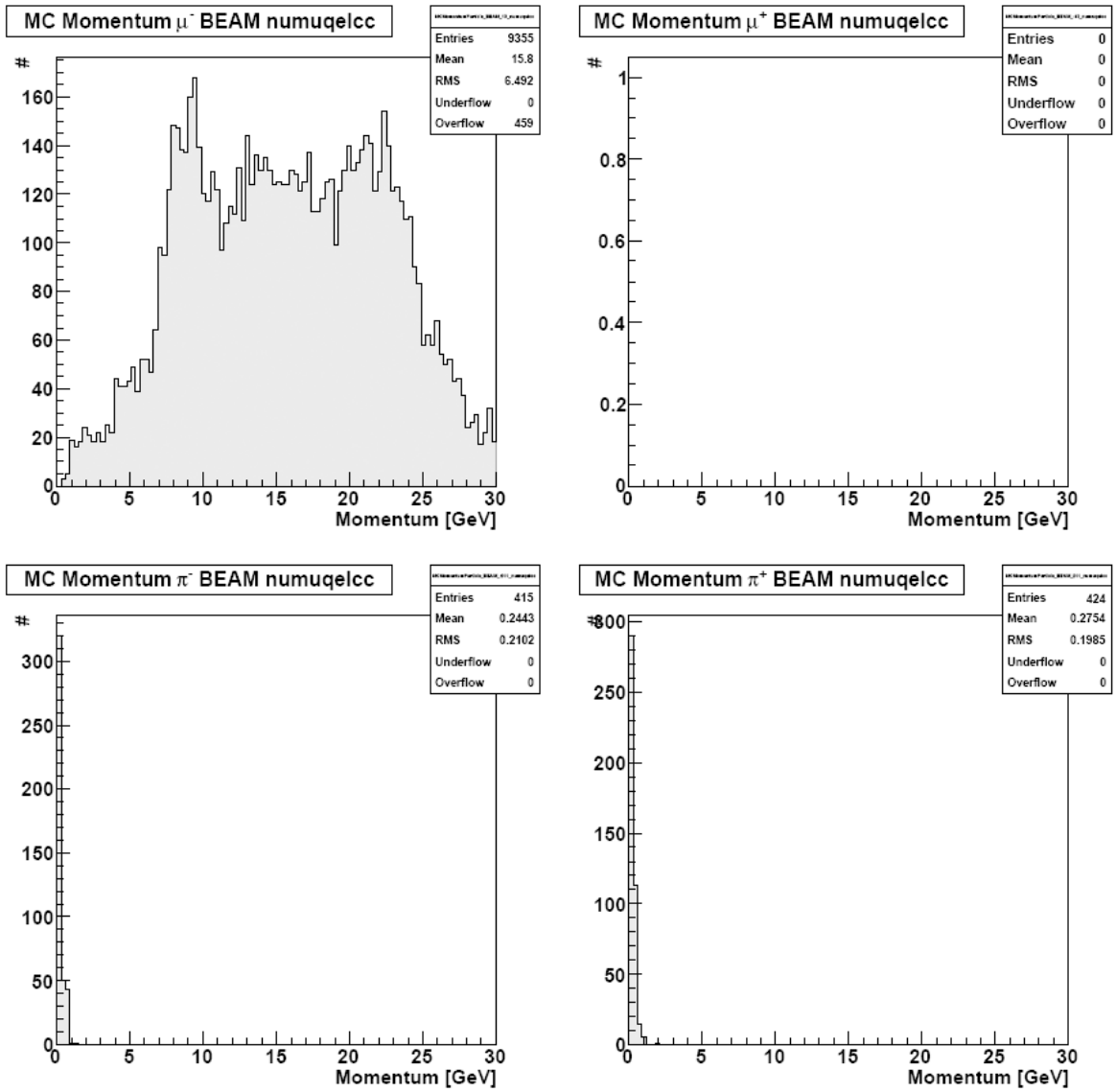

Figure A.14: Beam ν_μ QEL CC reactions MC momentum. **Top left:** μ^-, **top right:** μ^+, **bottom left:** π^-, **bottom right:** π^+.

A.2.3 Reconstructed Track Length

ν_μ DIS CC Reactions

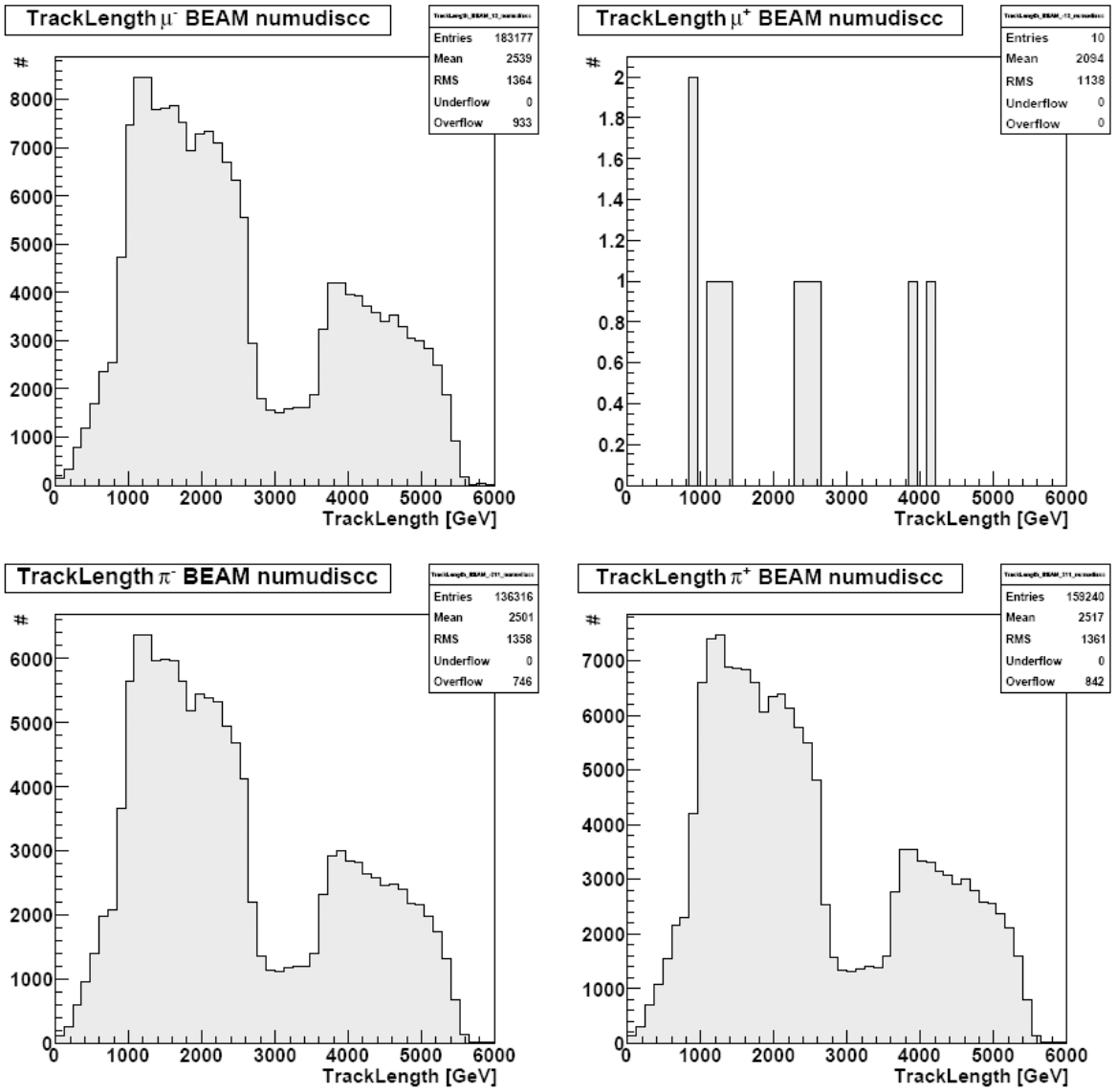

Figure A.15: Beam ν_μ DIS CC reactions reconstructed track length. **Top left:** μ^-, **top right:** μ^+, **bottom left:** π^-, **bottom right:** π^+.

ν_μ DIS NC Reactions

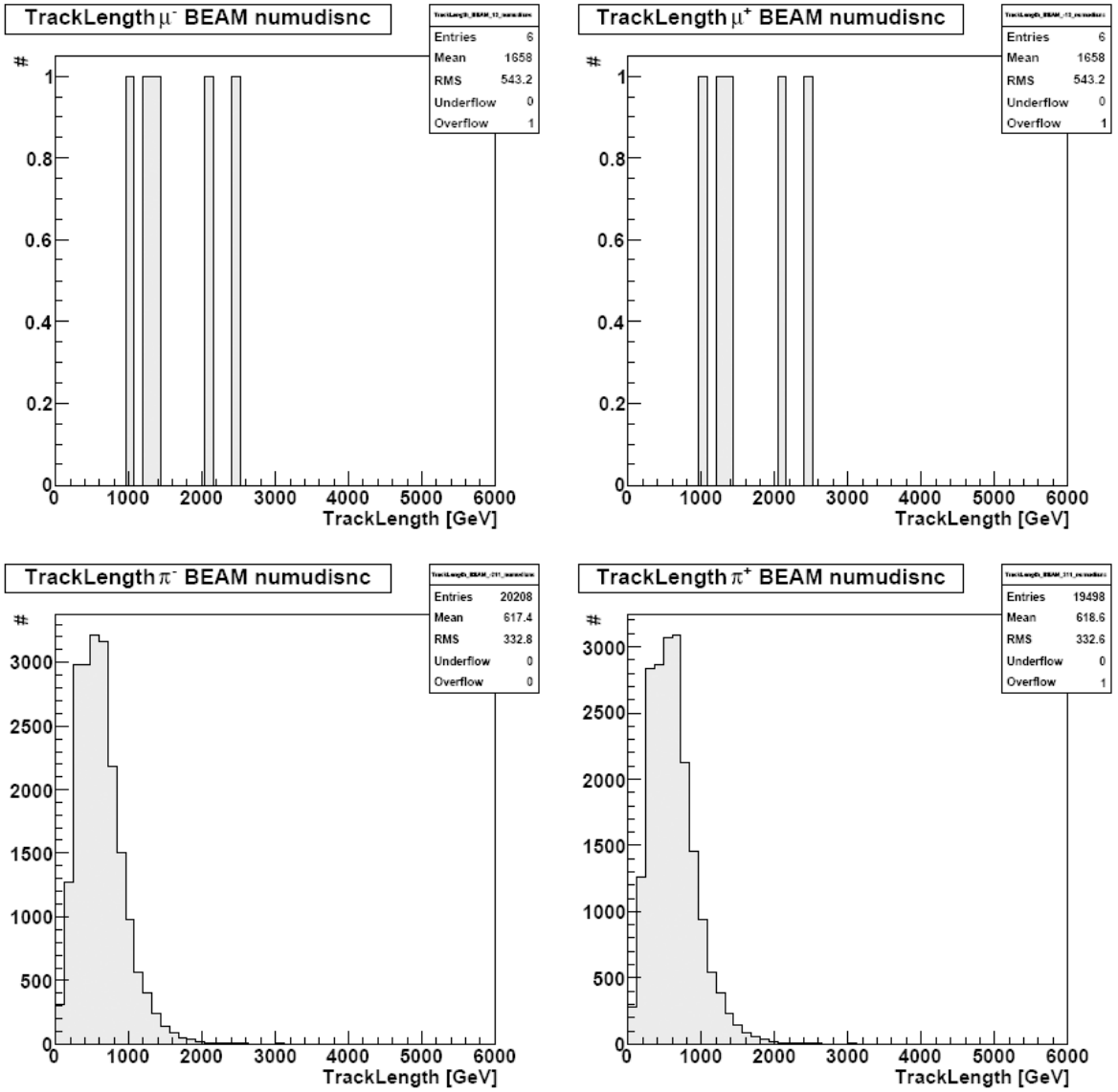

Figure A.16: Beam ν_μ DIS NC reactions reconstructed track length. **Top left:** μ^-, **top right:** μ^+, **bottom left:** π^-, **bottom right:** π^+.

ν_μ RES CC Reactions

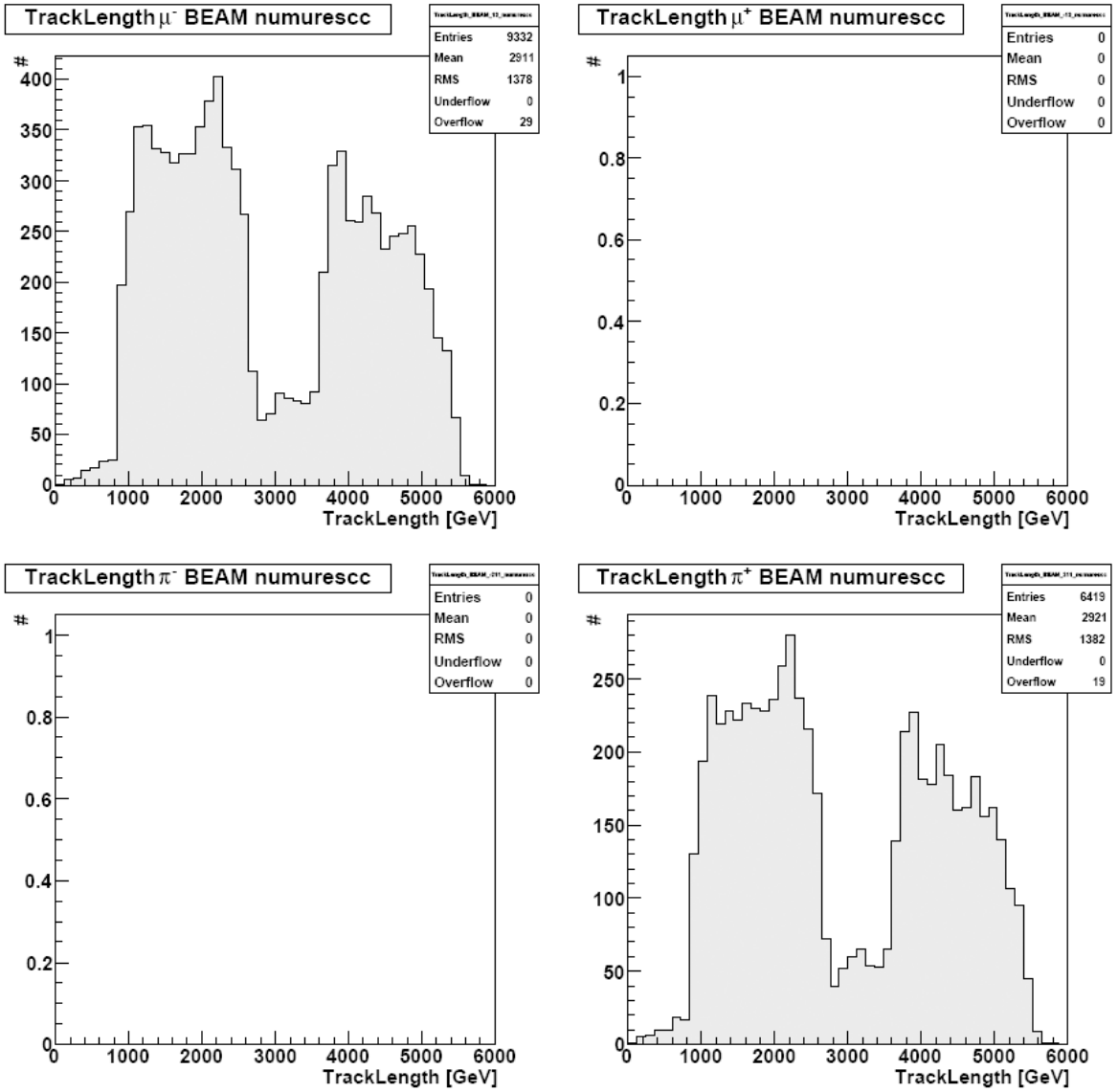

Figure A.17: Beam ν_μ RES CC reactions reconstructed track length. **Top left:** μ^-, **top right:** μ^+, **bottom left:** π^-, **bottom right:** π^+.

ν_μ RES NC Reactions

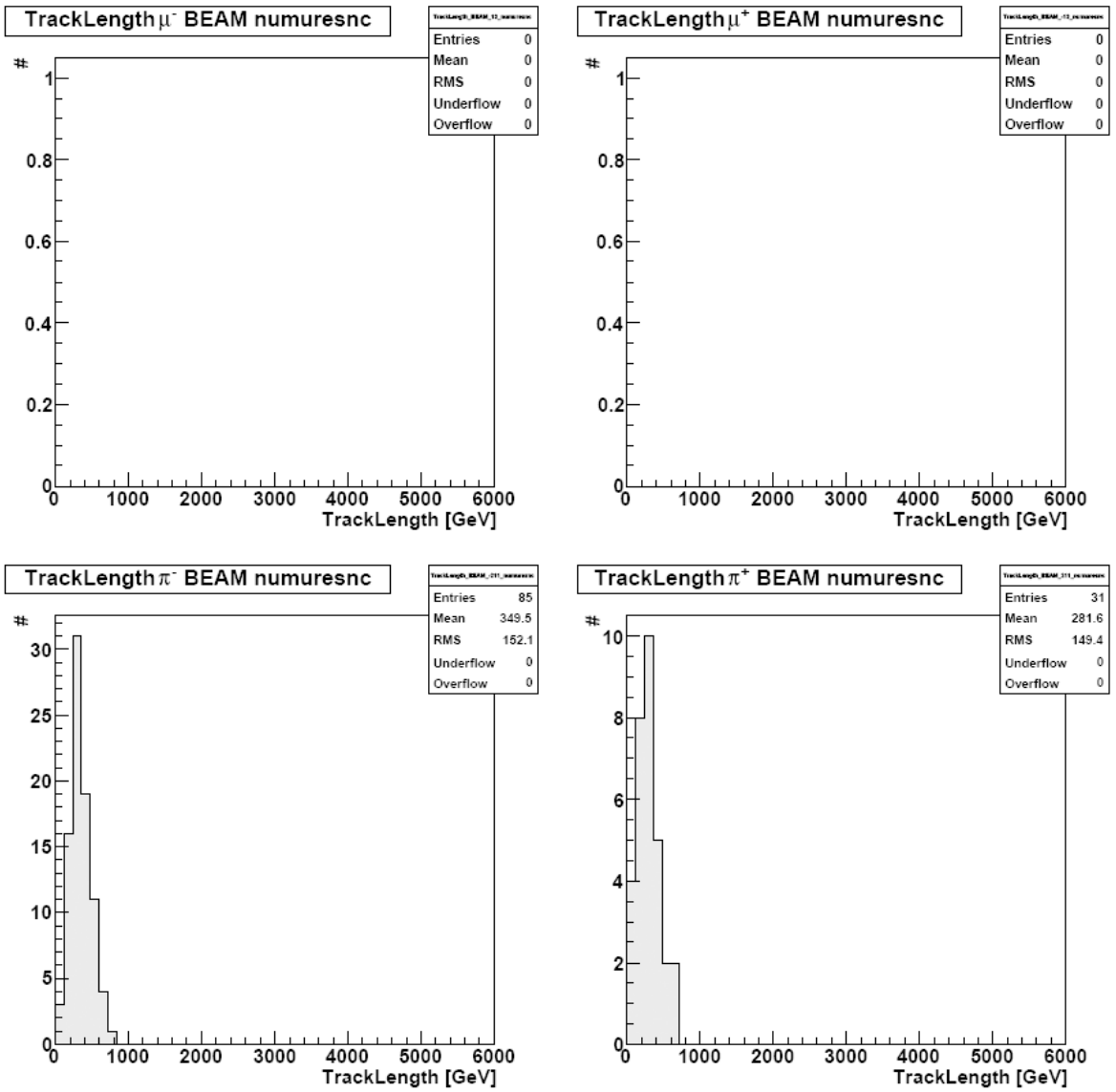

Figure A.18: Beam ν_μ RES NC reactions reconstructed track length. **Top left:** μ^-, **top right:** μ^+, **bottom left:** π^-, **bottom right:** π^+.

ν_μ QEL CC Reactions

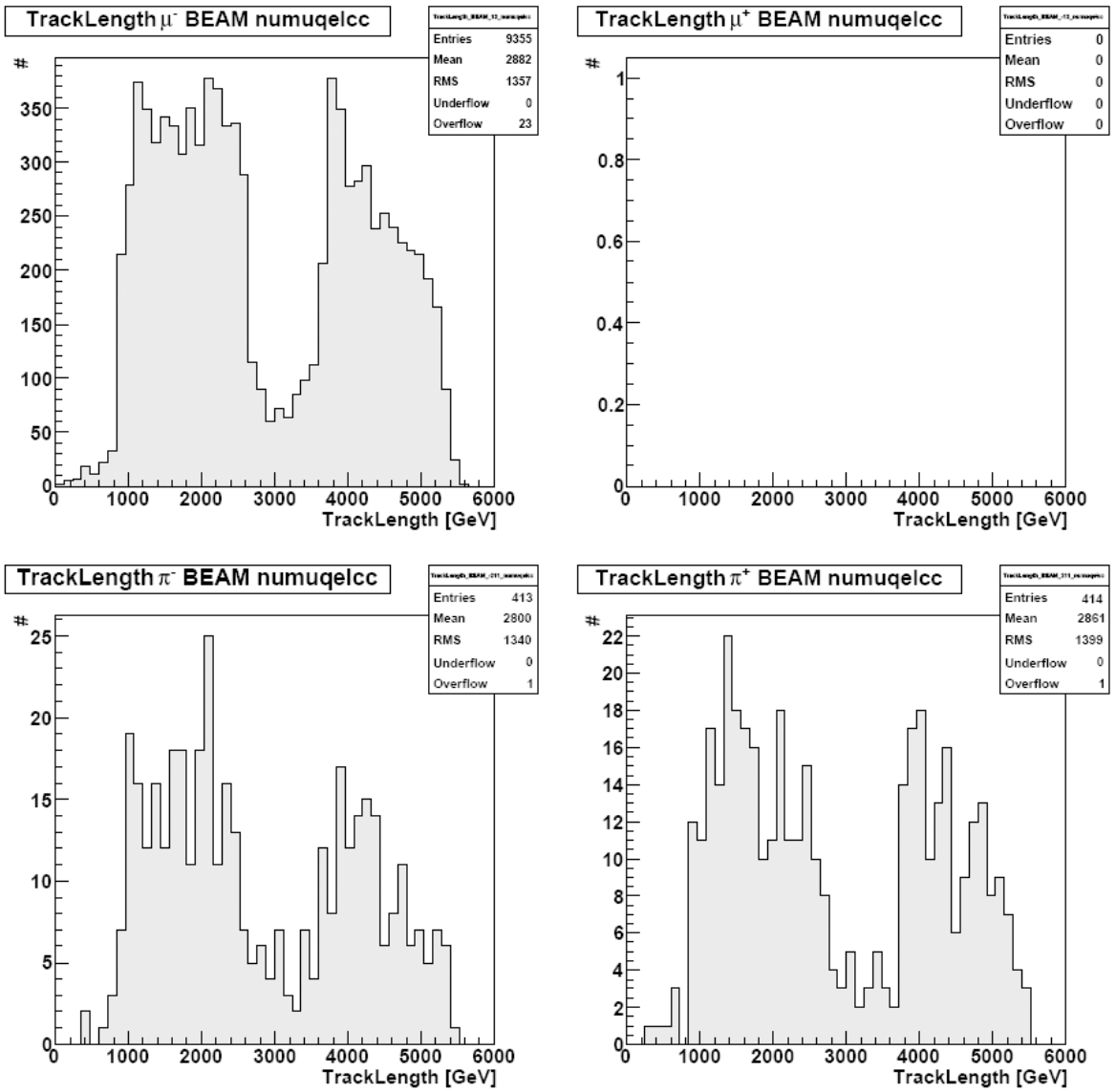

Figure A.19: Beam ν_μ QEL CC reactions reconstructed track length. **Top left:** μ^-, **top right:** μ^+, **bottom left:** π^-, **bottom right:** π^+.

A.2.4 Reconstructed Momentum

ν_μ DIS CC Reactions

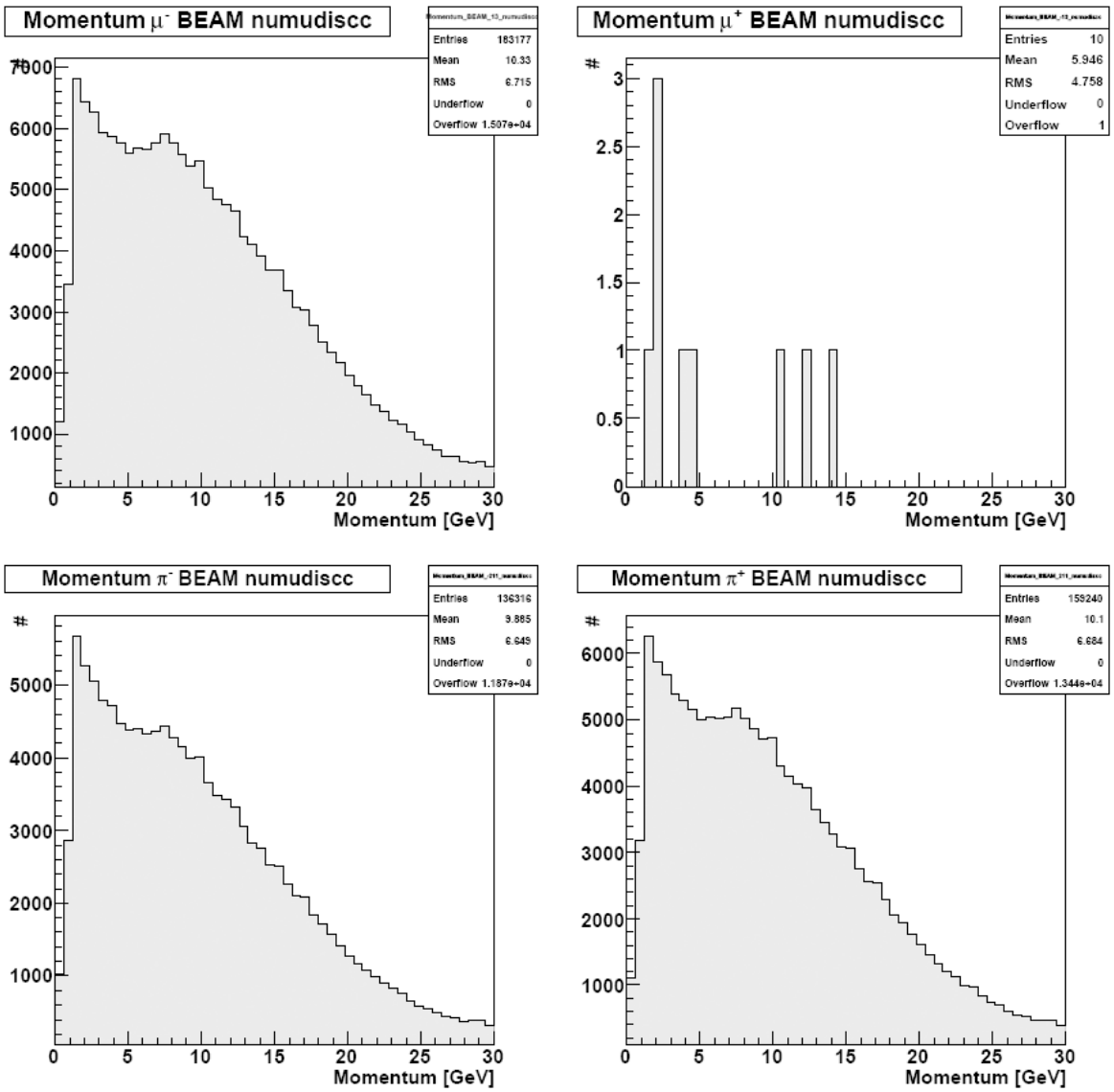

Figure A.20: Beam ν_μ DIS CC reactions reconstructed momentum. **Top left:** μ^-, **top right:** μ^+, **bottom left:** π^-, **bottom right:** π^+.

ν_μ DIS NC Reactions

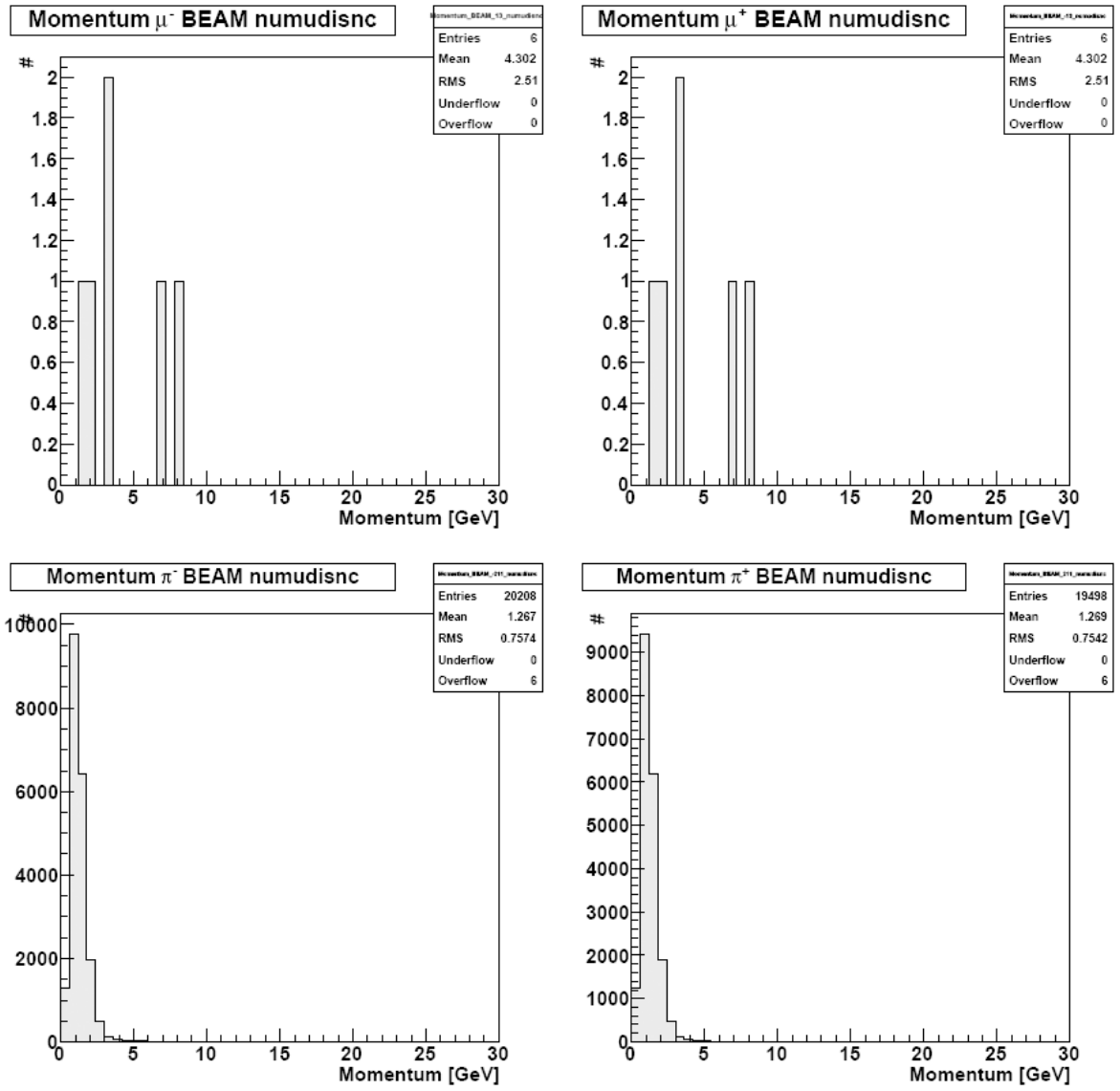

Figure A.21: Beam ν_μ DIS NC reactions reconstructed momentum. **Top left:** μ^-, **top right:** μ^+, **bottom left:** π^-, **bottom right:** π^+.

ν_μ RES CC Reactions

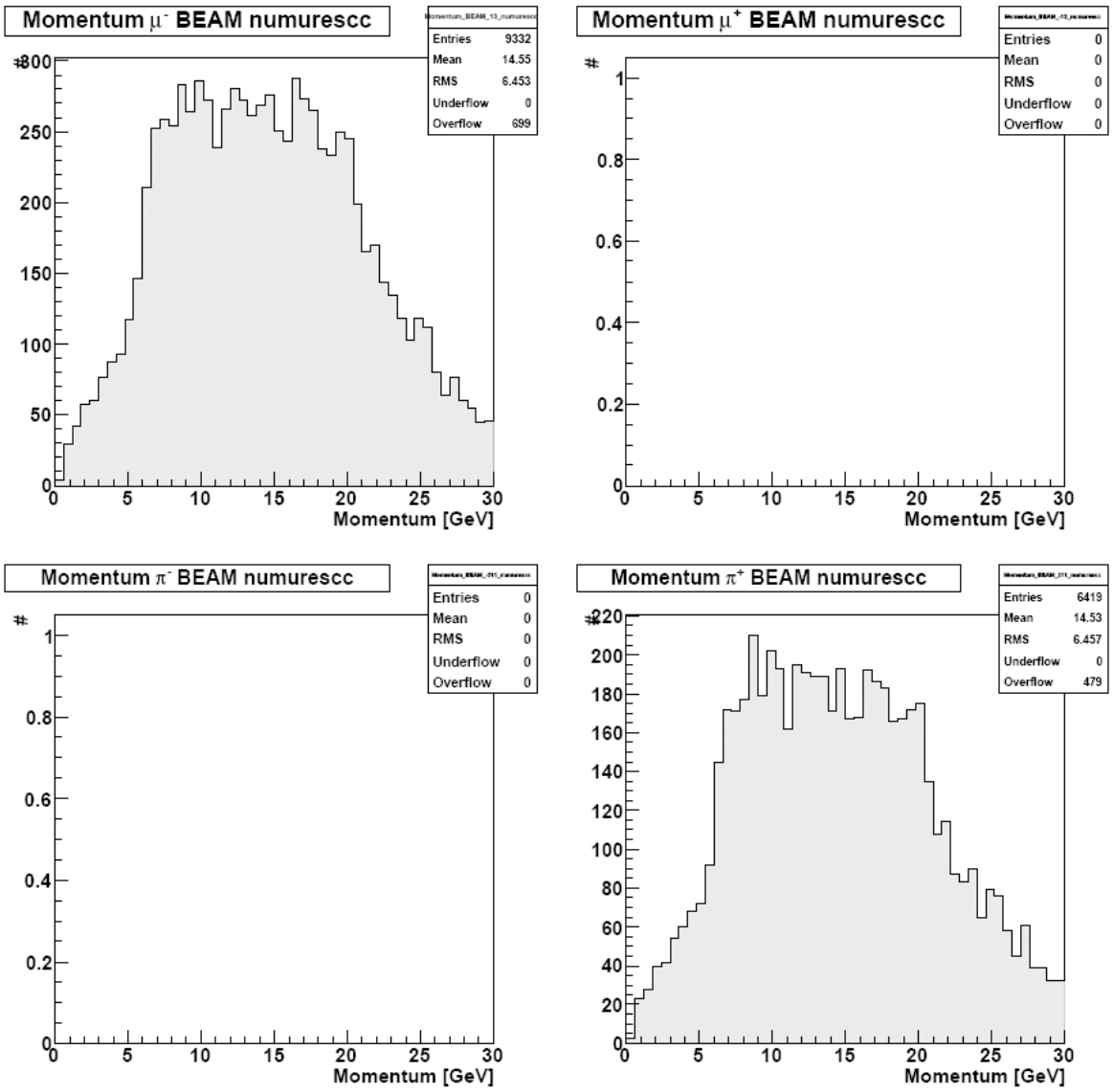

Figure A.22: Beam ν_μ RES CC reactions reconstructed momentum. **Top left:** μ^-, **top right:** μ^+, **bottom left:** π^-, **bottom right:** π^+.

ν_μ RES NC Reactions

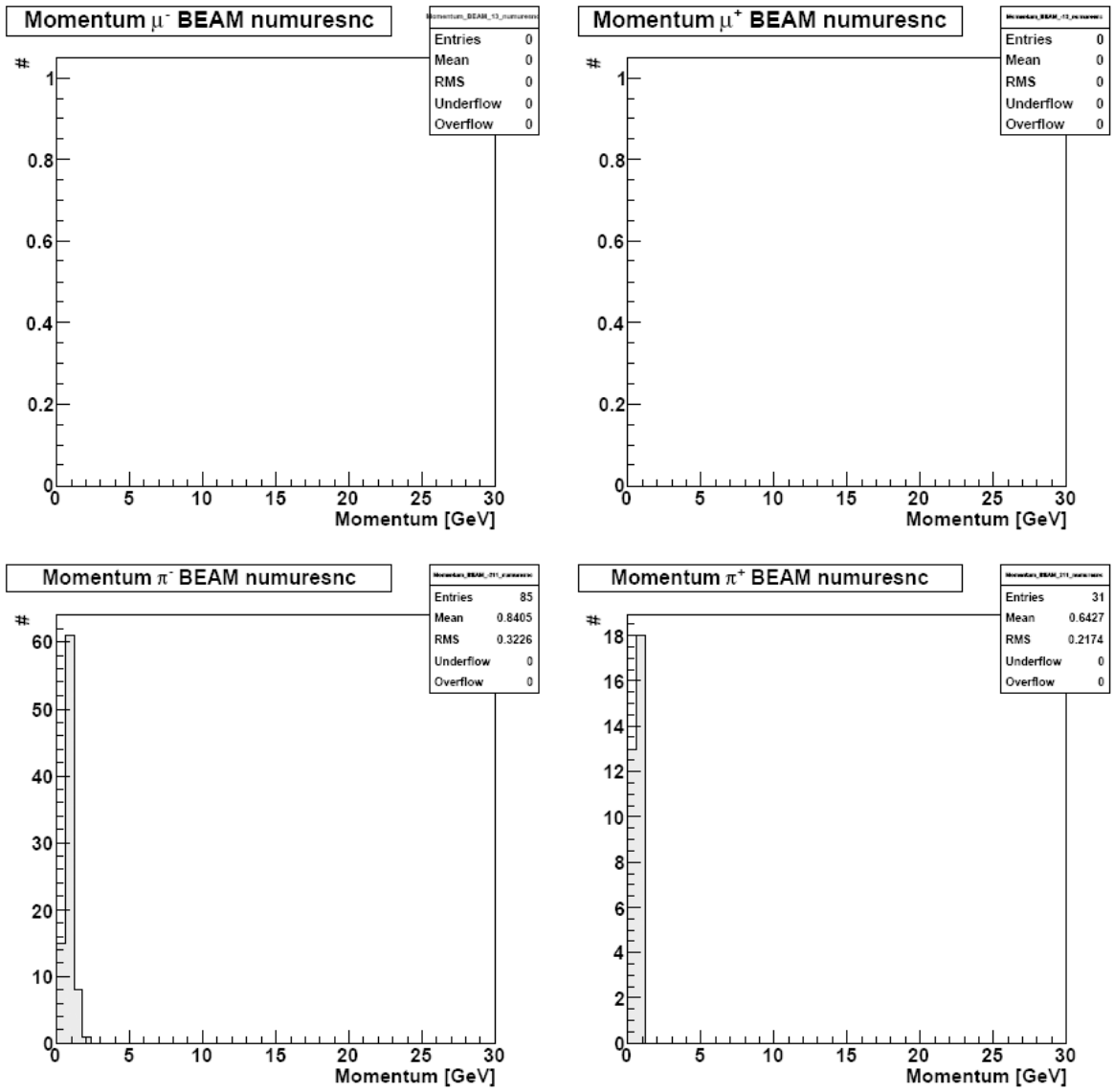

Figure A.23: Beam ν_μ RES NC reactions reconstructed momentum. **Top left:** μ^-, **top right:** μ^+, **bottom left:** π^-, **bottom right:** π^+.

ν_μ QEL CC Reactions

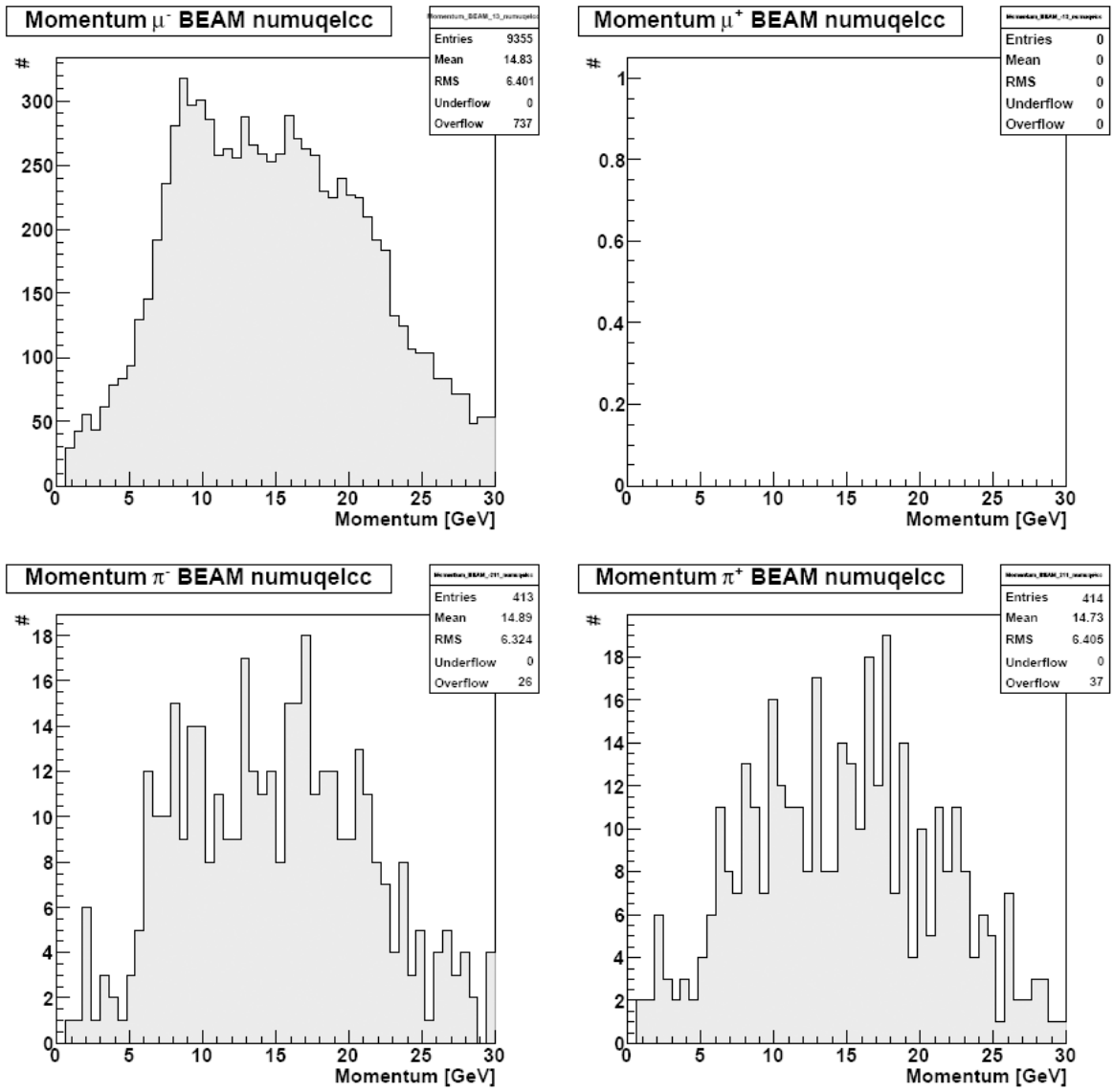

Figure A.24: Beam ν_μ QEL CC reactions reconstructed momentum. **Top left:** μ^-, **top right:** μ^+, **bottom left:** π^-, **bottom right:** π^+.

A.2.5 Reconstructed vs MC Momentum

All ν_μ Reactions

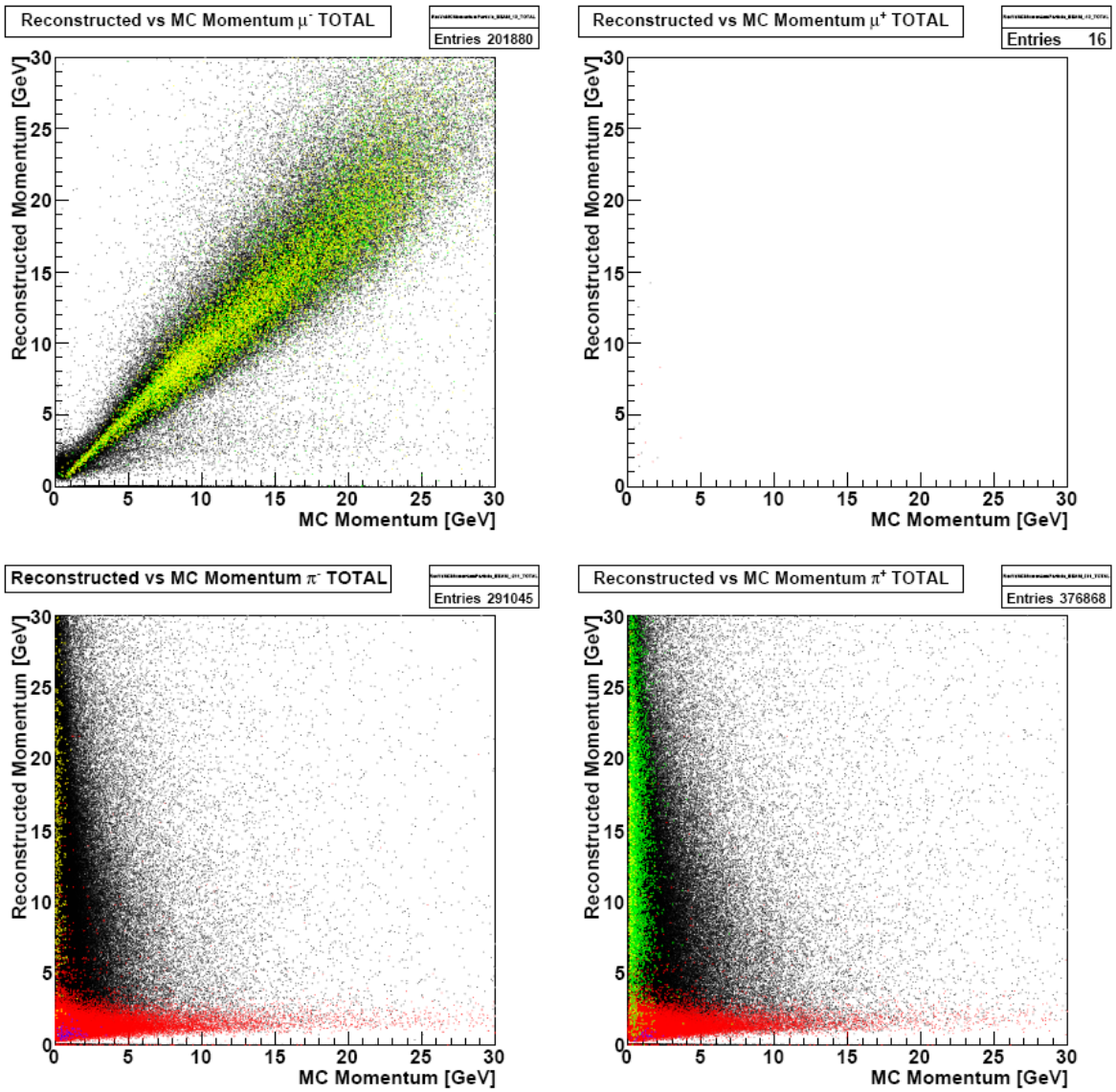

Figure A.25: Beam ν_μ reconstructed vs MC momentum. **Top left:** μ^-, **top right:** μ^+, **bottom left:** π^-, **bottom right:** π^+. **Black:** ν_μ DIS CC interactions, **red:** ν_μ DIS NC interactions, **green:** ν_μ RES CC interactions, **blue:** ν_μ RES NC interactions, **yellow:** ν_μ QEL CC interactions.

ν_μ DIS CC Reactions

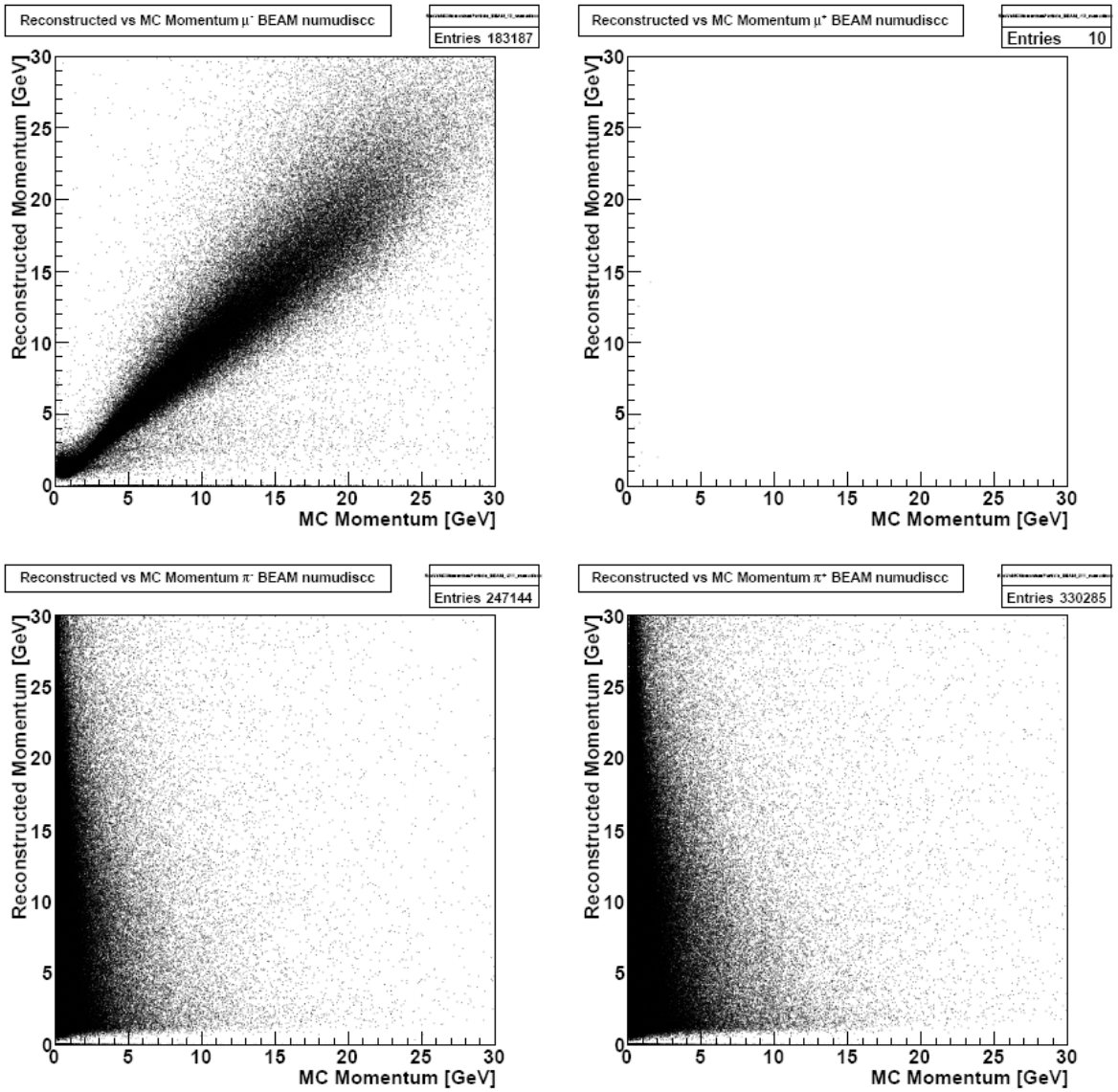

Figure A.26: Beam ν_μ DIS CC reactions reconstructed vs MC momentum. **Top left:** μ^-, **top right:** μ^+, **bottom left:** π^-, **bottom right:** π^+.

ν_μ DIS NC Reactions

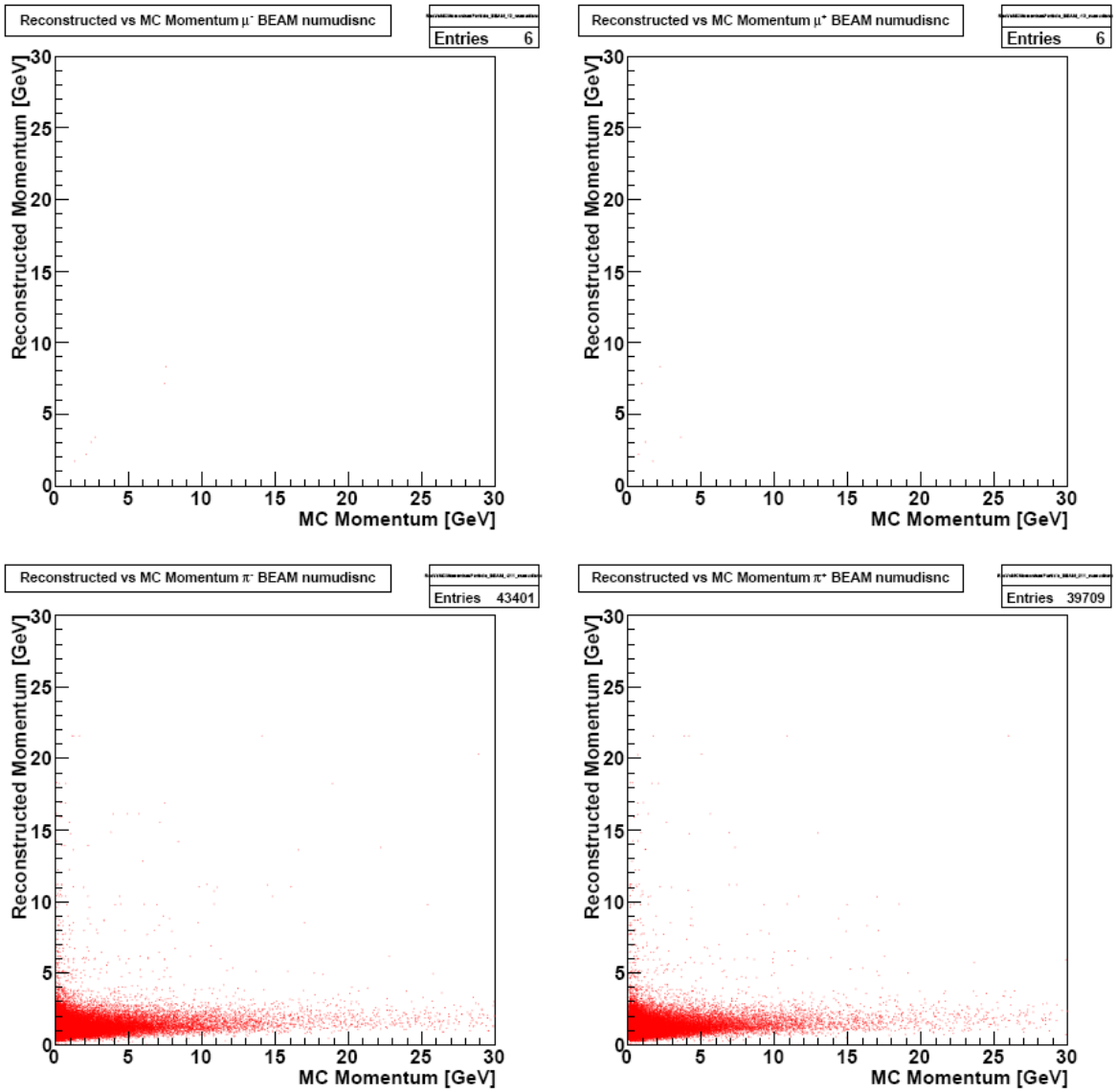

Figure A.27: Beam ν_μ DIS NC reactions reconstructed vs MC momentum. **Top left:** μ^-, **top right:** μ^+, **bottom left:** π^-, **bottom right:** π^+.

ν_μ RES CC Reactions

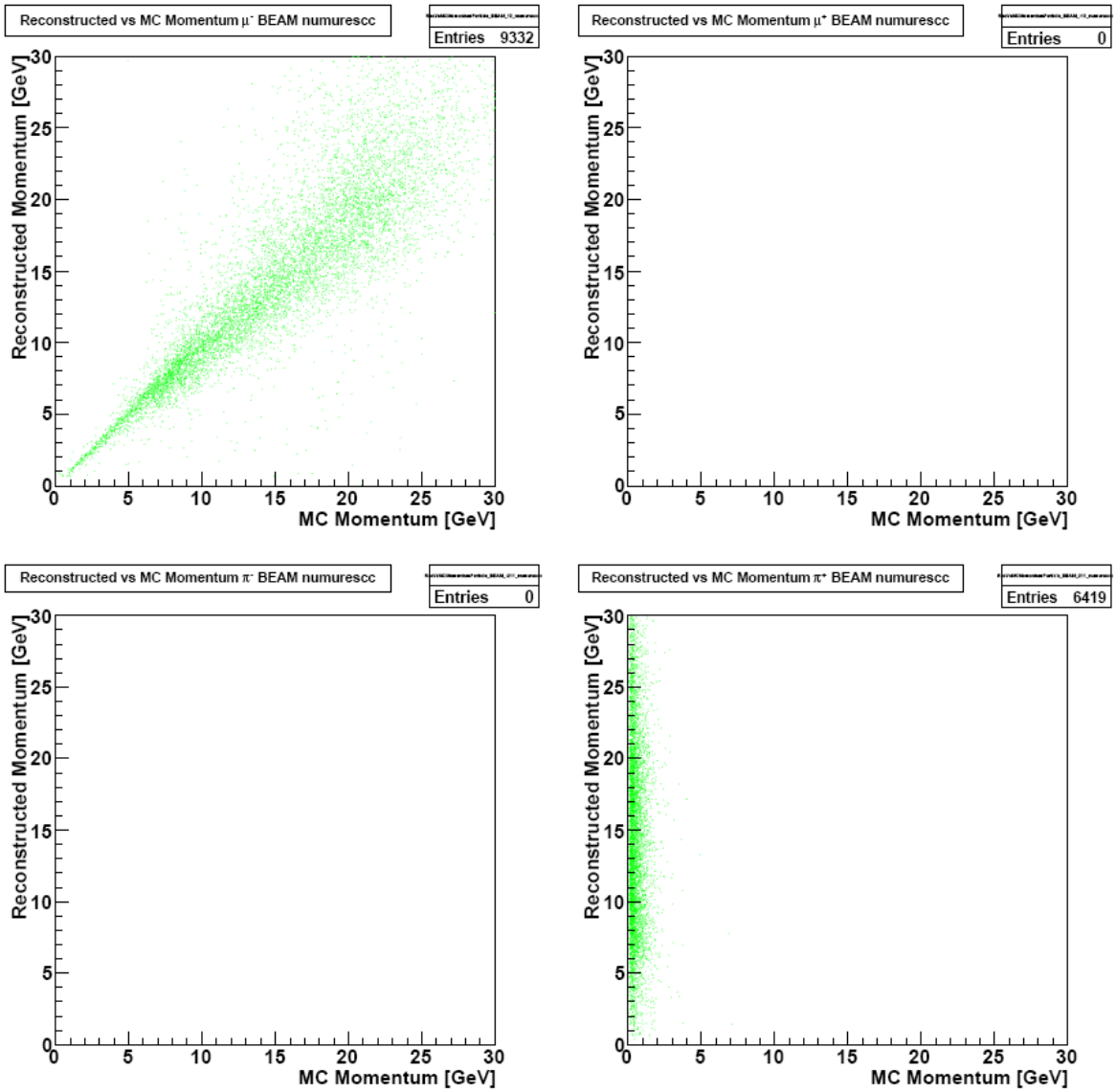

Figure A.28: Beam ν_μ RES CC reactions reconstructed vs MC momentum. **Top left:** μ^-, **top right:** μ^+, **bottom left:** π^-, **bottom right:** π^+.

ν_μ RES NC Reactions

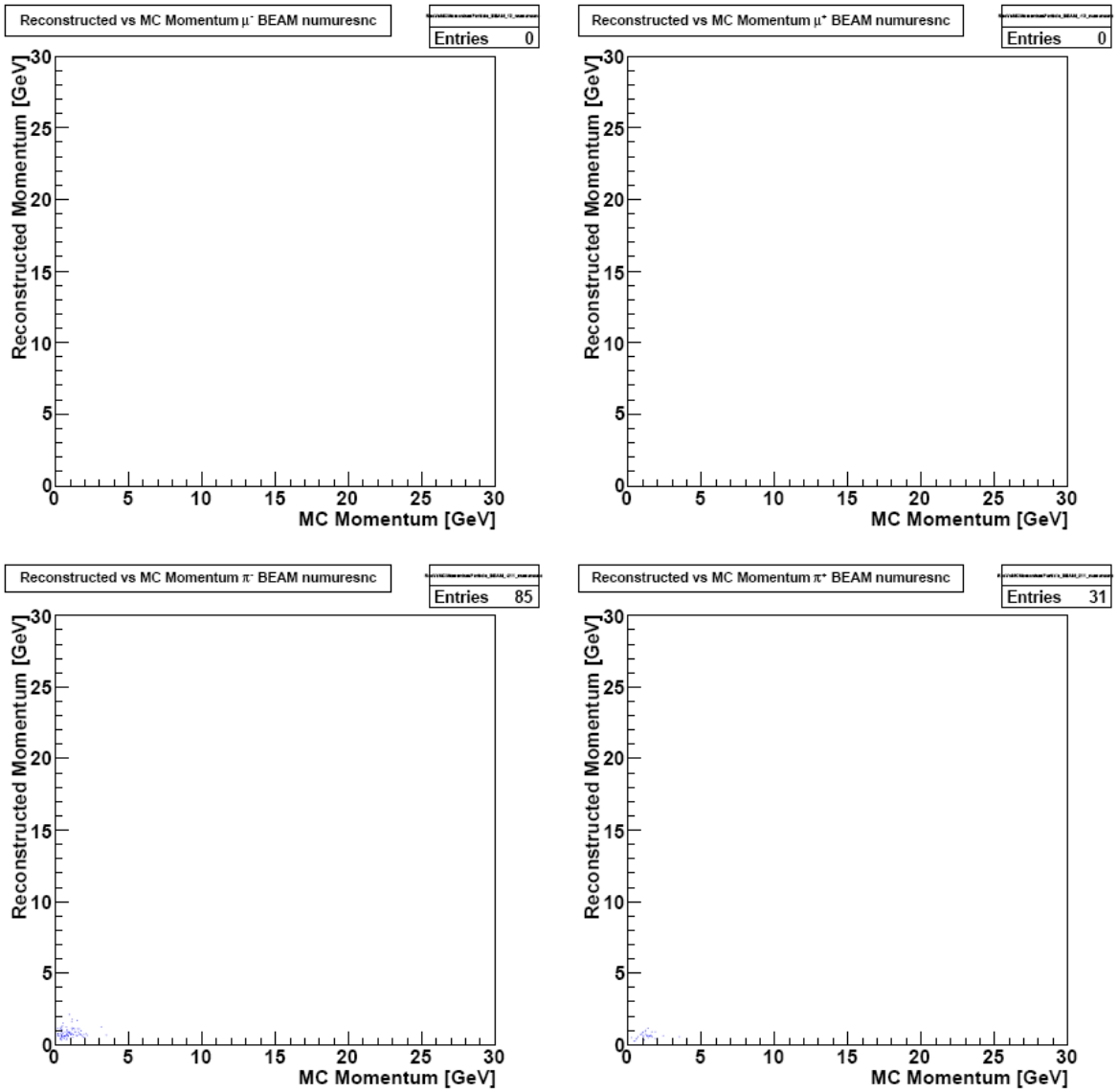

Figure A.29: Beam ν_μ RES NC reactions reconstructed vs MC momentum. **Top left:** μ^-, **top right:** μ^+, **bottom left:** π^-, **bottom right:** π^+.

ν_μ QEL CC Reactions

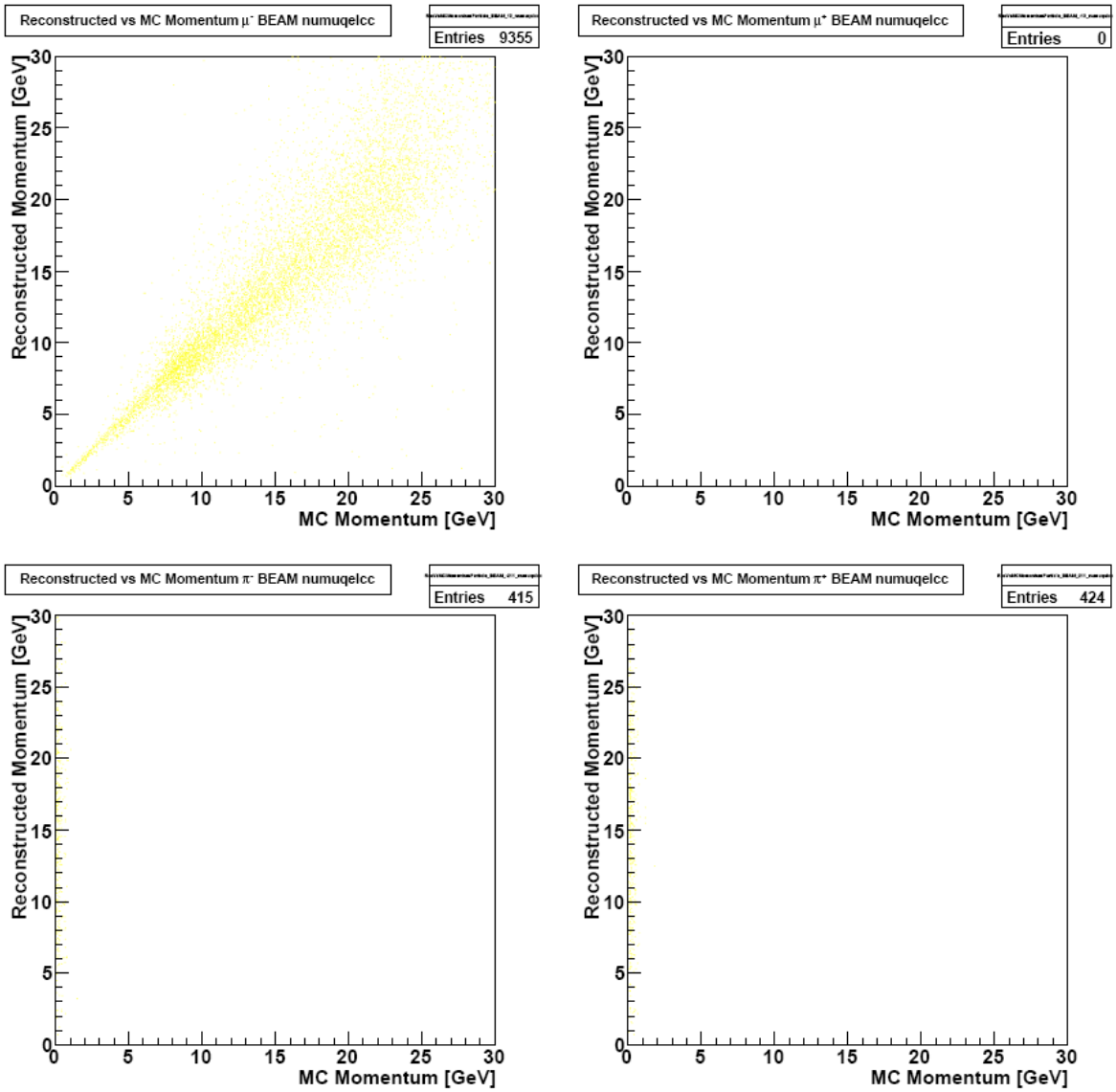

Figure A.30: Beam ν_μ QEL CC reactions reconstructed vs MC momentum. **Top left:** μ^-, **top right:** μ^+, **bottom left:** π^-, **bottom right:** π^+.

A.2.6 Momentum Variance

ν_μ DIS CC Reactions

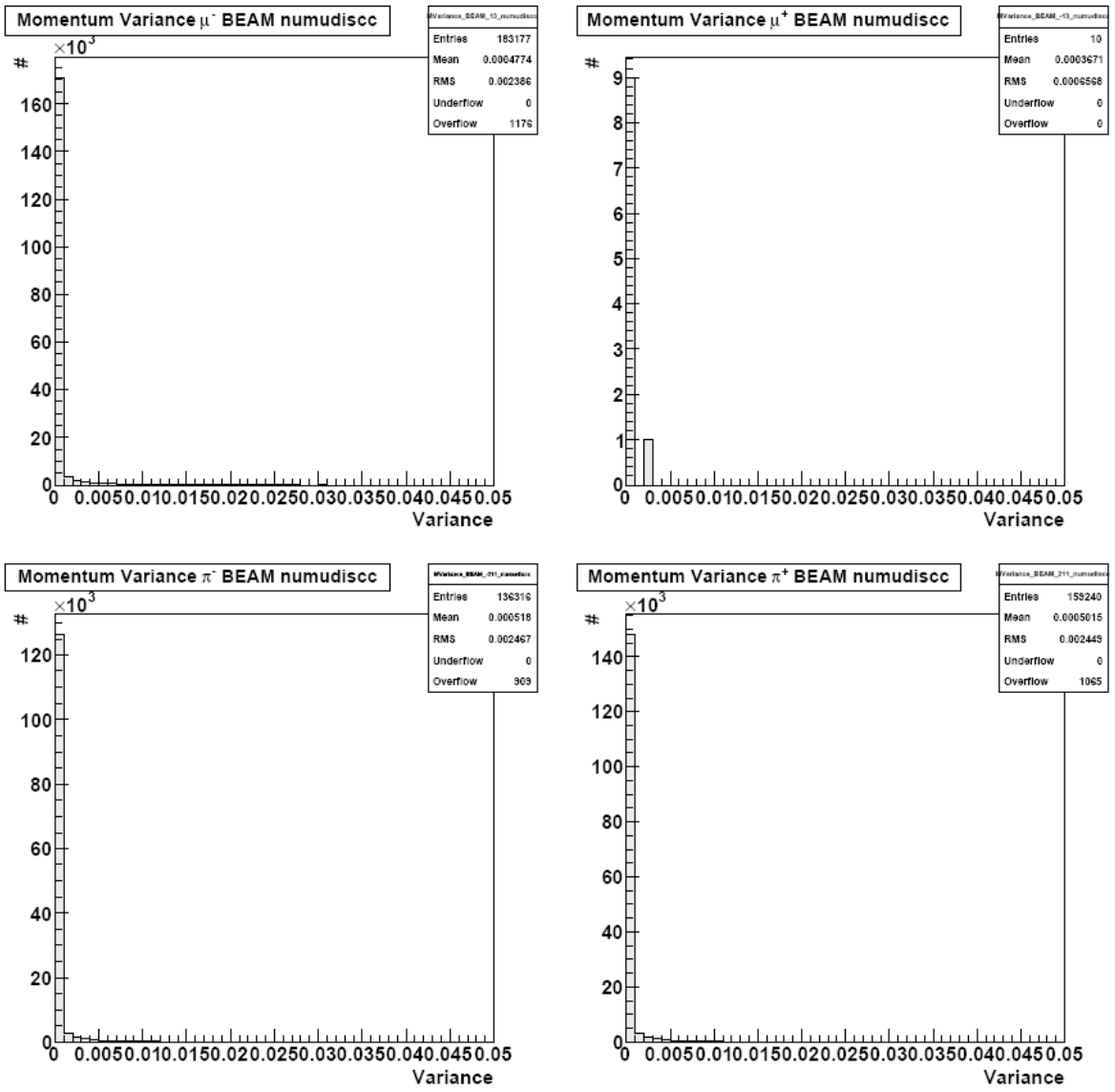

Figure A.31: Beam ν_μ DIS CC reactions momentum variance. **Top left:** μ^-, **top right:** μ^+, **bottom left:** π^-, **bottom right:** π^+.

ν_μ DIS NC Reactions

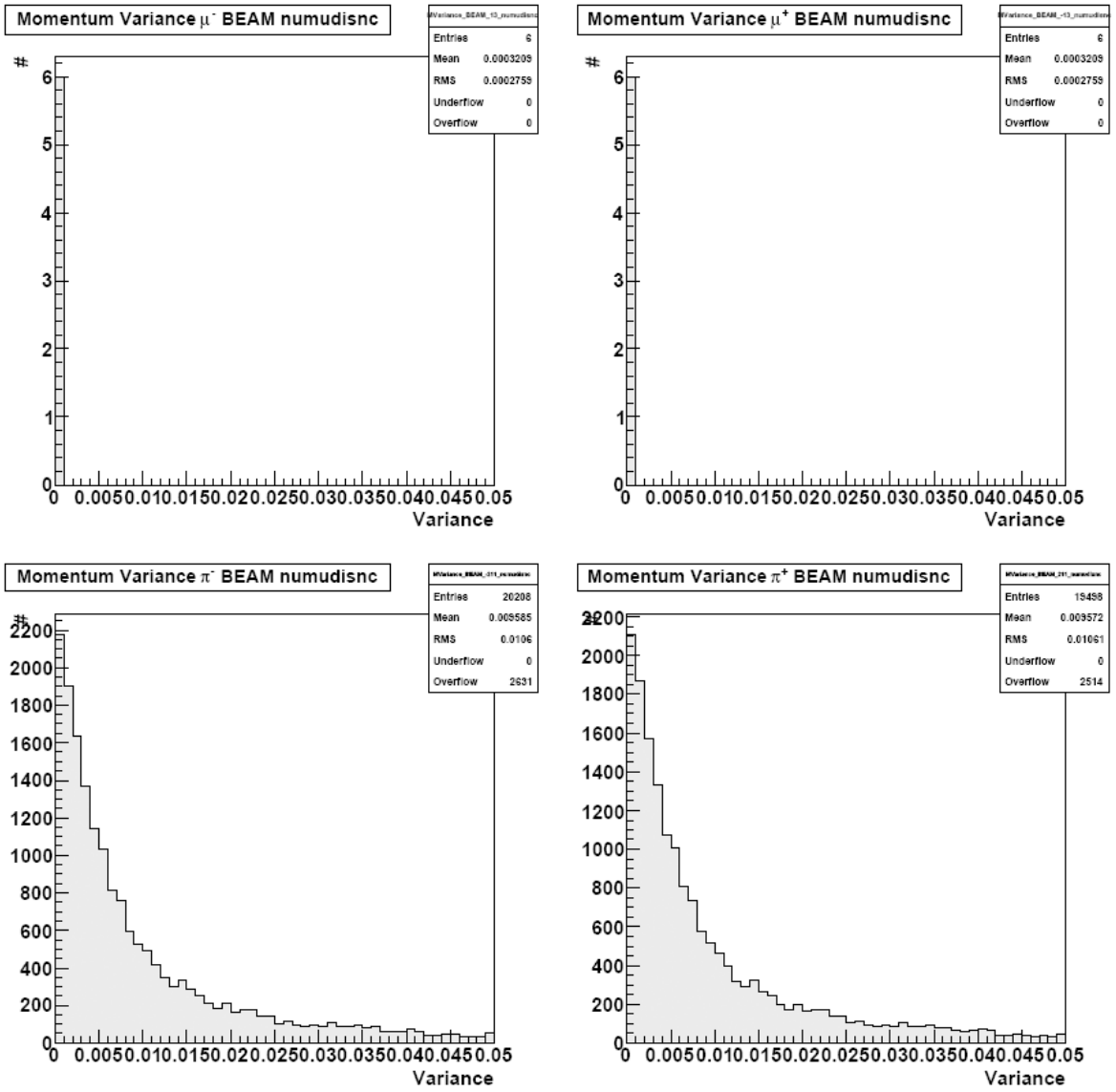

Figure A.32: Beam ν_μ DIS NC reactions reconstructed momentum variance. **Top left:** μ^-, **top right:** μ^+, **bottom left:** π^-, **bottom right:** π^+.

ν_μ RES CC Reactions

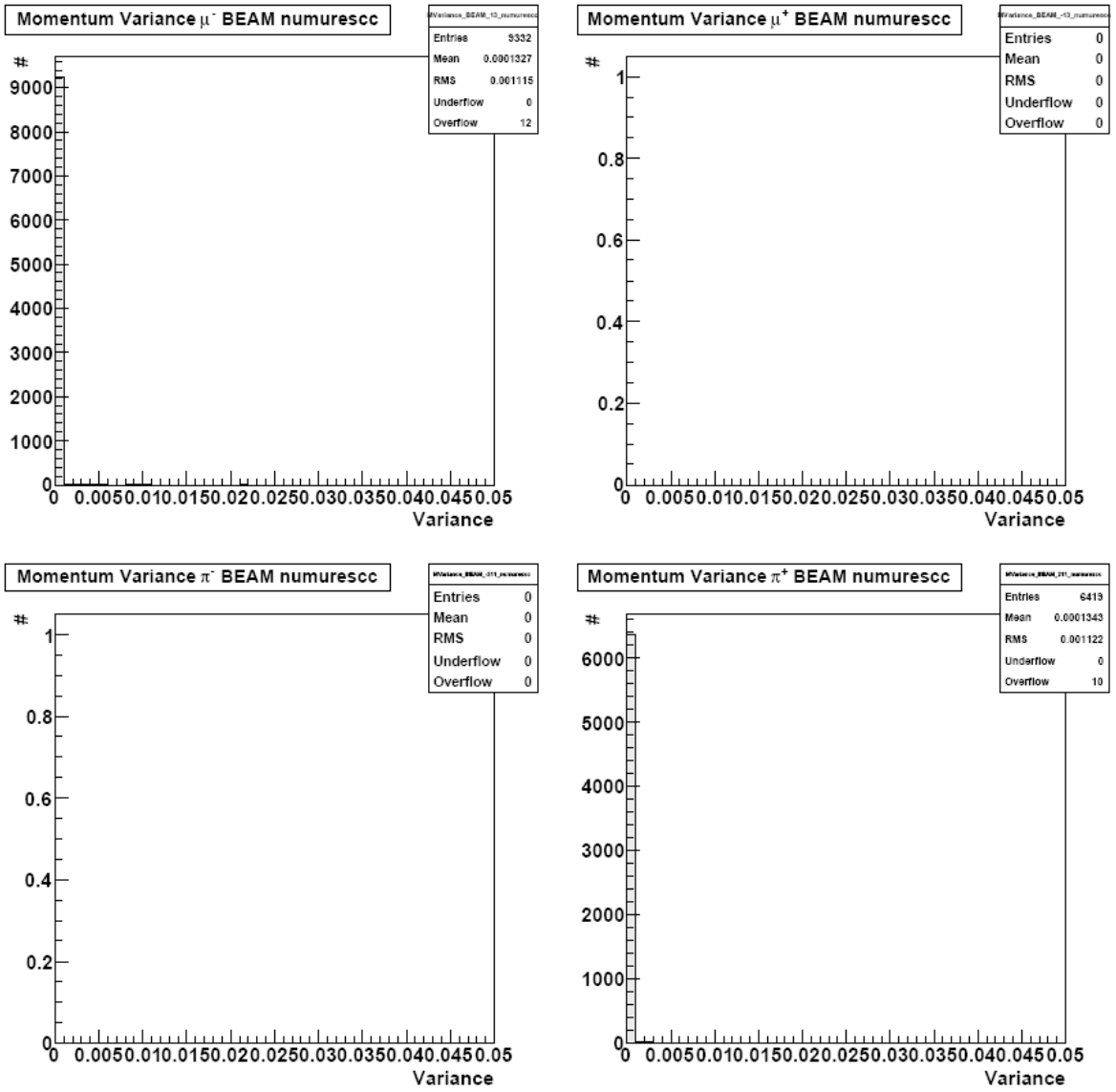

Figure A.33: Beam ν_μ RES CC reactions reconstructed momentum variance. **Top left:** μ^-, **top right:** μ^+, **bottom left:** π^-, **bottom right:** π^+.

ν_μ RES NC Reactions

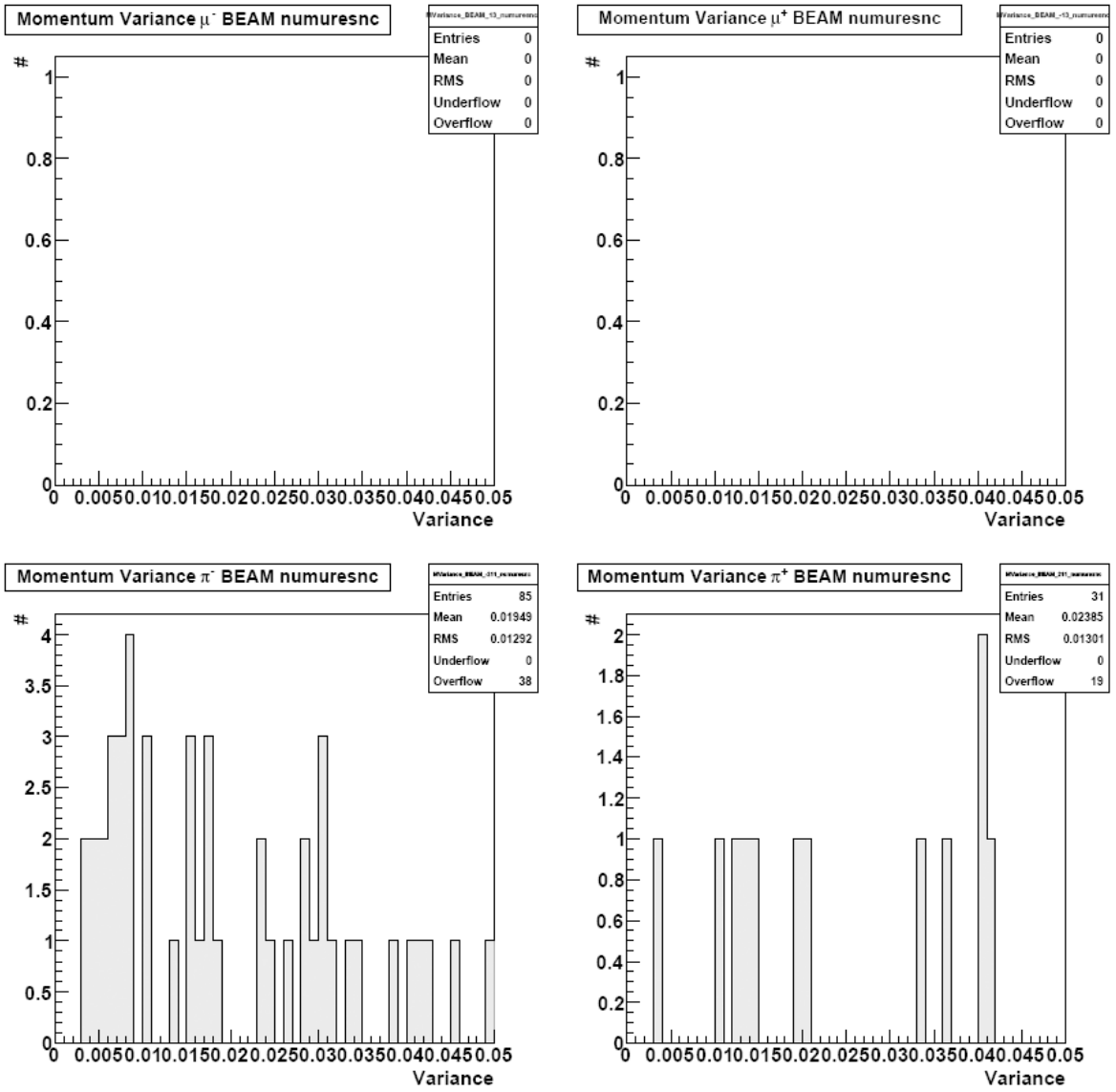

Figure A.34: Beam ν_μ RES NC reactions reconstructed momentum variance. **Top left:** μ^-, **top right:** μ^+, **bottom left:** π^-, **bottom right:** π^+.

ν_μ QEL CC Reactions

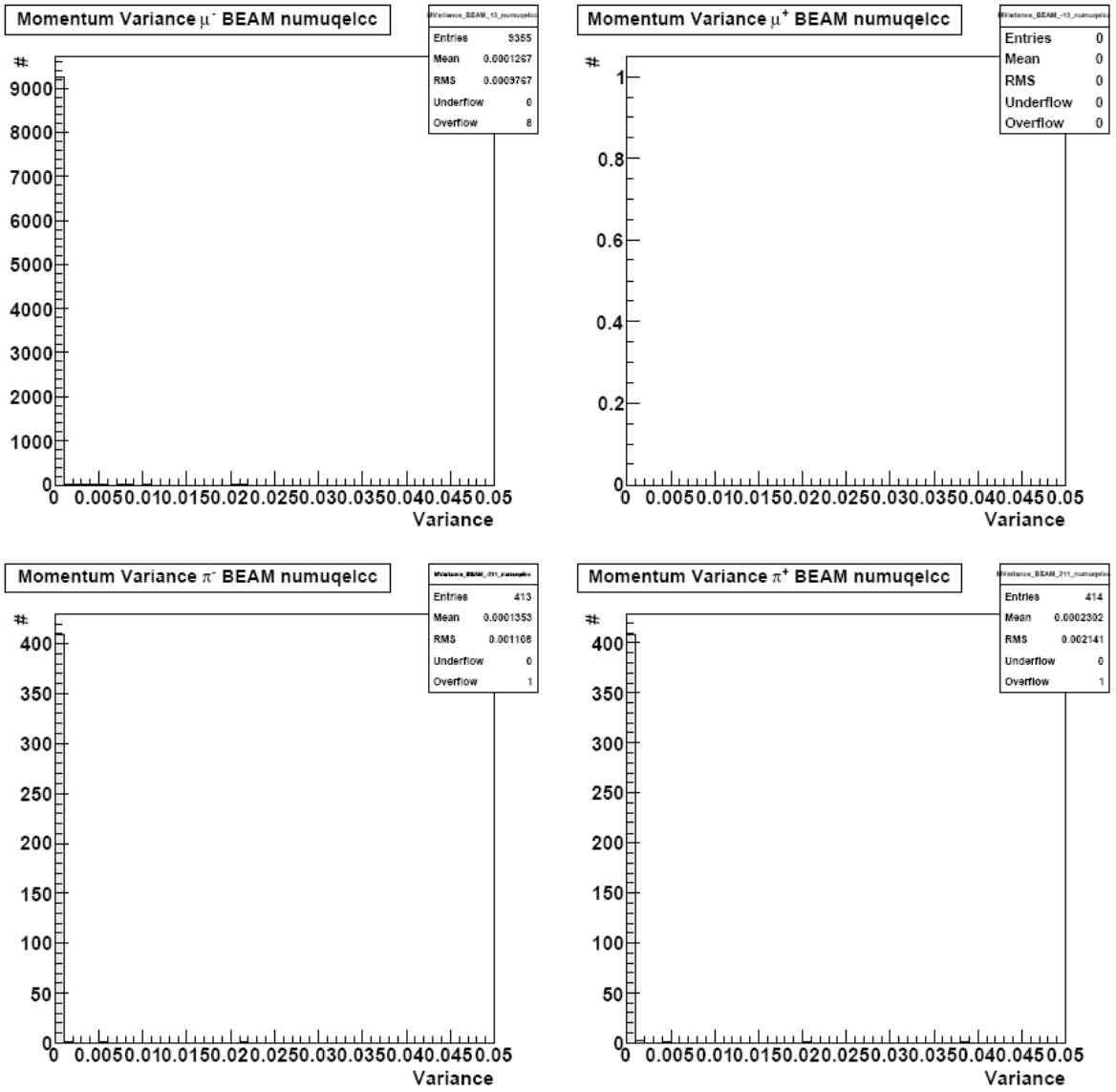

Figure A.35: Beam ν_μ QEL CC reactions reconstructed momentum variance. **Top left:** μ^-, **top right:** μ^+, **bottom left:** π^-, **bottom right:** π^+.

A.2.7 Reconstructed TSCIN Energy

ν_μ DIS CC Reactions

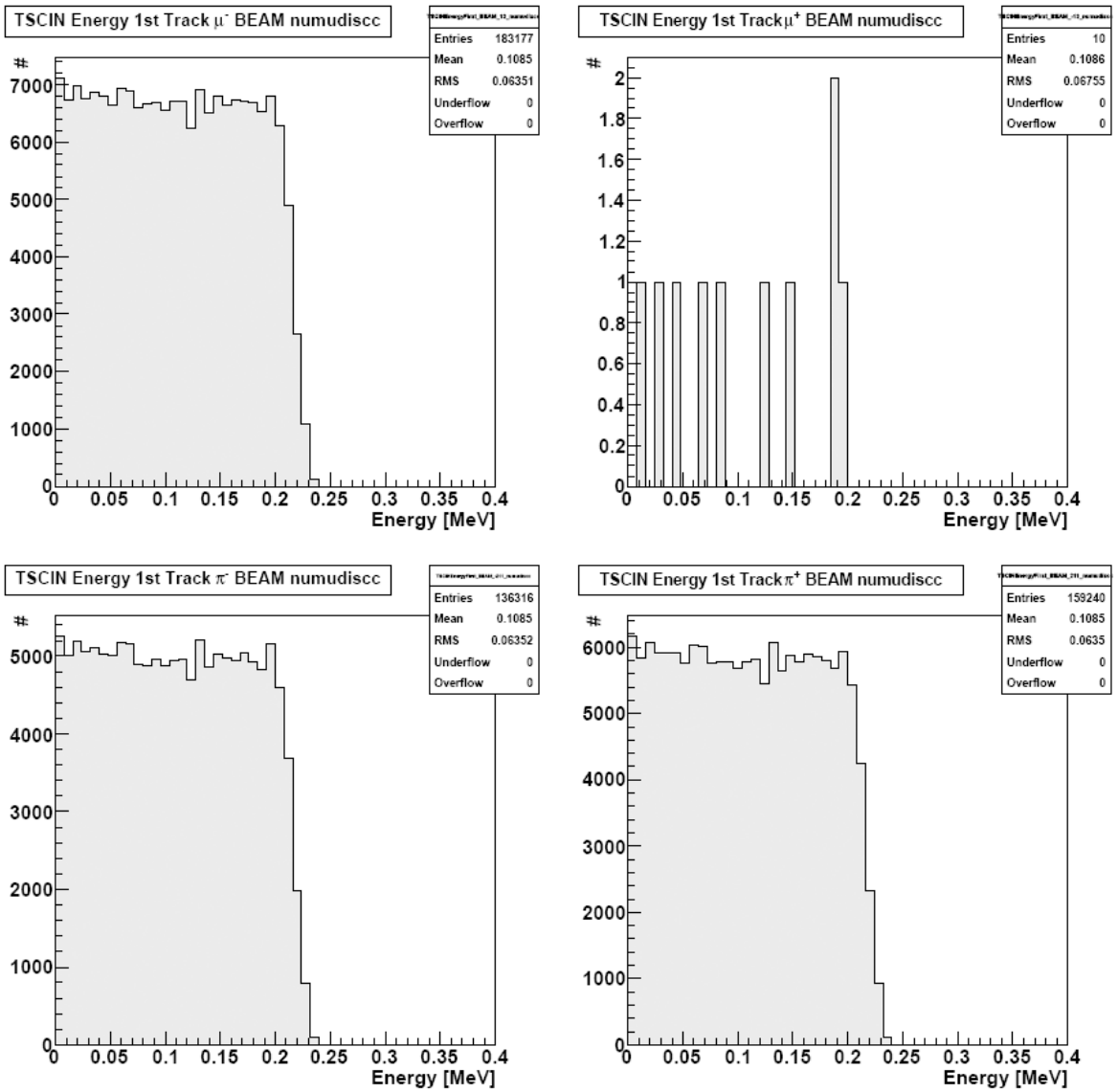

Figure A.36: Beam ν_μ DIS CC reactions reconstructed TSCIN energy. **Top left:** μ^-, **top right:** μ^+, **bottom left:** π^-, **bottom right:** π^+.

ν_μ DIS NC Reactions

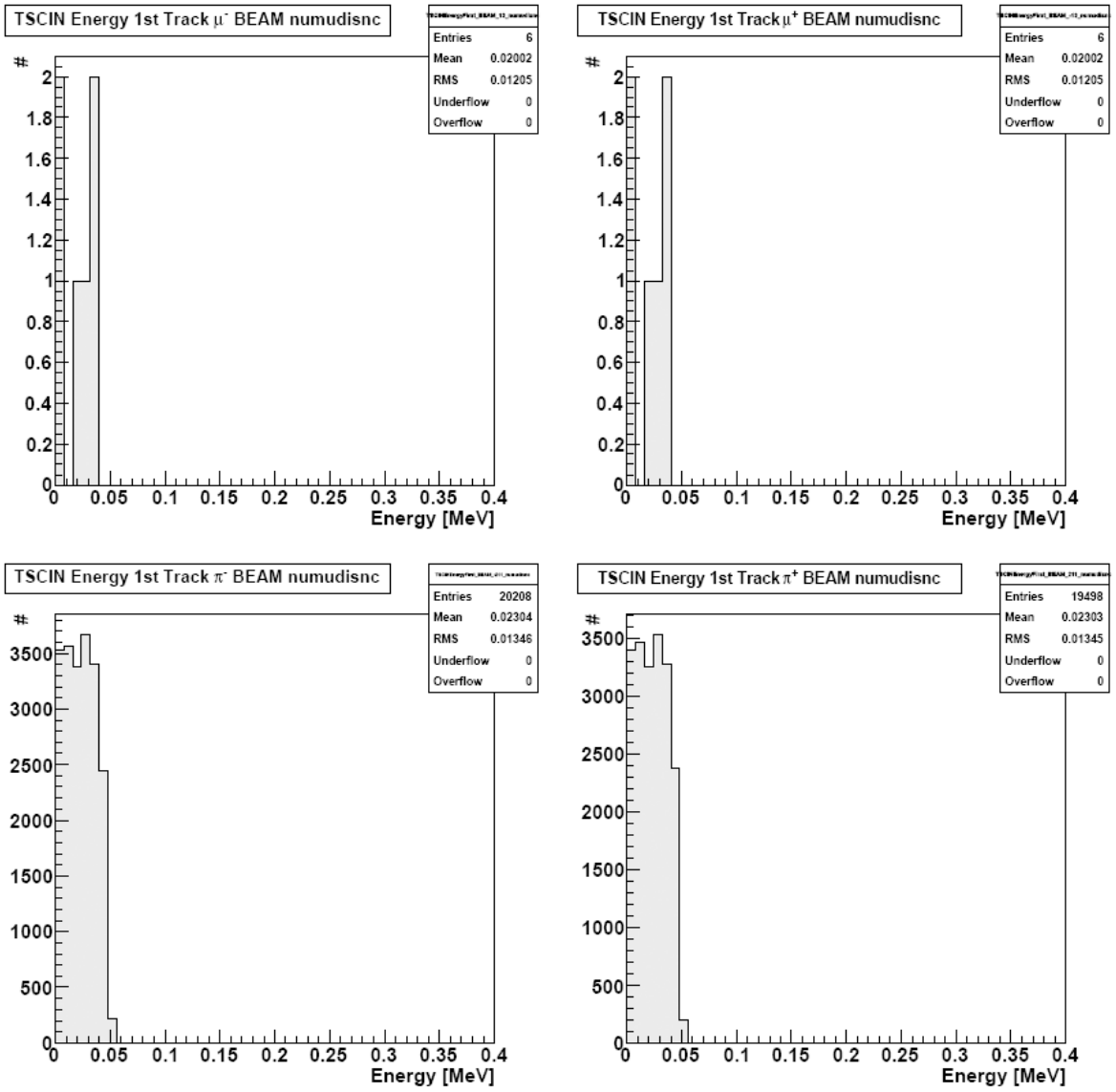

Figure A.37: Beam ν_μ DIS NC reactions reconstructed TSCIN energy. **Top left:** μ^-, **top right:** μ^+, **bottom left:** π^-, **bottom right:** π^+.

ν_μ RES CC Reactions

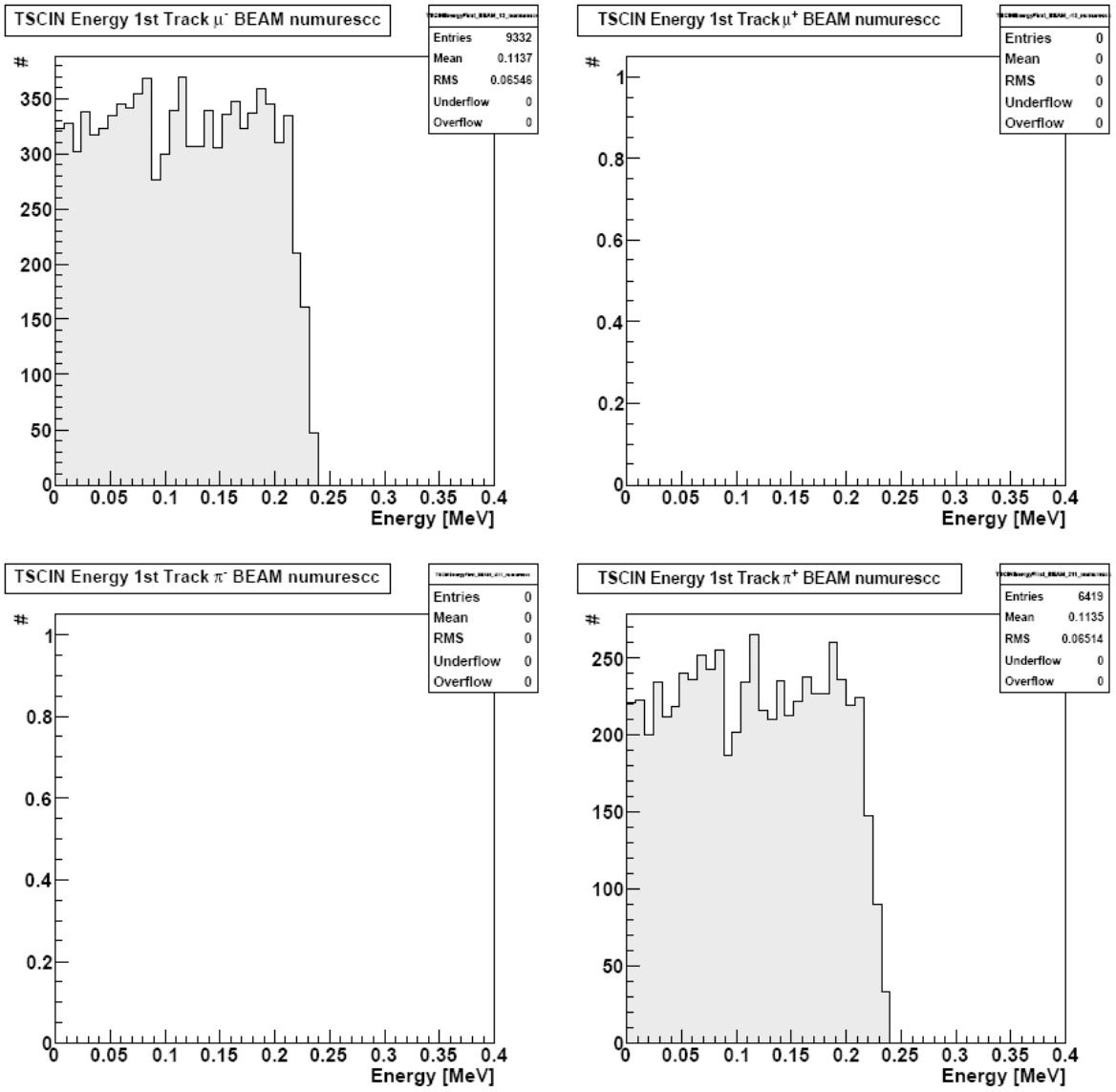

Figure A.38: Beam ν_μ RES CC reactions reconstructed TSCIN energy. **Top left:** μ^-, **top right:** μ^+, **bottom left:** π^-, **bottom right:** π^+.

ν_μ RES NC Reactions

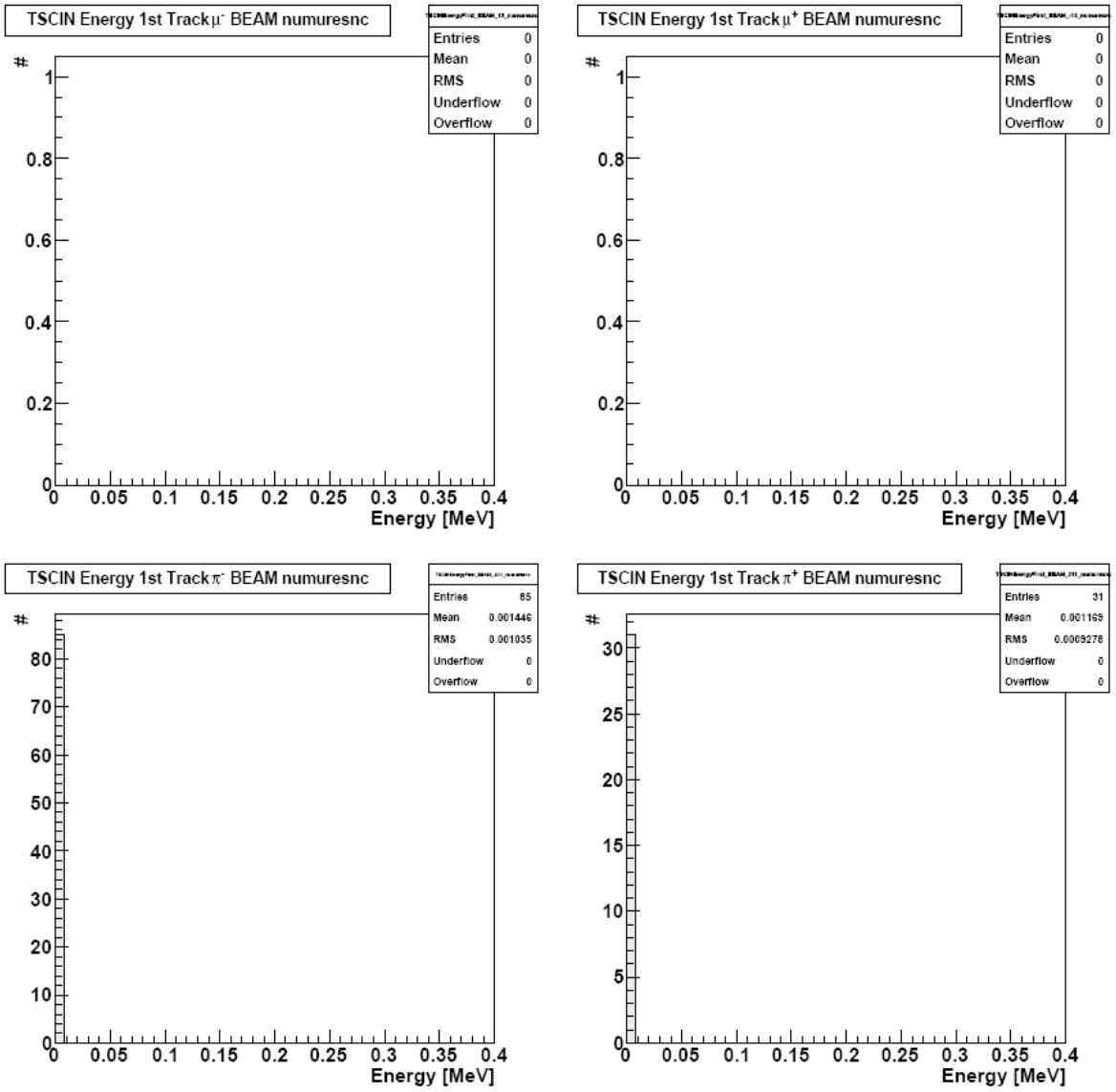

Figure A.39: Beam ν_μ RES NC reactions reconstructed TSCIN energy. **Top left:** μ^-, **top right:** μ^+, **bottom left:** π^-, **bottom right:** π^+.

ν_μ QEL CC Reactions

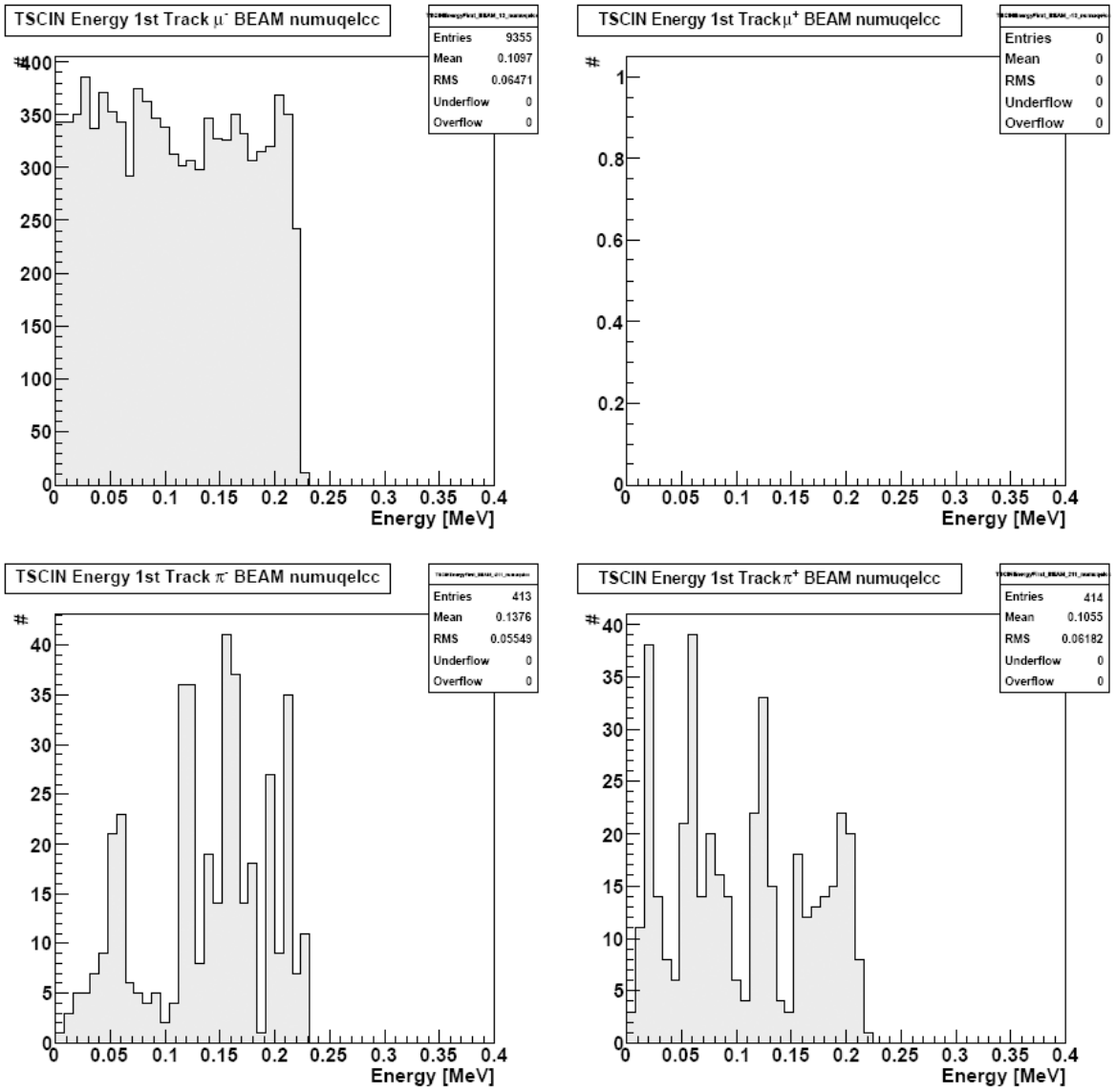

Figure A.40: Beam ν_μ QEL CC reactions reconstructed TSCIN energy. **Top left:** μ^-, **top right:** μ^+, **bottom left:** π^-, **bottom right:** π^+.

A.2.8 Reconstructed TSCIN Energy vs Track Length

All ν_μ Reactions

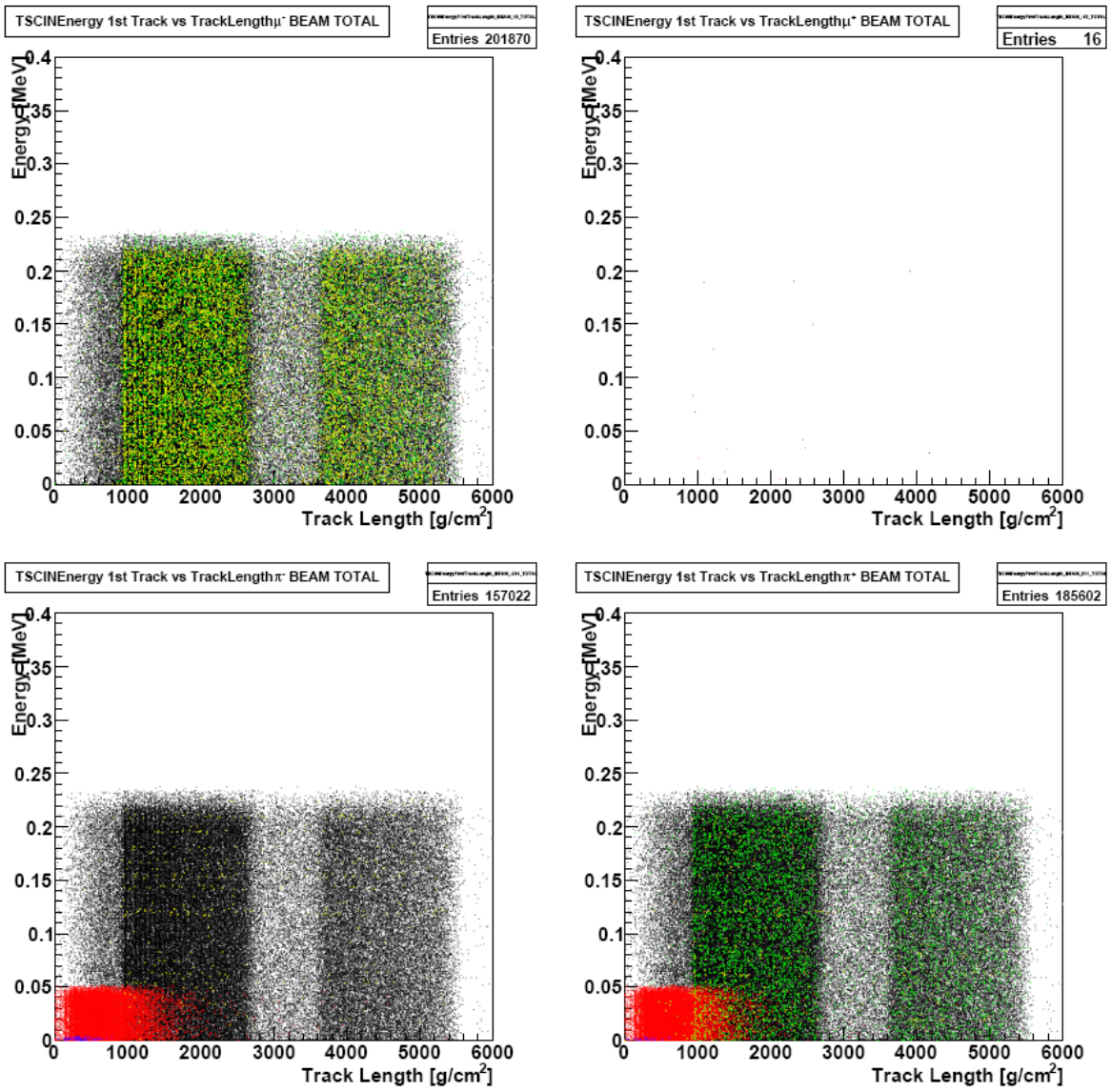

Figure A.41: Beam ν_μ reconstructed TSCIN energy vs track length. **Top left:** μ^-, **top right:** μ^+, **bottom left:** π^-, **bottom right:** π^+. **Black:** ν_μ DIS CC interactions, **red:** ν_μ DIS NC interactions, **green:** ν_μ RES CC interactions, **blue:** ν_μ RES NC interactions, **yellow:** ν_μ QEL CC interactions.

ν_μ DIS CC Reactions

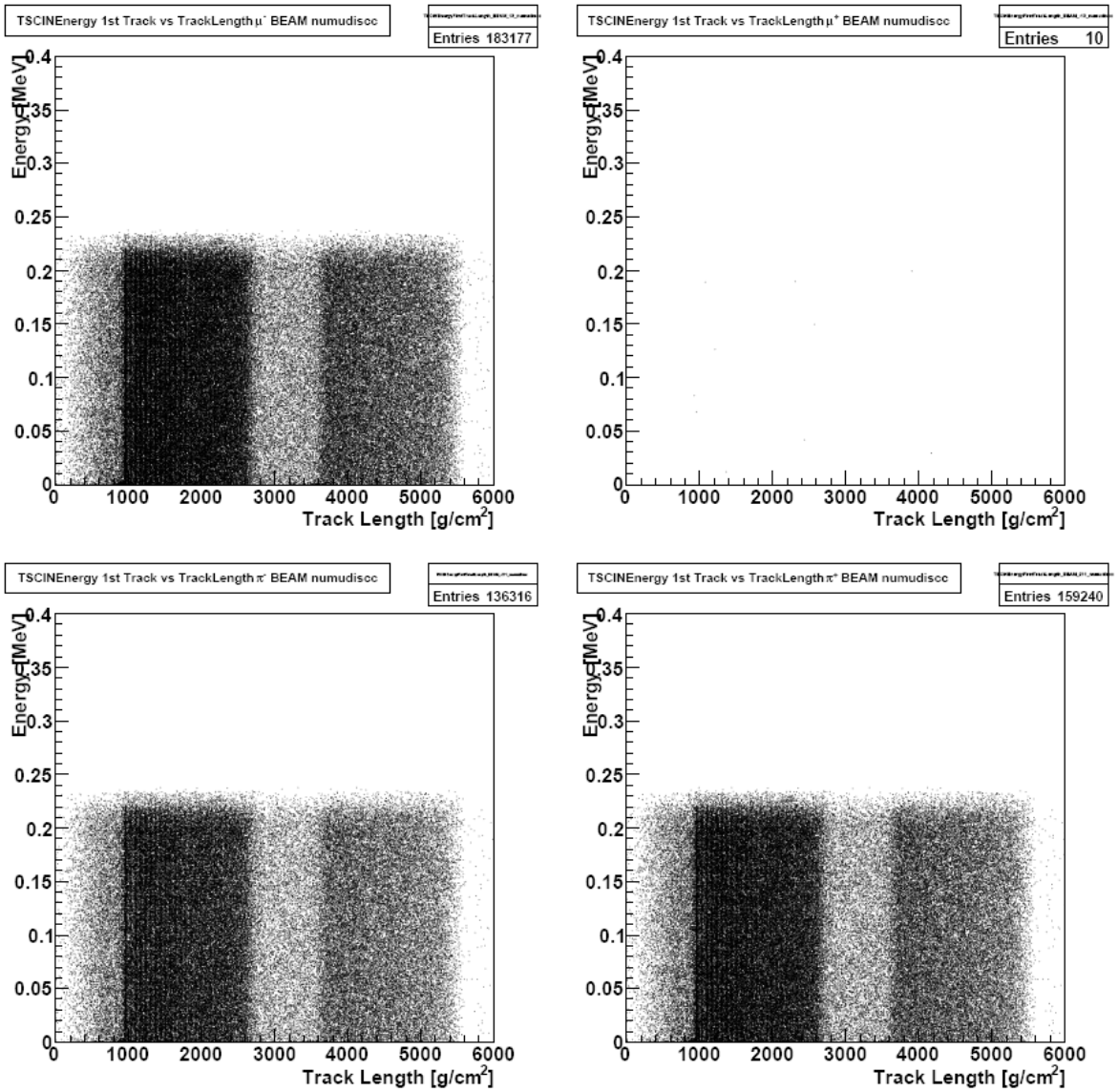

Figure A.42: Beam ν_μ DIS CC reactions reconstructed TSCIN energy vs track length. **Top left:** μ^-, **top right:** μ^+, **bottom left:** π^-, **bottom right:** π^+.

ν_μ DIS NC Reactions

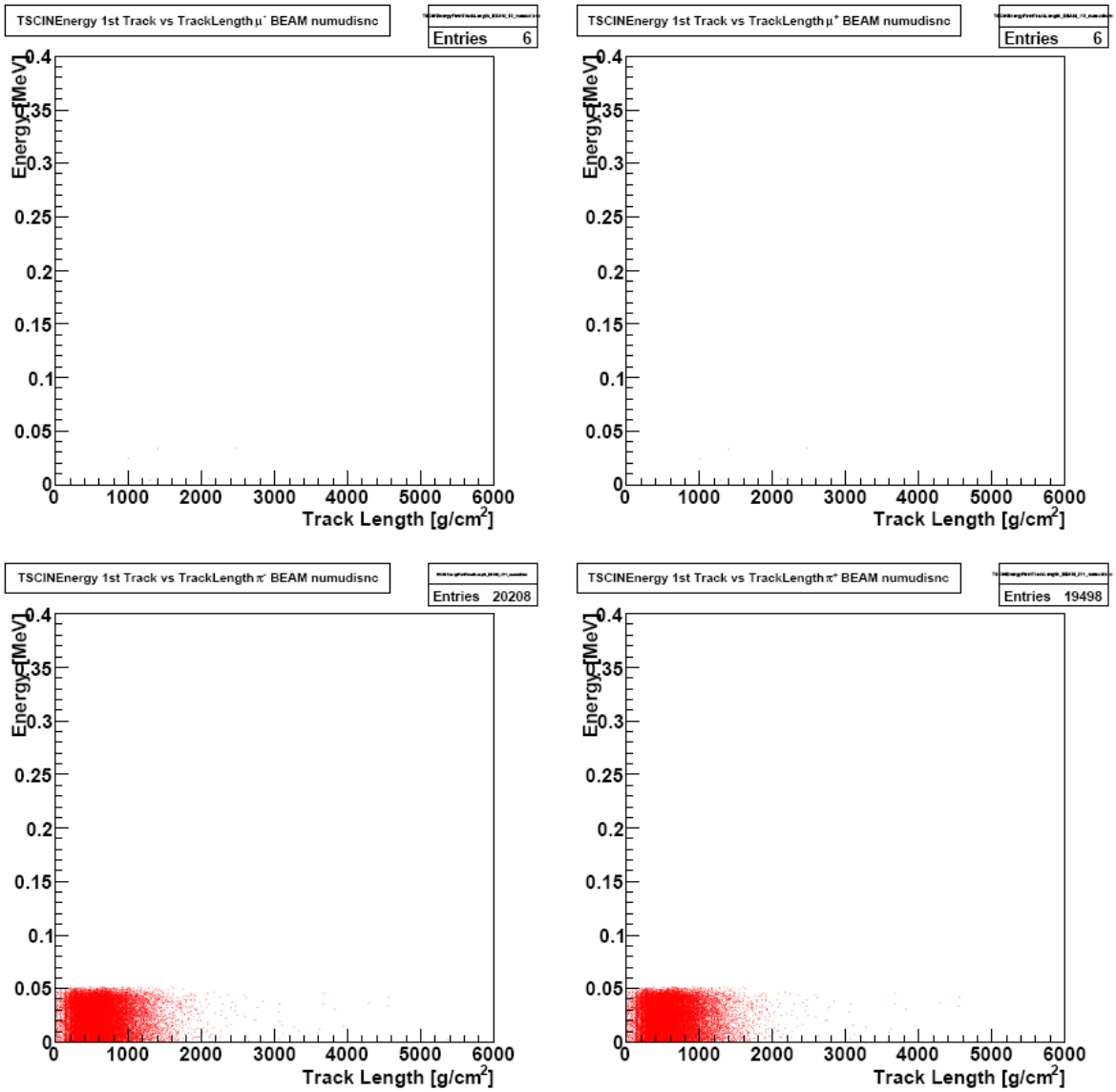

Figure A.43: Beam ν_μ DIS NC reactions reconstructed TSCIN energy vs track length. **Top left:** μ^-, **top right:** μ^+, **bottom left:** π^-, **bottom right:** π^+.

ν_μ RES CC Reactions

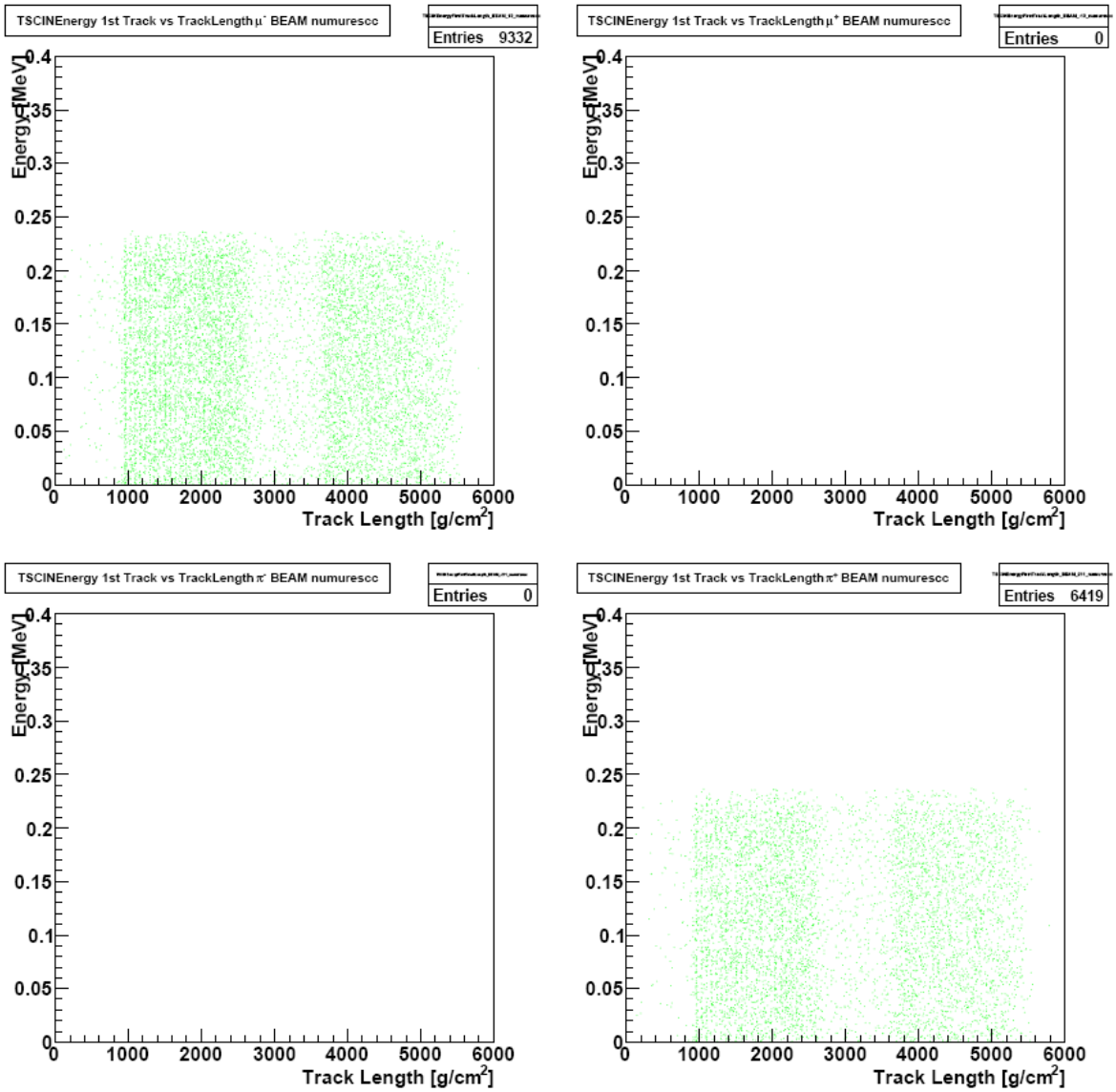

Figure A.44: Beam ν_μ RES CC reactions reconstructed TSCIN energy vs track length. **Top left:** μ^-, **top right:** μ^+, **bottom left:** π^-, **bottom right:** π^+.

ν_μ RES NC Reactions

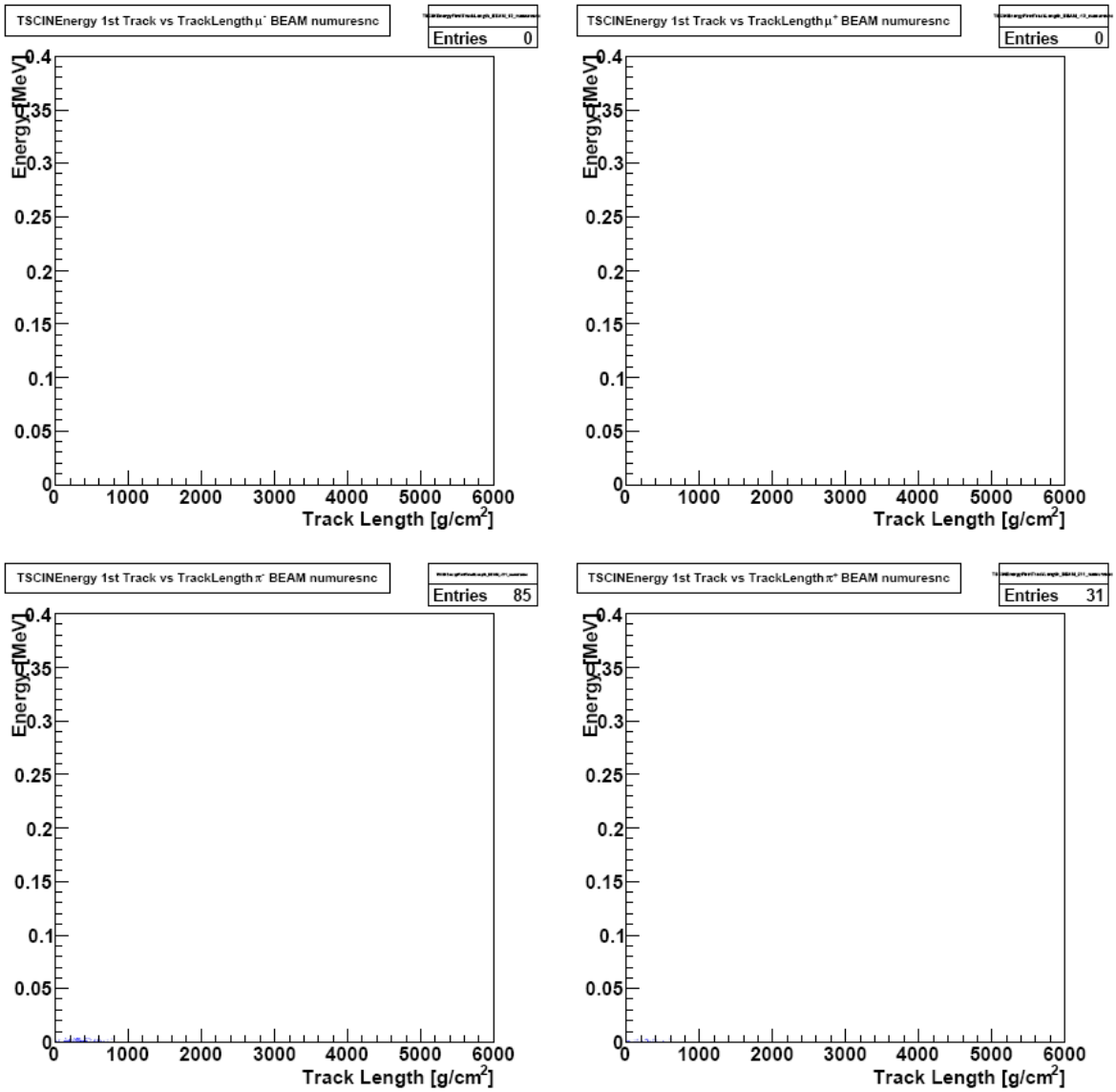

Figure A.45: Beam ν_μ RES NC reactions reconstructed TSCIN energy vs track length. **Top left:** μ^-, **top right:** μ^+, **bottom left:** π^-, **bottom right:** π^+.

ν_μ QEL CC Reactions

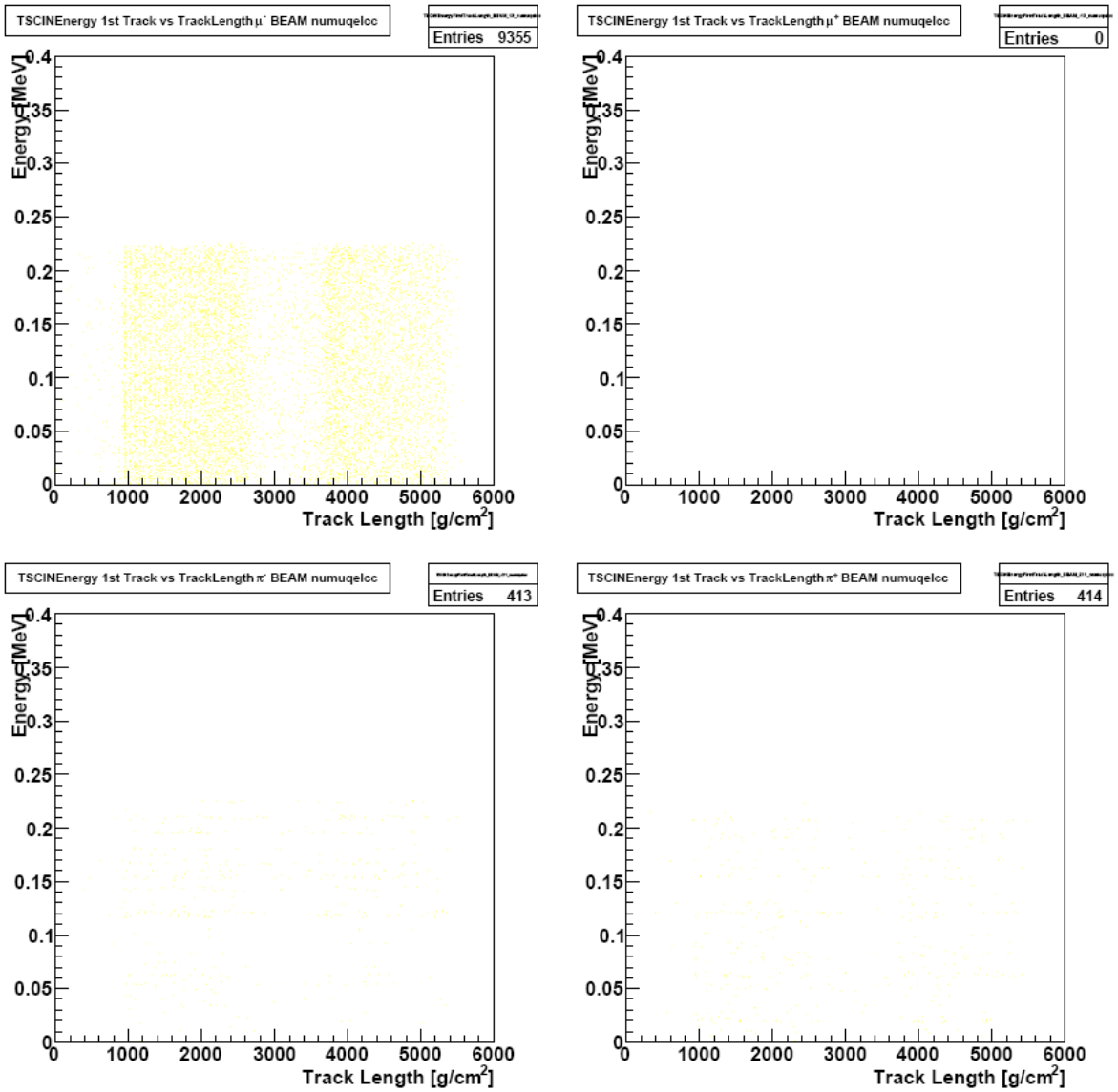

Figure A.46: Beam ν_μ QEL CC reactions reconstructed TSCIN energy vs track length. **Top left:** μ^-, **top right:** μ^+, **bottom left:** π^-, **bottom right:** π^+.

A.2.9 Reconstructed TSCIN Energy vs Momentum

All ν_μ Reactions

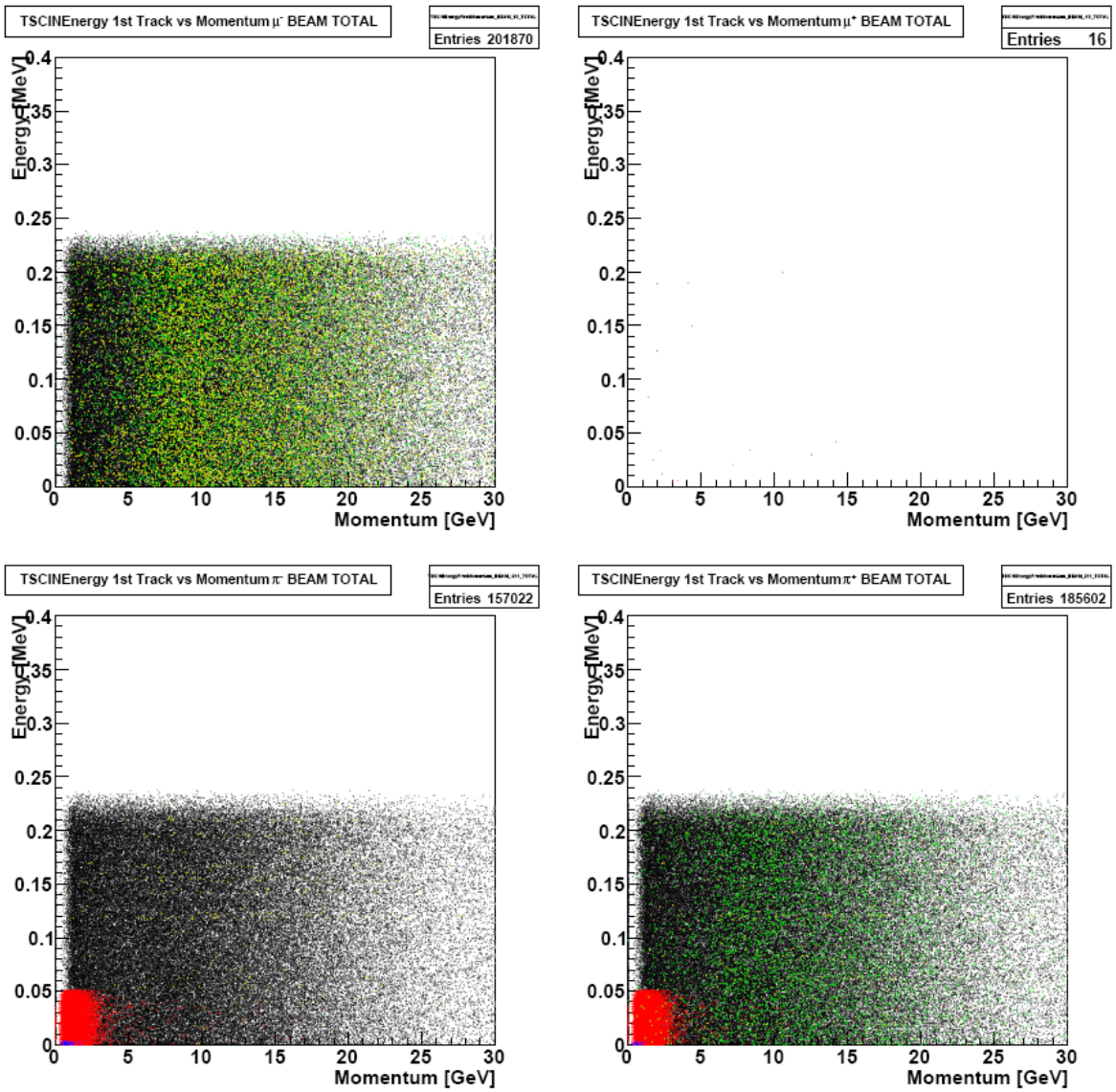

Figure A.47: Beam ν_μ reconstructed TSCIN energy vs momentum. **Top left:** μ^-, **top right:** μ^+, **bottom left:** π^-, **bottom right:** π^+. **Black:** ν_μ DIS CC interactions, **red:** ν_μ DIS NC interactions, **green:** ν_μ RES CC interactions, **blue:** ν_μ RES NC interactions, **yellow:** ν_μ QEL CC interactions.

ν_μ DIS CC Reactions

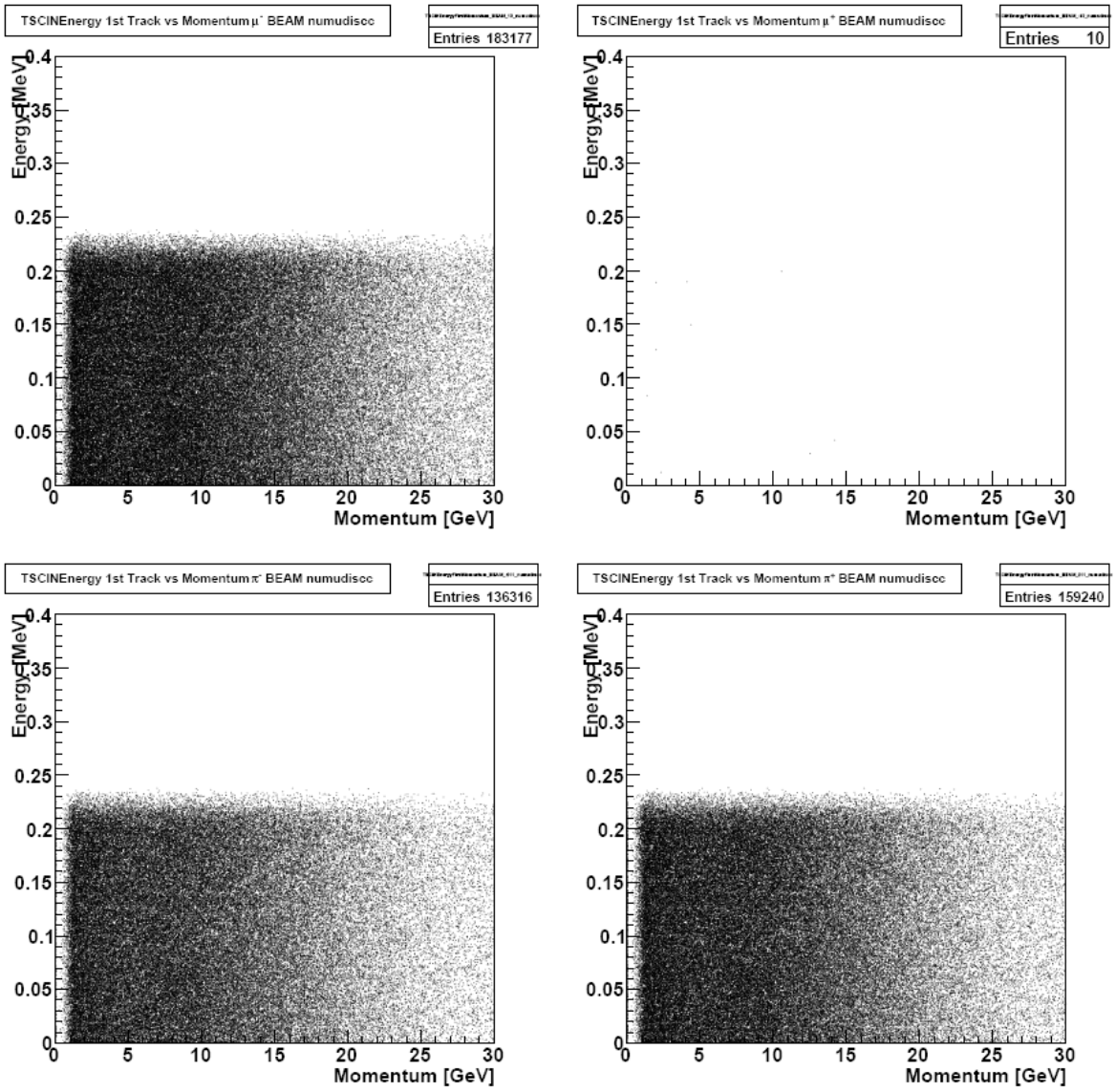

Figure A.48: Beam ν_μ DIS CC reactions reconstructed TSCIN energy vs momentum. **Top left:** μ^-, **top right:** μ^+, **bottom left:** π^-, **bottom right:** π^+.

ν_μ DIS NC Reactions

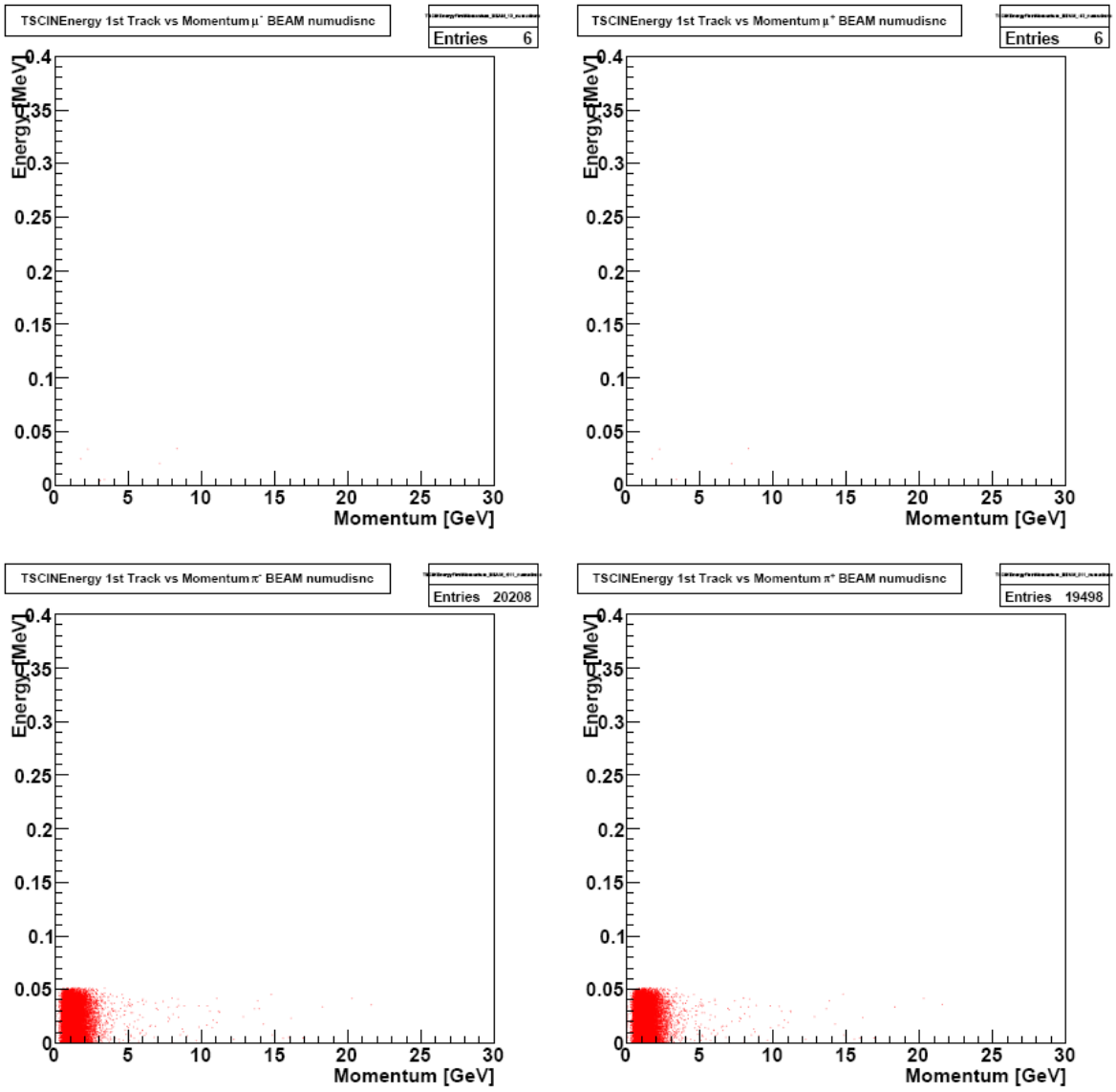

Figure A.49: Beam ν_μ DIS NC reactions reconstructed TSCIN energy vs momentum. **Top left:** μ^-, **top right:** μ^+, **bottom left:** π^-, **bottom right:** π^+.

ν_μ RES CC Reactions

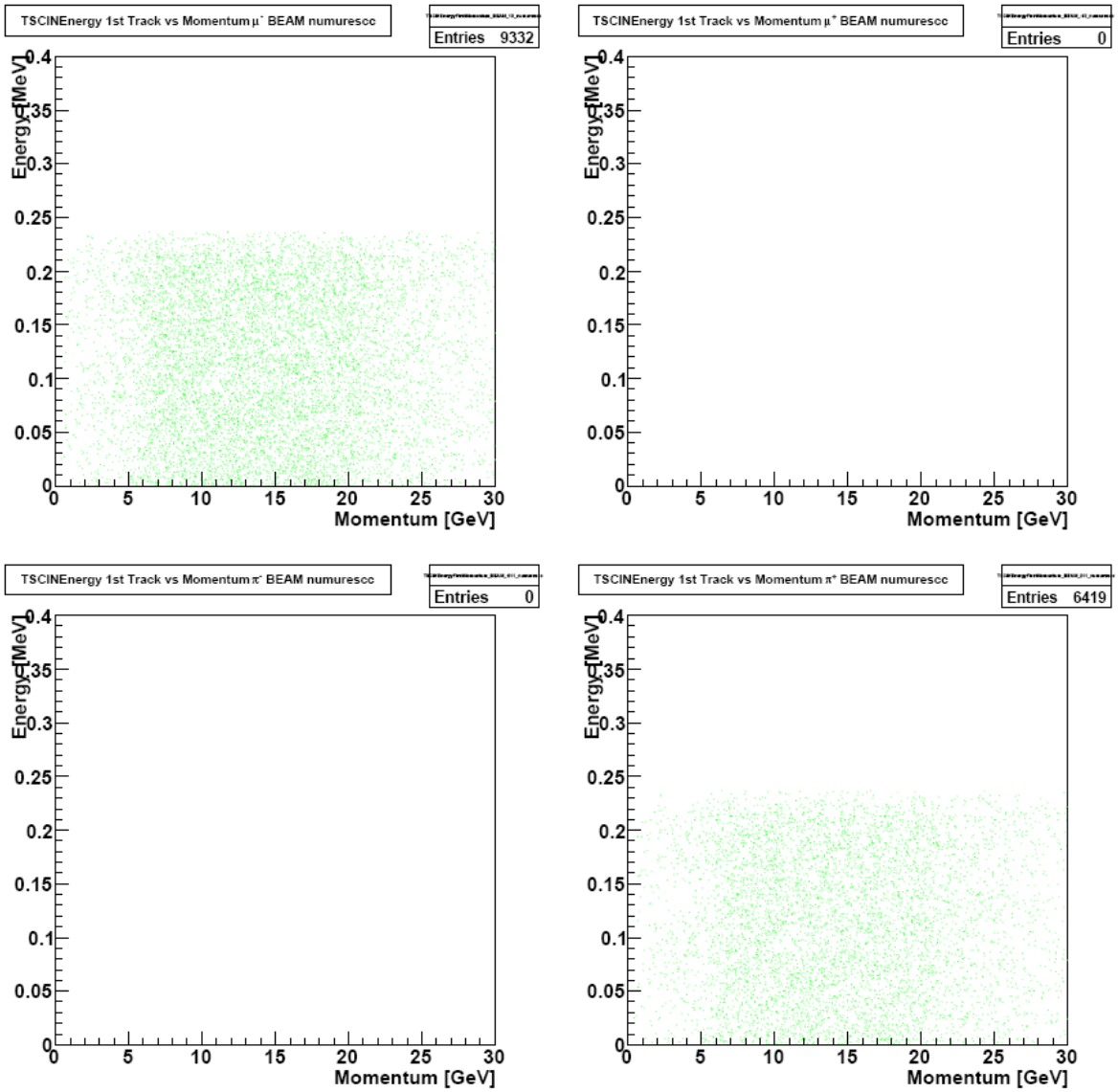

Figure A.50: Beam ν_μ RES CC reactions reconstructed TSCIN energy vs momentum. **Top left:** μ^-, **top right:** μ^+, **bottom left:** π^-, **bottom right:** π^+.

ν_μ RES NC Reactions

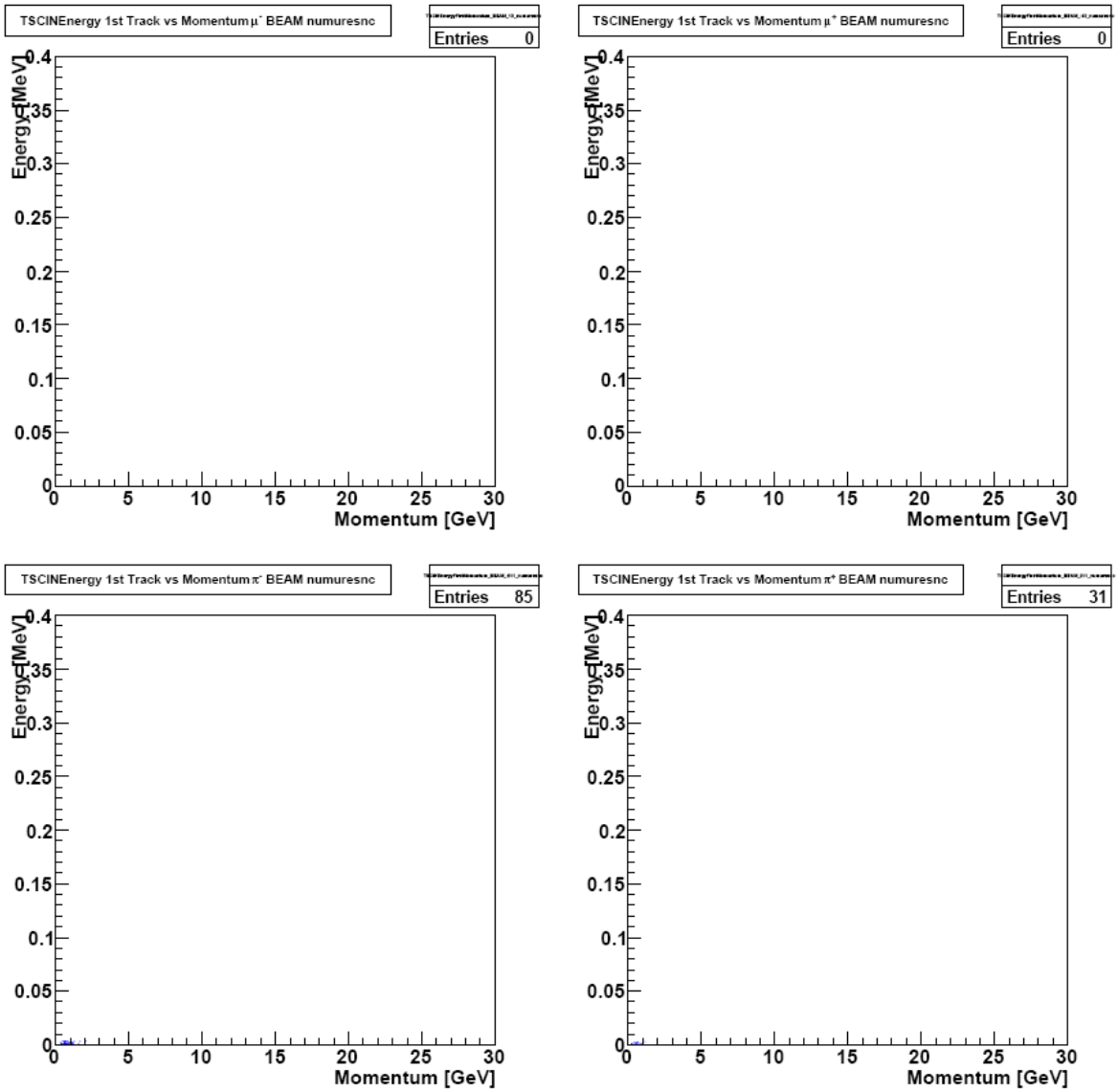

Figure A.51: Beam ν_μ RES NC reactions reconstructed TSCIN energy vs momentum. **Top left:** μ^-, **top right:** μ^+, **bottom left:** π^-, **bottom right:** π^+.

ν_μ QEL CC Reactions

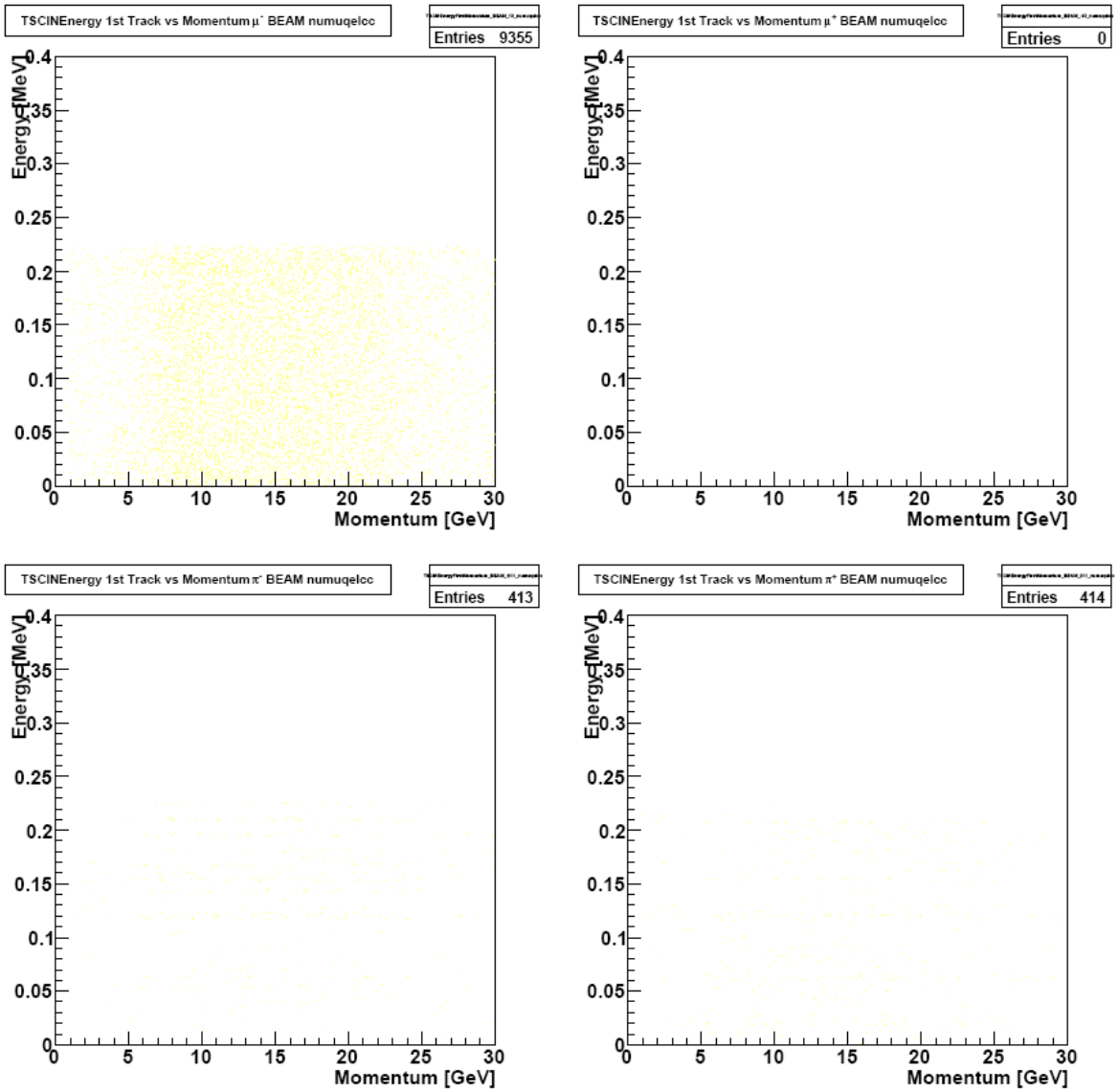

Figure A.52: Beam ν_μ QEL CC reactions reconstructed TSCIN energy vs momentum. **Top left:** μ^-, **top right:** μ^+, **bottom left:** π^-, **bottom right:** π^+.

A.2.10 Reconstructed Slope of 1st Track

All ν_μ Reactions

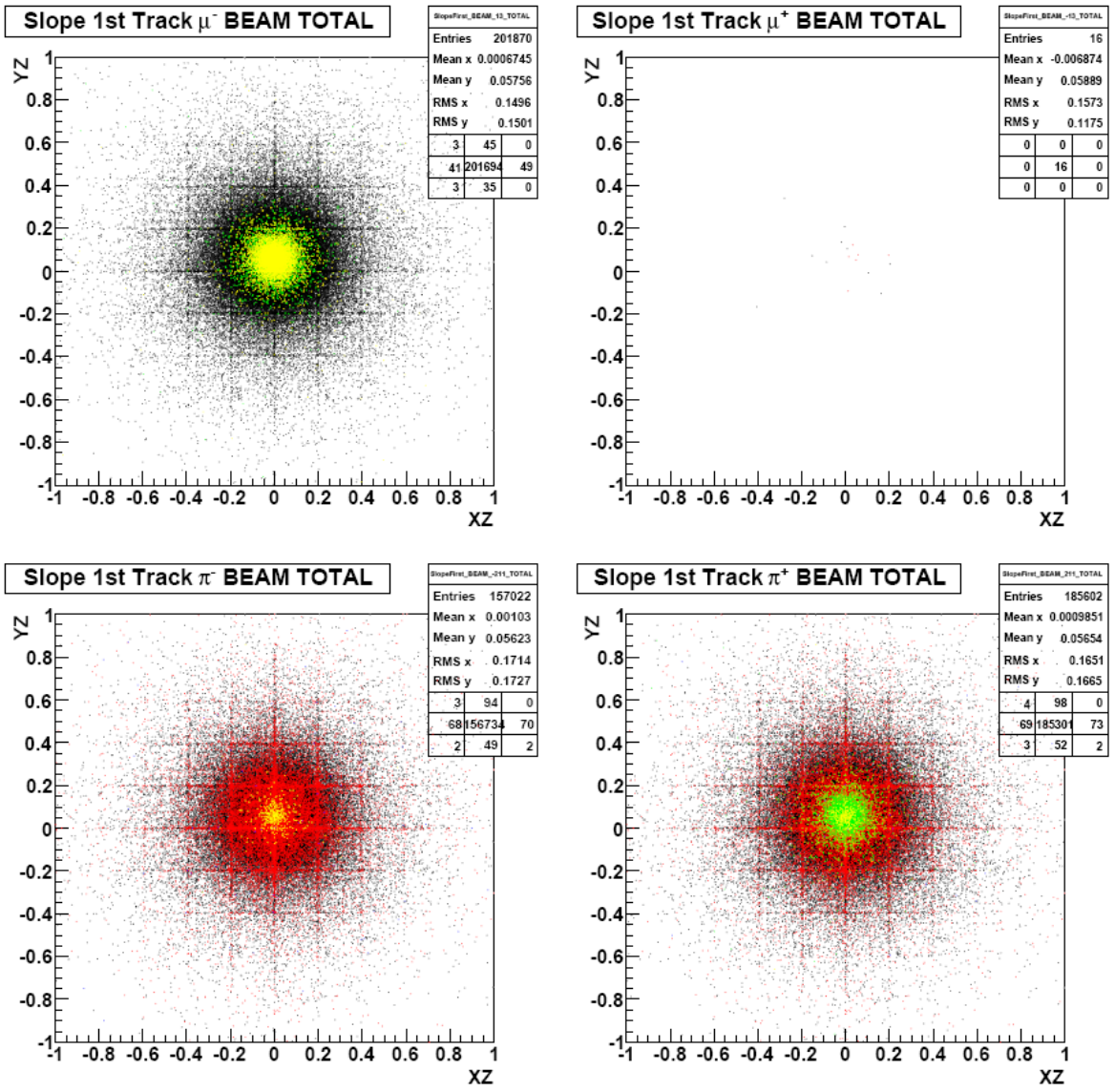

Figure A.53: Beam ν_μ reconstructed 1st track slope. **Top left:** μ^-, **top right:** μ^+, **bottom left:** π^-, **bottom right:** π^+.

ν_μ DIS CC Reactions

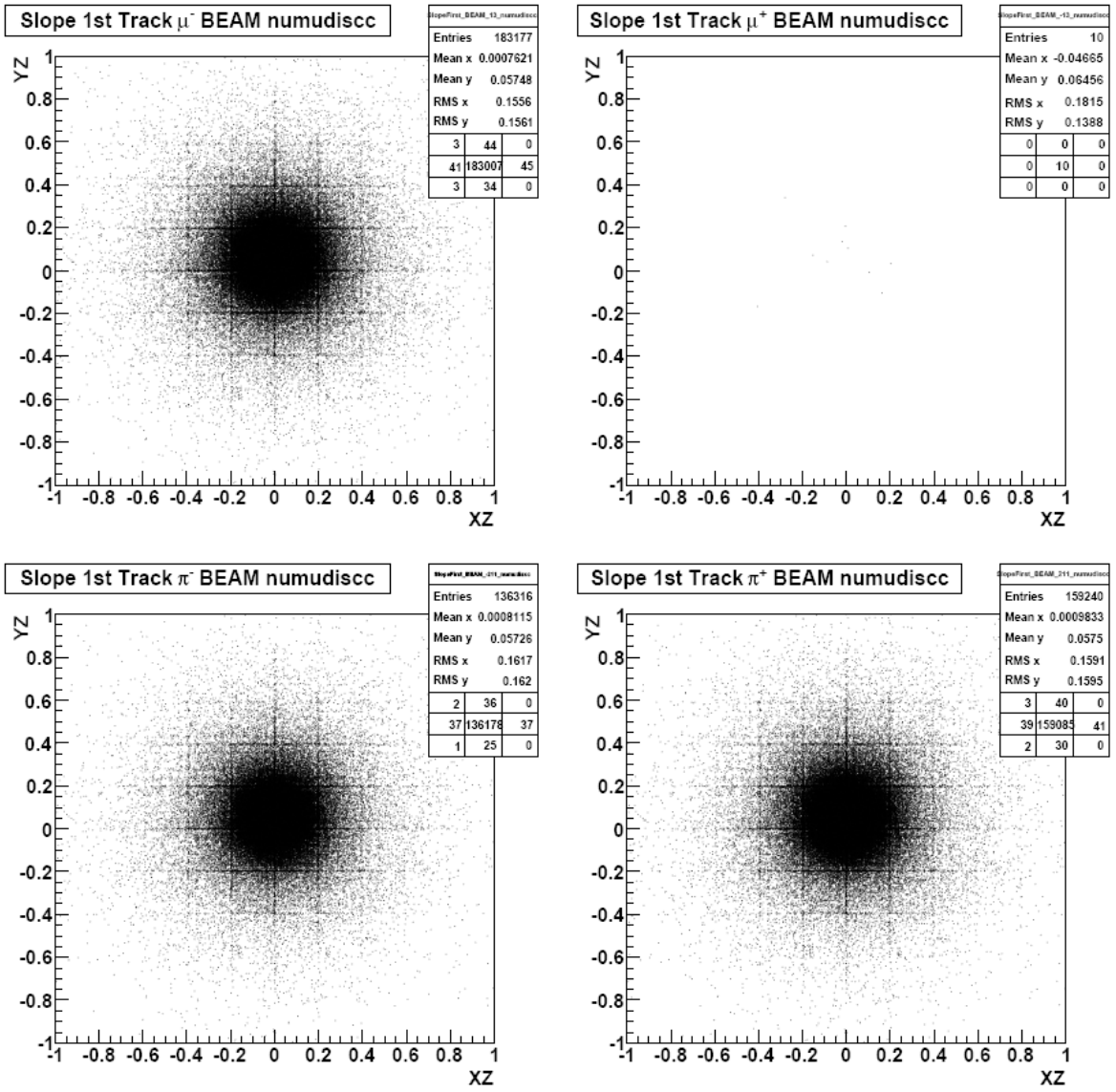

Figure A.54: Beam ν_μ DIS CC reactions reconstructed 1st track slope. **Top left:** μ^-, **top right:** μ^+, **bottom left:** π^-, **bottom right:** π^+.

ν_μ DIS NC Reactions

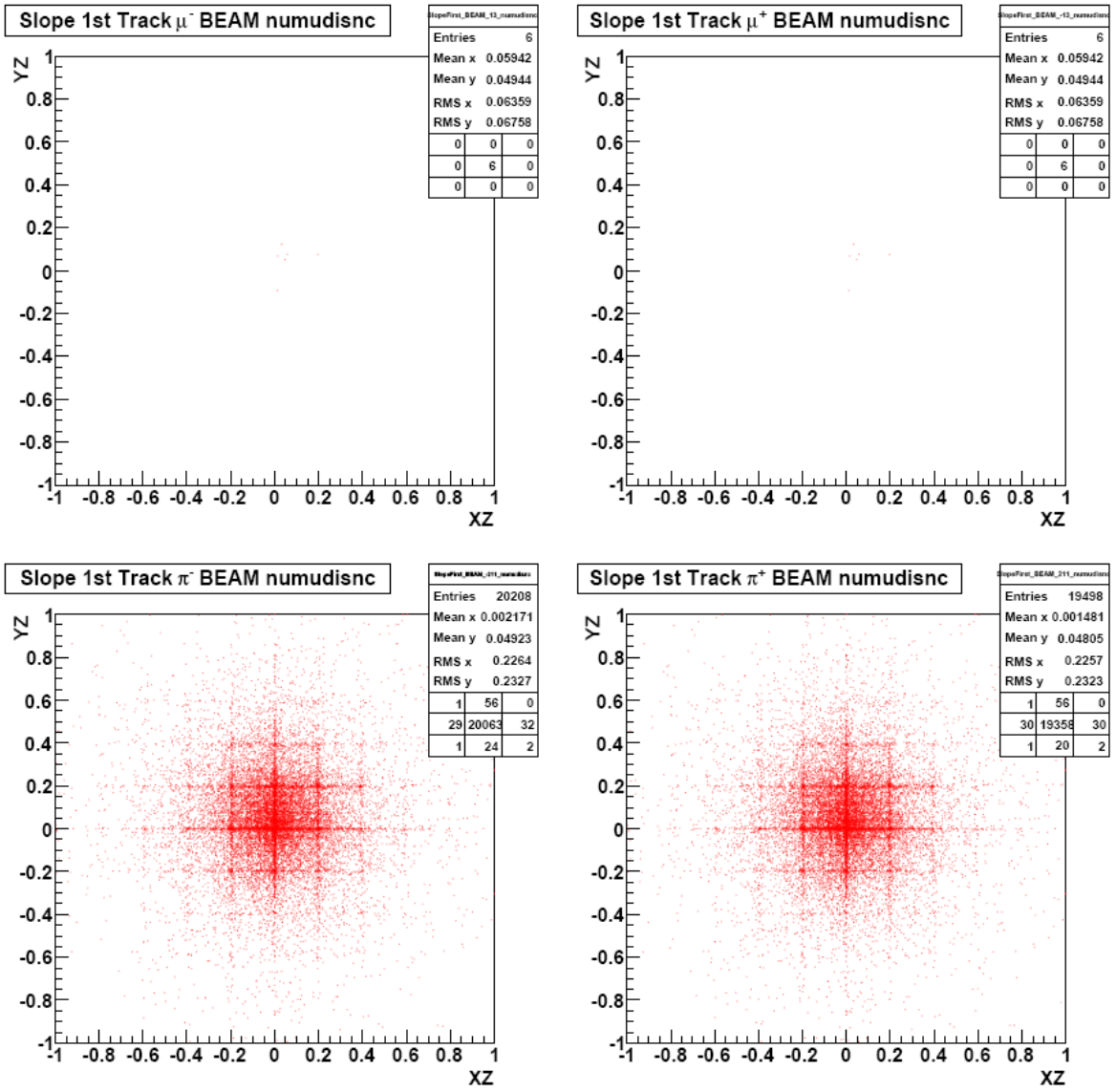

Figure A.55: Beam ν_μ DIS NC reactions reconstructed 1st track slope. **Top left:** μ^-, **top right:** μ^+, **bottom left:** π^-, **bottom right:** π^+.

ν_μ RES CC Reactions

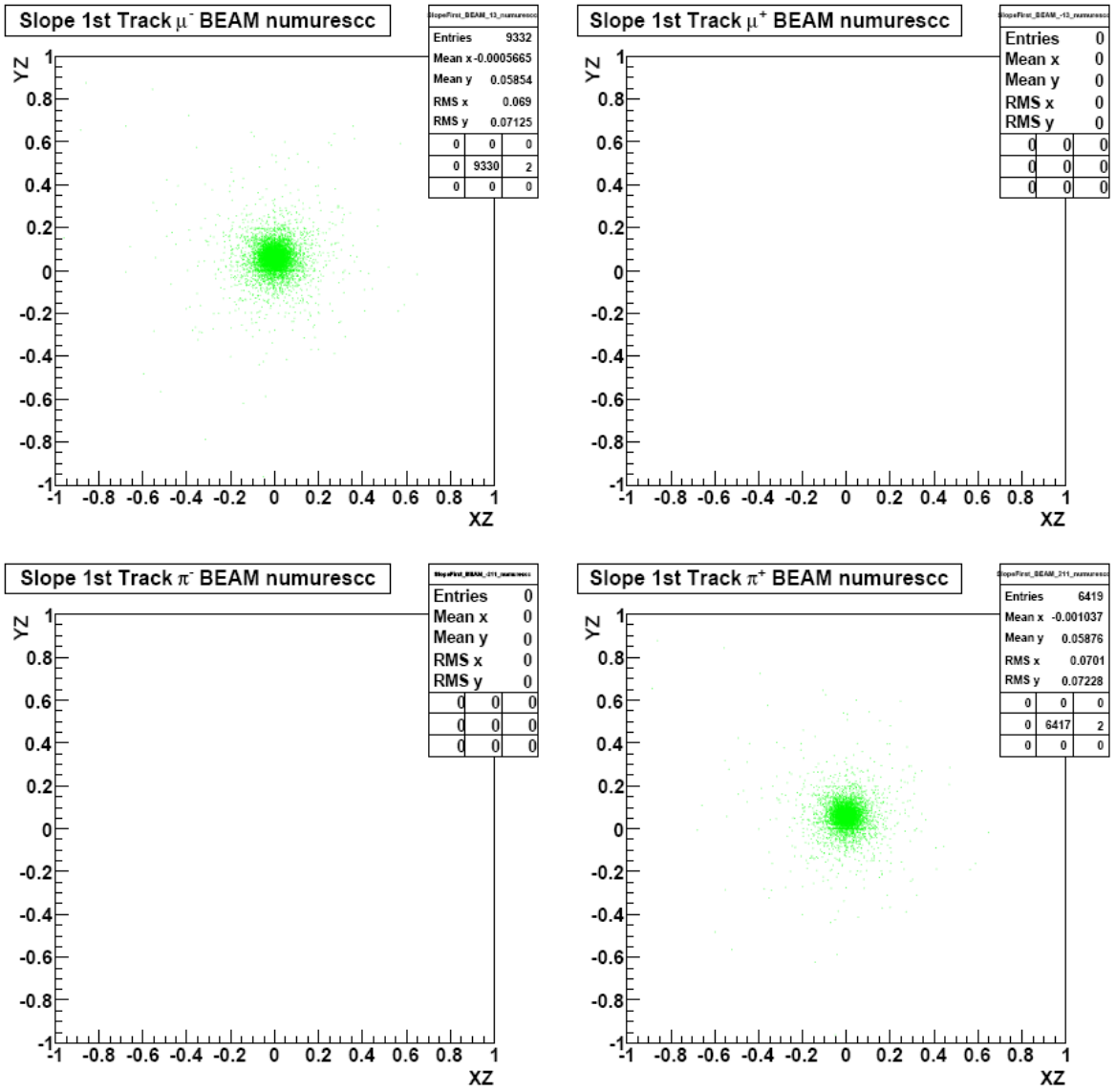

Figure A.56: Beam ν_μ RES CC reactions reconstructed 1st track slope. **Top left:** μ^-, **top right:** μ^+, **bottom left:** π^-, **bottom right:** π^+.

ν_μ RES NC Reactions

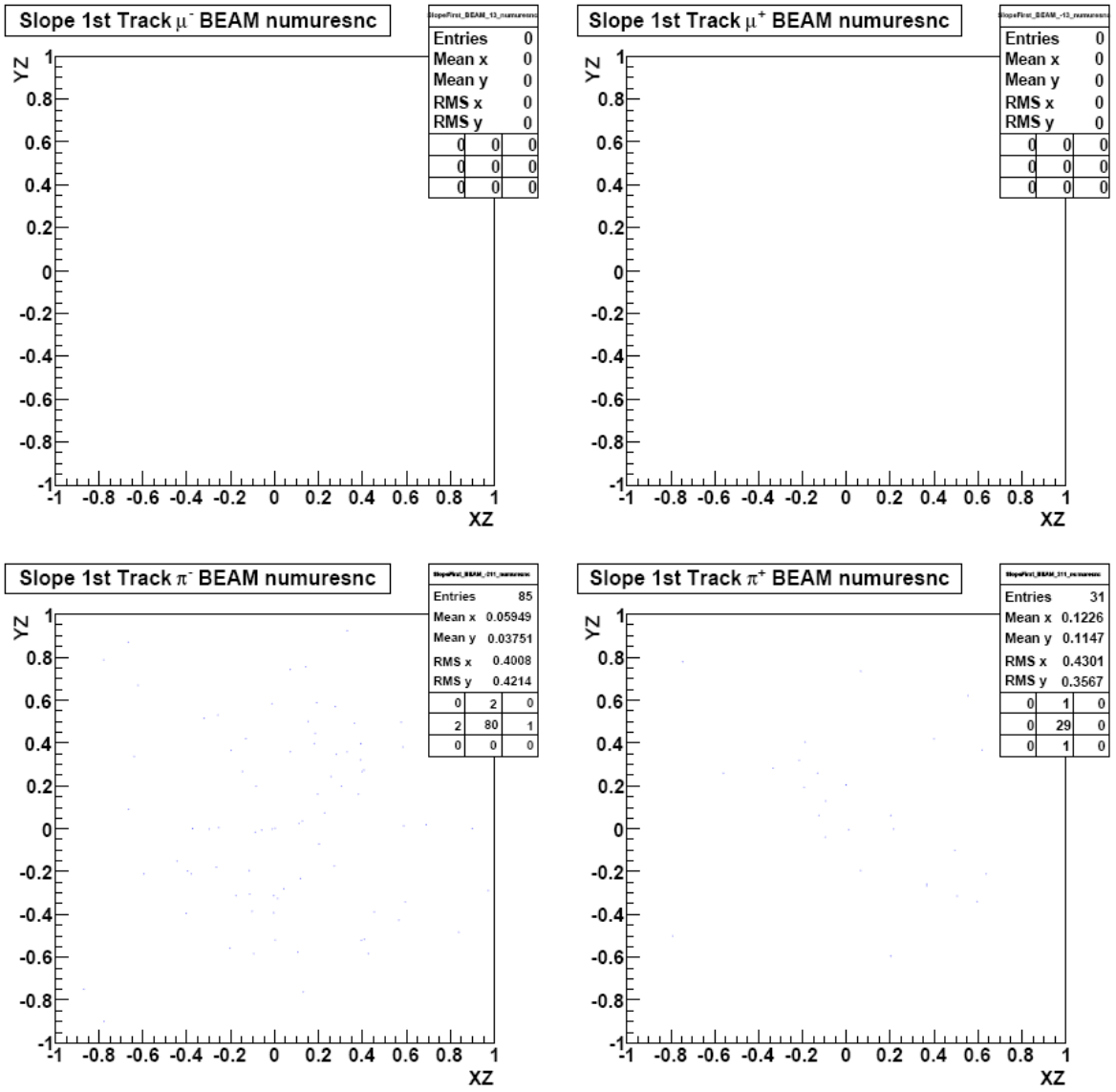

Figure A.57: Beam ν_μ RES NC reactions reconstructed 1st track slope. **Top left:** μ^-, **top right:** μ^+, **bottom left:** π^-, **bottom right:** π^+.

ν_μ QEL CC Reactions

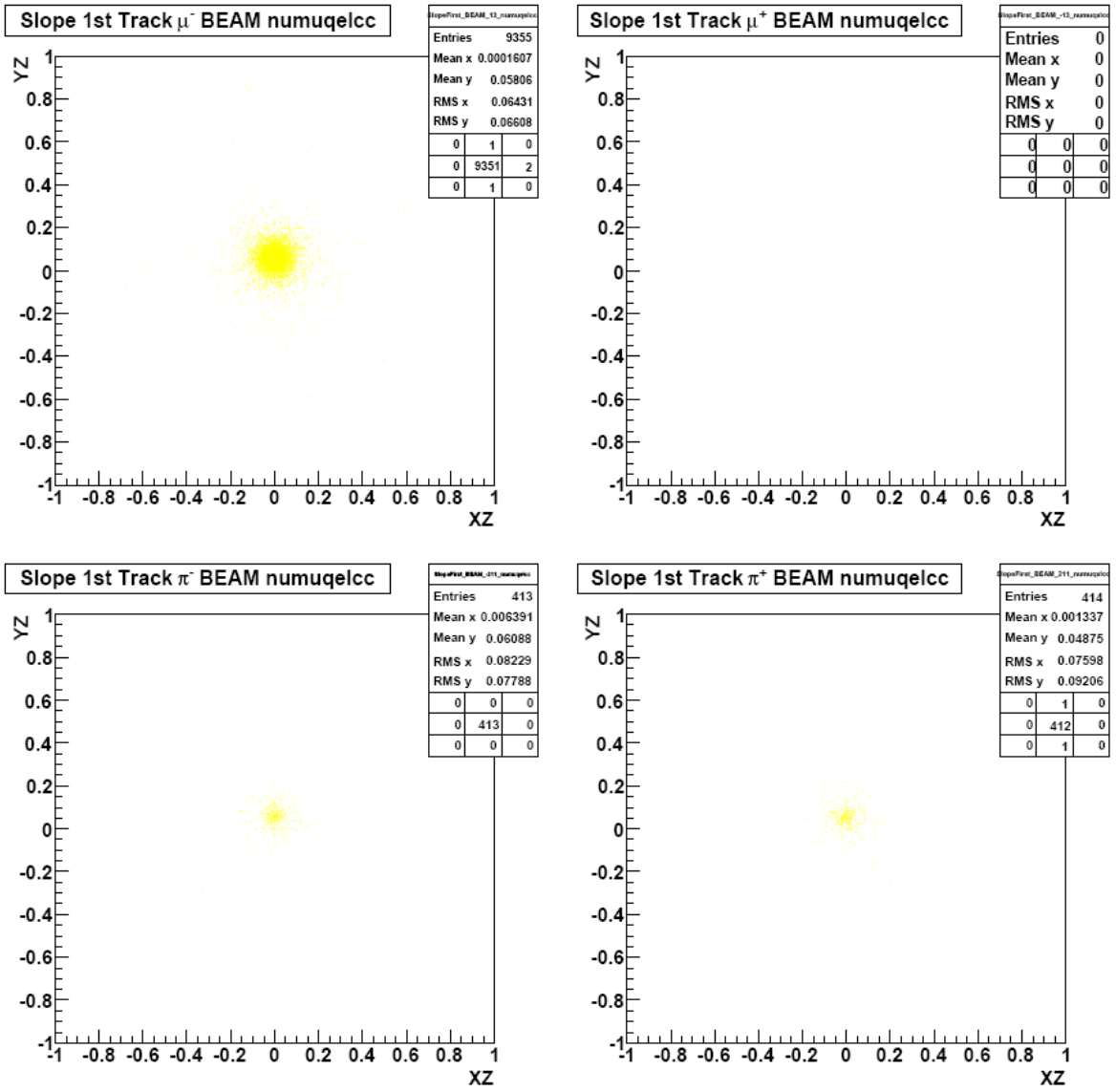

Figure A.58: Beam ν_μ QEL CC reactions reconstructed 1st track slope. **Top left:** μ^-, **top right:** μ^+, **bottom left:** π^-, **bottom right:** π^+.

A.2.11 Reconstructed Distance from 1st Track

All ν_μ Reactions

ν_μ DIS CC Reactions

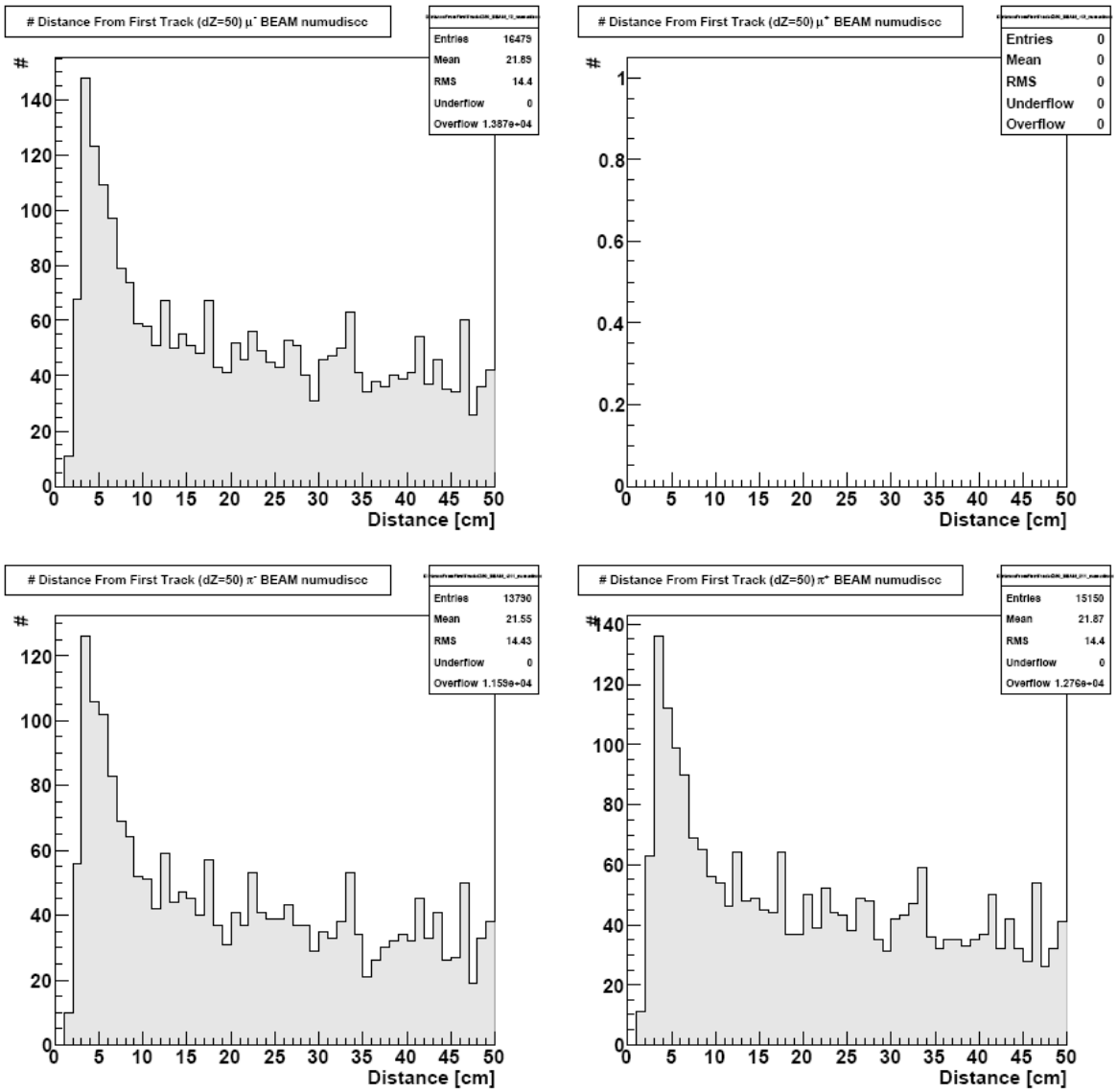

Figure A.59: Beam ν_μ DIS CC reactions reconstructed distance from 1st track. **Top left:** μ^-, **top right:** μ^+, **bottom left:** π^-, **bottom right:** π^+.

ν_μ DIS NC Reactions

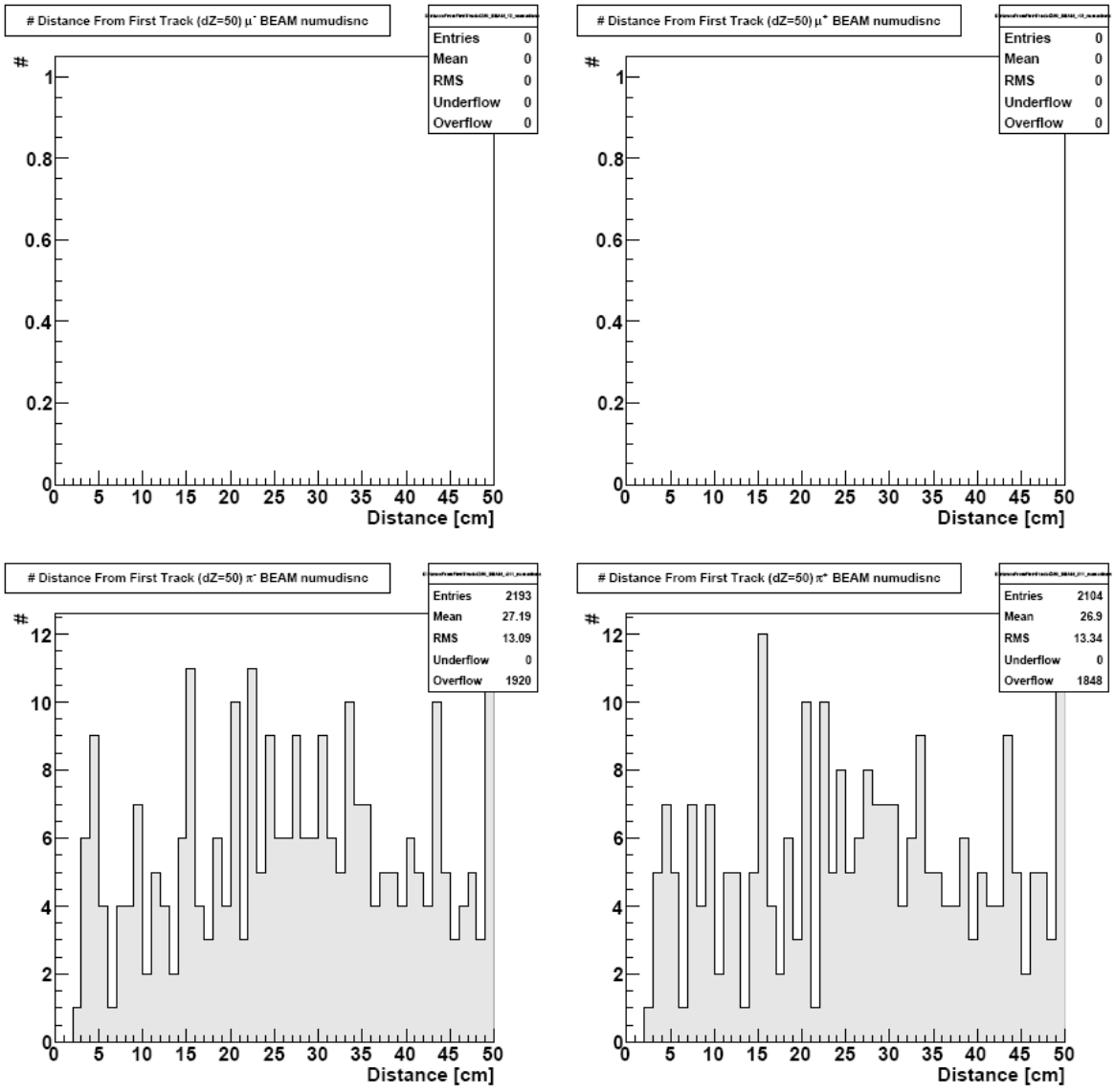

Figure A.60: Beam ν_μ DIS NC reactions reconstructed distance from 1st track. **Top left:** μ^-, **top right:** μ^+, **bottom left:** π^-, **bottom right:** π^+.

List of Figures

List of Tables

Bibliography

[Ada07] T. Adam et al., *The OPERA experiment Target Tracker*, [arXiv:physics/0701153v1], (2007).

[Ber06] C. Berger, *Elementarteilchenphysik*, Springer (German), (2006).

[Bic07] D. Bick, *Data Evaluation and CNGS Beam Localization with the Precision Tracker of the OPERA Detector*, Diploma Thesis, (2007).

[CER10] CERN CNGS website, http://proj-cngs.web.cern.ch/, (2010).

[CHO96] CHORUS Collaboration, *The CHORUS Neutrino Oscillation Search Experiment*, CERN-PPE/96-**196**, (1996).

[CHO99] CHOOZ Collaboration, *Limits on neutrino oscillations from the CHOOZ experiment*, Physics Letters **B466** (1999) 415.

[Chr72] C. J. Christensen at al., *Free-Neutron Beta-Decay Half-Life*, Physical Review **D5N7** (1972) 1628.

[CMT10] CMT website, http://www.cmtsite.org/, (2010).

[Cor10] N. Cords, *Verhältnis der Reaktionszahlen von Neutrinos im Target- und Spektrometerbereich beim OPERA-Experiment*, Diploma Thesis (German), (2010).

[Dak74] J. T. Dakin, G. J. Feldman, $\pi - \mu$ *Separation with a* $235\,\mathrm{g/cm^2}$ *Filter*, Nuclear Instruments and Methods **116** (1974) 323–327.

[Dan62] G. Danby et al., *Observation of High-Energy Neutrino Reactions and the Existence of Two Kinds of Neutrinos*, Physical Review Letters **9N1** (1962) 36.

[Dav98] R. Davis Jr. et al., *Measurement of the Solar Electron Neutrino Flux with the Homestake Chlorine Detector*, The Astrophysical Journal **496** (1998) 505.

[DON00] DONuT Collaboration, *Result from DONUT: First direct evidence for tau-neutrino*, 8th Asia Pacific Physics Conference (APPC), Taipei, Taiwan, (2000).

[DON02] DONuT Collaboration, *Detection and analysis of tau-neutrino interactions in DONUT emulsion target*, Nuclear Instruments and Methods in Physics Research **A493** (2002) 45.

[DON04] DONuT Collaboration, *Identification of neutrino interactions using the DONUT spectrometer*, Nuclear Instruments and Methods in Physics Research **A516** (2004) 21.

[DON07] DONuT Collaboration, *A first measurement of the interaction cross section of the tau neutrino*, [arXiv:hep-ex/0728v1], (2007).

[Eis86] F. Eisele, *High energy neutrino interactions*, Reports on Progress in Physics **49** (1986) 233.

[Els00] K. Elsener, *CNGS – Cern Neutrinos to Gran Sasso*, CERN-SL-2000-**018** EA, (2000).

[Fer06] T. Ferber, *Messung der Gaseigenschaften unter Einfluss von molekularem Sauerstoff und Aufbau eines Gassystems für das Driftröhren-Myon-Spektrometer des OPERA-Detektors*, Diploma Thesis (German), (2006).

[Fer10] T. Ferber, *Monte Carlo Studies on Different Magnetic Field Polarities of the OPERA Spectrometers*, Internal note, (2010).

[Fer10b] T. Ferber, *Unpublished*, Thesis, (2010).

[FLU10] FLUKA website, http://www.fluka.org/, (2010).

[Fra00] E. Fragiacomo et al., *A low-energy π/μ identifier*, Nuclear Instruments and Methods in Physics Research **A439** (2000) 45-52.

[Frr06] A. Ferrari et al., *An updated Monte Carlo calculation of the CNGS neutrino beam*, CERN-AB-Note-2006-**038**, (2006).

[Frr07] A. Ferrari, A. Guglielmi, P. R. Sala *CNGS neutrino beam: from CERN to Gran Sasso*, Nuclear Physics B (Proc. Suppl.) **168** (2007), 169–172.

[fnal10] Fermilab website, http://www.fnal.gov/, (2010).

[Gia07] G. Giacomelli, *The CNGS Neutrino Beam*, [arXiv:physics/0703247v1], (2007).

[Giu04] C. Giunti, M. Laveder, *Neutrino Mixing*, [arXiv:hep-ph/0310238v2], (2004).

[God00] B. Goddard, P. Knaus, G. Schröder, W. Weterings, J. Uythoven, *The New SPS Extraction Channel for LHC and CNGS*, EPAC Proceedings, Vienna, Austria, (2000).

[Her04] C. Heritier, *Identification et localisation des événements neutrino dans le détecteur OPERA*, Thesis (French), (2004).

[Hie07] M. Hierholzer, *Simulation kosmischer Myonen und die Slow-Control-Datenbank für den High-Precision-Tracker des OPERA-Experimentes*, Diploma Thesis (German), (2007).

[INF10] INFN website, http://www.lngs.infn.it/, (2010).

[Jol09] C. Jollet, A. Meregaglia, *Muon identification - Electronic detectors and emulsions matching*, Internal note, (2009).

[Kay05] B. Kayser, *Neutrino Physics*, [arXiv:hep-ph/0506165v1], (2005).

[Kay08a] B. Kayser, *Neutrino Oscillation Phenomenology*, [arXiv:hep-ph/08041121v3], (2008).

[Kay08b] B. Kayser, *Neutrino Mass, Mixing, and Flavour Change*, [arXiv:hep-ph/08041497v2], (2008).

[Kla04] H. V. Klapdor-Kleingrothaus, I. V. Krivosheina, A. Dietz, O. Chkvorets, *Search for neutrinoless double beta decay with enriched 76Ge in Gran Sasso 1990-2003*, Physics Letters **B586N3-4** (2004) 198.

[Kos92] M. Koshiba, *Observational Neutrino Astrophysics*, Physics Reports **220** (1992) 229.

[Kro10] B. v. Krosigk, *Energierekonstruktion hadronischer Schauer in den Sampling-Kalorimetern des Neutrino-Detektors OPERA*, Diploma Thesis (German), (2010).

[Len07] J. Lenkeit, *Kalibrationsmessungen für das Driftröhren-Myon-Spektrometer des OPERA-Detektors*, Diploma Thesis (German), (2007).

[LEP89] OPAL Collaboration, *Measurement of the Z^0 Mass and Width with the OPAL Detectot at LEP*, Physics Letters **B231N4** (1989) 530.

[LEP06] ALEPH, DELPHI, L3, OPAL, SLD Collaborations, LEP Electroweak Working Group, SLD Electroweak and Heavy Flavour Groups, *Precision Electroweak Measurements on the Z Resonance*, [arXiv:hep-ex/0509008v3], (2006).

[Mar09] J. Marteau, *The OPERA global readout and GPS distribution system*, [arXiv:physics/09061494v1], (2009).

[MIN10] MINOS Collaboration, *Official plots*, http://www-numi.fnal.gov/.

[Old09] C. Oldorf, *Studien zu den Nachweiseigenschaften des OPERA-Driftröhrenspektrometers*, Diploma Thesis (German), (2009).

[OPE97] OPERA Collaboration, H. Shibuya et al., *The OPERA emulsion detector for a long-baseline neutrino-oscillation experiment*, Letter of Intent, LNGS-LOI (1997).

[OPE00] OPERA Collaboration, *An appearance experiment to search for $\nu_\mu \leftrightarrow \nu_\tau$ oscillations in the CNGS beam*, Experiment Proposal, CERN/SPSC (2000) 028.

[OPE06] OPERA Collaboration, *First events from the CNGS neutrino beam detected in the OPERA experiment*, *New Journal of Physics* **8** (2006) 303.

[OPE08] OPERA Collaboration, *Emulsion sheet doublets as interface trackers for the OPERA experiment*, [arXiv:physics/08041985v1] (2008).

[OPE09a] OPERA Collaboration, *The OPERA experiment in the CERN to Gran Sasso neutrino beam*, 2009 *JINST* **4** P04018.

[OPE09b] OPERA Collaboration, *The detection of neutrino interactions in the emulsion / lead target of the OPERA experiment*, [arXiv:hep-ex/09032973v1] (2009).

[OPE10] OPERA Collaboration, *Observation of a first ν_τ candidate event in the OPERA experiment in the CNGS beam*, Physics Letters **B691** (2010) 138.

[OPw10] OPERA Collaboration, *Official plots*, http://emulsion.na.infn.it/wiki/.

[Pao10] A. Paoloni, *Cluster size studies on OPERA RPCs*, Internal note, (2010).

[Pas02] E. A. Paschos, J. Y. Yu, *Neutrino interactions in oscillation experiments*, Physical Review **D65** (2002) 1.

[Pau30] W. Pauli, *Dear radioactive ladies and gentlemen*, Phys. Today **31N9** (1978) 27.

[PDG08] C. Amsler et al., (Particle Data Group), Physics Letters **B667**, 1 (2008).

[Per75] M. L. Perl et al., *Evidence for Anomalous Lepton Production in e^+-e^- Annihilation*, Physical Review Letters **35N22** (1975) 1489.

[Pon57] B. Pontecorvo, *Mesonium and Antimesonium*, Sov. Phys. JETP **6** (1957) 429.

[Pon69] B. Pontecorvo, V. Gribov, *Neutrino Astronomy and Lepton Charge*, Physics Letters **B28** (1969) 493.

[Pon76] B. Pontecorvo, *Quark-Lepton Analogy and Neutrino Oscillations*, Physics Letters **B61** (1976) 248.

[Rei56] F. Reines, C. L. Cowan, *The Neutrino*, Nature **178** (1956) 446.

[Rei59] F. Reines, C. L. Cowan, *Free Antineutrino Cross section. 1. Measurement of the Free Antoneutrino Absorption Cross Section by Protons*, Physical Review **113N1** (1959) 273.

[ROO10] CERN ROOT website, http://root.cern.ch/, (2010).

[Roy05] P. Royole-Degieux, *Dévellopement d'un système de scan automatique pour la détection des particules chargées dans OPERA et séparation des π/μ de basse énergie*, Thesis (French), (2005).

[Sch95] P. Schmüser, *Feynman-Graphen und Eichtheorien für Experimentalphysiker*, Springer (German), (1997).

[Sch97] N. Schmitz, *Neutrinophysik*, Teubner Studienbücher Physik (German), (1997).

[Sch08] T. Schwetz, M. Tortola, J. W. F. Valle, *Three-flavour neutrino oscillation update*, *New Journal of Physics* **10** (2008) 113011.

[Sch10] T. Schwetz, M. Tortola, J. W. F. Valle, *Three-flavour neutrino oscillation update*, [arXiv:hep-ph/0808.2016v3] (2010).

[Sir07] G. Sirri, *The CNGS neutrino beam*, Nuclear Physics B (Proc. Suppl.) **172** (2007), 149–151.

[SNO02] SNO Collaboration, *Direct Evidence for Neutrino Flavor Transformations from Neutral-Current Interactions in the Sudbury Neutrino Observatory*, Physical Review Letters **89N1** (2002) 1.

[Ste08] B. Steinke, *Der Trigger für das OPERA-Driftröhrenspektrometer*, Diploma Thesis (German), (2008).

[Ter03] F. Terranova, *A full simulation of charge and momentum reconstruction in the OEPRA spectrometers*, OPERA note, (2003).

[Wol78] L. Wolfenstein, *Neutrino oscillations in matter*, Physical Review **D17N9** (1978) 2369.

[Won07] B. Wonsak, *Die Spurrekonstruktion für das Driftröhren-Myon-Spektrometer des Neutrino-Experiments OPERA*, Thesis (German), (2007).

[Zim05] R. Zimmermann et al., *The precision tracker of the OPERA detector*, Nuclear Instruments and Methods in Physics Research **A555** (2005) 435.

[Zim06] R. Zimmermann, *Status of the OPERA Experiment*, arXiv:physics/0604101v1 (2006).

[Zim07] R. Zimmermann, *A general track reconstruction scheme and its application to the OPERA drift tubes*, Internal note, (2007).

[Zim09] R. Zimmermann, *Charge sign determination with the Precision Tracker of OPERA*, Internal note, (2009).

Hiermit versichere ich, die vorliegende Arbeit selbständig und ausschließlich unter Verwendung der angegebenen Quellen und Hilfsmittel verfasst zu haben.

Mit der Veröffentlichung dieser Arbeit und der Auslage in der Bibliothek bin ich einverstanden.

Hamburg, 18.08.2010

Annika Hollnagel